Université Lille1
Sciences et Technologies

Université Lille Nord de France
Pôle de Recherche et d'Enseignement Supérieur

N° d'ordre : 41469

ECOLE DOCTORALE SCIENCES POUR L'INGÉNIEUR N° 72

THESE

pour obtenir le grade de

DOCTEUR DE L'UNIVERSITE LILLE 1

Spécialité : MÉCANIQUE,ENERGÉTIQUE,MATÉRIAUX

présentée par

Xiaogang WANG

Titre de la thèse :

STUDY OF PLASTIC DEFORMATION IN OLIGO- AND SINGLE CRYSTALS BASED ON KINEMATIC-THERMAL FULL-FIELD MEASUREMENTS

Soutenue le 16 juillet 2014 devant le jury :

Patrick VILLECHAISE	Directeur de Recherche CNRS, ENSMA Poitiers	Président
Hervé PRON	Maître de Conférences-HDR, Université de Reims	Rapporteur
Ludovic VINCENT	Ingénieur de Recherche-HDR, CEA Saclay	Rapporteur
Xavier FEAUGAS	Professeur, Université de La Rochelle	Examinateur
Ahmed EL BARTALI	Maître de Conférences, École Centrale de Lille	Co-Encadrant
Jean-François WITZ	Ingénieur de Recherche CNRS, École Centrale de Lille	Co-Encadrant
Eric CHARKALUK	Directeur de Recherche CNRS, École Centrale de Lille	Co-Directeur de thèse
Philippe DUFRENOY	Professeur, Université Lille 1	Co-Directeur de thèse

Acknowledgements

The work presented in this thesis has been an exciting, as well as a challenging one. I am grateful to the many who have supported me during my Ph.D study at the Laboratoire de Mécanique de Lille. Without their help, none of this would have been possible.

Foremost, I would like to express my sincere gratitude to my advisor Dr. Eric Charkaluk, for his continuous support of my research work. His guidance helped me in all the time of research and writing of this thesis. I have benefited a lot from his extensive knowledge, enthusiasm and enlightening ideas. I could not have imagined having a better advisor and mentor for my Ph.D study. The same gratitude should be attributed to Prof. Philippe Dufrénoy, the other advisor of my Ph.D thesis. I appreciate all his help and guidance in my research work. He provided me the opportunity to embark on a Ph.D thesis in France and the possibility to finish it even after the termination of my doctoral contract.

I appreciate all the technical guidance from Dr. Jean-François Witz, for the hands-on trainings and daily discussions. Those guidances have strengthened my competence significantly that allowed me to make progress effectively. I am also very thankful for all the help from Dr. Ahmed El Bartali. I learned a lot knowledges about plasticity and microstructures from him which constituted as the elements essential in my research work.

I also would like to express my gratitude to Prof. Xavier Feaugas and Dr. Abdelali Oudriss at the Université de La Rochelle. They provided me the opportunity to study the material nickel single crystal and helped me to conduct the experiments which finally allowed me to revisit the phenomenon of work hardening from a new point of view.

Besides them, I would like to thank the rest of my thesis committee: Dr. Hervé Pron, Dr. Ludovic Vincent and Prof. Patrick Villechaise, for their encouragement, insightful comments and interesting questions.

I would like to thank all my colleagues of LML during my Ph.D study, in particular, Rian Seghir, Emmanuel Berté, François Lesaffre, Zhifan Jiang, Long Wang, Pierre Baudoin, Romain Mandard, Nathalie Limodin and all the doctoral candidates and permanent staffs in the MaSTR research group, for their kindness and the friendly atmosphere they have created in the laboratory.

Finally, I would like to thank my parents, all my family and my friends who have always been supporting me and encouraging me during my life.

Contents

General introduction

It is known that any metallic material undergoing plastic deformation will dissipate a part of the mechanical energy input as heat. One of the very interesting issues associated with energy dissipation is that it is usually a very sensitive indicator of the microstructural changes occurring in the material during deformation. The idea of using heat release to study the mechanical behaviour of metallic materials can date back to the 1920s. Farren and Taylor (Farren & Taylor, 1925) conducted such a historical study on metallic bars by recording their heat developments during plastic deformation. In the following work, Taylor and Quinney (Taylor & Quinney, 1934) were able to determine the fraction of dissipated energy in the plastic work and to access the latent energy (or stored energy). With the dislocation theory proposed also by Taylor in the same year (Taylor, 1934), it had been well understood since that time that the latent energy is generally attributed to the development and rearrangement of the dislocations. These seminal works were pursued by numerous researchers in a time period of nearly a century (Stroh, 1953; Bever *et al.*, 1973; Chrysochoos, 1987; Rittel *et al.*, 2007). However, most of investigations remain at a macroscopic scale of specimens, and some insights on the interaction between microstructure evolution and energy changes have been rarely reported. To fulfill such research perspectives, there is a strong demand for more detailed information being experimentally accessible, such as the distributions of temperature and strain on the material surface during deformation. Recently, it became realizable thanks to the emergence of full-field measurement techniques, e.g., IRT (InfraRed Thermography) for temperature measurement and DIC (Digital Image Correlation) for displacement and strain measurements. Thanks to these technical advances, different energy aspects (mechanical energy, dissipated energy and stored energy) involved in a plastic deformation are hopefully to be resolved within a two-dimensional space. Relevant studies (Bodelot *et al.*, 2009; Chrysochoos *et al.*, 2010) were carried out on this line of research and have been recently pushed into a microstructure scale (Saai *et al.*, 2010; Badulescu *et al.*, 2011; Seghir *et al.*, 2013).

The first interest of the present study is to try to establish an experimental energy balance of metal deformation at the microstructure scale. It is in the continuity with the thesis studies of Bodelot (Bodelot, 2008) and Seghir (Seghir, 2012) on 316L stainless steel polycrystals, in which a local energy balance at the grain scale was established based on the kinematic-thermal coupled measurement. Indeed, their studies reveal more details on the energy evolution and its dependence on the microstructure development during deformation. At the same time, they demonstrate also the complexity of the thermomechanical behaviour at the microstructure scale. In our work, this complexity is hoped to be eased in the aspect of material, e.g., using the specimen with simple and well-defined crystallographic structure. To this end, oligocrystals of pure aluminum and single crystals of pure nickel are chosen as the testing materials in this work. Our efforts are also embodied in the

technical improvements, e.g., metrological studies on IRT and DIC, development for novel experimental set-ups compatible with the studied materials. All these improvements are expected to bring us new occasions to study the thermomechanical behavior of materials based on the full-field measurement and to build an experimental energy balance at the microstructure scale.

Another interest of our research is to study the work hardening problem in single crystal deformation based on the full-field measurement. A particular subject addressed in this investigation is the possible link between work hardening and strain/energy evolution in a heterogeneous deformation process.

The phenomenon of work hardening has drawn the attentions of metallurgists from very early times (Tylecote, 1976). A micromechanism explanation on crystal plasticity was once an enduring challenge in materials science until the introduction of the dislocation theory in the 1930s. Now it is well known that low temperature plastic deformation results from the long range movement of dislocations by glide under the action of applied stress. It is also common knowledge that the work hardening process is accompanied with the formation of new dislocations, dislocation interactions and an increment of dislocation density. With the advent of various experimental means for an observation at the microscopic scale, the dislocation structures and their evolution in different work hardening stages have been extensively studied in the past decades (Basinski & Basinski, 1979; Mughrabi, 1983; Kocks & Mecking, 2003). The microstructure observations generally showed that dislocations in deformed materials are not distributed randomly or homogeneously but, instead, exhibit a strong tendency to cluster locally (Mughrabi, 1993). This phenomenon is reasonably to be understood as the movement, storage and modification of dislocation structures are ultimately an effect of the current strain (Sevillano, 1993), which is not homogeneous either at the microscale or at the macroscale (Magid *et al.*, 2009). However, the strain heterogeneity and its role played in the work hardening process of single crystal deformation were few discussed (Takamura, 1987). Today the full-field displacement and strain measurements provide a new occasion to revisit the work hardening problem from the point of view of strain heterogeneity. Apart from strain, another important aspect of work hardening is the energy evolution, in particular the evolution of latent energy, which represents a direct result of the dislocation structures evolution during plastic deformation. It is thus also of great interest to investigate the relationship between latent energy evolution and work hardening. The kinematic-thermal fully-coupled measurement allows to study these subjects as a whole, and provides the opportunity to gain some insights on the interactions between them (strain heterogeneity, energy storage and work hardening).

This thesis is made of five chapters which are organized in the following order. First, a bibliographic study is presented in chapter 1 that discourses the thermomechanical behaviours of materials from the macroscopic scale to a microstructure scale, as well as the advantages of applying full-field measurements to such studies. Then, the two subsequent chapters are dedicated to the technical developments for realizing a quantitative kinematic-thermal fully-coupled measurement: chapter 2 the metrological studies on IRT and DIC, and chapter 3 the coupling of the two techniques. Tests, measurements and macroscopic analyses of nickel single crystals are presented in chapter 4, and the same issues for aluminum oligocrystals can be found in appendix A. Finally, a comprehensive analysis on the

kinematic-thermal full-field measurement results for nickel single crystals are detailed in chapter 5.

Chapter 1

Bibliographic study

The axis of the bibliographic study is to review the reference works on the mechanical behaviours of metals from macroscopic scale to grain scale from a thermomechanical point of view. It will be strongly combined with the recent applications of full-field measurements of temperature and strain in such studies. Hence, this chapter is unfolded into three sections: 1) framework of thermodynamics, 2) research works at the macroscopic scale and 3) research works at the grain scale.

1.1 Framework of thermodynamics

Before presenting the thermomechanical behaviours of materials, a framework of thermodynamics is first introduced. We invite the readers to peruse it with attention, in particular the section "heat sources", as certain terms defined in this part will be frequently used in the following sections. This is also why this "classical" framework is still preferred to be introduced in this study, even though it has been already detailed in many references.

The framework of thermodynamics adopted in this study is established based on continuum mechanics. For a complete development of this theoretical framework, the readers may refer to (Chrysochoos, 1987; Lemaitre & Chaboche, 1994), while in this study only the most important results will be presented.

1.1.1 First law

The first law of thermodynamics is the law of energy conservation. It is usually formulated by stating that the change in the internal energy of a closed system is equal to the amount of heat supplied to the system minus the amount of work done by the system on its surroundings.

For a volume D with the boundary ∂D, the first law can be expressed as

$$\frac{d}{dt}(E + K) = W_e + Q \tag{1.1}$$

where

– E is the internal energy, as $E = \int_D \rho e dV$, where e is the specific internal energy per unit of weight and ρ the density .

– K is the kinetic energy, as $K = \int_D \rho \overrightarrow{v} \cdot \overrightarrow{v} dV$, where $\overrightarrow{v}$ is the velocity field.

– W_e is the real power of external forces.

– Q is the heat rate received by the system, as $Q = \int_D r dV - \int_{\partial D} \overrightarrow{q} \cdot \overrightarrow{n} dS$, where r is the volume density of the heat generation at a distance, $\overrightarrow{q}$ is the heat flux and $\overrightarrow{n}$ is the normal direction to ∂D at any point.

Taking into account the kinetic energy theorem

$$\frac{d}{dt}K = \dot{K} = W_{(x)} + W_i \tag{1.2}$$

where W_i is the real power of internal forces.

The local form of the energy conservation becomes

$$\rho \frac{de}{dt} = r - div(\overrightarrow{q}) - w_i \tag{1.3}$$

where w_i is the power of internal forces per unit volume.

1.1.2 Second law

The second law of thermodynamics will help to clarify the concepts of intrinsic and thermal dissipation, by introducing the variables T, temperature, and s, entropy density. The rate of entropy production is always greater than or equal to the rate of heat received divided by the temperature, which results in

$$\rho \frac{ds}{dt} - \frac{r}{T} + div\left(\frac{\overrightarrow{q}}{T}\right) \geq 0 \tag{1.4}$$

Thus, the entropy production $\triangle S$ can be expressed as

$$\triangle S = \rho \frac{ds}{dt} - \frac{r}{T} + div\left(\frac{\overrightarrow{q}}{T}\right) = \frac{d}{T} \geq 0 \tag{1.5}$$

where d is the dissipation term, $d = T \triangle S \geq 0$.

The external heat source r can be canceled out by using the energy balance Eq. 1.3, and recall that $div\left(\frac{\overrightarrow{q}}{T}\right) = \frac{div\overrightarrow{q}}{T} - \frac{\overrightarrow{q} \cdot gradT}{T^2}$, inequality 1.4 becomes

$$\rho\left(T\frac{ds}{dt} - \frac{de}{dt}\right) - w_i - \frac{\overrightarrow{q}}{T} \cdot \overrightarrow{grad}T \geq 0 \tag{1.6}$$

Introducing the specific free energy ψ as $\psi = e - Ts$, depending on the n state variables α_j chosen to describe the system, we obtain the fundamental inequality of Clausius-Duhem

$$-w_i - \rho\frac{\partial \psi}{\partial \alpha_j}\dot{\alpha}_j - \frac{\overrightarrow{q}}{T}\overrightarrow{grad}T \geq 0 \qquad (j = 1 \cdots n) \tag{1.7}$$

The left term of the inequality 1.7 is the total dissipation d, which can usually be decomposed into two parts:

– Intrinsic volume dissipation d_1 as

$$d_1 = -w_i - \rho \frac{\partial \psi}{\partial \alpha_j} \dot{\alpha_j} \tag{1.8}$$

– Thermal volume dissipation d_2 as

$$d_2 = -\frac{\overrightarrow{q}}{T} \overrightarrow{grad} T \tag{1.9}$$

Thus the total dissipation d is the sum of intrinsic dissipation and thermal dissipation

$$d = d_1 + d_2 \tag{1.10}$$

In the deformation of metallic materials, the intrinsic dissipation is generally linked to microstructural changes of materials (e.g., dislocation movements) and thermal dissipation to heat diffusion.

The power of internal forces per unit volume w_i can be expressed as

$$w_i = -\sigma : D \tag{1.11}$$

where σ is the Cauchy stress tensor and D the strain rate tensor. Under the small perturbation hypothesis, w_i becomes

$$w_i = -\sigma : \dot{\varepsilon} \tag{1.12}$$

Though inequality 1.7 is satisfied whatever the envisaged transformation, it has a special form for the case of an ideal elastic transformation. Assuming that a elastic transformation takes place at a constant and uniform temperature and it does not change the internal variables, we can obtain an equation

$$\sigma = \rho \frac{\partial \psi}{\partial \varepsilon^e} \tag{1.13}$$

In this case, the dissipation is zero and the thermodynamic process is reversible.

1.1.3 Heat sources

In order to understand and specify the different heat sources in the thermodynamic process, the potential energy ψ needs to be integrated in the law of energy conservation. By choosing the temperature T and the state variables α_j, the differential of potential energy takes the form

$$\dot{\psi} = \frac{\partial \psi}{\partial \alpha_j} \dot{\alpha_j} - T\dot{s} \tag{1.14}$$

As the specific entropy $s = -\frac{\partial \psi}{\partial T}$, so

$$\dot{s} = -\frac{\partial^2 \psi}{\partial T^2}\dot{T} - \frac{\partial^2 \psi}{\partial T \partial \alpha_j}\dot{\alpha}_j \tag{1.15}$$

Thus

$$\rho\frac{de}{dt} = \rho\dot{\psi} = \rho\frac{\partial \psi}{\partial \alpha_j}\dot{\alpha}_j - \rho(T\frac{\partial^2 \psi}{\partial T^2}\dot{T} + T\frac{\partial^2 \psi}{\partial T \partial \alpha_j}\dot{\alpha}_j) \tag{1.16}$$

The local energy conversation can therefore be developed as

$$\rho\frac{\partial \psi}{\partial \alpha_j}\dot{\alpha}_j - \rho(T\frac{\partial^2 \psi}{\partial T^2}\dot{T} + T\frac{\partial^2 \psi}{\partial T \partial \alpha_j}\dot{\alpha}_j) = r - div(\overrightarrow{q}) - w_i \tag{1.17}$$

Finally put $C = -T\frac{\partial^2 \psi}{\partial T^2}$ (or $C = -T\frac{\partial s}{\partial T}$), the specific heat at α_j constants, the energy balance leads to the coupled heat equation:

$$\rho C\dot{T} + div\overrightarrow{q} = d_1 + \rho T\frac{\partial^2 \psi}{\partial T \partial \alpha_j}\dot{\alpha}_j + r \tag{1.18}$$

The three terms on the right of the equation represent the heat sources: the intrinsic dissipation, thermomechanical couplings and external sources. The two terms on the left mean that a portion of the heat energy increases the temperature and the rest is spread by conduction. This is the energy balance equation that used most frequently in the framework of thermodynamics. The different heat sources, especially the intrinsic dissipation, will be detailed and specialized for the self-heating test in the following studies.

1.2 Research works at the macroscopic scale

The thermomechanical behaviours of materials can be classified according to the expected deformation types at room temperature: elastic, visco-elastic, elasto-plastic, etc. In this study, only elasticity and elasto-plasticity of metallic materials are discussed, and the emphasis will be placed on the cyclic plasticity, which leads to the fatigue phenomenon.

The bibliographic study in this section is mainly concerned with the "classical" studies at the macroscopic scale. Both their achievements and shortcomings are resumed, and the necessity for transforming the research from macroscopic scale to the microstructure scale is pointed out.

1.2.1 Elasticity

In an elastic deformation under adiabatic conditions, the temperature of the deforming specimen changes. This thermoelastic effect was first recognized by Weber in 1830 and was given a theoretical foundation in 1853 by Lord Kelvin. Kelvin derived a linear relationship between the temperature change of a solid and the change in the sum of the principal stresses for isotropic materials.

In the case of a linear isotropic elastic behaviour, the total deformation ε is equal to the elastic deformation ε^e. Thus, the energy balance Eq. 1.18 turns to be

$$\rho C\dot{T} - k \triangle T = \rho T \frac{\partial^2 \psi}{\partial T \partial \varepsilon^e} \dot{\varepsilon^e} + r \tag{1.19}$$

where k is the isotropic thermal conductivity.

Assuming that the elastic behaviour occurring under the adiabatic condition in a tensile (or compression) test and satisfying the following conditions: it does not exist any external heat source and the strain rate is high enough to neglect the heat conduction effects. In this case, Eq. 1.19 can be simplified by

$$\rho C\dot{T} = \rho T \frac{\partial^2 \psi}{\partial T \partial \varepsilon^e} \dot{\varepsilon^e} \tag{1.20}$$

The only heat source in thermoelasticity is the thermomechanical coupling term. The resulting temperature variations are assumed very low, by using the classical Hooke's law between the stress and strain, the conventional thermoelasticity equation can be achieved, which links the heat generation rate to the time derivative of the stress tensor σ

$$\dot{T} = -T \frac{\alpha}{\rho C} tr(\dot{\sigma}) \tag{1.21}$$

where α is the thermal expansion coefficient.

Eq. 1.21 indicates that a perfect elastic behaviour is accompanied with temperature decrease in a tensile test and temperature increase in a compression test. The experimental validation of this thermoelastic effect using non-contact infrared technique was first conducted by Belgen in 1967 (Belgen, 1967). In this pioneering work, he used an infrared radiometer to measure the small temperature variation in a vibrating cantilevered beam, and related it to the stress through the thermoelasticity theory.

The potentials of the thermoelasticity theory for the stress assessment were developed soon after. In 1978 the first prototype of the commercially available thermography system for TSA (Thermoelastic Stress Analysis) was developed by Mountain and Webber (Mountain & Webber, 1978), namely the SPATE (Stress Pattern Analysis by Thermal Emission) system. After that a British company began developing the first commercial SPATE system, and a major technique improvement appeared in the early 1990s when the focal plane array detector was incorporated in place of the single cell detector. In the following years, the thermoelasticity has been extensively studied by using infrared camera (Offermann *et al.*, 1996; Offermann *et al.*, 1997; Offermann *et al.*, 1998).

In the case of cyclic loading, for a stress change $\Delta\sigma$ (in the sum of principal stresses), the temperature change related to the thermoelasticity can be derived

$$\Delta T = -\frac{\alpha}{\rho C} T \Delta\sigma = -K_m T \Delta\sigma \tag{1.22}$$

where $K_m = \frac{\alpha}{\rho C}$ is conventionally defined as the thermoelastic coefficient of the material.

The above relation is valid provided that the adiabatic condition prevails. For TSA applications an adiabatic condition can be achieved by cyclic loading with an adequate frequency, in order to maintain a dynamic energy equilibrium.

Here it is worth emphasizing that the thermoelasticity exists in any elasto-plastic behaviour (monotonic, cyclic or fatigue), when the heat dissipation is estimated from temperature variations, the contribution of thermoelasticity should be isolated. The following parts of plasticity and fatigue will make this point more straightforward. For readers more interested in the applications of thermoelasticity for stress evaluation and parameters identifications in solid mechanics, please refer to the reviews (Stanley, 2008; Greene *et al.*, 2008).

1.2.2 Monotonic plasticity

The energy aspect is an important issue in studying the plasticity of metallic materials. When a metal is subjected to plastic deformation, most of the plastic work (or cold work) is dissipated as heat while the left portion is stored in the material, so-called stored energy or latent energy. The stored energy is associated with microstructural physical changes of materials. To assess this stored energy is important, which can help to understand the plasticity as well as the microstructural damage mechanism.

The plasticity discussed in this section concerns only the monotonic plasticity. The characteristics of cyclic plasticity is different in many ways from that of monotonic plasticity, which will be discussed in the next section.

1.2.2.1 Energy storage

If the metal is plastically deformed under adiabatic conditions, its temperature rises; if the plastic deformation is carried out isothermally, heat is evolved. These effects are characteristics of plastic deformation and, in contrast to the thermoelastic effect, have the same sign for the tension and compression deformation processes. In other words, the plastic deformation signifies an irreversible process in thermodynamics as the intrinsic dissipation is possible.

In the case of elasto-plastic deformation, the total strain ε can be divided into two parts: elastic strain ε_e and plastic strain ε_p

$$\varepsilon = \varepsilon_e + \varepsilon_p \tag{1.23}$$

The ideal plastic material, by definition, deforms with no work hardening. For the plastic deformation of such a material, the whole work is converted into heat, in other words, no energy is left within the material. However, no actual metal is ideally plastic. There is always a part of the energy that is stored in the material, owing to the facts such as an increase of the dislocation density during the cold work process.

By separating the elastic component from the plastic component, the energy balance equation Eq. 1.18 can be reformulated by

$$\rho C\dot{T} - k\Delta T = d_1 + \rho T\frac{\partial^2\psi}{\partial T\partial\varepsilon^e}\dot{\varepsilon^e} + \rho T\frac{\partial^2\psi}{\partial T\partial\alpha_j}\dot{\alpha_j} + r \tag{1.24}$$

The different energy aspects involved in this energy balance are illustrated in Fig. 1.1. The irreversible energy parts related to plastic deformation are detailed below.

$$W_{mechnical} = E_{total} = \left| \begin{array}{l} E_{elastic} \\ + \\ E_{plastic} \end{array} \right. = \left| \begin{array}{ll} E_{intrinsic} & \\ \quad dissipation & \\ + & (\beta = \frac{E_{stored}}{E_{plastic}}) \\ E_{stored} & \end{array} \right.$$

Figure 1.1: Different energy aspects involved in an elasto-plastic deformation of metals

According to Eq. 1.8, the intrinsic dissipation d_1 can be obtained by

$$d_1 = -w_i - \rho\frac{\partial\psi}{\partial\varepsilon^e}\dot{\varepsilon^e} - \rho\frac{\partial\psi}{\partial\alpha_j}\dot{\alpha_j} = -w_i^p - \rho\frac{\partial\psi}{\partial\alpha_j}\dot{\alpha_j} \tag{1.25}$$

where the power of the plastic work $w_i^p = w_i + \rho\frac{\partial\psi}{\partial\varepsilon^e}\dot{\varepsilon^e} = -\sigma : \dot{\varepsilon^p}$.

Then, the power of the stored energy $\dot{E_s}$ can be expressed by

$$\dot{E_s} = \rho\frac{\partial\psi}{\partial\alpha_j}\dot{\alpha_j} \tag{1.26}$$

The fraction of the stored energy in the plastic work can be defined as

$$\beta = \frac{E_s}{W_p} = \frac{E_s}{-\sigma : \varepsilon^p} \tag{1.27}$$

where W_p stands for the plastic work.

β is an important parameter that is used frequently for the characterization of the evolution of stored energy.

1.2.2.2 Quantitative assessment

In order to establish the energy balance of a tensile test at low strain rate, for more than a century numerous studies have been dedicated on measuring the fraction of the stored energy during the work hardening.

The earliest contributions can be attributed to Taylor and his collaborators (Farren & Taylor, 1925; Taylor & Quinney, 1934). These authors measured the fraction β for mild steel and copper specimens, and found that it was of the order of 10%. The result for the

annealed mild steel is shown in Fig. 1.2.

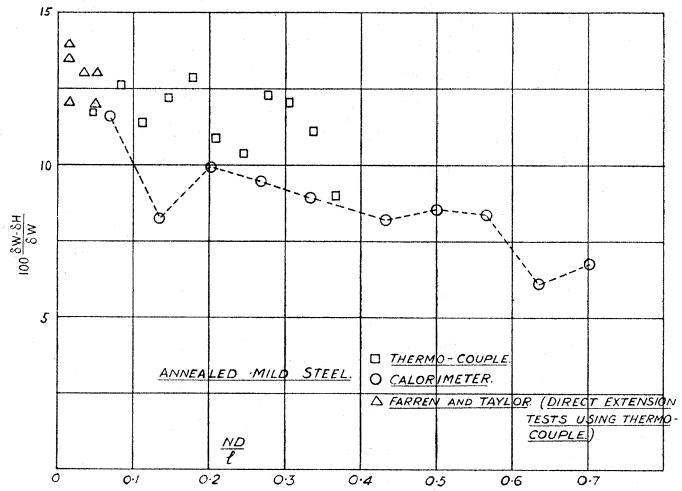

Figure 1.2: β measured in specimen subjected to plastic twisting (Taylor & Quinney, 1934)

This study showed that the fraction of stored energy β was strain dependent during the plastic deformation. It had a relatively high value at the beginning and then decreased and stabilized at a certain level, around 10% for steel. Nevertheless, the study (Chrysochoos, 1987) showed that at a low macroscopic plastic deformation β can reach higher than 30% even when it turned into the stabilization stage.

In the above works the measurements (temperature, strain) were generally realized during the deformation. These methods are classified as "single-step methods". The alternative methods are called "two-step methods": the deformation is carried out first and the stored energy is measured at a later time (Bever *et al.*, 1973).

In two-step methods the stored energy is found by comparing the thermal behaviour of the cold-worked specimen with that of a standard specimen in a suitable process, for example, annealing. The hypothesis is that the stored energy produced in the cold work, along with the dislocation multiplications in the microstructure, can be released by the special thermal treatments as the dislocations are recovered.

The stored energy can be estimated from the measurements of the heat dissipation and expended energy (Chrysochoos & Louche, 2000; Louche & Chrysochoos, 2001). These approaches are relatively indirect. It is also very interesting to find the ways to determine the stored energy more directly, for example, based on the microstructural changes.

Observation of the intragranular misorientations provides a way to access the stored energy (Godfrey *et al.*, 2005). Assuming that the latent energy during the cold work is mainly stored in the form of dislocations and the low-angle grain boundaries dominate in the microstructure, the stored energy can be estimated by

$$E_s = S_v\gamma + E(\rho_0) \tag{1.28}$$

where S_v is the area per unit volume of boundary, γ the boundary energy per unit area and $E(\rho_0)$ the contribution from individual dislocations in the volume between the dislocation boundaries. Here it is worth noting that there are two kinds of dislocations: GNDs (Geometrically Necessary Dislocations) and SSDs (Statistically Stored Dislocations). If only one of them is taken into account in the calculation, the stored energy will be unavoidably underestimated. Some more detailed studies about the microstructural based methodology will be further discussed in section 1.3.3.

Another noteworthy philosophy is to access the stored energy directly from the macroscopic stress-strain curve. Oliferuk (Oliferuk & Maj, 2009) considered that an important part of the stored energy was related to the residual stress, which can be extracted directly from the macroscopic stress-strain curve using a graphical approach, as shown by Fig. 1.3. The area AEB in the figure represents this significant part of stored energy related to residual stress. For readers interested in the theoretical development of this methodology, please refer to the paper (Oliferuk & Maj, 2009; Aravas *et al.*, 1990).

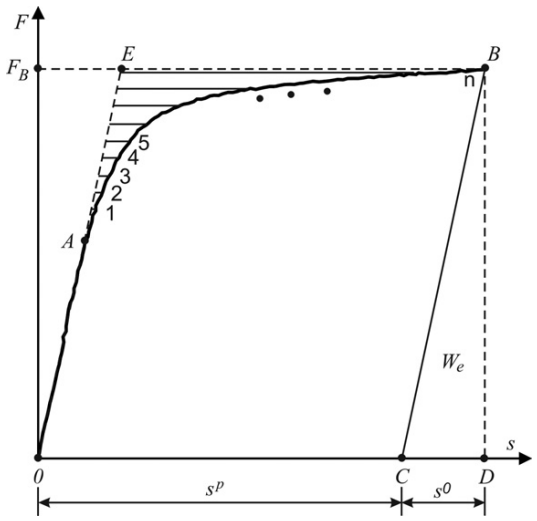

Figure 1.3: Calculation of the part of stored energy from stress-strain curve (Oliferuk, 2009)

1.2.3 Cyclic plasticity and fatigue

In this section, cyclic plasticity and high cycle fatigue are discussed. The emphases are placed on their thermomechanical effects and how the different thermal indicators are used in studying these problems. Besides, the generally used image processing approaches and relevant interpretations are also introduced in order to promote a better understanding of the current researches at the macroscopic scale.

1.2.3.1 Cyclic plasticity

In the case of cyclic plasticity, for a given material, there is a wide variety of mechanical responses due to the control mode of the test (stress or strain control) and the stress lev-

els (Francois *et al.*, 1992). In most of cases, the stress ratio R_σ ($= \sigma_{min}/\sigma_{max}$) also plays an important role.

Not considering the particular case of the "ratchetting" effect, two typical types of responses can be obtained depending on the loading conditions:

1) Elastic shakedown: after initial cycles the deformation becomes stabilized with a cyclic elastic behaviour at a steady state, as shown in Fig. 1.4(a)

2) Plastic shakedown: after initial cycles the deformation becomes stabilized with an elasto-plastic behaviour at a steady state, as shown in Fig. 1.4(b).

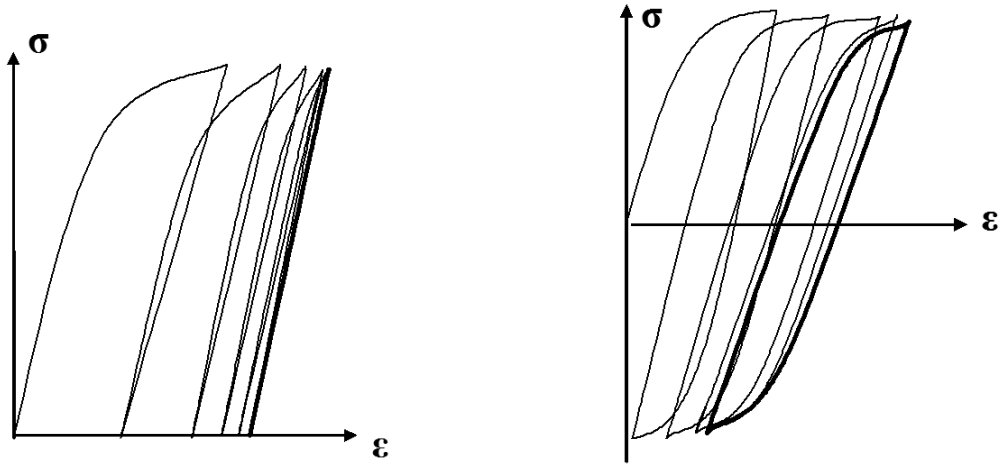

Elastic shakedown (a)

Plastic shakedown (b)

Figure 1.4: The two typical mechanical behaviours in cyclic tests: elastic shakedown and plastic shakedown

It is of great interest to observe the variations of the stored energy and/or dissipated energy in the processes of elastic or plastic shakedown.

Yang (Yang *et al.*, 2001) studied the thermomechanical behaviour of a martensitic steel cyclically loaded near its macroscopic elastic limit. The stress-strain curve and temperature variation profile were recorded simultaneously, as shown in Fig. 1.5(a) and (b), respectively. The figure shows clearly that a steady state is reached on the same time period for the strain and for the temperature, right after the first 20 cycles of the cyclic loading. The temperature showed a rapid fall before reaching the steady state, which can be attributed to the elastic shakedown phenomenon in the current case of a positive stress ratio ($R_\sigma = 0.2$).

The mechanical energy dissipated per cycle, proportional to the area of the hysteresis loops of the stress-strain curve, varies substantially during cyclic plastic deformation. Although some of this energy is blocked in the material, it is reasonable to state that this

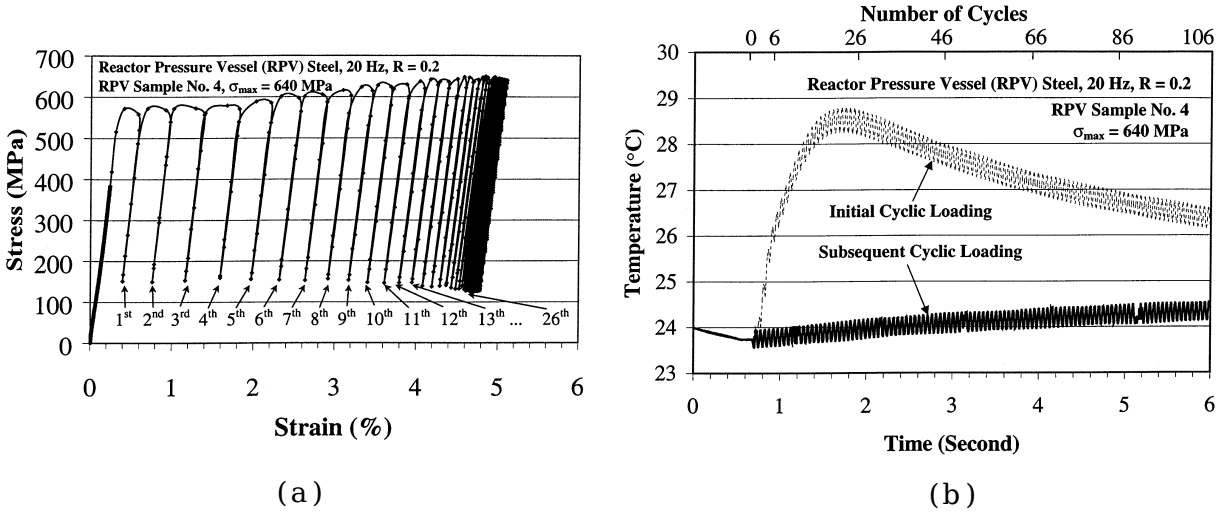

Figure 1.5: (a)Stress versus strain profile (b)Temperature versus time profile (Yang *et al.,* 2001)

mechanical behaviour has a major impact on the intrinsic dissipation, which therefore should decrease as cycling in the case of elastic shakedown, and remain approximately constant in the case of plastic shakedown (Maquin, 2006).

This inference was verified in the following work of Maquin and Pierron (Maquin & Pierron, 2009). In this study they managed a test to observe the intrinsic dissipations of metallic specimens during the very first cycles of mechanical loading but at two different aspect ratios ($R_\sigma = 0.1$ and $R_\sigma = -1$). In this specific study case, the positive stress ratio ($R_\sigma = 0.1$) corresponds to an elastic shakedown behaviour of material and the negative one ($R_\sigma = -1$) corresponds to a plastic shakedown behaviour. A comparison of the thermal behaviours in respect to the two loading conditions is shown by Fig. 1.6(a), where it can be found that the energy dissipations show the evolution trends as predicted.

The mechanism of heat generation was also interpreted: the extra energy produced at the very first cycles of the test was associated to the micro-plasticity (the macroscopic stress is still under the conventional yield stress) and the stable energy part through the whole test is due to the visco-elastic effect ("internal friction"), as schematically illustrated in Fig. 1.6(b). E_p is the energy generated by the micro-plasticity effect and E_{VE} the energy produced by the visco-elastic effect. According to this interpretation, the internal friction effect in the plastic shakedown process should be much less important than that in the elastic shakedown process (Maquin & Pierron, 2009).

Internal friction is a term that gathers a number of dissipative phenomena attributed to the movements of atoms from their equilibrium positions. This is caused either by some local defects in the lattice or by the movements of dislocations (Caillard & Martin, 2003). The links between intrinsic dissipation (or stored energy) and internal friction (or visco-elasticity) on the macroscale were demonstrated by many studies (Meyendorf *et al.*, 2002; Audenino *et al.*, 2003; Crupi, 2008; Connesson *et al.*, 2011).

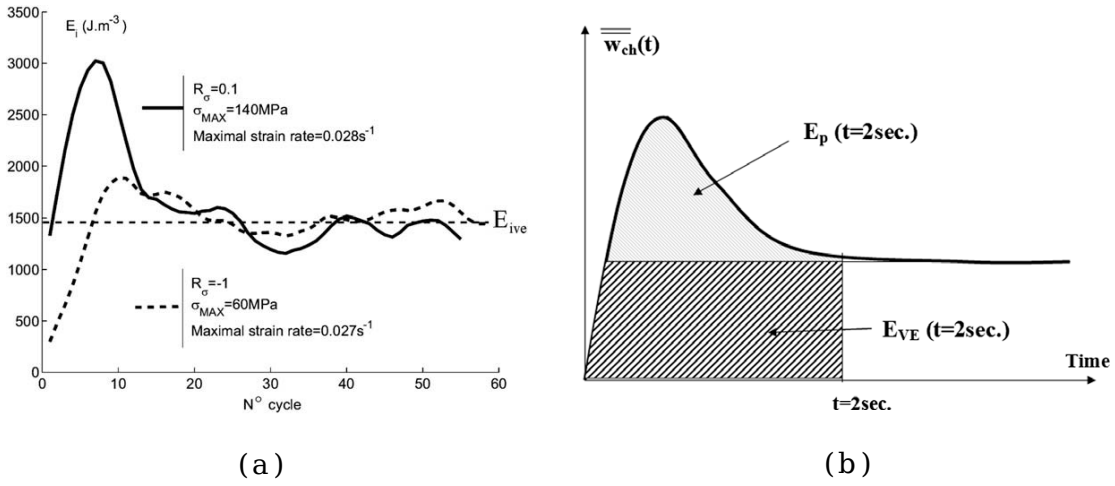

Figure 1.6: (a)Comparison of the evolution of dissipated energy per cycle for two tests: one at $R_\sigma = 0.1$ and one at $R_\sigma = -1$ (b)Principle of calculating dissipated energies E_p and E_{VE} during the first two seconds of the test (Maquin & Pierron, 2009)

1.2.3.2 High cycle fatigue

In high cycle fatigue, the metallic material is cyclically loaded below the macroscopic elastic limit, the final failure may occur after $10^5 - 10^6$ cycles or more cycles strongly depending on the material properties. In this case, the traditional macroscopic constitutive laws can not account for the dissipation due to the dislocation movements at the onset of micro-plasticity. Therefore, few experimental studies are based on a descriptive model, and often limited to simple observations or assumptions (Maquin, 2006).

Nevertheless, it is of great interest to understand the fatigue phenomenon and build the fatigue criteria from the standpoint of energy conversion. The first attempt can be attributed to a special thermography-based methodology developed for the fatigue properties assessment. The work principle is that it considers, in general, the intrinsic dissipation (or temperature) as a very sensitive indicator of the fatigue damage, which is potential to be used for evaluating the fatigue properties of metallic materials.

A popular experimental approach is to observe the heat dissipation levels of the specimen when subjected to different applied loads that are progressively increasing. Some first experimental results (Luong, 1995; Luong, 1998; Rosa & Risitano, 2000) suggest that the stress level that leads a sharp increase of the temperature on the material surface corresponds to its fatigue limit, the one which is conventionally defined in the case of high cycle fatigue. Due to its quickness to assess the fatigue limit comparing to the traditional method, this methodology is also named by the "rapid fatigue limit determination" method. A typical example illustrated by the following figure shows how the method determines the fatigue limit by using a graphical approach.

This philosophy was afterwards pursued to evaluate the fatigue *S-N* curve by introducing a "limiting energy" concept (Fargione *et al.*, 2002). It assumes that the material has a threshold of the dissipation energy during the high cycle fatigue before the failure occurs,

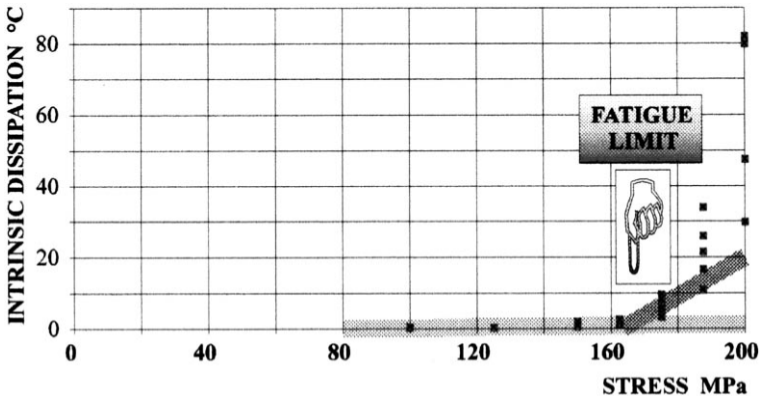

Figure 1.7: Graphical determination of fatigue limit of a connecting rod (Luong, 1998)

and this threshold, i.e., the "limiting energy", can be characterized by a function based on the surface temperature variation of the tested specimen. This method was recently improved by introducing an energy expression of Miner's rule (Wang *et al.*, 2010), the linear damage accumulation law.

The above methods showed some applications in the industry (Krapez *et al.*, 1999; Krapez & Pacou, 2002), but until now it is still not a mature technology. One of the issues concerning this kind of methodology is still open owing to the fact that these approaches generally do not rely on a solid physical basis, in other words, they are more likely to be sorted as empirical formulas.

In the recent works, Jiang (Jiang *et al.*, 2004) considered that the temperature changes during fatigue were related to the hysteresis effect, which can be integrated into the classical Coffin-Manson formula, thus capable of predicting the fatigue life for Low Cycle Fatigue (LCF). While other authors (Doudard *et al.*, 2007; Poncelet *et al.*, 2007; Poncelet *et al.*, 2010) proposed the descriptive models in the domain of High Cycle Fatigue (HCF). And there are also other kinds of indicators derived from the temperature measurement, like the entropy, were used to predict the fatigue properties (Naderi & Khonsari, 2010; Amiri & Khonsari, 2010; Ezanno *et al.*, 2013).

In the author's opinion, by integrating temperature variation as a variable into the classical fatigue criteria or descriptive models is a hopeful research perspective, but it can not be easily achieved if the bridge between the thermal behaviour and the stress-strain state is not clear. To this end, the temperature is preferred to be converted into energy and to be linked with the mechanical energy input, towards to build an experimental energy balance on the macroscale. In the following we will discuss how to process the raw temperature data (or thermal image) and its interpretations associated with the material mechanical behaviours.

1.2.3.3 Image processing and interpretations

Chrysochoos and his collaborators (Chrysochoos *et al.*, 1989; Boulanger *et al.*, 2004; Chrysochoos *et al.*, 2010) made distinguished contributions on the thermal image processing, which here will be summarized briefly.

First of all, the energy balance Eq. 1.24 should be simplified under several hypotheses (Boulanger *et al.*, 2004), e.g., temperature variations induced by the fatigue test have no influence on the micro-structural state. Then, a compact form of energy balance can be reached

$$\rho C \frac{\partial \theta}{\partial t} - k\Delta\theta = s \tag{1.29}$$

where $\theta = T - T_0$ represents the temperature variation, while s stands for the overall heat source due to dissipation and thermoelastic effects.

Considering a thin, flat specimen, let us denote L, l and e as the length, width and thickness, respectively, of the specimen gauge part. The associated coordinates are in turn x, y and z.

Several options, from 2D to 0D solutions, can be proposed:

(1) Two-dimensional diffusion problem

The first option considers that the source averaged over the specimen thickness is representative of what happens throughout the thickness. Integration of the heat equation according to this dimension then leads to a 2D diffusion problem. By denoting $\bar{f}(x,y,t) = \frac{1}{e}\int_{-e/2}^{+e/2} f(x,y,z,t)$ as the mean operation applied to f, we finally get

$$\rho C \left(\frac{\partial \bar{\theta}}{\partial t} + \frac{\bar{\theta}}{\tau_{th}^{1D}} \right) - k \left(\frac{\partial^2 \bar{\theta}}{\partial x^2} + \frac{\partial^2 \bar{\theta}}{\partial y^2} \right) = \bar{s} \tag{1.30}$$

where the time constant τ_{th}^{1D} characterizes heat losses through the specimen surfaces $z = \pm e/2$.

This solution was used in the studies (Chrysochoos & Louche, 2000; Morabito *et al.*, 2007; Pastor *et al.*, 2008) to estimate 2D distribution of heat sources in monotonic or cyclic tests. It was found, however, not well adapted for fatigue test. The signal-to-noise ratio and sampling rates are often not good enough to compute relevant heat source distributions in fatigue test, as the 2D Laplacian operator is indeed a heavy noise amplifier (Boulanger *et al.*, 2004).

(2) One-dimensional diffusion problem

To improve the signal-to-noise ratio and reduce the number of numerical space derivations, we may assume that the mean heat sources associated with each cross-section S of the specimen is relevant for describing what happens throughout S. By denoting $\bar{\bar{f}}(x,t) = \frac{1}{S}\int_{-t/2}^{+t/2}\int_{-e/2}^{+e/2} f(x,y,z,t)dzdy$, the heat equation becomes

$$\rho C\left(\frac{\partial\bar{\bar{\theta}}}{\partial t}+\frac{\bar{\bar{\theta}}}{\tau_{th}^{2D}}\right)-k\left(\frac{\partial^2\bar{\bar{\theta}}}{\partial x^2}\right)=\bar{\bar{s}} \tag{1.31}$$

where the time constant τ_{th}^{2D} characterizes heat losses at the cross-section boundaries ($y = \pm l/2$, $z = \pm e/2$).

This method was successfully used to track specimen cross-sections where strain localization occurred (Louche & Chrysochoos, 2001).

(3) A simple differential equation for diffusion problem

A third option can be formulated to further simplify Eq. 1.31. Like stress and strain fields, we may suppose that, before localization onset, the heat source distribution is uniform at any time within the specimen gauge part. In such cases, the spectral solution of the heat equation can be analytically determined using eigenfunctions of the Laplacian operator. For symmetric linear boundary conditions and initial conditions corresponding to uniform temperature fields, the spectral solution may then be well approximated by considering only the first eigenfunction (Chrysochoos & Louche, 2000). The heat equation can then be simplified as

$$\rho C\left(\frac{d\theta}{dt}+\frac{\theta}{\tau_{eq}}\right)\approx s \tag{1.32}$$

where θ is now the temperature variation at the center of the specimen gauge part, with τ_{eq} characterizing all local heat losses. For mechanical tests on the macroscale θ is identified to the mean temperature of a small centered area, typically $2 \times 2\ mm^2$.

For the reasons analyzed above, the Eq. 1.32, or say 0D solution, is the most used method in the case of HCF studies (Boulanger *et al.*, 2004; Giancane *et al.*, 2009; Dumoulin *et al.*, 2010; Chrysochoos *et al.*, 2010).

An interesting application of this method can be found in the paper (Boulanger *et al.*, 2004). In this work, the authors measured the dissipated energy in a series of cyclic tests under different load levels, and found that a visible decrease in dissipation can happen at the beginning of the test when the maximum load is close to the macroscopic yield strength of material. This is very similar to the phenomenon observed by Maquin and Pierron (Maquin & Pierron, 2009) as discussed in the section 1.2.3.1. The argument, however, lies in: which effect, "material effect" (micro-plasticity) or "structure effect" (non-uniformity of heat sources), is predominant in this regime? If the structure effect prevails, the 0D solution, assuming a uniform heat source distribution, can not be considered as valid any more, in such a case 1D or 2D solution is preferred. But if the structure effect occurs (like microcracks), probably at a stress level higher than that activating only material effect, it is reasonable to suppose that it may be a mix of the two effects.

In the same work (Boulanger *et al.*, 2004) the authors attempted to extend the test by adding four more blocks at constant stress range, the results of the whole test is presented in Fig. 1.8(a). In this figure we can observe a rapid increase in dissipation at the last block,

and this was proofed due to the onset of a fatigue crack, see Fig. 1.8(b). This can be concluded as a structure effect assuming that a material effect would lead to a monotonous development of dissipation. Nevertheless, without microstructural arguments, it is still unclear which effect is responsible for the former decrease of heat dissipation (from 4000 s to 8000 s in Fig. 1.8(a)).

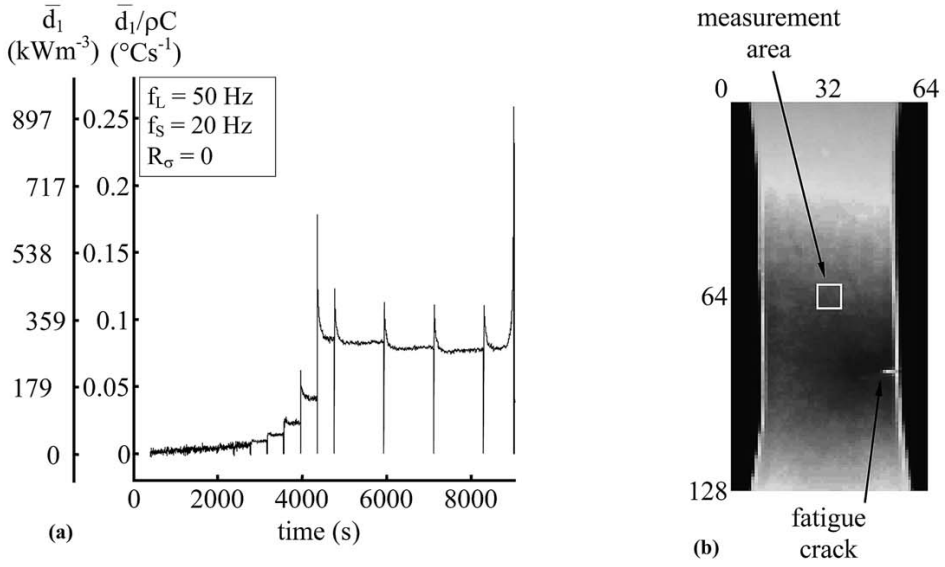

Figure 1.8: (a) Evolution of the mean dissipation until crack onset (b) Temperature field during crack propagation (Boulanger *et al.,* 2004)

Comparing to heat dissipation, the stored energy should be a more essential quantity, thus a better indicator for a further mechanism study.

In recent works of Chrysochoos's research group (Berthel *et al.*, 2007; Chrysochoos *et al.*, 2008b; Berthel *et al.*, 2008), another full-field measurement technique DIC was incorporated into the measurements. DIC technique was employed for strain measurement and stress identification through a variational inverse method, then the deformation energy can be determined on the basis of the estimated strain and stress. In this case, the stored energy E_s can be obtained through an indirect way, by subtracting the intrinsic dissipation from the plastic deformation energy.

The energy balance achieved in the work (Chrysochoos *et al.*, 2008b) showed that in the HCF for DP 600 steel, around the half of the deformation energy associated with mechanical hysteresis loop was dissipated while the other half corresponded to stored energy variations. This means a fraction β around 50% that is considerably higher than that measured in the monotonic test (Bever *et al.*, 1973). Nevertheless, it is not evident to compare the results from different studies owing to the great variations on the aspects of material, loading condition, measurement technique, image processing approach, etc.

This part of bibliographic study delivers an important message: a reliable estimation

of heat sources from a noisy measurement by the macroscopic approaches is often found difficult and sometimes problematic, so is the following estimation of stored energy in an indirect way. These macroscopic approaches generally ignore several important active factors in the deformation process of metals: initial crystallographic structure, strain heterogeneity and microstructure evolution. These important elements can be, however, more easily accessible at a microstructure scale. To this end, experimental investigations on oligocrystals and single crystals are interesting to be conducted. The following section will focus on the relevant bibliographic study on the research works at the grain scale.

1.3 Research works at the grain scale

This section is unfolded into four parts. First, the mechanical behaviour of FCC (Face Centered Cubic) metals at the grain scale is presented followed by a special introduction of the low cycle fatigue behaviour of nickel single crystal. Then, a brief review on the energy aspects of deformation in polycrystals and single crystals is introduced. And finally, some recent advances on the full-field coupled measurement at the grain scale are summarized.

1.3.1 Material mechanical behaviour

During plastic deformation of metals, the dislocations manifest, intensify and are rearranged, which gives birth to a heterogeneous structure. This heterogeneous microstructure can vary in different forms depending on the stress-strain state, loading conditions and the initial material state. Numerous studies (Mughrabi, 1978; Mughrabi, 1983; Feaugas, 1999a) have been dedicated to study the formations of these microstructures, and attempted to explain the material mechanical behaviours from the microscopic point of view.

In order to dissociate these heterogeneities with some intrinsic defects, for example the grain boundaries, nickel single crystal was chosen as the investigated material. Some other FCC materials, such as copper and 316L steel, exhibiting certain mechanical behaviours similar to nickel (Haddou, 2003; Feaugas & Haddou, 2007), will be also introduced as references.

This review is divided into two parts, with respect to two loading conditions: monotonic loading and cyclic loading. The introduction will be generally arranged in the order by presenting the macroscopic mechanical behaviours first, and then the associated microstructures and dislocation arrangements, and finally the interpretations of the material mechanical behaviours from the microscopic point of view.

1.3.1.1 Monotonic testing

In a uniaxial tensile test, the work hardening curve of FCC material has three distinct and successive stages: stage I, II and III, whether in single or multiple slip. Fig. 1.9(a) shows schematically the evolution of the shear stress as a function of shear strain, which allows individual recognition of the three stages of work hardening. We present also the hardening

curves of single crystal copper in multiple slip (Diehl, 1956), as shown in Fig. 1.9(b).

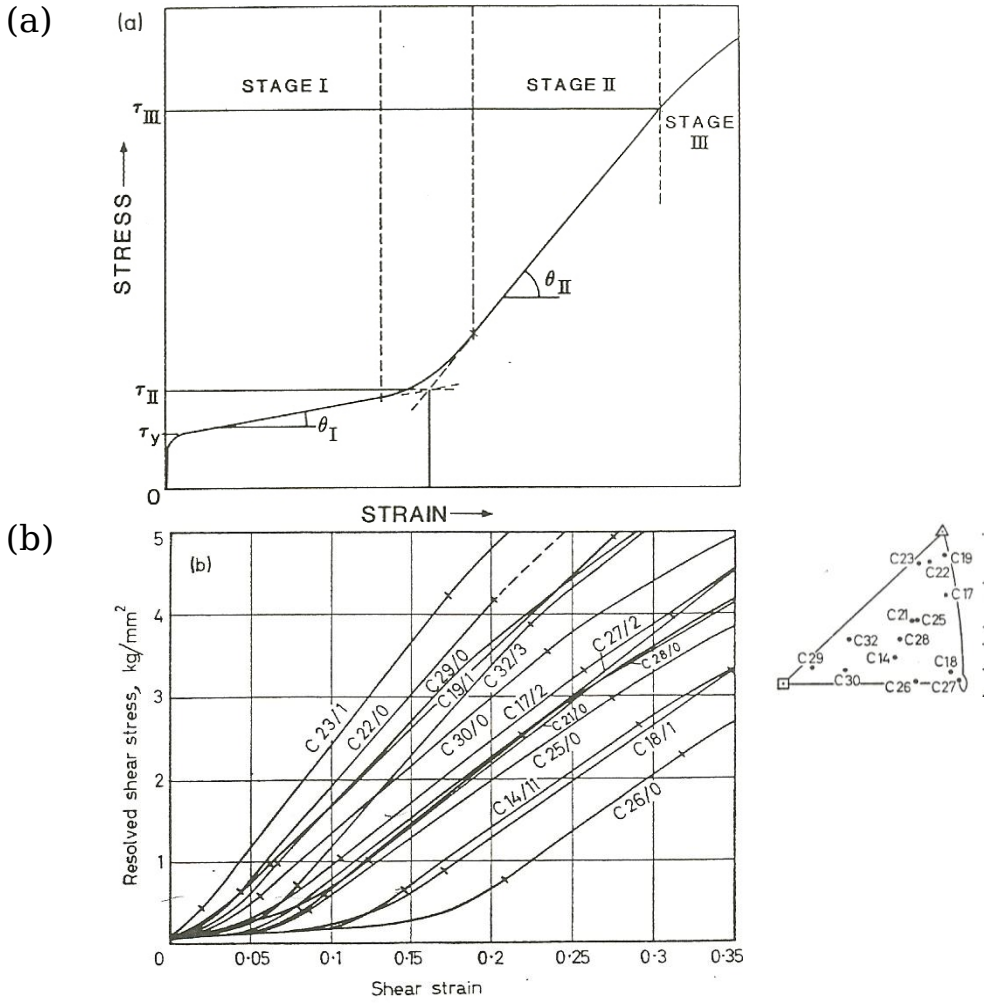

Figure 1.9: (a) Example of a hardening curve with three different stages in simple slip (b) Hardening curves of single crystal copper in multiple slip (Diehl, 1956)

During each stage of strain hardening, different structural phenomena occur. They generally result from the activation of one or more slip systems and the dislocation emission. When the strain rate increases, the dislocations adopt specific arrangements. These arrangements have a heterogeneous character. Indeed, according to the strain rate, the crystallographic orientation and the stress level, these arrangements may form dipole clusters, grids, dislocation walls and cells.

The characterization of these heterogeneities associated with tensile strain was the subject of many studies (Mughrabi, 1968; Mughrabi, 1983; Feaugas, 1999b; Feaugas & Haddou, 2007) . TEM (Transmission Electron Microscope) was generally used to observe and characterize these microstructures, such as clusters, walls and dislocation cells. Here we will present the structural phenomena that occur during each stage of work hardening in a tensile test, accompanied with the typical TEM images shown in Fig. 1.10. Most of this

introduction is referred to the work of Oudriss (Oudriss, 2012).

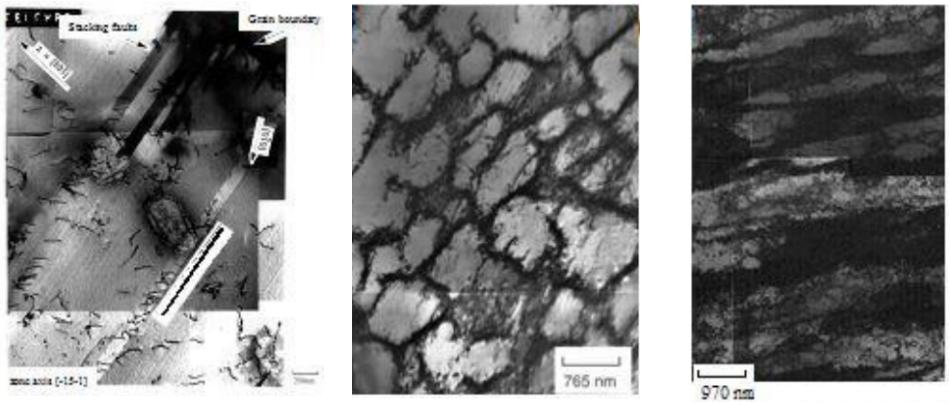

(a) (b) (c)

Figure 1.10: (a) Dislocation pile-ups in stage I (b) Equiaxed dislocation cells in stage II (c) Extended dislocation cells in stage III (Oudriss, 2012)

Stage I: An easy slide due to low hardening occurs, which is, however, generally absent in polycrystals. In this stage, the deformation occurs mainly by activating the primary slip systems, and gives rise to typical arrangements of dipoles and multipoles.

Generally, observations by TEM can distinguish these arrangements of dipoles and multipoles. Nevertheless, at this stage the dislocation pile-ups are still the most reported phenomenon, as shown in Fig. 1.10(a).

Stage II: In stage II, the hardening is linear as in stage I, but it is about one order of magnitude larger than the previous stage. This stage is characterized by the presence of strong long-range internal stress. Their origin lies mainly in the activation of one or more secondary slip systems, it then generates interactions between dislocations that lead to the formation of dipole clusters, Lomer-Cottrell locks and grids.

When the strain rate increases, a dislocation densification occurs, which gives rise to the formation of walls and cells, as shown in Fig. 1.10(b). Note that the walls of dislocations contain high densities of dislocations, and they define cells. The latter contain relatively few dislocations.

Stage III: In the last stage III, the strain hardening becomes parabolic and lower than that in stage II. It is characterized by a high density of tangles and a decrease in size of dislocation cells as the strain increases, as shown in Fig. 1.10(c). On the other hand, the dislocation cells are bounded by walls and dislocation walls which exhibit high misorientations. These walls are called geometrically necessaries (GNB: Geometrically Necessary Boundary). Inside the GNBs, the walls of dislocation cells are called incidental dislocation walls (IDB: Incidental Dislocation Boundary). They are disorganized tangles of dislocations.

In the case of FCC polycrystalline materials, the deformation structures are dependent

on the crystallographic orientation of grains, grain size and the stacking-fault energy. A fourth stage of work hardening can be achieved for some FCC materials. However, it is very rare due to a high strain amplitude. Typical microstructures of this stage are disoriented cells and sometimes twins for materials with a low stacking-fault energy, such as 316L steel.

1.3.1.2 Cyclic testing

During cyclic loading, it can be distinguished up to four stages of work hardening: stage I, II_0, III_0 and III, whether in single or multiple slip. Fig. 1.11 shows an example of cyclic hardening curves for nickel and copper (Feaugas, 1999a).

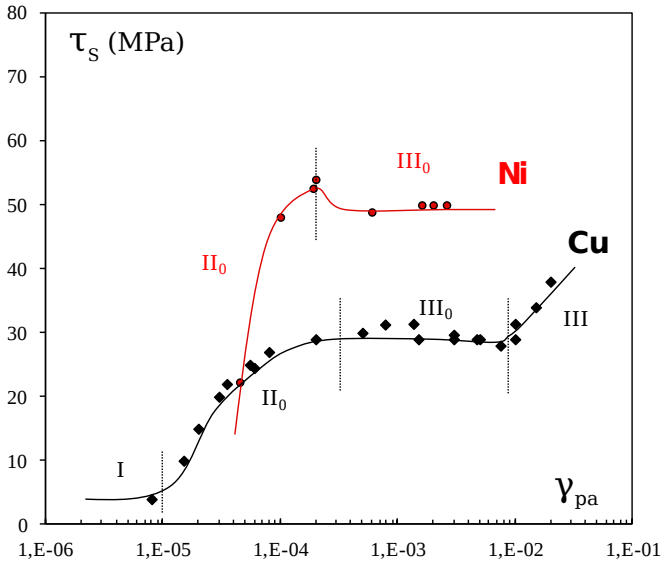

Figure 1.11: Cyclic hardening curves of nickel and copper (Feaugas, 1999a)

According to many studies (Mughrabi, 1978; Pedersen, 1990; Feaugas, 1999b), the structures associated with stages I and III in cyclic testing are similar to those developed in monotone tensile test at the same stages, while in stages II_0 and III_0 the associated dislocation structures are considered specific to the cyclic loading. According to the number of cycles, the strain rate and the crystallographic orientation, dislocations emitted after activating the slip systems during the cyclic test can be rearranged in forming different dislocation structures.

The structural phenomena that occur during the two specific stages II_0 and III_0 for cyclic loading can be summarized as follows, with some typical TEM images shown in Fig. 1.12 (Oudriss, 2012):

Stage II_0: During cyclic loading in stage II_0, the change in direction of stress leads to the formation of dislocations of opposite signs. At this stage of loading, the cross slip is considered as the main carrier of the dislocation formations (Feaugas, 1999a).

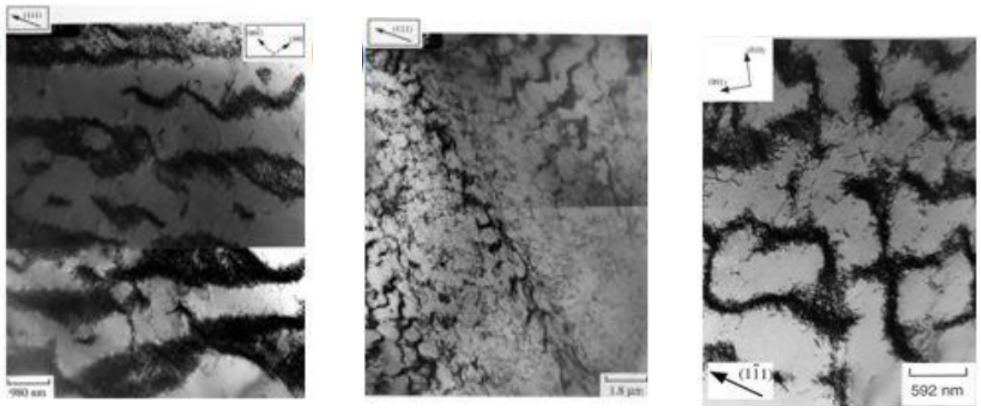

(a) (b) (c)

Figure 1.12: (a) Veins in stage II_0 (b) PSBs in stage III_0 (c) Labyrinths in stage III_0 (Oudriss, 2012)

With the increase in strain amplitude, the dislocations are arranged in clusters of dipoles or multipoles "corners", separated by channels, which results in structures known as veins, as shown in Fig. 1.12(a). The morphology of the veins is highly dependent on the number of active slip systems (Feaugas & Gaudin, 2001). At the end of stage II_0, veins occupy more than 50% of the material.

Stage III_0: In stage III_0, according to some crystallographic orientations favorable to single and double slips, the structure "ladder" forms. The most representative structures are PSBs (Persistent Slip Bands), as shown in Fig. 1.12(b). And others structures include dipolar walls and labyrinths, the latter is shown in Fig. 1.12(c). These structures are the result of a reorganization of the dipoles in the walls in order to reduce the stored elastic energy. The fraction of walls at this stage accounts no more than 10%.

Whether in monotonic or cyclic testing, the presence of different strain hardening stages is associated with the changes of dislocation structures: clusters, walls, cells, PSBs, etc. Thus, Pedersen (Pedersen, 1990) proposed a general formalism which assembles all structural changes in monotonic and cyclic testing, known as Pedersen map.

The Pedersen map is generally represented as a diagram: the maximum plastic strain ε_{pmax} as a function of the accumulated plastic strain ε_{pcum}, defined as:

$$\varepsilon_{pcum} = (4N + 1)\varepsilon_a \tag{1.33}$$

where ε_a is the strain amplitude and N the number of cycles.

An example of Pedersen map for 316L steel is illustrated in Fig. 1.13, which is constructed by combining the observations of stages I, II, III and IV in monotonic test and of stages I, II_0, III_0 and III in cyclic test. This map was built by Feaugas and his collaborators (Feaugas, 1999a; Feaugas & Gaudin, 2001; Feaugas & Pilvin, 2009) based on experimental data such as stress-strain curves and microscopic observations by TEM. Thanks to this map, all the structural heterogeneities, associated with different stages of work harden-

ing in monotonic or cyclic test, can be integrated.

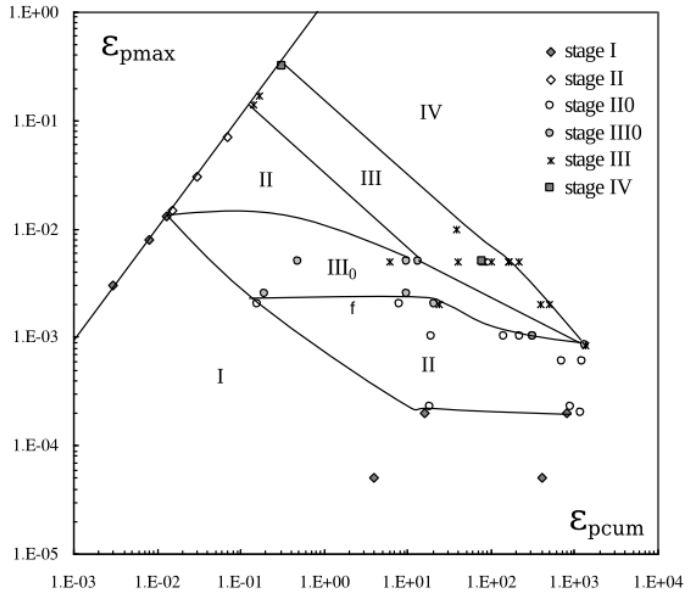

Figure 1.13: Pedersen map of 316L steel (Feaugas, 1999a; Feaugas & Gaudin, 2001; Feaugas & Pilvin, 2009)

The microstructures observed by TEM in cyclic testing, especially the PSBs, are considered as very important phenomena in the fatigue study, as they are associated directly with the fatigue mechanism of material. In the following section, some further investigations on this association will be detailed for nickel single crystal in the case of low cycle fatigue.

1.3.2 Low cycle fatigue

Cyclic plastic strain localization in PSBs is now accepted as a general and very important feature of cyclic straining in crystalline materials, which can be regarded as the first sign of fatigue damage (Man *et al.*, 2009a). The early stages of surface relief evolution of PSMs (Persistent Slip Marks) are formed in areas where PSBs intersect the free surfaces. Different measurement technologies, such as TEM, AFM (Atomic Force Microscopy) and EBSD (Electron Backccattering Diffraction), were employed to characterize the features of the surface relief, and theoretical models were built to study the associated fatigue mechanisms (Man *et al.*, 2009b).

The studied material concerning low cycle fatigue is nickel single crystal. Blochwitz and his co-workers (Blochwitz & Veit, 1982; Mecke & Blochwitz, 1982; Mecke *et al.*, 1982) made significant contributions on the low cycle fatigue study of nickel single crystal. The following introduction is mostly cited from their foundings.

In the low cycle fatigue testing for FCC metals, PSBs can be observed only above a "nucleation stress" amplitude τ_n, which depends on the plastic strain amplitude ε_{ap}. Generally,

the nucleation stress τ_n lies below the saturation stress amplitude τ_{as}, as the mechanical saturation occurs only after a considerable number of cycles, the time period for the nucleation of the first PSBs (Mecke *et al.*, 1982). The nucleation stress can be determined experimentally by a method proposed in the work (Mughrabi, 1978).

The external plastic strain amplitude ε_{ap} has major influence on the dislocation structure development. The first important parameter is the threshold value of the strain amplitude ε^*_{ap}, under which the PSBs do not form. Before the transformation into PSBs, with the greater strain amplitude the dislocation structure is more like "ladder-like" structure rather than "vein-like" structure. In the transformation phase, it was observed in the study (Mecke *et al.*, 1982) that the PSB structure and the matrix structure develop beside each other. Concerning the final PSBs, the volume fraction of the PSBs increases quasi-linearly with the strain amplitude.

Blochwitz (Blochwitz & Veit, 1982) proposed a two-phase model to interpret the plateau behaviour of fatigued FCC single crystals. In this model, the dislocation structure is considered as the combination of "hard" matrix structures and "soft" PSBs, which are connected in series.

Assuming that the PSB and matrix are subjected to the same external shear stress:

$$\tau = \tau^{(B)} = \tau^{(M)} \tag{1.34}$$

where $\tau^{(B)}$ stands for the shear stress of the PSB and $\tau^{(M)}$ the matrix.

The plastic resolved shear strains γ_p for PSB and matrix depend on their respective volumes in the material:

$$\gamma_p = f\gamma_p^{(B)} + (1-f)\gamma_p^{(M)} \tag{1.35}$$

where f is the fraction of the PSB volume.

As under the same shear stress, the PSB is much softer than the matrix, so it is reasonable to infer that the PSB volume has much higher plastic strain amplitude than the matrix volume. This thesis was proofed by numerous studies (Blochwitz & Veit, 1982).

The above model was also verified by the phenomenon of "secondary" CSSC (Cyclic Stress-Strain Curve). The secondary CSSC represents the mechanical behaviour of material when the strain amplitude is reduced after the saturation in the plateau range, which is believed as the "true" CSSC of the PSBs. Correspondingly, the CSSC before reaching the plateau can be regarded as the matrix CSSC. Both the primary and secondary CSSCs are illustrated in Fig. 1.14 (Mecke & Blochwitz, 1982).

The crystallographic orientation also has an important influence on the mechanical behaviour of nickel single crystal. In the work (Mecke & Blochwitz, 1982), two typical orientations of nickel single crystal [-149] and [001], corresponding to the single slip system and multiple slip system, respectively, were studied particularly. The results showed that for [001]-oriented single crystals there were actually no "plateau range" existed in the CSSC,

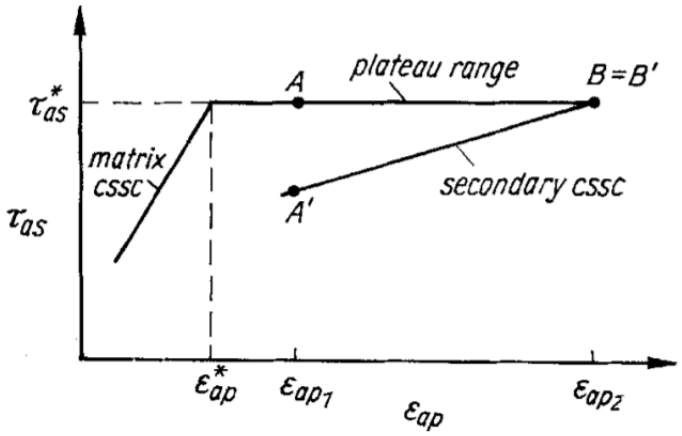

Figure 1.14: The primary and secondary CSSCs (Mecke & Blochwitz,1982)

and its threshold value of the plastic strain amplitude was obviously higher than that demonstrated by [-149]-oriented single crystals. In the subsequent microscopic observations, the macro-bands were found for [-149]-oriented single crystals, and a mixture of the crystallographic and non-crystallographic slips were exhibited on the surface of [001]-oriented single crystals, both are shown in Fig. 1.15.

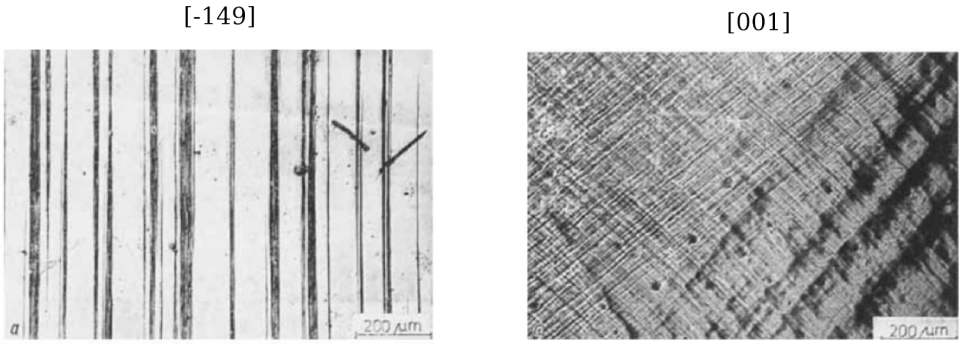

Figure 1.15: The microscopic observations of two different oriented nickel single crystals (Mecke & Blochwitz, 1982)

Nevertheless, a single slip system is not a required condition to reach a plateau in the CSSC, concluded in the study of Buque (Buque, 2001). The existence of the plateau depends essentially on the microstructure: 1) the dominance of the PSBs; 2) a cyclic deformation dominated by PSBs.

Generally the transformation from the matrix volume to the PSB volume is realized by broadening the macro-bands. The width of the PSB for nickel single crystals can reach from 10 μm to near 200 μm with increasing plastic strain amplitude, as shown in Fig. 1.16.

The studies reviewed in this section and the section precedent did not involve any energy dissipation analysis. To our knowledges, most of the former works on energy storage in

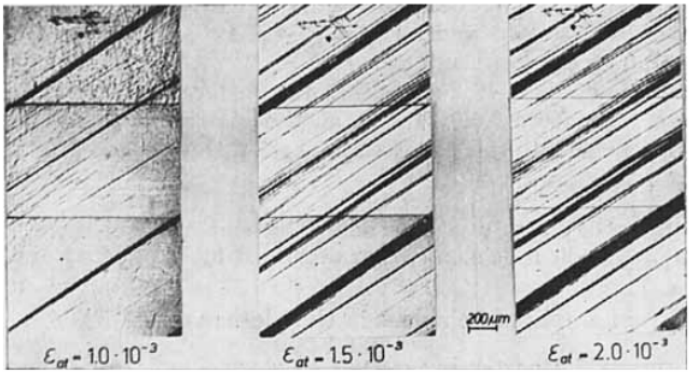

Figure 1.16: PSBs expand with increasing plastic strain amplitude (Blochwitz & Veit, 1982)

single crystals and polycrystals were carried out before the 1980s. The main achievements of that time will be summarized in the following section.

1.3.3 Energy aspects

This section is divided into two parts: 1) stored energy and grain structures; 2) stored energy and dislocation structures.

1.3.3.1 Stored energy and grain structures

One of the first investigations of the energy stored by single crystals was carried out by Farren and Taylor (Farren & Taylor, 1925). In this work the stored energy of two single crystals of aluminum deformed by extension were measured, and the storage ratio β was about 5%, only the half of that obtained with polycrystalline aluminum in the same investigation. After this pioneering work, many researches were followed to study the stored energy of cold work for single crystals and polycrystals.

The storage ratio β received considerable attentions. The results showed that it appeared to be independent of grain orientation when comparisons were made at equal strains (Bever *et al.*, 1973). Meanwhile, certain studies (Nakada, 1965; Williams, 1965; Wolfenden, 1967; Wolfenden, 1968) showed that the crystals oriented with a well defined easy glide region stored more energy than crystals of other orientations under the same shear strain. This can be explained by a proportional greater strain energy (or shear stress) for the case of the crystals oriented for extensive easy glide (Bever *et al.*, 1973).

Concerning polycrystalline structures, the results generally showed the fine-grained material stored more energy than the coarse-grained material under the same strain levels, in particular at small strains (Clarebrough *et al.*, 1958; Williams, 1961; Wolfenden, 1971). This phenomenon was studied by Baker (Baker *et al.*, 1995), and the explanation is that: the stored energy is a function of dislocation density, a fine grain-sized material generally has a higher dislocation density than a coarse grain-sized material for a given plastic strain,

thus tends to store more energy on the same condition.

Comparing the single crystal and polycrystals, a noteworthy founding is that with increasing strain the storage ratio β tends to decrease in polycrystalline metals but, on the contrary, it tends to increase for single crystals. This phenomenon can be illustrated by the following comparison figure pairs (a) (Nakada, 1965) and (b) (Clarebrough *et al.*, 1958). In Fig. 1.17(a) the energy evolution curves characterizing single crystal are expressed in stored energy versus shear strain, two of the three are concave upward and one concave downward. In Fig. 1.17(b) the curves are expressed in stored energy versus expended energy, where both of the two curves for polycrystals show concave downward tendencies.
i

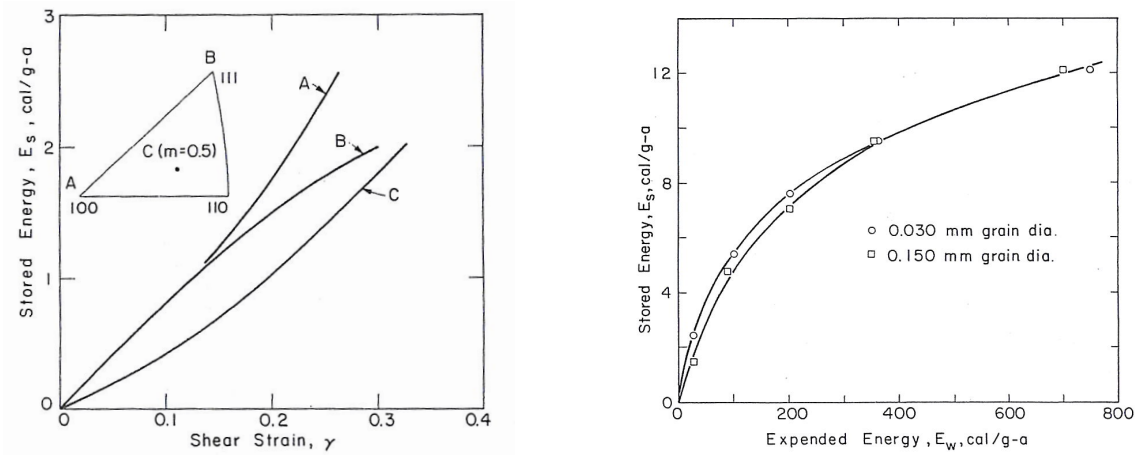

(a) (b)

Figure 1.17: (a)Stored energy versus shear strain for single crystal (Nakada 1965); (b) Stored energy versus expended energy for polycrystalline specimens (Clarebrough *et al.*, 1958)

Different theoretical explanations on this phenomenon were given depending on specific models of the dislocation structure and of the mechanism by which the structure develops. In general the theories were conceived primarily as theories of work hardening, that is as explanations of the dependence of the flow stress on strain. Under the hypothesis of Taylor's parabolic work hardening ($\bar{\sigma} \propto \bar{\varepsilon}^{\frac{1}{2}}$), relevant computations were conducted by different investigators (Koehler, 1941; Seitz & Read, 1941; Stroh, 1953), and the same conclusion have been reached: the stored energy increases approximately linearly with strain. Nevertheless, such a predicted concave-upward curve is not the case the most usually observed in experiments, especially for polycrystals.

The theories are not in satisfactory accord with the observed dependence of the stored energy on strain. There are two possible reasons for this. The first reason is that the increase rate of dislocation density with strain is generally sensitive to the strain levels. Strain hardening in polycrystalline metals is not generally parabolic: the flow stress is a weaker function of strain than $\bar{\sigma} \propto \bar{\varepsilon}^{\frac{1}{2}}$ and the dislocation density increases with strain more weakly than linearly. The second reason is that the stored energy was generally calculated by us-

ing the term of strain energy of dislocation, but which can only be an approximate. This problem will be further discussed in the next section.

1.3.3.2 Stored energy and dislocation structures

Numerous studies (Stroh, 1953; Bailey & Hirsch, 1960; Nabarro *et al.*, 1964; Kocks & Scattergood, 1969) have demonstrated that the stored energy attributable to dislocations is proportional to the dislocation density. It was also proofed that the flow stress is proportional to the square root of the dislocation density and hence that the stored energy is proportional to the square of the flow stress. Be aware that these relationships are also material dependent and temperature dependent.

Stroh (Stroh, 1953) made the first calculation of the strain energy of the dislocations in a pile-up. He derived the following equation for the self-energy of a single pile-up of n edge dislocations of unit length:

$$E_1 \approx \frac{n^2\mu b^2}{4\pi(1-\nu)} ln \frac{4\pi(1-\nu)\bar{\sigma}e^{\frac{1}{2}}R}{n\mu b} \tag{1.36}$$

where μ is the shear modulus, b is the Burgers vector and $(1-\nu)$ the corresponding value for an edge dislocation. $\bar{\sigma}$ represents the applied stress that piles up the dislocations and R is the size of the crystal.

Stroh also calculated the energy of interaction between groups of piled-up dislocations. He argued that only the interaction between groups at either end of a slip line of length $2L$ made a contribution to the energy. By considering n dislocations in a pile-up to be equivalent to a superdislocation with Burgers vector nb an interaction energy was computed

$$E_2 \approx \frac{n^2\mu b^2}{4\pi(1-\nu)} ln \frac{R}{2L} \tag{1.37}$$

The energy attributable to one pile-up in the dislocation structure is thus given by $E = E_1 + E_2$, or

$$E = \frac{n^2\mu b^2}{4\pi(1-\nu)} ln \frac{8\pi(1-\nu)\bar{\sigma}e^{\frac{1}{2}}L}{n\mu b} \tag{1.38}$$

The numbre of dislocations in a pile-up n and the slip distance L are assumed independent of strain. Thus the total energy of the entire dislocation structure is given by

$$E = N\frac{n\mu b^2}{4\pi(1-\nu)} ln \frac{8\pi(1-\nu)\bar{\sigma}e^{\frac{1}{2}}L}{n\mu b} \tag{1.39}$$

It can be seen that the energy is proportional to the dislocation density N.

Bailey and Hirsch (Bailey & Hirsch, 1960) were first to provide experimental evidence that the stored energy is proportional to the dislocation density, and so is the square of the flow stress. In their experiments, Bailey and Hirsch deformed silver by extension and

measured the stored energy and the flow stress; they combined these measurements with measurements of the dislocation structure by TEM. Fig. 1.18 presents the average dislocation densities and the stored energies obtained in their experiment. In the table, E_s stands for the stored energy and E_r the fraction of the stored energy that was released during the recovery (or pre-recrystallization processes).

True strain, $\bar{\varepsilon}$	Dislocation density, N_d, cm/cm^3	Stored energy, cal/g-atom		Energy per dislocation, eV/atom plane	
		E_r	E_s	E_r/N_d	E_s/N_d
0.11	2.2×10^{10}	1.25	2.7	4.2 ± 1.0	9.1 ± 2.5
0.20	5.2×10^{10}	2.8	5.1	4.0 ± 1.0	7.3 ± 2.5
0.28	6.8×10^{10}	4.9	7.7	5.3 ± 1.0	8.4 ± 2.5

Figure 1.18: Measured dislocation densities and stored energies in deformed silver (Bailey & Hirsch, 1960)

In the same paper Bailey and Hirsch attempted to calculate the stored energy as arising from groups of piled-up dislocations. Similar to the work of Stroh (Stroh, 1953), the stored energy was considered as the sum of the self-energies of dislocations and their interaction energies. Nevertheless, there were some arguments on the intensity (or fraction) of the interaction energy, by which different models on accounting for the interaction energy were proposed (Clarebrough *et al.*, 1961; Seeger & Kronmüller, 1962; Kocks & Scattergood, 1969).

Independently of the arrangement of the dislocations in a cold-worked metal their strain energy can always be formally expressed as the sum of a self-energy and an interaction energy. Ideally the self-energy is given by

$$E = \frac{\mu b^2}{4\pi K} ln \frac{R}{r_0} + \text{core energy} \tag{1.40}$$

where K lies between 1 and $(1 - \nu)$. r_0 is the radius of the dislocation core.

Only for the theoretical "random" distribution of dislocations, the interaction energy is zero (Kocks & Scattergood, 1969). The sign of the interaction energy has meaning for the dislocation structure. A positive interaction energy implies that dislocations inside a volume of radius R are arranged so that their stresses reinforce each other. In such a case, the dislocations may form a pile-up. A negative interaction energy implies that the dislocations are arranged conversely to the former case so that their stress fields tend to cancel each other (Bever *et al.*, 1973).

Let us define a positive interaction between dislocations as occurring if the strain energy of a dislocation is greater than $(\mu b^2/4\pi K) ln(R/r_0)$, where R is the cell size, and a negative interaction as occurring if the strain energy is smaller.

If we write

$$E_s = \alpha_s \mu b^2 N \tag{1.41}$$

then

$$\alpha_s = \begin{cases} > \frac{lnR/r_0}{4\pi K} \\ = \frac{lnR/r_0}{4\pi K} \\ < \frac{lnR/r_0}{4\pi K} \end{cases} \tag{1.42}$$

depending on whether the interaction is positive, zero or negative.

As the flow stress is proportional to the square root of the dislocation density

$$\tau = \alpha \mu b N^{\frac{1}{2}} \tag{1.43}$$

where the constant α is approximately 0.5.

Then the coefficient α_s can be expressed as

$$\alpha_s = \frac{\alpha^2 E_s \mu}{\tau^2} \tag{1.44}$$

Based on this formula, experimental values of α_s for pure metals range normally from 2 to 14, and most are between 2 and 3 (Bever *et al.*, 1973).

The energy storage fraction β, estimated according to above principles, were often found small, namely of the order 5% (Stroh, 1953; Nabarro *et al.*, 1964; Langford & Cohen, 1969). As an example, Nabarro (Nabarro *et al.*, 1964) gave the following derivation of the ratio dE_s/dE_w:

$$dE_w = \tau d\gamma = \frac{d\gamma}{d\tau} \tau d\tau \tag{1.45}$$

The stored energy and flow stress can be obtained from Eq. 1.39 and Eq. 1.41, respectively, therefore

$$\frac{dE_s}{dE_w} = \frac{2\alpha_s}{\alpha^2 \mu} \frac{d\tau}{d\gamma} \tag{1.46}$$

Taking

$$\frac{d\tau}{d\gamma} = \frac{\mu}{500} \text{ and } \alpha_s = 2.5,\ \alpha = 0.5 \tag{1.47}$$

then

$$\frac{dE_s}{dE_w} \approx 4\% \tag{1.48}$$

This derivation brings out the parallelism between the rate of energy storage and the rate of work hardening.

Moreover, some other researchers concerned the stored energy only with the work hardening of single crystals in Stage II of stress-strain curve. For further information, please refer to the review (Bever *et al.*, 1973) in the section 6.3.7.1.

The "historical" works reviewed in this section are possibly to be revisited by the emerging full-field measurement techniques. In fact, it has already drawn many attentions of researchers in the recent years. The next section will deal with the applications of kinematic-thermal full-field measurements in studying the mechanical behaviour of metals at the grain scale.

1.3.4 Full-field coupled measurements

Recently, full-field coupled measurements of strain and temperature were realized through a technique integration of DIC and QIRT. This technique advance is meaningful as it enhances the technical capacity towards building a local energy balance, no longer only on the global level as presented in the precedent section. As known that the strain heterogeneity is a very important characteristic of the deformation of metals at the grain scale, thanks to the full-field information on strain and temperature, the role of crystallographic structure and microstructure evolution in the deformation process can be better investigated and understood.

In the study of Bodelot (Bodelot, 2008), a coupled kinematic-thermal measurement system was built by introducing a "filter-mirror", which allowed the two cameras (IR and CCD) to measure the same surface of the specimen. In order to realize an investigation at the grain scale, some heat treatments for recrystallization were firstly applied on the studied material (AISI 316L stainless steel) that enabled to obtain a final average grain size 118 μm in diameter. Then, a high magnification lens called G1 for IR camera was employed that brought a spatial resolution 30×30 μm^2, and meanwhile the CCD camera provided a compatible spatial resolution. Hence, the observations at a grain scale can be reached, which promoted an in-depth interpretation from the standpoint of the microstructure.

In addition to the in-situ kinematic and thermal measurements, an EBSD analysis was carried out in the following work of Seghir (Seghir, 2012). More interestingly, a new methodology of crystallography-based field projection was proposed in this work.

The principle of this original method is to project the primal fields (temperature and displacement) on the specimen microstructure in units of grains. As these grains constitute a natural set of continuous and smooth spatial-temporal domains separated by grain boundaries where kinematic and thermal continuities are not necessarily ensured. It was realized in the study (Seghir, 2012) by fitting the raw data (temperature and displacement) as second-ordered polynomials within each grain, regardless of the grain boundaries. An example of the thermal field projection is shown in Fig. 1.19, where (a) represents the raw temperature field after the calibration and (b) the projected temperature field on the crystallographic structure given by the EBSD.

One can clearly observe a smoothed field in the projected temperature field and the contribution of each grain to the global field can be identified and measured. It exhibited a 100 mK thermal gradient from a specific area toward the gage section borders, which clearly reflected a conductive phenomenon from the center circled area towards the specimen border. Note that the hot region was not centered within the gage section, which

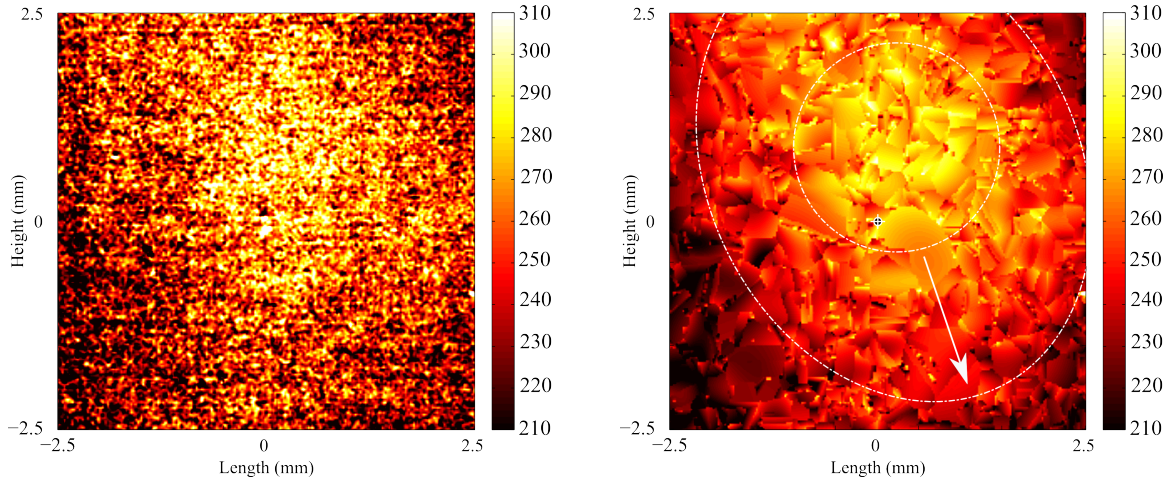

(a) (b)

Figure 1.19: A comparison between (a) raw temperature field (mK) and (b) projected temperature field (mK) (Seghir, 2012)

was certainly the sign of a thermal localization due to the microstructure and not to the specimen geometry. This point was confirmed in the strain field, for more details please refer to the works (Seghir, 2012; Seghir *et al.*, 2013).

Some other works (Saai *et al.*, 2010; Badulescu *et al.*, 2011; Delpueyo *et al.*, 2012) have been carried out on the materials with more simple and well-defined crystallographic structures, for example, the oligocrystal.

In the work of Saai (Saai *et al.*, 2010), the thermo-mechanical behaviour of an aluminum bi-crystalline specimen was studied by using full-field measurements and micromechanical modeling. The DIC and IR thermography were employed for the full-field measurements and the finite element simulation was conducted through a dislocation-based model of FCC single crystal behaviour (Tabourot *et al.*, 1997).

The experimental results show that the heterogeneity of strain and heat source fields in the specimen is induced by the difference in grain orientations and grain interactions. And the variations of local strains and local heat sources (dissipated powers) are more important in the grain center than on the grain boundary, which are in agreement with the simulation results. Nevertheless, it is also noticeable that an apparent out-of-plane deformation took place right on the grain boundary. Its possible influences on the optical measurements, in particular on IRT, were however neglected by the authors.

The plastic deformation of aluminum oligocrystal subjected to a tensile test was also investigated by Badulescu (Badulescu *et al.*, 2011). The full-field measurements of the strain and the temperature were performed by the grid method and IR thermography, respectively. The results show that the distributions of the heat source and the strain increment are, on the whole, in agreement, as shown in Fig. 1.20. The sub-figure (a) is the temperature dif-

ference (accumulated from the beginning), (b) corresponds the estimated heat source and (c) the simultaneous longitudinal strain field.

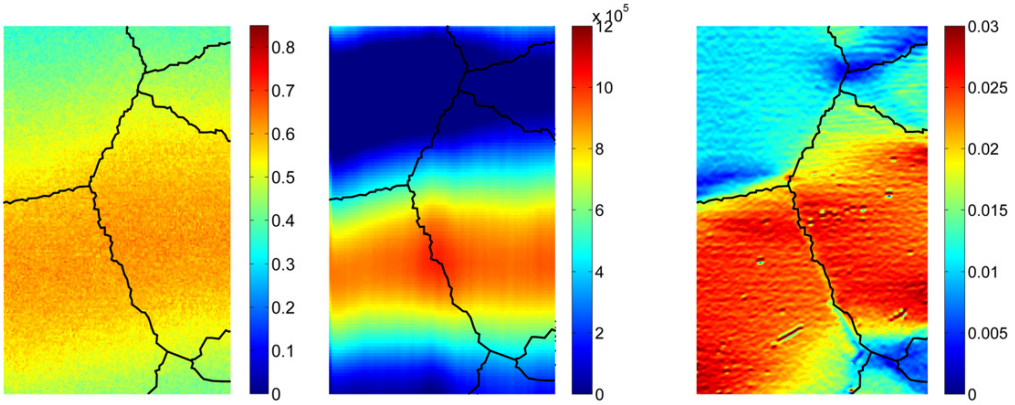

a- temperature difference θ b- heat source d (W/m^3) c- ΔE_{yy} between t=26 s and t=28 s.

Figure 1.20: Compare of the fields of heat source and strain (Badulescu *et al.,* 2011)

A good similarity can be found between (b) the heat source field and (c) the strain field in Fig. 1.20. Some secondary differences are probably related to the data processing of the temperature fields (smooth strategy), as explained by the authors. However, according to our practical experiences, an aluminum oligocrystal specimen will generally experience a strong out-of-plane deformation in the tensile test. This point was somehow not discussed by the authors, neither the out-of-plane deformation itself nor its possible influences on both IRT and DIC measurements.

Recently, a study on the phase transformation in a single crystalline Cu-Al-Be shape memory alloy was carried out (Delpueyo *et al.*, 2012). The impact of the transformation (from austenite to martensite) in terms of strain and temperature was observed and analyzed by the grid method and IR thermography. A good agreement on the distribution patterns between strain fields and heat source fields can be achieved both in loading and unloading phases, which can be reasonably explained by the same microstructure base. A set of images of strains, heat source and the microstructure interpretation in the unloading process is shown by Fig. 1.21.

It should be emphasized that the amplitude of the latent heat is negative observed from the sub-figure (b), which was interpreted by the authors that the phase transformation from martensite to austenite is endothermic. It is also worth noting that the heat map is suffered by a poor spatial resolution (38 $\times$ 139 pixels), as the price of a high sampling frequency 436 HZ. Another remark is that this work was performed on the macroscale (measured zone 17.78 $\times$ 55 mm^2), a further study at a more reduced scale was however prospected by the authors.

Other investigations related to the phase transformation by using kinematic-thermal coupled measurements can be found in (Favier *et al.*, 2007), and in (Schlosser *et al.*, 2007; Delpueyo *et al.*, 2011) via only IR thermography. It is worth mentioning that in the work (Delpueyo *et al.*, 2011) the thermomechanical coupling effects were analyzed in the case of

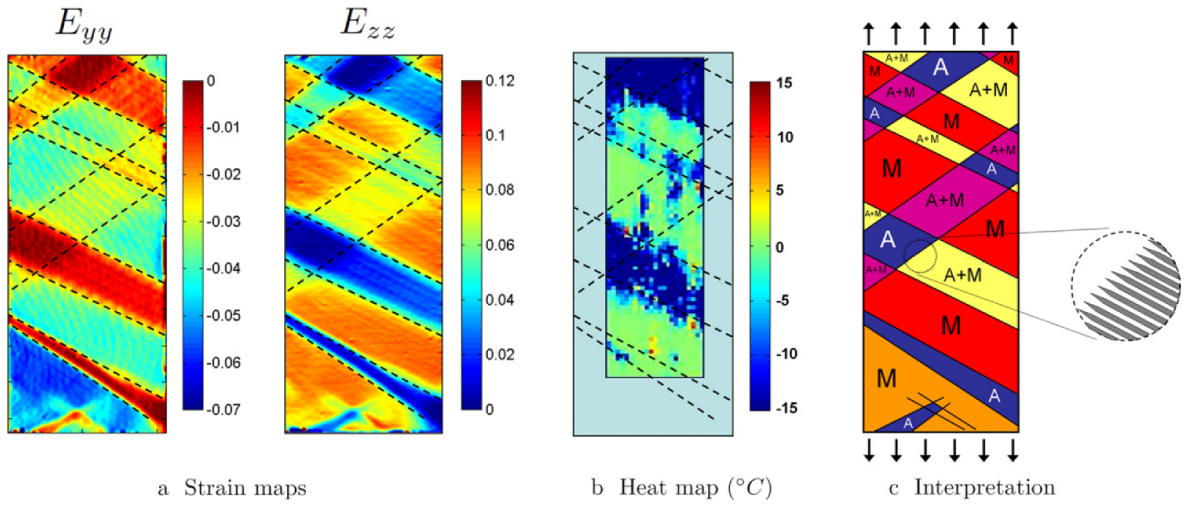

Figure 1.21: Interpretation in terms of microstructure (Delpueyo *et al.*, 2012)

the cyclic test.

Beside the experimental measurements, numerical modelings on the energy evolution of material during the self-heating test have also been studied (Cuitiño & Ortiz, 1993; Kuchnicki *et al.*, 2006; Lee *et al.*, 2010; Diligent *et al.*, 2001). Especially concerning the metal fatigue, Sangid and his co-workers (Sangid *et al.*, 2011a; Sangid *et al.*, 2011b) built an energy-based microstructure model for the purpose of predicting the fatigue crack initiation and account for fatigue scatter in polycrystals. The role of grain boundary and its interactions with PSB were emphasized in this model, and the grain boundary energies were taken into account in the energy balance analysis. The results given by this model showed that the vast majority (96%) of the crack initiation happened on the twin boundaries for the studied material (a Ni-based superalloy), and 55% is the type of "a single large grain".

1.4 Conclusion

A comprehensive bibliographic study was carried out in this work that is towards for a full-field measurement and microstructure based investigation of the plastic deformation in oligo- and single crystals.

First of all, a general framework of thermodynamics was introduced, and the concerning problem of heat sources in the metal deformation was addressed. Then, the thermomechanical behaviours of materials at the macroscale were presented, which were unfolded into three aspects: 1) elasticity, 2) monotonic plasticity and 3) cyclic plasticity and fatigue. The interests of the author were particularly focused on two points: the fraction of the stored energy in the plastic deformation and the access to the dissipation energy from the thermographic measurement. This part of overview is rather classical in the field of experimental solid mechanics, more specifically, the thermographic studies of materials.

In the last and the most important section of the bibliographic study, an investigation

of the researches on the grain scale was conducted. In this part, the mechanical behaviours of single crystals in the plastic deformation as well as in the low cycle fatigue were firstly introduced. And then the energy aspects, such as the relationships of the stored energy, dislocation density and stress flow, of single crystals and polycrystals were discussed by recalling the theories and experiments studied by the traditional macroscopic approach. The emerging full-field measurement techniques, in both kinematic and thermal measurements, provide a new occasion to revisit these problems and have already shown its unique advantages as addressed at the end of the study.

Chapter 2

Metrology

Two kinds of full-field measurements are involved in our studies: thermal measurement and kinematic measurement. The thermal measurement is realized by QIRT (Quantitative InfraRed Thermography) and the kinematic measurement by DIC (Digital Image Correlation), or say image registration from a technical point of view in this study. The full-field measurement information provided by these two techniques, such as temperature, displacement and strain, are crucial for the study of material mechanical behaviours, in particular for the investigations at a microstructure scale. For promoting a precise and reliable measurement, the metrological study on the two techniques is a necessity.

The general principles of the methods will be first introduced, and then the focus will be placed on the new technical improvements and specific data treatment strategies adapted to our research cases. The QIRT will be first presented, and then the DIC and image registration.

2.1 Quantitative Infrared Thermography

The existence of infrared radiation was first discovered in 1800 by William Herschel. Though infrared-based detection and temperature measurement have a long history, its extensive applications in engineering happened in the past fifty years, in the wake of the first commercial infrared imagers available in 1965.

In infrared thermography, the radiation is detected and measured with infrared imagers. Since infrared radiation is emitted by all objects above absolute zero, thermography makes it possible to see one's environment with and without visible illumination. It is particularly useful to military and surveillance as warm objects can easily stand out against cooler backgrounds. Nevertheless, most of these applications are sort of qualitative but not quantitative. In order to realize a quantitative thermographic measurement, a metrology study on QIRT was conducted in this work.

The objective of QIRT is to make a quantitative temperature measurement. To this end, the employed infrared imager (or infrared camera) should be first of all calibrated. Calibration is considered as the key in the thermographic measurement that involves several important technical aspects, such as non-uniformity correction, bad pixel detection and

integration time selection. These elements can all influence the accuracy of the measured temperature, on its spatial distribution as well as on its absolute values. The other essential element for an accurate temperature measurement is the knowledge of the object's emissivity. As known that a small error in emissivity can lead an apparent deviation on the measured temperature. In particular, for an object with a modest emissivity, the reflection effect from the environment can not be neglected.

The aspects mentioned above are the emphases in this study, and before that some fundamentals of the infrared radiation will be presented.

2.1.1 Fundamentals

Matter continuously emits and absorbs electromagnetic radiation. Electromagnetic radiation is a form of energy emitted and absorbed by charged particles, which exhibits wave-like behaviour as it travels through space.

Infrared light is electromagnetic radiation with longer wavelengths than those of visible light, extending from the nominal red edge of the visible spectrum at 0.75 μm to 1 mm. This range of wavelengths corresponds to a frequency range of approximately 1 THz to 400 THz, and includes most of the thermal radiation emitted by objects near room temperature (Liew, 2006)

Thermal emission by solids is usually treated in terms of the concept of a black body, defined to be an object capable of totally absorbing all incident radiation, whatever its wavelength (Gaussorgues, 1994). The emission of radiation by a black body is described by Planck'law which employs the concepts of statistical thermodynamics (Gibbs, 1902) and takes the form

$$\frac{d\Phi(\lambda,T)}{d\lambda} = \frac{2hc^2}{\lambda^5}\frac{1}{e^{\frac{hc}{\lambda kT}}-1} \tag{2.1}$$

where λ is the wavelength, $d\Phi(\lambda,T)/d\lambda$ is the spectral emittance (or spectral radiative flux), i.e., the power emitted per unit area per unit wavelength, $h = 6.6256 \times 10^{-34} J \cdot s$ is Planck's constant, $k = 1.38054 \times 10^{-23} J/K$ is Boltzmann's constant, $c = 2.998 \times 10^8 m/s$ is the speed of light and T is the absolute temperature of the black body in degrees Kelvin (K). The temperature conversion is

$$K = {}^\circ C + 273.15 \tag{2.2}$$

By integrating of Planck's law between $\lambda = 0$ and $\lambda = \infty$, Stefan-Boltzmann law is derived. It gives the total emittance of a black body at given temperature T:

$$\Phi = \sigma T^4 \tag{2.3}$$

where the Stefan's constant $\sigma = 2\pi^2 k^4/15c^2h^3 = 5.67 \times 10^{-8} W m^{-2} K^{-4}$.

The emittance of a black body in a given spectral band, between λ_a and λ_b, is obtained by integrating Planck's law over the spectral interval:

$$\Phi_{\lambda_a}^{\lambda_b} = \int_{\lambda_a}^{\lambda_b} \frac{d\Phi(\lambda, T))}{d\lambda} d\lambda \tag{2.4}$$

Normal objects are not generally black bodies and the above laws do not apply to them unless certain corrections are made. Non-black bodies absorb only a fraction A of incident radiation; they reflect a fraction R and transmit a fraction T. These different factors are selective, i.e., they depend on the wavelength.

Consider an object of this kind, exposed to a given amount of incident radiation. When the systems is in a state of thermodynamic equilibrium, the energy released into the ambient medium as radiation plus energy reflected and transmitted, must equal the energy introduced into the system, as illustrated in Fig. 2.1.

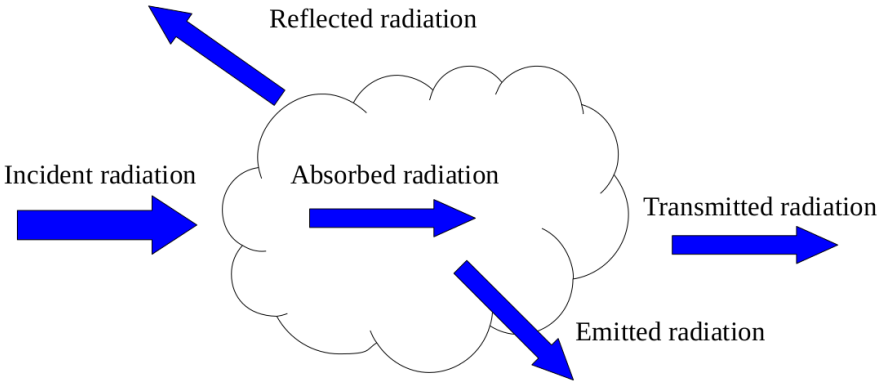

Figure 2.1: Radiation energy balance

It is thus necessary to introduce the spectral emissivity $\varepsilon(\lambda)$ whose role is to balance the absorptance $\alpha(\lambda)$, where

$$\alpha(\lambda) = \varepsilon(\lambda) \tag{2.5}$$

Thus, the total radiation energy balance is derived:

$$\varepsilon(\lambda) + \rho(\lambda) + \tau(\lambda) = 1 \tag{2.6}$$

Some special cases are listed below:

$$\begin{cases} Opaque\ body: & \tau(\lambda) = 0 \quad and \quad \varepsilon(\lambda) + \rho(\lambda) = 1 \\ Black\ body: & \varepsilon(\lambda) = 1 \quad and \quad \rho(\lambda) = 0 \quad \tau(\lambda) = 0 \\ Grey\ body: & \varepsilon(\lambda) = constant(\lambda) \end{cases} \tag{2.7}$$

The spectral emittance of any body can thus be expressed in terms of Planck's law:

$$\frac{d\Phi(\lambda, T)}{d\lambda} = \varepsilon(\lambda) \frac{d\Phi_{bb}(\lambda, T)}{d\lambda} \tag{2.8}$$

The power (or optical flux) radiated through surface S of a body at a temperature T in a given spectral band $\Delta\lambda$ is given by (in W)

$$\Phi_{\Delta\lambda} = \int_{\Delta\lambda} \varepsilon(\lambda) \frac{d\Phi_{bb}(\lambda, T)}{d\lambda} S \tag{2.9}$$

Thermographic cameras can detect radiation in the infrared spectrum roughly 0.9-14 μm. Typically, they are designed in a specific spectral band depending on the selected optics and detector materials. The MWIR (Mid Wave InfraRed) band of 3-5 μm tends to be employed with highly sensitive detectors for high-end R&D.

2.1.2 Calibration

The infrared camera is a "photon counting device". Depending on the amount of photons received, it returns the electrical voltage before being converted as numerical signal, so-called DL (Digital Level). The photon-volt-DL transfer functions are linear functions. Finally the DL needs to be converted into temperature through calibration.

The calibration is conducted by using a BB (BlackBody) reference source. A commercial extended BB, the ControlMaster SR-800, was adopted in this work, as shown in Fig. 2.2. The left-hand in the image presents the controller, and the right-hand is the extended area of the BB. The emissivity of the extended area is 0.97±0.01, and the temperature can be controlled at a precision of 0.001 K (i.e., 1 mK).

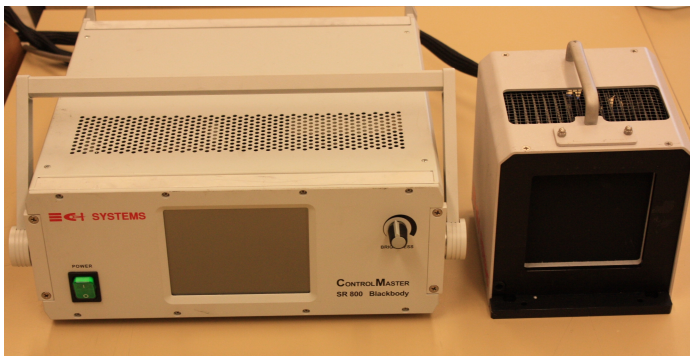

Figure 2.2: Extended Black Body

As the BB gives the temperature value, then the radiative flux is known through Stefan-Boltzmann law, thus the DL-flux relationship can be determined experimentally in a specific calibration range (or temperature range). As mentioned before calibration is the key for a quantitative thermographic measurement, and it can be sophisticated especially when a high precision of measurement is expected.

Because of the general existence of radiometric artefacts in the infrared imaging, the non-uniformity correction becomes an indispensable step in the calibration, which will be first studied in this work. Other important issues in the measurement, such as bad pixel detection and integration time selection, will be also discussed. And after taking into account all the factors, an experimental calibration method is proposed in the end.

2.1.2.1 Radiometric artefacts

Infrared FPA (Focal Plane Arrays) cameras have several aberrations and measurement artefacts with different material origins: lenses, sensors, ROC (Read-Out-Circuits), etc. These effects are considered as "radiometric artefacts" when they induce a change in the measured luminance of the object or "geometrical aberrations" when they induce an apparent displacement or deformation of the object (Poncelet *et al.*, 2011).

Two typical radiometric artefacts, namely the Narcissus and vignetting effects, were particularly studied.

The Narcissus effect occurs when an infrared detector, through unintended reflections of internal lens surfaces, sees sources at temperatures other than the background ambient; these sources are usually reflections of the detector (or FPA) itself, hence the term "Narcissus" (Lau, 1977).

Considering that the Narcissus effect is issued from the FPA, the received flux by the camera, denoted by Φ_{cam}, for a given pixel $P(x, y)$ in the Narcissus-affected zone can be expressed in the form

$$\Phi_{cam}(x, y) = \varepsilon_{obj}\Phi_{obj}(x, y) + (1 - \varepsilon_{obj})\varepsilon_{FPA}\Phi_{FPA}(x, y) \tag{2.10}$$

where the first term refers to the flux emitted by the object, and the second refers to the reflected flux from the FPA of the camera.

While for a pixel $P(x, y)$ out of the Narcissus-affected zone, the received flux Φ_{cam} on this point is

$$\Phi_{cam}(x, y) = \varepsilon_{obj}\Phi_{obj}(x, y) + (1 - \varepsilon_{obj})\varepsilon_{amb}\Phi_{amb}(x, y) \tag{2.11}$$

where Φ_{amb} is the radiative flux emitted by the ambiance.

During the operation of the infrared camera, for the most of the detector materials the FPA should be cooled down to a low temperature, for example 77 K for the camera used in this study. In this case, Φ_{FPA} is lower than Φ_{amb} in the case of room temperature, thus the camera should receive less flux from the Narcissus-affected zone than the unaffected zones under the same condition. This effect is more evident when the object's emissivity is low, which brings out the reflection effect.

The Narcissus artefact generally appears in the center of the thermal image, which is right the projected position of the FPA on the object. Fig. 2.3 shows the thermal image of a well-polished metal surface acquired in the ambient temperature. A strong non-uniformity is found in the image center that is mainly induced by the Narcissus effect. As a result, it gives much lower and untrue temperature values.

The Narcissus effect can be reduced by several methods:

1) By changing the viewing angle so that there is no stray reflection;

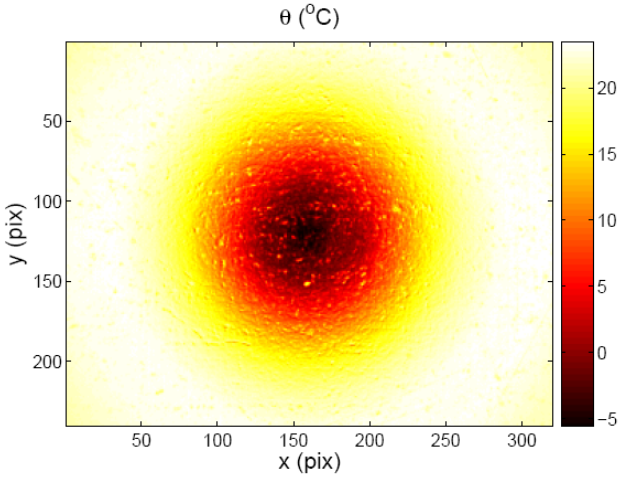

Figure 2.3: An evident Narcissus effect caused by a low emissivity

2) By using high emissivity coating on the object surface so as to minimize the reflection effect;

3) By changing some physical components of the camera, e.g., the detector material, in order to close the gap between the camera internal temperature and the ambient temperature.

Except the Narcissus effect, there is another principle optical artefact: vignetting effect. In photography and optics, vignetting is a reduction of an image's brightness at the periphery compared to the image center. For infrared optical system, it corresponds to a transmission coefficient decreasing with the distance to the optical axis, causing a darkening of the image at its periphery, where signal is only due to the temperature of the camera case (Poncelet *et al.*, 2011). Fig. 2.4 shows a raw DL map of the BB at a temperature of 24 $°C$. A typical vignetting effect can be found in this non-calibrated thermal image, where the corners of the image manifest lower dynamics (in DL).

By taking into account the vignetting effect in Eq. 2.10, it can be improved as

$$\Phi_{cam}(x,y) = f_{vig}(x,y)[\varepsilon_{obj}\Phi_{obj}(x,y) + (1-\varepsilon_{obj})\varepsilon_{FPA}\Phi_{FPA}(x,y)] \tag{2.12}$$

where f_{vig} stands for the vignetting effect.

Building physics-based model to eliminate the radiometric artefacts is complicated, because its feasibility is strongly dependent on the validation of the underlining model. It is thus necessary to understand the different artefacts that can be encountered in the real measurement conditions (Castelein, 2003). A more generic approach is to consider the camera as a black box, and the correction is the calibration of the measuring chain as a whole. This methodology does not distinguish between the influences of the different components of the camera (Shi *et al.*, 2005; Kumar *et al.*, 2007). This philosophy is actually the calibration-based non-uniformity correction applied in this work, which will be presented in the following section.

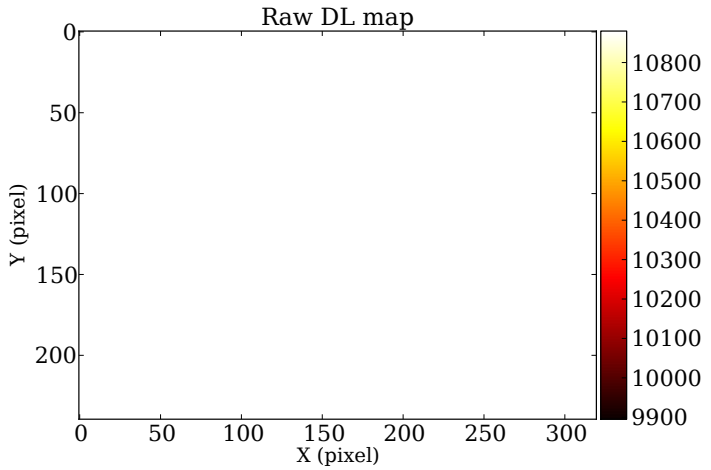

Figure 2.4: An example of the vignetting effect appearing in the corners of the infrared image in DL

2.1.2.2 Non-uniformity correction

A severe problem associated with the use of infrared FPA is the spatial photoresponse non-uniformity. The non-uniformity arises because each individual detector element in the FPA exhibits a characteristic response that differs from those of its neighboring elements (Schulz & Caldwell, 1995). NUC (Non-Uniformity Correction) is therefore an indispensable work in the calibration.

The calibration-based technique is the most common NUC method, used to correct non-uniformities. Calibration-based methods include single point correction, two points correction and N points correction. In these methods, the gain and offset parameters are estimated by exposing the FPA to different uniform blackbody temperatures depending on the algorithm adopted. The calibration-based techniques provide reasonably good estimates of the non-uniformity, and after NUC, the resulting IR images are radiometrically accurate (Ratliff *et al.*, 2005). In calibration-based methods, the NUC has to be performed on a regular basis since non-uniformity tends to drift over time (Mudau *et al.*, 2011).

N points NUC is the most complete version of NUC. It considers not only the gain and offset for a given calibration range, but also its potential non-linearity. In practice, in order to apply N points NUC, the camera FPA should be exposed to the extended BB at N different temperatures, thus N different fluxes. Then, the measured DLs by the IR camera at different flux levels are fitted into a polynomial function, by means of the least square method.

The applied algorithm is not a global approach, but a local approach, called "pixel-to-pixel" N points NUC. It means that the NUC is performed pixel by pixel. Thus, the measured DLs of each pixel are corrected individually in order to approach the mean values of DLs for given radiation fluxes. For a given pixel $P(x, y)$ with measured $DL(x, y)$, it

agrees to the following polynomial

$$\langle DL \rangle = \sum_{k=0}^{p} \alpha_k(x,y)(DL(x,y))^k \tag{2.13}$$

where $\langle DL \rangle$ represents the mean value of DLs of thermographic image, and α_k are the coefficients of the polynomial of degree p.

The method of least squares allows to optimize the coefficients α_k and thus to access the corrected values DL_c through

$$arg\ min \left\| DL_c(x,y,\alpha_k) - \langle DL \rangle \right\|^2 \tag{2.14}$$

where DL_c represents the DL after the correction.

Through the polynomial fitting, the corrected $DL_c(x,y)$ are approaching to the $\langle DL \rangle$ for a given flux. Hence, the uniformity of obtained thermographic images can be improved.

The corrected DLs can be further related to the given radiative fluxes, thus accomplishing the calibration. The NUC may constitute the principal part of a calibration. Nevertheless, there are also other practical issues needed to be considered in the calibration, such as the bad pixel detection and integration time selection. Thus, in this work a calibration procedure will be formulated after studying all these factors, where the effect of NUC will be also checked in a calibration test.

2.1.2.3 Bad pixel detection

In addition to NUC, another problem encountered in the application of FPA is the existence of bad pixels, which necessitates the BPD (Bad Pixel Detection).

The non-corrected pixels in the NUC are regarded as bad pixels. Some bad pixels are due to the non-functional sensors, but most of bad pixel are owning to so-called poorly-functional sensors which exhibit excessive noise. All the bad pixels should be recognized as they do not make any physical sense.

The conventional BPD methods can be classified according to the criteria: offset-based, gain-based and noise-based (Schulz & Caldwell, 1995). In this study, a more comprehensive method, so-called gradient-based BPD, is developed.

As the name suggests, the gradient-based BPD is based on the gradient map of the DL. The hypothesis is that the response of the bad pixel should differ widely from its neighboring pixels, thus it will result in a significant change on its nearby gradient values, forming therefore a distinctive pattern in the gradient map. A schematic diagram is shown by Fig. 2.5. The black grid in the image center corresponds to a bad pixel, its four affected neighboring pixels, highlighted in red, can thus be noticed obviously in the gradient map. Hence, they can be regarded as the indicators to find the bad pixel.

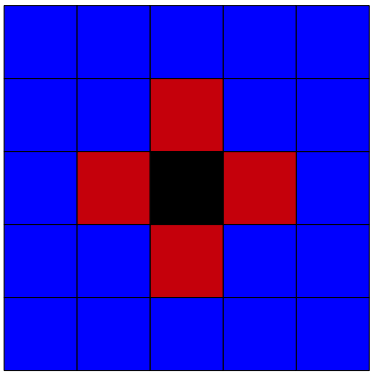

Figure 2.5: Pattern generated by the presence of a bad pixel

For a given pixel $P(x, y)$, it has a DL value $DL(x, y)$. The "analysis energy of image" for each point $P(x, y)$ can be denoted by $E_{IM}(x, y)$ that is defined as

$$E_{IM}(x, y) = \sqrt{\nabla_x^2 DL(x, y) + \nabla_y^2 DL(x, y)} \tag{2.15}$$

A factor c is chosen as the criterion for the determination of the bad pixels. The pixel $P(x, y)$ is regarded as a bad pixel if it meets

$$E_{IM}(x \pm 1, y \pm 1) > c\bar{E}_{IM} \tag{2.16}$$

where $E_{IM}(x \pm 1, y \pm 1)$ present the E_{IM} values of the four neighboring pixels of $P(x, y)$, and $\bar{E}_{IM}$ is the mean E_{IM} value of the whole DL map.

The factor c depends on the quality of the employed FPA and as well as the "stringency" imposed on the poorly-functional sensors. A suitable criterion should give a rather stable number of bad pixels in the whole calibration range. To our experience, the factor c can be chosen between 2 and 4. And in our experiments, the developed algorithm for BPD was proofed outperforming the conventional methods. Here it is also worth noting that in our tests the surface of BB is uniform without any spots, thus the flux emitted by BB is supposed uniform without any heterogeneities. Hence, the detected bad pixels are only due to the sensors of camera but not to the BB.

The DL given by a bad pixel represents an invalid data which should not be considered in a thermographic measurement. In this case, the temperature (or flux) on this pixel can usually be evaluated by referring to the measurement results of its neighboring pixels, e.g., through replacement or interpolation.

2.1.2.4 Integration time

The detectivity of an IR camera, which means the smallest temperature difference such a camera can detect, can be controlled by varying its exposure, or so-called IT (Integration Time) for thermal imaging systems, a term that is defined as the exposure time of the camera to produce a single frame. IT is a key parameter in the thermographic measurement,

which actually decides how many photons to be received by the camera.

The conventional strategy for choosing IT is to look for the longest possible IT before reaching saturation in case of static test. The limit of saturation for the applied thermographic system is 16384 (=2^{14}), which should be avoided when selecting the IT. The effect of IT selection in a thermographic measurement can be schematically illustrated in Fig. 2.6, where the DL-flux relationships resulted by choosing different ITs are shown. A reference range of radiative flux [400 $W.mm^{-3}$, 480 $W.mm^{-3}$] is also marked in this figure, which was validated in our experiments.

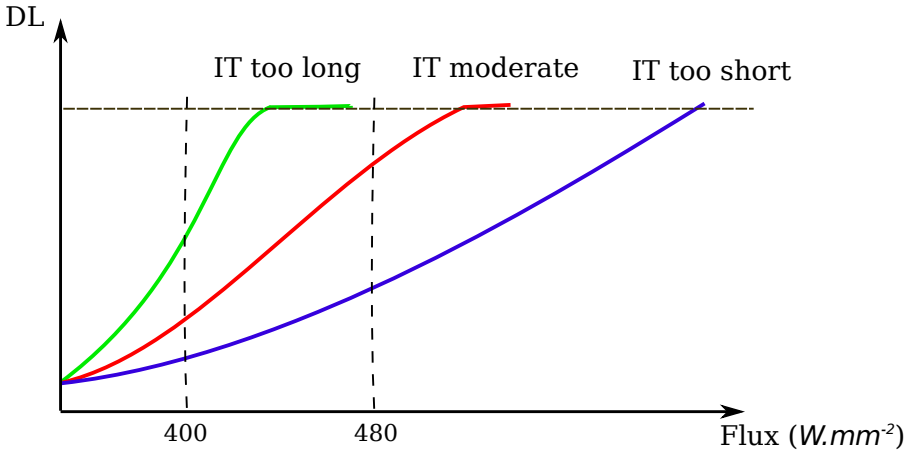

Figure 2.6: The DL-flux relationships by choosing different ITs

For the purpose of promoting a better understanding of IT, the relationship between DL, IT and radiative flux was studied.

If the object is a grey body, the radiative flux of the object Φ_{obj} in the spectral band [λ_1, λ_2] can be expressed through Stefan-Boltzmann law in the form

$$\Phi_{obj} = \int_{\lambda_1}^{\lambda_2} \frac{\mathrm{d}\Phi}{\mathrm{d}\lambda} d\lambda = \varepsilon \int_{\lambda_1}^{\lambda_2} \frac{\mathrm{d}(\sigma T^4)}{\mathrm{d}\lambda} d\lambda \tag{2.17}$$

where the spectral band [λ_1, λ_2] corresponds to that of the IR camera.

DL depends on flux and IT, thus

$$DL = f(\Phi_{obj}, IT) \tag{2.18}$$

IT controls the actual flux received by the camera Φ_{cam}, a fraction of the total flux Φ_{obj} emitted by the object. By receiving a certain flux, the Φ_{cam} needs to be transferred first to the analogical signal and then to DL. It is a complex process, for readers interested in the details please refer to the work (Genov & Cauwenberghs, 2004). In this study the relationship between Φ_{cam} and DL is assumed linear in order to simplify this problem, in this case

$$DL = \kappa \Phi_{cam} \tag{2.19}$$

where the coefficient κ is constant.

To perform an experimental verification of DL as a function of IT and flux, the calibration-based approach can be used once again. In the calibration test, the DLs are expected to be obtained under different ITs and fluxes (of BB), and then the function $f(\Phi_{obj}, IT)$ can be fitted as a polynomial which gives

$$DL = \sum_{i=0}^{p} \sum_{j=0}^{p} \alpha_i \beta_j (IT)^i (\Phi_{obj})^j \tag{2.20}$$

where $\alpha_i \beta_j$ are the coefficients of the polynomial of degree p.

The polynomial fitting can be achieved using the method of least squares, as that shown in the NUC. Thus the coefficients $\alpha_i \beta_j$ in the above equation can be solved.

Such a calibration test was carried out in a temperature range [20 $°C$, 30 $°C$], with IT set in the range [200 μs, 3500 μs], and the ambient temperature was quasi constant around 23 $°C$. The measured data were fitted according to Eq. 2.20 by choosing the order $p = 2$. Here the calculation was not carried out pixel to pixel but only at a global level, i.e., by using the average value of DLs (of all pixels) for each Flux-IT pair. The fitted surface is shown by Fig. 2.7.

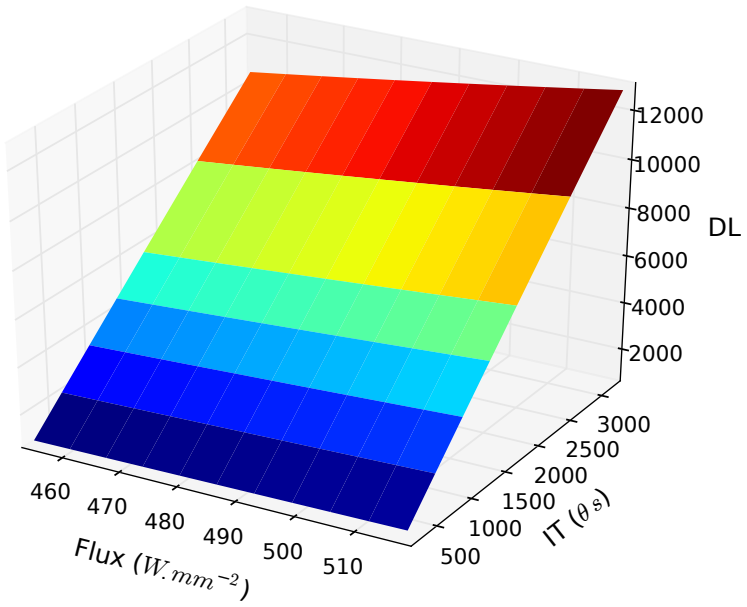

Figure 2.7: DL as a function of flux and IT in a calibration test of temperature range [20 $°C$, 30 $°C$] and in an ambient temperature of 23 $°C$

Fig. 2.7 shows a quasi-plane surface that crosses a large dynamic range, from about 800 DL to near 13000 DL. This suggests that the relationship between DL, IT and Flux is approximately linear. Thus, it is reasonable to assume that the function $f(\Phi_{obj}, IT)$ is linear, in this case the DL can be expressed as

$$DL = \kappa\delta\Phi_{obj} = \kappa\delta\varepsilon \int_{\lambda_1}^{\lambda_2} \frac{\mathrm{d}(\sigma T^4)}{\mathrm{d}\lambda} d\lambda \tag{2.21}$$

where the coefficient δ is defined as

$$\delta = \frac{IT - IT_{min}}{IT_{max} - IT_{min}} \tag{2.22}$$

where IT_{min} equals to 0, and IT_{max} is the upper limit of the IT in the model (corresponding to the saturation level).

Thus, the relationship between Φ_{cam} and Φ_{obj} depending on IT can be expressed as

$$\Phi_{cam} = \delta\Phi_{obj} = \frac{IT - IT_{min}}{IT_{max} - IT_{min}}\Phi_{obj} \tag{2.23}$$

The parameter δ varies from 0 to 1, identical to the range of the emissivity ε. Further more, in Eq. 2.21 the effects of the parameter δ and ε are the same in the sense mathematical, this property could be potential in some applications, for example the IT-based calibration. This method was, however, not adopted in this work.

By varying IT one can change the signal intensity (or DL), this does not however bring about any intrinsic change of the radiative flux, which is determined only by the temperature and emissivity of the object (not considering the reflections from the environment). These two contributing factors can not be separated in the signal processing unless one of them is known beforehand, or a simultaneous measurement technique is employed. For readers keening on the simultaneous measurement of temperature and emissivity, please refer to the works (Negreanu, 2009; Kasem *et al.*, 2010; Herve *et al.*, 2012). Nevertheless, these advances on temperature-emissivity coupled measurement are still limited on point measurements by using two-color pyrometer or IR detectors with two different wavelengths. To our knowledge, a full-field temperature-emissivity simultaneous measurement using IR cameras is, by far, still a technical challenging.

2.1.2.5 Calibration method and verification

With a sensible selection on IT, the calibration test can be carried out. In the calibration test, the BB with N different flux levels is measured by the IR camera, resulting therefore N corresponding thermal images in DL. Then the DL-Flux relationship is expected to be established from the calibration measurement data.

As explained in the section "non-uniformity correction", the calibration can be divided into two steps. The first step is the NUC on the raw DL to obtain the corrected DL_c, and the second step is the determination of DL_c-Flux relationship. Nevertheless, a more practical and efficient way is to integrate these two steps into one by

$$\Phi(x, y) = \sum_{k=0}^{p} \alpha_k(x, y)(DL(x, y))^k \tag{2.24}$$

where α_k are the coefficients of the polynomial of degree p.

By applying the above formula, the DL can be directly converted into Φ through NUC without the passage to DL_c. The polynomial fitting serves not only the non-uniformity correction but also the DL-Flux transformation.

A calibration test was conducted in order to verify the proposed method. The tested IR camera was the Cedip Jade III MW, which has a FPA made of 320 × 240 sensors (or 76800 pixels). The selected calibration range was [18 $°C$, 29 $°C$] with a sampling interval 1 $°C$, thus 12 points in total were acquired. The polynomial fitting as indicated in Eq. 2.24 was performed for each pixel of FPA. Fig. 2.8 shows the whole flux calibration curves for the FPA sensors.

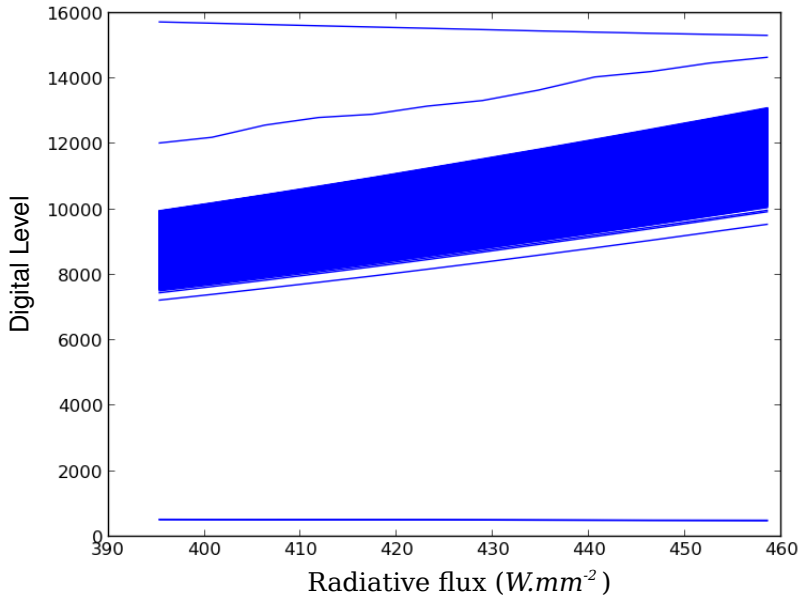

Figure 2.8: Calibration curves for all sensors of FPA for a temperature range [18 °C, 29 °C]

In Fig. 2.8 it is remarkable that there are several exceptional curves with very high or very low DL values. They represent actually the responses of the bad pixels, which can also be detected by the proposed BPD method. Except these few abnormal pixels, one can observe that the general responses of most sensors vary as large as 3000 DL under the same radiative flux (or temperature) throughout the calibration range. This gives evidence of the necessity for carrying out a pixel-to-pixel calibration strategy.

The effect of the NUC by the proposed method was also checked in this study. An example is illustrated here concerning a given temperature of BB in the calibration range, 24 $°C$ (or 428.89 Wmm^{-2} in radiative flux), its raw DL map and calibrated flux map are illustrated in Fig. 2.9 (a) and (b), respectively.

The non-uniformity in the raw DL map of BB shown in Fig. 2.9(a) is caused by several reasons. The main responsibility should be attributed to the radiometric artefacts, involving both the Narcissus effect and vignetting effect, as having been already discussed. Except

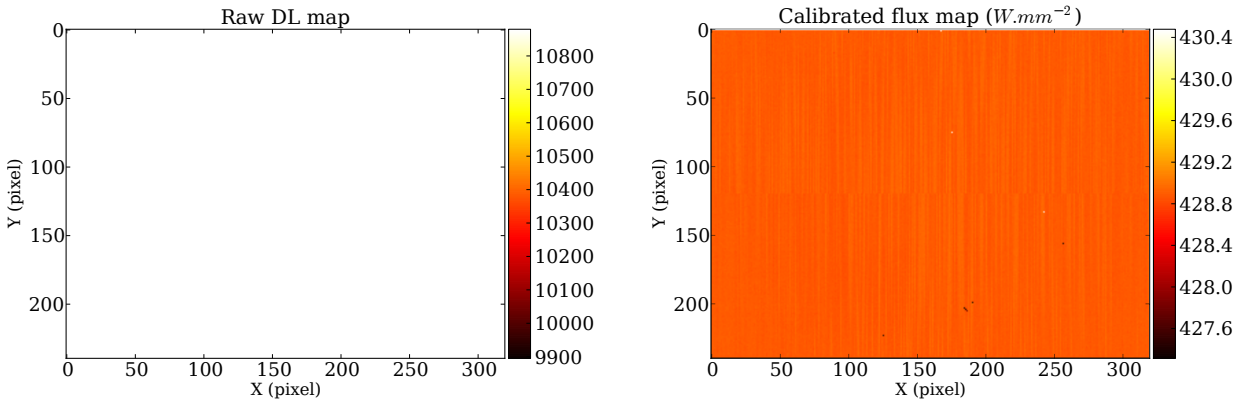

(a) (b)

Figure 2.9: For the BB with a given temperature 24 $°C$ in: (a) raw DL map and (b) calibrated flux map

these optical artefacts, there are also electronic artefacts that can be noticed in Fig. 2.9(a), appearing in the form of vertical lines. The other reason for the appearing non-uniformity is the non-identities of the FPA sensors, as each sensor has its own dynamic characteristics. The "pixel-to-pixel" calibration through N points NUC provides a generic approach to correct the image non-uniformity regardless of its origin. The calibrated thermal field in Fig. 2.9(b) has already shown a satisfactory result.

Besides the verification on BB, the performance of the developed calibration method was also verified for a given object of measurement. The selected testing object was a well-designed perforated plate, so-called the micro-target, which will be used in the following studies. The micro-target was filmed by the IR camera in the ambiance without any special heat source or radiation source. Fig. 2.10(a) shows its raw thermal image in DL before the calibration and 2.10(b) the calibrated thermal image in flux.

The main radiometric artefacts appearing in the raw thermal image Fig. 2.10(a) are the vignetting effect at the periphery of image and the electronic artefacts throughout the image (vertical lines), which affect the image quality gravely. Thanks to the NUC in the calibration, these artefacts can not found any more in the calibrated thermal image Fig. 2.10(b) that reveals the true face of the micro-target.

A complete calibration method has been developed in this work, and was verified through two tests. Another important element in the thermographic measurement, the emissivity, will be tackled in the following section.

2.1.3 Emissivity

The radiative flux, which can be measured by an IR camera, is an a priori unknown function of the emissivity and temperature of the radiating elements. The emissivity depends

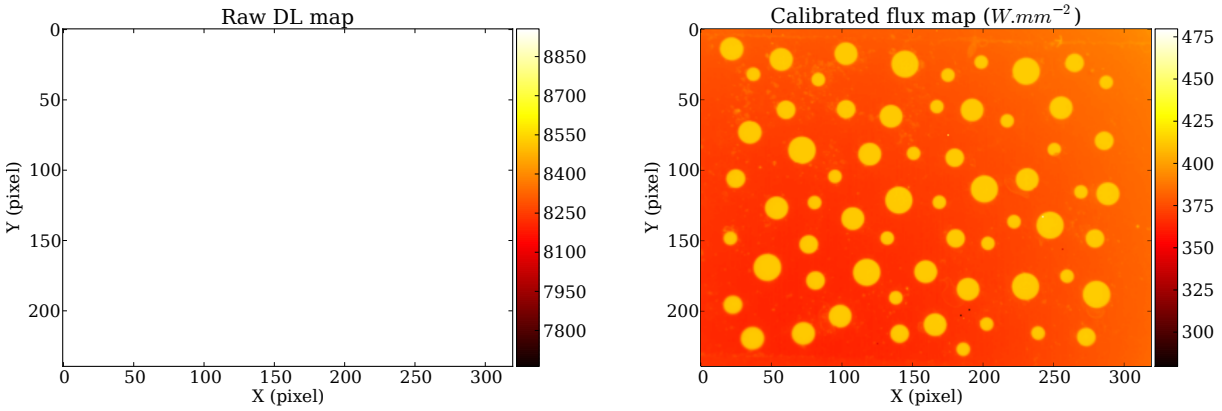

(a) (b)

Figure 2.10: The micro-target in: (a) the raw thermal image in DL and (b) the calibrated thermal image in flux

on the direction of observation relative to the radiation surface and on the temperature of the surface (Gaussorgues, 1994).

For a given material, the emissivity is often evaluated at normal incidence and integrated over all wavelengths:

$$\varepsilon = \frac{1}{\sigma T^4} \int_0^\infty \varepsilon(\lambda) \frac{d\Phi(\lambda, T)}{d\lambda} d\lambda \tag{2.25}$$

In the practical measurement, for an IR camera with a spectral band $[\lambda_1,\ \lambda_2]$, the measured emissivity actually corresponds to

$$\varepsilon_{[\lambda_1, \lambda_2]} = \frac{\int_{\lambda_1}^{\lambda_2} \varepsilon(\lambda) \frac{d\Phi(\lambda,T)}{d\lambda} d\lambda}{\int_{\lambda_1}^{\lambda_2} \frac{d\Phi(\lambda,T)}{d\lambda} d\lambda} \tag{2.26}$$

It is important to note that the emissivity measurement in our study is restrained at room temperature. In other words, the measured emissivity of material is the one around 20 $°C$. The influence of a small variation of ambient temperature on the emissivity is tiny, so it is negligible.

There are different ways to measure the emissivity, by using varied test instruments (Poncelet *et al.*, 2007; Negreanu, 2009; Herve *et al.*, 2012). The philosophy adopted in this study is to use the IR camera and to take BB as the reference of emissivity. In principle there are two ways: direct measurement and indirect measurement.

The direct measurement is to compare the radiation from the object to that from BB at the same temperature. In this case, the radiation levels depend only on the emissivity. With the known emissivity of BB, the object's emissivity can be solved:

$$\varepsilon_{obj} = \frac{\varepsilon_{bb} \Phi_{obj}(T)}{\Phi_{bb}(T)} \tag{2.27}$$

The idea is simple, but in reality to provide "the same temperature" condition is yet a technical challenge. In particular when an emissivity map is looked for, the temperature should be ensured being uniform on the material surface. A temperature controlling approach is possible, by heating or cooling the object. It is, however, very demanding on the temperature controlling technique, which we did not succeed in our experiments. Finally we attempted to make use of the ambient temperature: put the object and BB together in an enclosed chamber and measure their radiations by an infrared camera at the same moment. The hypothesis is that at the same instant and in the laboratory conditions, their temperatures are the same and they are uniformly distributed on the surface of each of them. Moreover, the reflection effect from the environment is ignored in this method.

The alternative choice is the indirect approach, which was adopted in the investigations (Berthel, 2007; Poncelet *et al.*, 2007; Bodelot, 2008). The principle of this method is to make use of BB as an emitting body and the specimen a reflecting body. It has a special experimental set-up, as illustrated in Fig. 2.11. The specimen surface for measurement should be tiled by 45° both with respect to the normal of BB and that of IR camera. Here it is worthy to note that this indirect method is usually used for estimating the global emissivity (or average emissivity) of a specific material but not for obtaining an emissivity map (Berthel, 2007; Poncelet *et al.*, 2007; Bodelot, 2008), in particular when the specimen surface shows a very heterogeneous emissivity distribution.

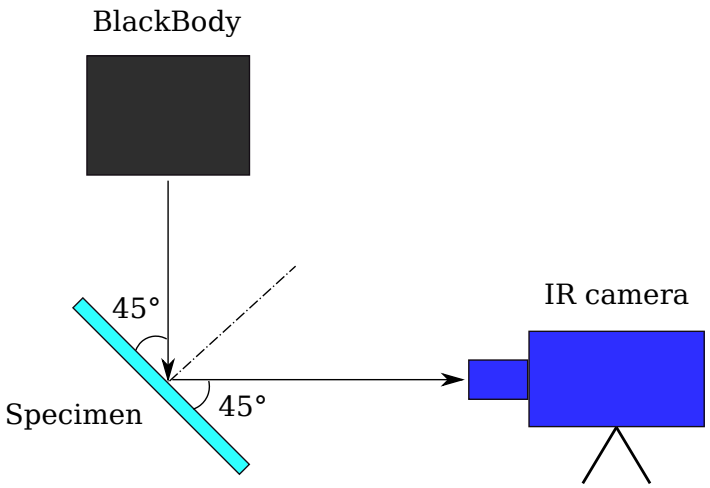

Figure 2.11: Experimental set-up of the indirect measurement

To conduct the indirect measurement, it needs to set two different temperatures for BB, T_1 and T_2, and then to perform two measurements for T_1 and T_2, respectively. Thus, two groups of data can be obtained:

$$\begin{cases} \Phi(T_1) = \varepsilon_{bb}(1-\varepsilon_{obj})\Phi_{bb}(T_1) + \varepsilon_{obj}\Phi_{obj} \\ \Phi(T_2) = \varepsilon_{bb}(1-\varepsilon_{obj})\Phi_{bb}(T_2) + \varepsilon_{obj}\Phi_{obj} \end{cases} \tag{2.28}$$

It is worth noting that Φ_{obj} is assumed to be constant during the two measurements. Thus, the interval between the two measurements should be as short as possible.

Subtracting one group by the other in Eq. 2.28, the flux emitted by the object itself can be canceled out and its emissivity is derived:

$$\varepsilon_{obj} = 1 - \frac{\Phi(T_2) - \Phi(T_1)}{\varepsilon_{bb}(\Phi_{bb}(T_2) - \Phi_{bb}(T_1))} \tag{2.29}$$

The selection of the two temperatures T_1 and T_2 should be cautious. If the selected temperatures are too high, it risks heating the surface of the object, thus the Φ_{obj} is altered. If the selected temperatures are too low, the signal-to-noise ratio will not be satisfactory.

The emissivity of the coating carbon black was measured by both the direct and indirect methods.

The result given by the direct solution was 0.967 in an ambient temperature of 26 $°C$, and in another test 0.968 in an ambient temperature of 25 $°C$. The emissivity evaluated by the indirect solution was 0.970 by selecting two different temperatures 27 $°C$ and 29 $°C$ of BB. Both of the results showed that the emissivity distribution of the carbon black was rather uniform.

The difference between the results obtained by the two different methods is less than 0.003. Considering the measurement errors and uncertainties, it is reasonable to suppose 0.97 as the emissivity of the carbon black at room temperature.

Until now, the metrological study on QIRT has been accomplished. The next section will be focused on the other metrology, the DIC for kinematic field measurement.

2.2 DIC and image registration

This part of study is concerned with the kinematic measurement in order to obtain the displacement and strain fields. The technique used for realizing such an objective is the DIC, or say image registration. There is actually no genuine difference between the two terms: DIC usually used in the field of solid mechanics (Sutton *et al.*, 2009; Grédiac & Hild, 2011) and image registration in the field of medical imaging (Maintz & Viergever, 1998; Hill *et al.*, 2001; Rueckert & Schnabel, 2011) or more broadly. In most of cases, the objective of DIC is to access the displacement and strain fields in the mechanical tests. And the goal of image registration is to register the images by using a function of transformation, which allows also the assessment of displacement and strain fields.

In this work, "elastix" (Klein & Staring, 2011), an open-source software for image registration, was adopted for the assessment of displacement and strain fields. In order to promote a better understanding of our approaches, the technical issues concerning the image treatment will be discussed in the framework of image registration in the following presentation. And some necessary backgrounds about full-field measurements in solid mechanics and its experimental aspects will still adopt the term DIC. Here a brief introduction about the development of the DIC technique will be first given in the following.

DIC is an optical metrology based on digital image processing and numerical computing. It was first proposed at the beginning of the 1980s when applied in solid mechanics (Sutton *et al.*, 1983; Chu *et al.*, 1985; Sutton *et al.*, 2009), inspired at its early stage from image correlation velocimetry methods in fluid mechanics (Dudderar & Simpkins, 1977). Through 30 years of development, the DIC method has been well accepted in the field of experimental solid mechanics, and has been widely used as an innovative and powerful tool for the full-field measurements and model/parameter identifications. It is changing the face of the solid mechanics and is currently experiencing a spectacular growth.

The basic purpose of the DIC method is to measure the displacement fields of the specimen under mechanical loading, from images acquired at different stages of the loading process. A specific feature of this tool is that it uses digital images, mostly acquired by optical means, then without contact. Nowadays, their digital imaging means progress considerably in quality, at a cost more and more modest (Grédiac & Hild, 2011).

The DIC technique can be compatible and easily varying in a wide range of space and time scales. The applicable physical scale can vary from nanometers to meters depending upon the magnification means of the optical cameras. It is worth noting that the physical scale has a negligible impact on the correlation results, provided that a random texture of the digital image can always be guaranteed in the image acquisition. For the time scale now it is possible to exploit the images acquired by the fast and ultrafast cameras with a speed up to the magnitude of microsecond. Moreover, nowadays the developed DIC technique is not limited to 2D in-plane deformation measurement, but is also used for 3D deformation measurement (in-plane and out-of-plane) thanks to a multi-camera set-up. And the new DVC (Digital Volume Correlation) technique has also been developed recently in order to exploit the 3D volume deformation measurement through the instrumentality of the tomography. Nevertheless, the investigations in our study are still focused on the in-plane measurement using the 2D-DIC technique.

This part is arranged as followings: first of all, the specimen preparation and imaging system are introduced. Then, the basic principle and several important elements of the image registration method are presented. And the calculation from displacement to strain are discussed. Finally, an experimental error analysis on the proposed image registration method was carried out.

2.2.1 Specimen and imaging system

A schematic illustration of the DIC imaging system is shown by Fig. 2.12. The digital camera is placed with its optical axis normal to the specimen surface, imaging the planar specimen surface onto its sensor plane. The lights are introduced in the system in order to provide uniform and stable lighting on the specimen surface.

The DIC method works on a texture that has to be a signature of each surface element, simply convected by the displacement field, without any alteration. In addition, the gray levels must have a wide dynamic that covers the best the depth of the gray levels of the digital image, but without showing saturation (Grédiac & Hild, 2011). This kind of texture

can be made artificially by depositing a speckle pattern on the specimen surface. It can be realized by spraying fine droplets of black paint on a white background (or inversely), using aerosol spray, or by airbrush for a finer textured effect. In the mechanical testing the speckled paint should deform together with the specimen, functioning as a carrier of the deformation information.

Fig. 2.13(a) illustrates a typical speckled paint and (b) its corresponding image histogram. The histogram shows that the standard deviation of gray levels is about 30.1 in a dynamic range [0, 255] for the illustrated image of speckled paint. It is worth mentioning that for some studies on the microscale, the specimen surface is not necessarily to be covered by a special coating. The microstructure of material revealed by the chemical etching (or electric etching) can be suitable for the DIC technique (El Bartali *et al.*, 2008).

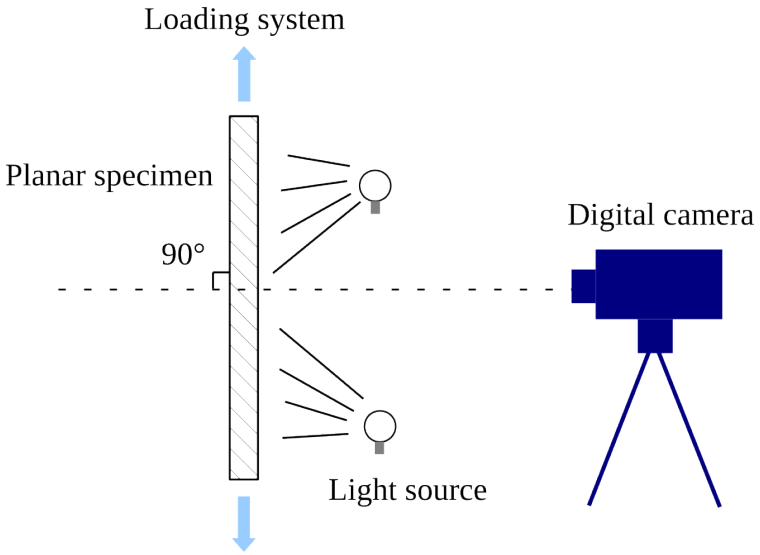

Figure 2.12: DIC imaging system

For the 2D-DIC system with a single camera set-up, an accurate in-plane kinematic measurement can be made provided that (Pan *et al.*, 2009): 1) The specimen surface must be flat and remain in the same plane parallel to the sensor target of the camera during loading. 2) The imaging system should not suffer from geometric distortion. These two conditions can be considered as the main sources of error for the in-plane kinematic measurement and should draw the attention of the experimenters.

Another important issue in conducting a DIC test is the selection of the lighting systems. An ideal lighting is expected to be powerful, cold and stable. A powerful lighting will help to reduce the exposure time efficiently, and the "cold" is mainly for the consideration of the thermographic measurement which will be coupled with DIC measurement applied to the same specimen. A stable lighting can ensure more stable and reliable images to be captured. Several different lighting solutions were investigated in this work, as presented in the following.

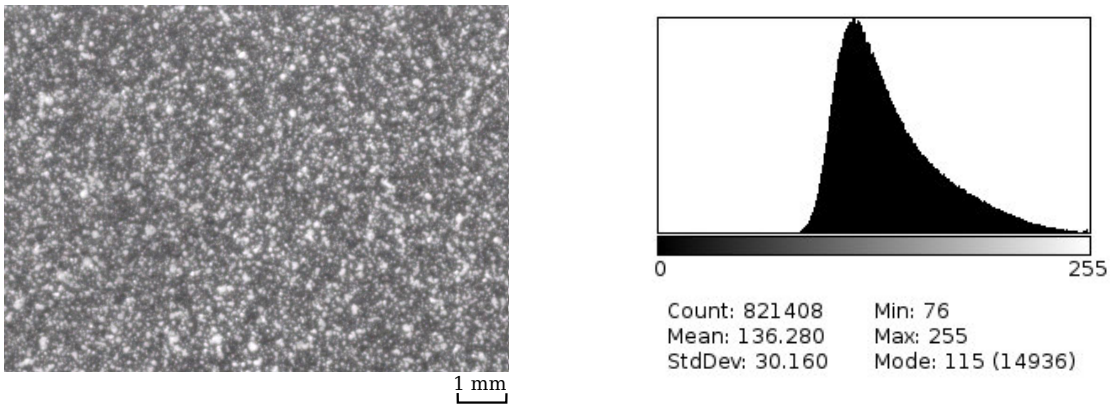

(a) (b)

Figure 2.13: (a) A typical speckled paint, (b) the corresponding image histogram

1) Projector

The projector is a high-power illuminant. It can shorten the exposure time massively, up to as low as 0.01 ms. However, the projector can heat the specimen during the test, thus affecting the thermographic measurement. For this reason, it is not applicable for our experiments.

2) Fiber optic illumination

The fiber optic illumination was adopted in a pertinent investigation (Bodelot, 2008) and showed good performance. A typical image of the fiber optic light system is shown in Fig. 2.14. Its main advantages include that the fiber optic is very flexible, easily to be adapted into the experimental set-up. And the fiber optic light can provide strong and uniform illumination on a very local zone, which is convenient for the studies on the microscale. Generally it can shorten the exposure time up to $5 \sim 10$ ms, sufficient for most studies.

In this work, the fiber optic illumination was employed in the microscale investigation on nickel single crystals.

3) LED (Light-Emitting Diode)

The LED can generally provide stable, powerful and cold illumination, meeting all the desirable criteria. In this study, a special LED light kit was designed and home made, as shown in Fig. 2.15. This LED light kit is an assembly of four panels that contain many small LEDs. The annulus design is to provide a focused and uniform light source in order to eliminate (at least weaken) the possible reflection effects. By using the LEDs, the exposure time can be reduced up to 3 ms. The LED light kit was employed in the macroscale study on the aluminum oligocrystals.

Figure 2.14: Fiber optic light system

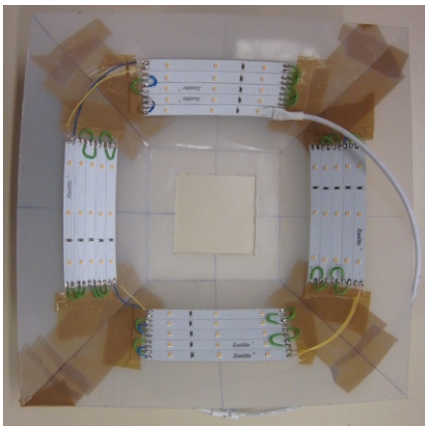

Figure 2.15: LED light kit

By means of the external illumination, a relative short exposure time can be chosen in the parameter settings, so that the sampling frequency of camera can be enhanced. Here it is also worth noting that the exposure time can not be set too low to provide a wide dynamic range of the digital image, i.e., the saturation should be avoided.

2.2.2 Basic principle and elements

Two images are involved in the image registration, which characterize the original and deformed surface of a material subjected to a known loading. An image is a scalar function of the spatial coordinate that gives the gray level at each discrete point (or pixel) of coordinate x. The images of the reference and deformed states are called $f(x)$ and $g(x)$, respectively. The displacement field $u(x)$ is necessary to be introduced. Thus, this field allows one to relate the two images by requiring the conservation of the optical flow (Westerweel, 1997; Chang *et al.*, 2002; Besnard *et al.*, 2006):

$$f(x) = g[x + u(x)] = g[T(x)] \tag{2.30}$$

where $T(x) = x + u(x)$ is defined as the transformation, and $g[T(x)]$ is generally called as the corrected deformed image.

The goal of the image registration is to solve the problem of finding a transformation $T(x)$ that makes $g[x + u(x)]$ spatially aligned to $f(x)$. The quality of alignment is defined by a distance or similarity measure S. Because this problem is ill-posed for nonrigid transformations T , a regularization or penalty term P is often introduced that constrains T.

Commonly, the registration problem is formulated as an optimization problem in which the cost function C is minimized with respect to T:

$$\hat{T} = arg\ min C[T; f(x), g(x)] \tag{2.31}$$

$$C[T; f(x), g(x)] = -S[T; f(x), g(x)] + \gamma P(T) \tag{2.32}$$

where γ weights similarity against regularity.

To solve the above minimization problem, the parametric method is generally adopted. In parametric methods, the number of possible transformations is limited by introducing a parametrization model of the transformation. The original optimization problem thus becomes:

$$\hat{T}_\mu = arg\ minC[T_\mu; f(x), g(x)] \tag{2.33}$$

where the subscript μ indicates that the transform has been parameterized.

The error of image registration can be evaluated through the residual image $r(x)$, which represents the difference between the reference image $f(x)$ and the corrected deformed image $g[T_\mu(x)]$, i.e.,

$$r(x) = f(x) - g[T_\mu(x)] \tag{2.34}$$

The residual image serves often as a reference for the local error verification in the image registration. Here an example is illustrated to show how to interpret the residual image. Fig. 2.16(a) shows a reference image $f(x)$ and (b) the corrected deformed image $g[T_\mu(x)]$ through a transformation T_μ. Both of the two images show a round in black appearing in the center of image against the white background. The resulting residual image $r(x)$ in this image registration is shown in Fig. 2.16(c). Two crescent-shaped zones (one in black and the other in white) emerge nearby the circle boundary indicate that the corrected deformed image is not spatially matched (or registered) with the reference image, so these two shadow zones represent actually the local errors of image registration. Here it is also worthy to note that the residual image is expressed in gray levels but not in pixels.

In our study, an open-source software elastix (Klein & Staring, 2011) is used for the implementation of image registration. A large part of its code is based on ITK (Insight Toolkit). Fig. 2.17 shows the basic components in the process of the image registration in elastix.

The fixed image and moving image in Fig. 2.17 correspond to the images of the specimen surface in the original and deformed states, respectively. The "metric" is the similarity measure, a concept similar to the correlation criterion in DIC.

For a better understanding of the principle of the image registration method and a proper use of the software elastix, some important elements involved are introduced below.

1) Metrics

Several choices for the similarity measure can be found in the literatures. The most commonly used metrics include: SSD (Sum of Squared Differences), NCC (Normalized Cross-Correlation), and MI (Mutual Information).

The SSD is defined as:

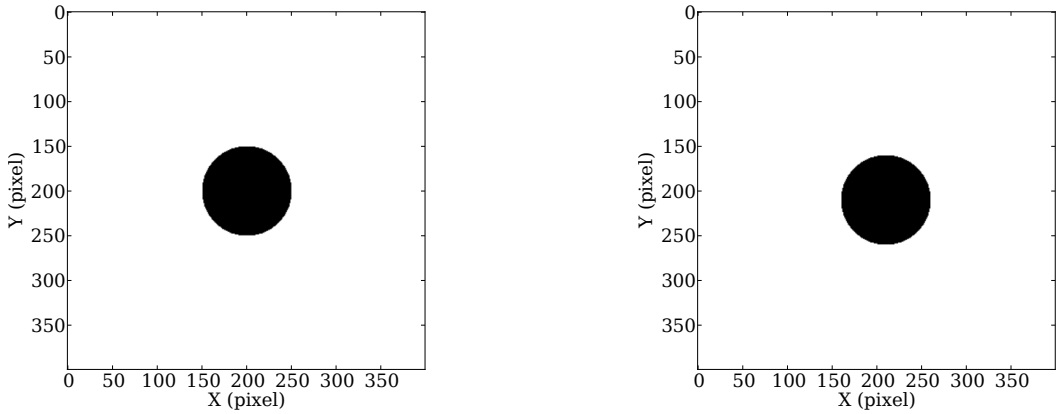

(a) (b)

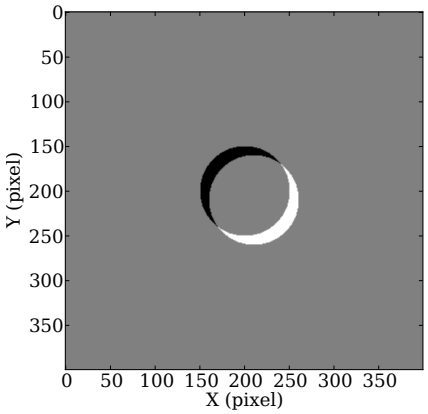

(c)

Figure 2.16: (a) The reference image $f(x)$, (b) the corrected deformed image $g[T_\mu(x)]$ and (c) the residual image $r(x)$

$$\mathrm{SSD}(\mu; I_F, I_M) = \frac{1}{|\Omega_F|} \sum_{x_i \in \Omega_F} (I_F(x_i) - I_M(T_\mu(x_i)))^2 \tag{2.35}$$

with Ω_F the domain of the fixed image I_F , and $|\Omega_F|$ the number of pixels. Given a transformation T, this measure can easily be implemented by looping over the pixels in the fixed image, taking $I_F(x_i)$, calculating $I_M(T_\mu(x_i))$ by interpolation, and adding the squared difference to the sum.

The NCC is defined as:

$$\mathrm{NCC}(\mu; I_F, I_M) = \frac{\sum_{x_i \in \Omega_F} (I_F(x_i) - \bar{I_F})(I_M(T_\mu(x_i)) - \bar{I_M})}{\sqrt{\sum_{x_i \in \Omega_F} (I_F(x_i) - \bar{I_F})^2 \sum_{x_i \in \Omega_F} (I_M(T_\mu(x_i)) - \bar{I_M})^2}} \tag{2.36}$$

with the average gray values $\bar{I_F} = \frac{1}{|\Omega_F|} \sum_{x_i \in \Omega_F} I_F(x_i)$ and $\bar{I_M} = \frac{1}{|\Omega_F|} \sum_{x_i \in \Omega_F} I_M(T_\mu(x_i))$.

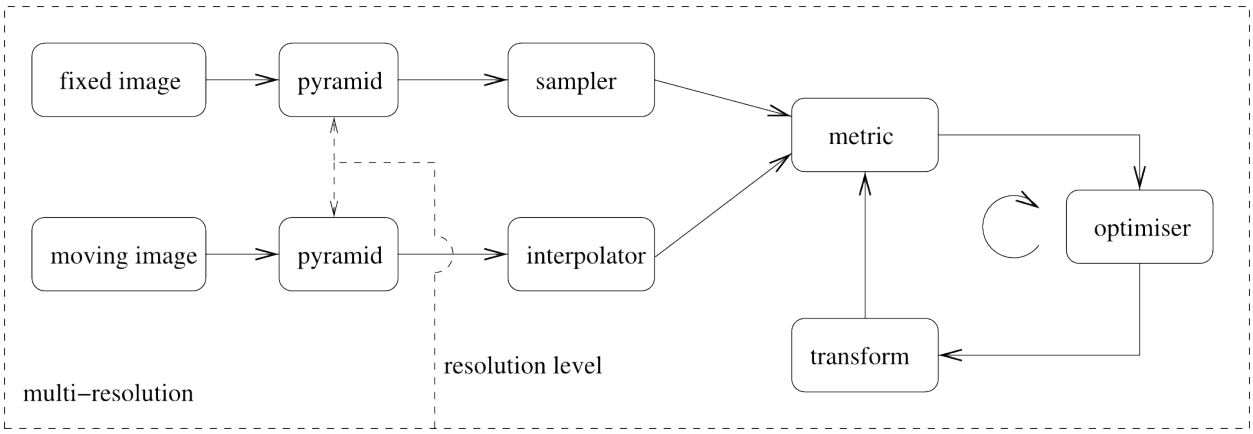

Figure 2.17: The basic image correlation components (Klein & Staring, 2011)

The definition of MI in elastix is given by (Thévenaz & Unser, 2000):

$$\mathrm{MI}(\mu; I_F, I_M) = \sum_{m \in L_M} \sum_{f \in L_F} p(f, m; \mu) log_2 \left[\frac{p(f, m; \mu)}{p_F(f) p_M(m; \mu)} \right] \tag{2.37}$$

where L_F and L_M are sets of regularly spaced intensity bin centres, p is the discrete joint probability, and p_F and p_M are the marginal discrete probabilities of the fixed and moving image, obtained by summing p over m and f, respectively. The joint probabilities $p(f, m; \mu)$ are estimated using B-spline Parzen windows.

The SSD criterion is a criterion that is only suited for two images with an equal intensity distribution. NCC is less strict, it assumes a linear relation between the intensity values of the two images, and can therefore be used more often. The MI criterion is even more general: only a relation between the probability distributions of the intensities of the original and deformed image is assumed. Hence, as its versatility, MI is encouraged to be considered as a priority choice (Pluim *et al.*, 2003). An important application of MI in this study is in the spatial matching between the visible image and IR image of the same reference target, in which the MI criterion shows its particular utility. It serves for realizing a kinematic-thermal coupled measurement, and this specific point will be detailed in the next chapter.

2) Image samplers

In the most cases, a full sampler is not necessary, and a subset may suffice (Klein *et al.*, 2007). The subset may be selected in different ways: random, on a grid, etc.

The grid sampler defines a regular grid on the fixed image and selects the coordinates x_i on the grid. Effectively, the grid sampler thus downsamples the fixed image (not preceded by smoothing). It is the most used strategy. The grid size is a user input, which is a key parameter in the image registration computation.

3) Transformations

The transformation model used for T_μ determines what type of deformations between the fixed and moving image. In order of increasing flexibility, the choice of the transformations can be translation, rigid body, similarity, affine, nonrigid B-spline, etc. The B-spline transformation is generally used in the case of non-homogeneous deformation. In elastix the B-splines (Rueckert *et al.*, 1999) are used as a parameterization:

$$T_\mu(x) = x + \sum_{x_k \in N_x} p_k \beta^3(\frac{x - x_k}{\sigma}) \tag{2.38}$$

with x_k the control points, $\beta^3(x)$ the cubic multidimensional B-spline polynomial (Unser, 1999), p_k the B-spline coefficient vectors (loosely speaking, the control point displacements), σ the B-spline control point spacing, and N_x the set of all control points within the compact support of the B-spline at x.

It is also worth noting that in elastix it is possible to initialize a nonrigid image correlation problem by performing a rigid or affine transformation in advance.

4) Interpolation

During the optimization the value $g(T_\mu(x))$ is evaluated at non-pixel positions, for which intensity interpolation is needed. Several methods for interpolation exist, from the nearest neighbour interpolation to a higher-order B-spline interpolation, varying in quality and speed. A 3rd order B-spline can usually give satisfactory results for a non-homogeneous deformation.

5) Optimisation

To solve the optimisation problem in Eq. 2.33, i.e., to obtain the optimal transformation parameter vector μ, commonly an iterative optimisation strategy is employed:

$$\mu_{k+1} = \mu_k + a_k d_k \tag{2.39}$$

with d_k the "search direction" at iteration k ($k = 0, 1, 2, \cdots$)

$$d_k = \frac{\partial C([T_\mu; f(x), g(x)])}{\partial \mu} \tag{2.40}$$

and a_k a scalar gain factor controlling the step size along the search direction.

The available optimisation methods in elastix include quasi-Newton (QN), nonlinear conjugate gradient (NCG), gradient descent (GD), Robbins-Monro (RM), ect. More detailed information about these methods can be found in (Klein & Staring, 2011; Klein *et al.*, 2007; Nocedal & Wright, 1999).

6) Multi-resolution (or multi-scale)

The multi-resolution approach is a necessary and efficient way to reduce the data complexity as well as the transformation complexity of the given images. It is highly recommended for a non-homogeneous deformation case. For a comprehensive understanding of the multi-resolution strategies, please refer to the survey (Lester & Arridge, 1999).

2.2.3 From displacement to strain

The image registration provides the displacement field as the direct output via the solved transformation. While in most cases, the strain field is preferred for the applications in solid mechanics. With the transformation from the displacement to strain arises the question of the differentiation of noisy experimental data, implying a particular treatment in order to reduce the effect of noise on the results (Grédiac & Hild, 2011). The relevant methods adopted in our studies are discussed in this section.

The displacement given by the image registration through digital images are discrete points on a grid, which can be expressed as

$$\underline{\tilde{u}}(\underline{x}_i),\ i \in [1, N] \tag{2.41}$$

where $\underline{x}_i$ is the position of the data point i.

Obtained from an experimental measurement, the displacement field can be considered as the sum of two terms: the mechanical displacement field $\underline{u}_{ex}$ (which is desired to derive the gradient) and the measurement errors $\delta\underline{u}$ (both systematic and random errors). In this case,

$$\underline{\tilde{u}}(\underline{x}_i) = \underline{u}_{ex}(\underline{x}_i) + \delta\underline{u}(\underline{x}_i),\ i \in [1, N] \tag{2.42}$$

The strain field can be reconstructed (infinitesimal) by

$$\underline{\underline{\varepsilon}} = \frac{1}{2}(\nabla\underline{u} + \nabla^t\underline{u}) \tag{2.43}$$

The problem of calculating the gradient returns to estimate the derivatives of the displacements that are discrete and noisy. The solutions may include: finite difference, projection and image processing (such as filtering, denoising). The first two approaches are involved in our study. A brief description about them is given as below.

1) Finite difference method

Since the data are discrete, the most direct approach to estimate the gradient is to use the finite difference method. It is actually discretize the derivative operators of the finite growth between data points by the formulas of varying complexity depending on the chosen method. These approaches are derived from the solution of differential equations and partial differential equations and do not take into account the particular measurement noise (Grédiac & Hild, 2011).

In elastix the finite difference method can be realized by the B-spline transformation, with a specification on the final grid spacing. The grid spacing defines how dense the grid

is, in other words, how fine the structure is expected to be modeled. Elastix also provides the function "transformix" to calculate the spatial Jacobian matrix using the shape function derivation, from which the strain fields can be obtained.

2) Projection method

The projection method is an approximated approach. The idea is to project the measurements on a functional base through interpolation, where only the derivation of the produced function is taken into account for the strain computation. By choosing the regular basis functions, a good noise filtering can be ensured by this approach. In most of cases, a polynomial basis suffices for a good performance, and the interpolation can be generally achieved through the minimization of the least squares.

Concerning the materials deformation at the microstructure scale, the deformation pattern is often heterogeneous and closely associated with the crystallographic structure and microstructure evolution of materials, such as the grain boundaries and slip bands activations. They provide very valuable information for determining the kinematic basis and the details of the projection method (Seghir, 2012). The microstructure-based projection approach is an important strategy for the data treatment adopted in this study. It specific applications in oligocrystals and single crystals will be detailed in chapters 4 and 5.

2.2.4 Experimental error analysis

The employed image registration method gives access to quantitative measurements of displacement and strain fields. It is therefore crucial to evaluate the errors associated with its implementation.

According to the error sources, the errors can be classified into two types. The first type of errors is extrinsic to image registration because they result from image acquisition. Its respective error sources mainly include:

1) Intrinsic noise in digital images depending on the camera quality;

2) Optical artifacts induced by the objective lens and magnifications;

3) Changes in local contrast and brightness on the material surface due to a relevant variation of the lighting or caused by other possible reasons, such as a damage occurred in the deposited paint during deformation.

The second type of errors is directly associated with the adopted image registration method. The cases one may encounter include:

1) The selected function of transformation is unable to describe the real transformation T_μ of the object;

2) The chosen interpolation method does not satisfy optimal evaluations of gray levels

at the non-pixel positions;

3) The ultimate calculation results do not converge for varied reasons, such as inappropriate selections on metrics, multi-resolutions and optimisation algorithms.

To identify different error sources in a real test is a very challenging issue, not to mention to access the error level for each type of errors. In this study, we consider all kinds of errors as a whole, and the interest is to estimate the ultimate errors in the outputs of image registration, i.e., the displacement and strain fields. To this end, a dedicated test was conducted for evaluating the experimental error levels of the developed kinematic measurement system in this study.

The test aimed at the transformation type in image registration as simple as possible. Firstly, an image of the testing specimen was taken at its initial position, so-called the reference image. And then another image was taken when the specimen was moved by a certain amount of displacements but without any deformation imposed on the specimen. This image is named by the "deformed" image. The two above images are now involved in the image registration, as shown in Fig. 2.18. Generally speaking, the transformation type "affine" involves all the possible transformations between the two images: translation, rotation, scaling, shear mapping, etc. Thus, a basic hypothesis in this error analysis is that the calculation results (of displacements and strains) using affine transformation are considered as the reference, i.e., without any error. And the object for error assessment is actually the image registration algorithm using B-spline transformation. The ultimate resulting errors (extrinsic and intrinsic) with the use of it are considered as the respective level of errors of our kinematic measurement system, because the B-spline transformation is the general image registration strategy adopted in this study for the displacement and strain measurements in the mechanical tests.

For a better comparison of the two image registration calculations by affine and B-spline transformations, the parameters in their common options were set as the same, e.g., the metrics, optimisation and multi-resolution. Here an important parameter to be defined in the B-spline transformation is the final grid size, which determines to a certain level how fine the deformation is expected to be modeled. In general, with a smaller grid size, the smaller and more local deformation can be characterized, and vice versa. In this thesis study, the B-spline transformations with final grid size selections 64×64 pixels and 16×16 pixels were adopted in the image registration for the conducted mechanical tests, so they will be concerned particularly in this error analysis. Here it is worthy to note that the selection on the grid size is strongly dependent on the speckled paint as well as the image resolution.

Now let us first check the basic feature of the affine transformation between the two involved images. Fig. 2.19 shows the deformed image after processing the affine transformation $T(x)$, so-called the corrected deformed image. In other words, it corresponds to $g(T(x))$ in Eq. 2.30, thus $f(x)$ the reference image and $g(x)$ the deformed image. The black zones in this corrected deformed image correspond to the zones that can be observed in the reference image but not in the deformed image, since they were actually beyond the area of observation (of camera) when the specimen was displaced in the test. Fig. 2.19 reveals that at least an important translation in the horizontal direction plus a rotation are involved in

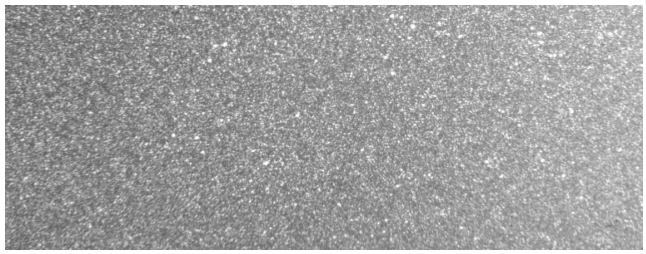

(a)

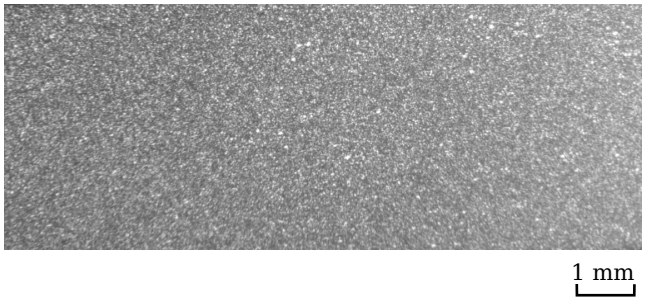

(b)

Figure 2.18: Two images involved in the image registration: (a) reference image and (b) deformed image

the affine transformation.

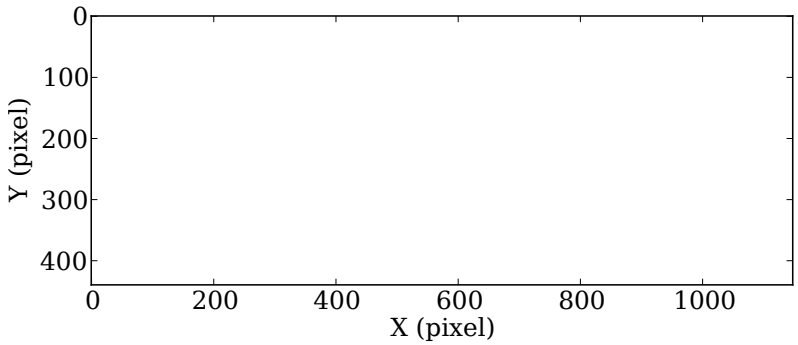

Figure 2.19: The corrected deformed image using affine transformation

For a further evaluation, the calculated displacements using affine transformation are mapped on the reference image, as shown in Fig. 2.20(a), where the arrows contain information both in absolute displacement values (displacement norm) and displacement directions. Fig. 2.20(a) shows that the transformation feature and its resulting distribution of displacements can be better revealed. In fact, the B-spline transformation can provide similar displacement results with the affine transformation, as shown in Fig. 2.20(b) in the case of a final grid size selection 64 × 64 pixels. Fig. 2.20(a) and (b) do not demonstrate

apparent differences. In this case, the axial and transverse displacements (corresponding to the horizontal and vertical directions respectively) are expected to be further compared between the two types of transformations.

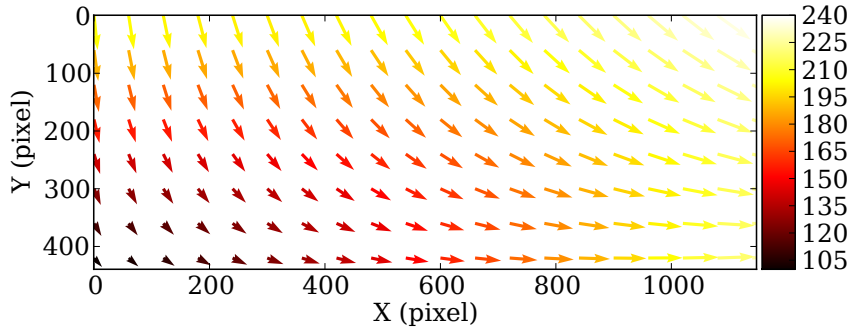

(a)

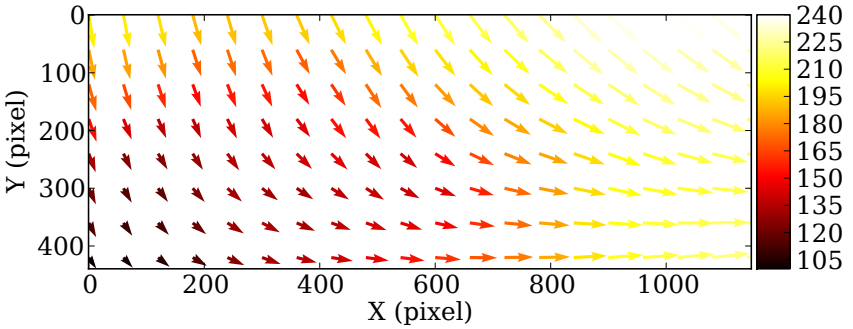

(b)

Figure 2.20: (a) Displacement norms calculated using affine transformation, (b) displacement norms calculated using B-spline transformation with a final grid size selection 64 × 64 pixels

Fig. 2.21(a) shows the axial displacement field through affine transformation, and (b) and (c) the displacement fields obtained using B-spline transformations with grid size selections 64 × 64 pixels and 16 × 16 pixels, respectively.

Firstly, Fig. 2.21(a)-(c) show comparable displacement values which range from 0 to 90 pixels with an average around 46 pixels. Then regarding their spatial distribution, some differences can still be noticed between Fig. 2.21(a) and (b), though they exhibit, on the whole, a rather similar pattern. By adopting a smaller final grid of 16 × 16 pixels in the B-spline transformation, the resulting axial displacement field shown in Fig. 2.21(c) demonstrates a more unsmooth and heterogeneous distribution feature. The same analysis was also carried out on the transverse displacement fields. They are shown in Fig. 2.22(a), (b) and (c), corresponding to the results given by affine transformation, B-spline transformations with grid size selections 64 × 64 pixels and 16 × 16 pixels, respectively.

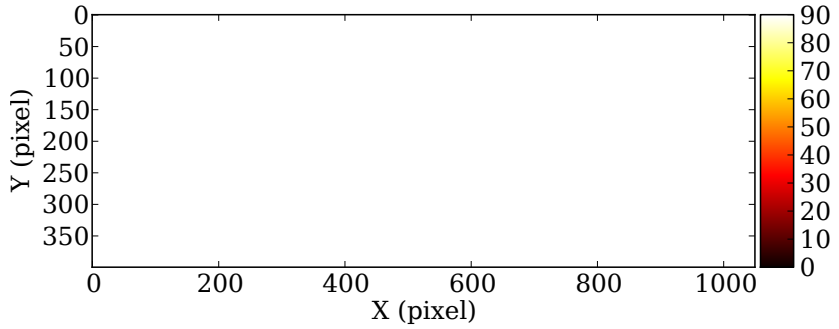

(a)

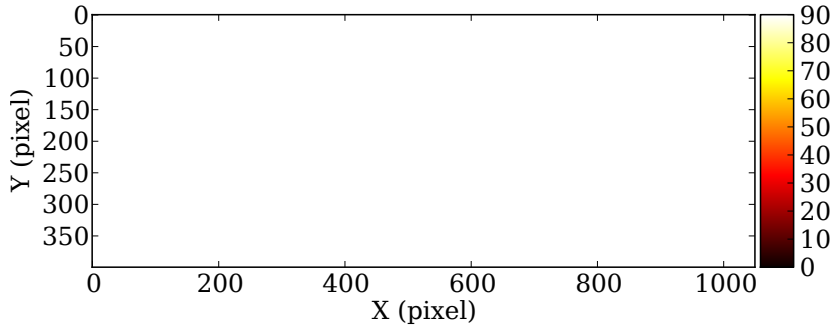

(b)

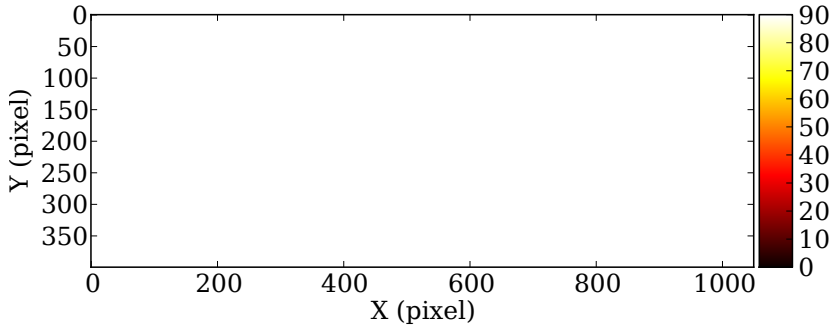

(c)

Figure 2.21: Axial displacement fields obtained through (a) affine transformation, (b) B-spline transformation with final grid size selection 64 × 64 pixels and (c) B-spline transformation with final grid size selection 16 × 16 pixels

The transverse displacement fields in Fig. 2.22(a)-(c) show also similar absolute values that range from -10 to 90 pixels with an average around 40 pixels. Their spatial distribution demonstrates the same phenomenon as observed in the axial displacement fields: with greater grid size adopted in the B-spline transformation, the resulting displacement field becomes more smooth, approaching to that given by affine transformation; and with smaller grid size, the resulting displacement field tends to be unsmooth, showing a rather

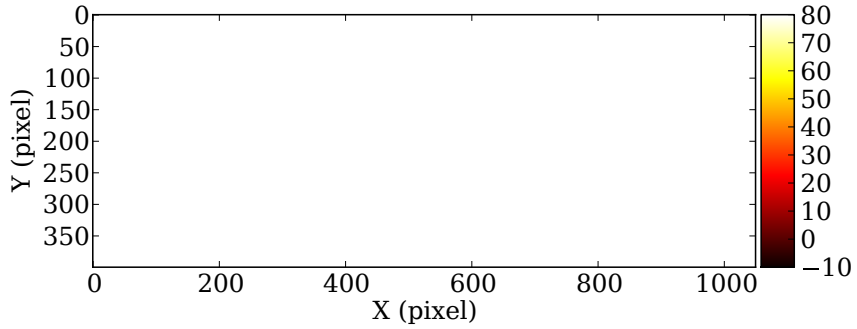

(a)

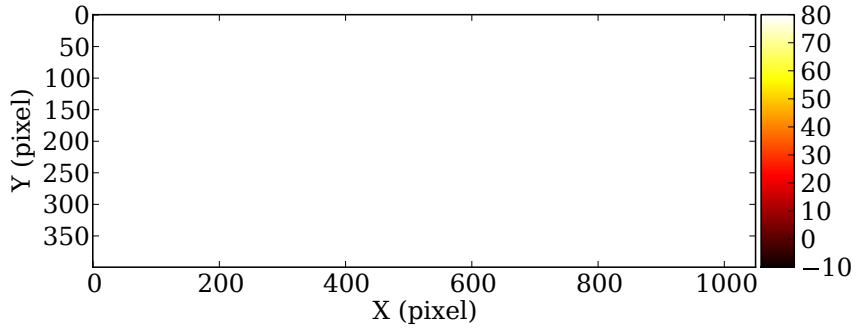

(b)

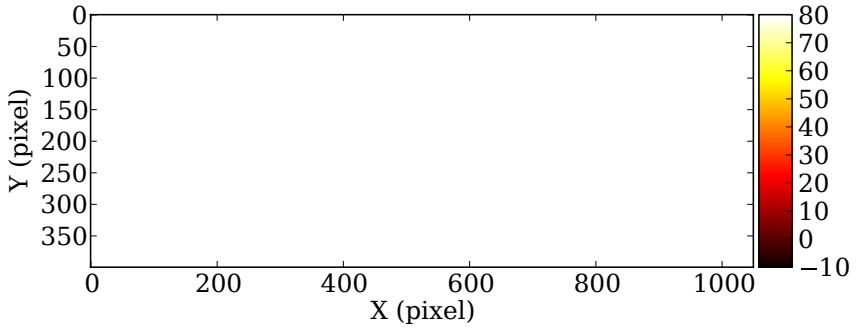

(c)

Figure 2.22: Transverse displacement fields obtained through (a) affine transformation, (b) B-spline transformation with final grid size selection 64 × 64 pixels and (c) B-spline transformation with final grid size selection 16 × 16 pixels

heterogeneous distribution pattern. This result is reasonable as the affine transformation is supposed as the reference transformation between the two images involved for the image registration. Thus, any supernumerary heterogeneities emerging in the displacement field by using B-spline transformation and its influences on the displacement values are regarded as errors of image registration in this work.

For quantifying the errors in displacement produced by applying B-spline transformation, both the average values and standard deviations of displacement fields were calculated. The errors were evaluated both in absolute terms (in pixel) and in relative terms (in percentage) by taking the relevant results given by affine transformation as the reference. For example, for the average axial displacement $\bar{u}$, the error in pixel is assessed according to

$$\delta_1 = |\bar{u}_{bsp} - \bar{u}_{aff}| \tag{2.44}$$

or in percentage by

$$\delta_2 = \left| \frac{\bar{u}_{bsp} - \bar{u}_{aff}}{\bar{u}_{aff}} \right| \times 100\% \tag{2.45}$$

where $\bar{u}_{aff}$ and $\bar{u}_{bsp}$ present the average axial displacements provided by affine and B-spline transformations, respectively.

Except the displacement averages ($\bar{u}$, $\bar{v}$), another indicator involved in the error evaluation is the standard deviations of displacement fields, thus $\sigma(u)$ and $\sigma(v)$. The different statistics for the error analysis of B-spline transformations (both 64 × 64 pixels and 16 × 16 pixels) are shown in Tab 2.1.

	$\bar{u}$ (pixel)	$\bar{v}$ (pixel)	$\sigma(u)$ (pixel)	$\sigma(v)$ (pixel)
Affine	46.18	39.92	19.32	17.44
B-spline (64 × 64 pixels)	46.51	38.36	21.26	18.57
Error δ_1 (pixel)	0.33	1.56	1.94	1.13
Error δ_2	0.7%	3.9%	10.0%	6.5%
B-spline (16 × 16 pixels)	45.91	39.02	20.53	19.81
Error δ_1 (pixel)	0.27	0.9	1.21	2.37
Error δ_2	0.6%	2.3%	6.3%	13.6%

Table 2.1: The errors in displacement for the B-spline transformations (both 64 × 64 pixels and 16 × 16 pixels)

Tab. 2.1 shows that the displacement results obtained by both of the two B-spline transformations are close to that given by affine transformation. Their respective errors for average axial displacement are only 0.33 pixel (64 × 64 pixels) and 0.27 pixel (16 × 16 pixels) in a total displacement about 46 pixels, or 0.7% and 0.8%. The corresponding errors in average transverse displacement show values a little greater, 1.56 pixels for bigger grid selection (64 × 64 pixels) and 0.9 pixel for smaller grid selection (16 × 16 pixels), or 3.9% and 2.3%, respectively. Another indicator, the errors in standard deviation for the applied B-spline transformations vary from a minimum 6.3% to a maximum 13.6%. The current level of displacement deviation is relatively important which may influence the strain evaluation. For a further verification, the strain fields are analyzed.

The axial and transverse strains (ε_{xx}, ε_{yy}) can be calculated from their respective displacement fields using the finite difference method as detailed in the last section. As for affine transformation the resulting strain fields are made of single strain values, 0.063 for the axial strain and 0.140 for the transverse strain, thus their uniform strain distribution will not be displayed. Concerning the two B-spline transformations, their axial strain fields are illustrated in Fig. 2.23(a) and (b), which correspond to the axial displacement fields in Fig. 2.21(b) and (c).

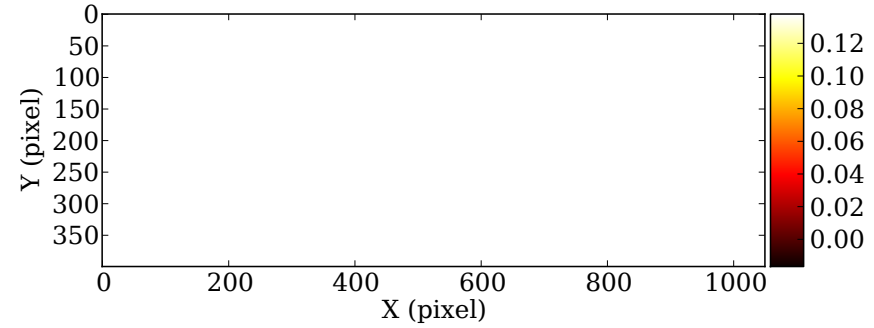

(a)

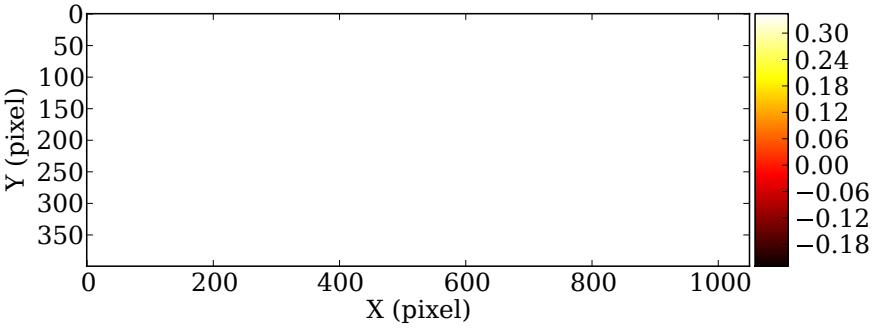

(b)

Figure 2.23: Axial strain fields obtained through B-spline transformations with grid size selections (a) 64 × 64 pixels and (b) 16 × 16 pixels

The transverse strain fields using B-spline transformations are illustrated in Fig. 2.24(a) and (b), corresponding to the transverse displacement fields in Fig. 2.22(b) and (c).

Both the axial and transverse strain fields in above figures show that the B-spline transformation with bigger grid selection (64 × 64 pixels) demonstrates a more homogeneous pattern than the other with smaller grid selection (16 × 16 pixels). Nevertheless, the strain fields provided by both of the two B-spline transformations are still far from a homogeneous distribution. The relevant errors in strain can be quantified in the same way with that in displacement, in terms of absolute values and relative values. The different statistics for the error analysis, including the averages $\bar{\varepsilon}_{xx}$, $\bar{\varepsilon}_{yy}$ and standard deviations $\sigma(\varepsilon_{xx})$, $\sigma(\varepsilon_{yy})$, are illustrated in Tab. 2.2. It needs to note that the relative error in standard deviation $\delta_2[\sigma(\varepsilon)]$

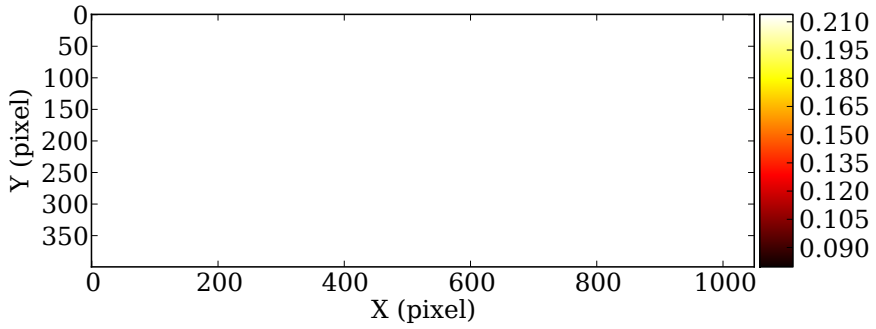

(a)

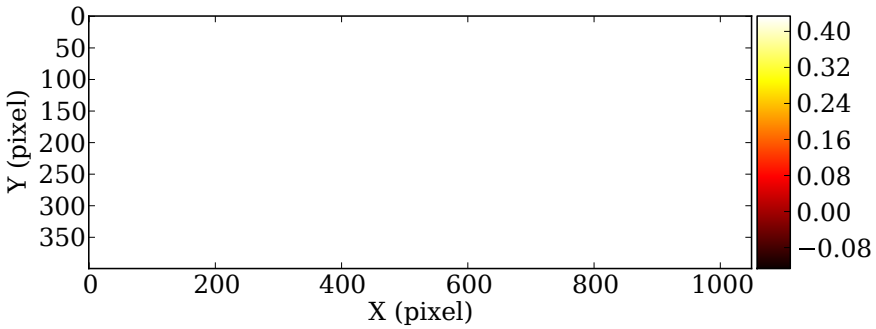

(b)

Figure 2.24: Transverse strain fields obtained through B-spline transformations with grid size selections (a) 64 × 64 pixels and (b) 16 × 16 pixels

for B-spline transformation is actually not available (N/A), as the reference standard deviation $\sigma(\varepsilon)$ for the affine transformation is zero.

Tab. 2.2. shows that the B-spline transformation with bigger grid selection (64 × 64 pixels) generally demonstrates lower error levels than the one with smaller grid selection (16 × 16 pixels). The error in average axial strain for the former is 0.002 or 3.1%, and in transverse strain 0.006 or 4.3%. Considering a relatively important displacement imposed on the specimen in the test, in particular with an apparent rotation, the current error levels in strain are considered reasonably low. The errors in average strain produced by the other B-spline transformation are relatively higher, which can attain 10% for a total strain 0.14. It is however not surprising as its corresponding displacement fields have already demonstrated some unexpected heterogeneities, contrast to the smooth distribution of displacement given by the affine transformation. These local errors can be much magnified in the error assessment by the adopted finite difference method. In this case, it is suggested to consider a smooth or approximation treatment on the initial displacement field in order to remove the unexpected noises, and then to calculate the strain. In this study, a dedicated projection approach was developed in the kinematic field analysis of nickel single crystal deformation, which will be detailed in chapter 5 with relevant error analyses.

	$\bar{\varepsilon}_{xx}$	$\bar{\varepsilon}_{yy}$	$\sigma(\varepsilon_{xx})$	$\sigma(\varepsilon_{yy})$
Affine	0.063	0.140	0	0
B-spline (64 × 64 pixels)	0.061	0.146	0.039	0.033
Error δ_1 (pixel)	0.002	0.006	0.039	0.033
Error δ_2	3.1%	4.3%	N/A	N/A
B-spline (16 × 16 pixels)	0.057	0.154	0.143	0.140
Error δ_1 (pixel)	0.006	0.014	0.143	0.140
Error δ_2	9.5%	10.0%	N/A	N/A

Table 2.2: The errors in strain for the B-spline transformations (both 64 × 64 pixels and 16 × 16 pixels)

In conclusion, the experimental error analysis demonstrates the performance of the image registration method adopted in this study, and as well as the feasibility of the whole DIC measurement system. Here it is also important to note that the example presented in this analysis focuses on a pure displacement of specimen without any deformation, which is substantially different from that in a mechanical test. For a true mechanical deformation, the local errors are usually more important, in particular concerning a very heterogeneous deformation process. On the one hand, the strain localization zones mean greater deformation levels. And on the other hand, they are accident-prone zones of material damage or out-of-plane deformation which may produce extrinsic errors in the image registration. In this case, the residual image (or image of errors) provides a very useful tool on examining the local errors. They are reliable indicators of the local quality of the registration between images, and are therefore strongly recommended to be checked in each image registration calculation.

2.3 Conclusion

A thorough metrology study has been carried out on QIRT and DIC in this chapter.

The main contributions on QIRT is that a complete calibration procedure has been established, which includes non-uniformity correction, bad pixel detection, integration time selection, etc. Another key issue on QIRT, emissivity, was also studied. Two solutions for the emissivity measurement, the direct method and indirect method, were proposed. These achievements make QIRT a reliable tool for the full-field temperature measurement.

Concerning the kinematic measurement, the image registration method has been studied systematically in this work. Firstly, the principle of image registration based on optical flow is introduced. And the different elements involved in an image registration were discussed in details, as well as the assessment of strain from the measured displacement. Then,

a great part of this work was focused on an experimental error analysis of the proposed image registration method. And the performance of the adopted kinematic measurement system was validated in this analysis. The results showed that on the one hand the B-spline transformation can provide reliable measurement on displacement, and on the other hand the precision of strain calculation can not be assured by applying a direct finite difference method.

In the next chapter the coupling of the two experimental techniques will be studied. And the research objective is to follow the temperature and strain variations of the same physical point on material surface at the same instant.

Chapter 3

Coupled kinematic-thermal measurement

As known that in the kinematic measurement the strain fields given by the DIC method are in Lagrangian coordinates, for the purpose of tracking the material points. The same interest may be found in the thermal measurement, where if the temperature fields can be described in Lagrangian coordinates, the temperature variations of the material points could therefore be tracked. Thus a problem arises: the transition from Eulerian coordinate system to Lagrangian coordinate system for the thermal field.

This problem can be solved if the kinematic fields can be projected properly on the thermal fields. In other words, the kinematic fields and thermal fields (or visible images and thermal images) need to be coupled (or matched), spatially and temporally. It is right the theme of our studies in this chapter: coupled kinematic-thermal measurement.

To this end, a technical review on the kinematic-thermal coupling measurement will be first presented, in which the relevant technical possibilities will be discussed and a solution adaptable for our experiments will be determined. Then three general technical problems involved in realizing such a fully-coupled measurement will be studied respectively, which are spatial matching, synchronization and data fitting.

3.1 Technical review

To our knowledge, it exists actually four different experimental techniques that have been developed in the last few years for achieving the coupled kinematic-thermal field measurements. Among them, each technique has its advantages and disadvantages, regarding on the studied material, measurement scale and expected precision. Nevertheless, it is important to note that QIRT and DIC usually have contrast technique restraints, in particular on choosing the surface coating for the specimen. QIRT generally prefers a uniform coating with a very high emissivity, such as carbon black, thus an accurate infrared measurement can be ensured. On the contrary, DIC requires a very heterogeneous coating, such as speckled paint, for the purpose of tracking material points that should differ widely in gray levels. Several ways of achieving such a coupling are presented as follows.

1) Two-face measurement

Each imaging device (IR and visible camera) observes one face of the specimen. This experimental set-up was employed in the works (Chrysochoos *et al.*, 2008a; Chrysochoos *et al.*, 2008b; Badulescu *et al.*, 2011), as shown in Fig. 3.1 (Chrysochoos *et al.*, 2010).

The main advantage of this set-up is that each technique has the flexibility to choose the surface coating for its own good, without special constraints. This point can be essential for the measurement precision on each side of the two metrologies. Its desirable application case is: a thin, flat specimen being studied on a macroscale, where it can be assumed that the two faces of the specimen show virtually the same thermomechanical behaviours. However, if the study is carried out at the microstructural scale, this experimental set-up requires the same microstructure on the two faces of the specimen.

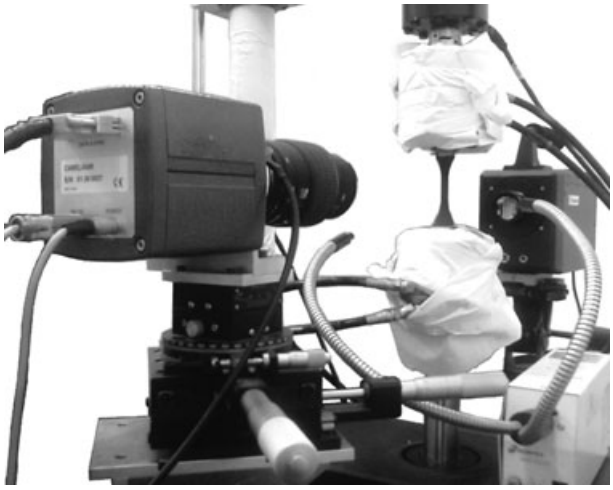

Figure 3.1: The experimental set-up of the two-face solution (Chrysochoos *et al.*, 2010)

2) Single-face measurement

Both IR and visible cameras observe the same face of the specimen. Two kinds of the experimental set-up can be found:

a) Introducing an angle between the IR and visible cameras. This technique was applied in the works (Saai *et al.*, 2010; Dumoulin *et al.*, 2010), as shown in Fig. 3.2 (Dumoulin *et al.*, 2010).

Generally this kind of experimental set-up needs a correction of the image distortions introduced by the inclination of the camera with respect to the normal direction to the specimen surface (at least for one camera). This angle should be as small as possible, but restricted yet by the physical volumes of the cameras. The inclination effect may bring difficulties for the spatial matching on the two kinds of images (IR and visible), especially for the investigations on a microscale.

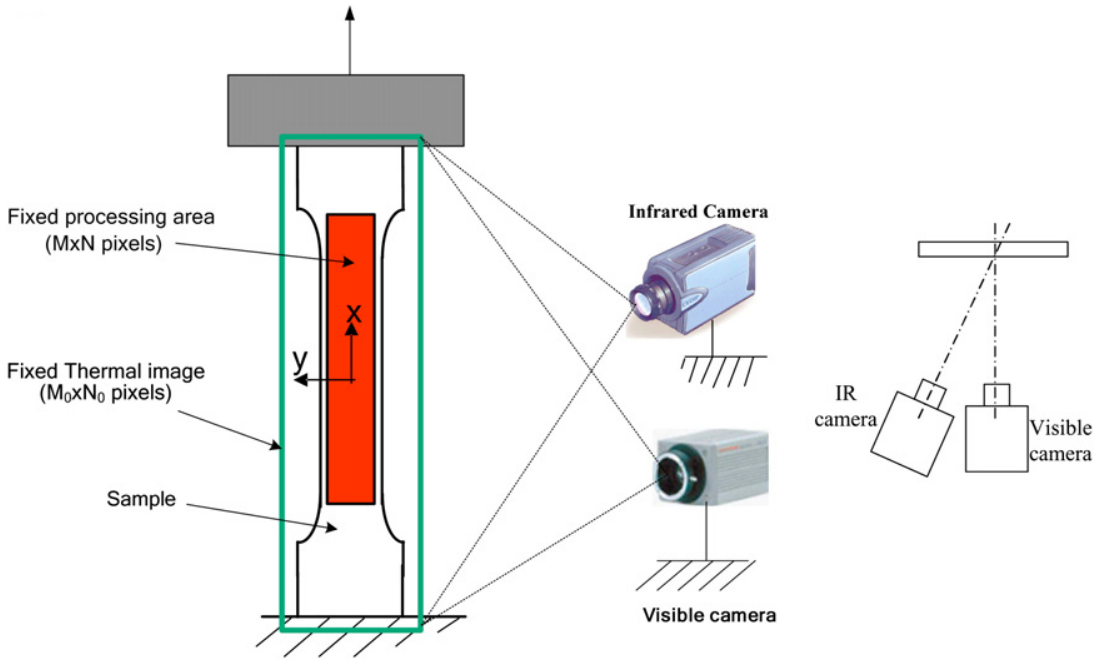

Figure 3.2: The experimental set-up of the single-face solution (Dumoulin *et al.,* 2010)

b) Introducing a dichroic mirror (or filter-mirror). It was originally developed in the work (Bodelot, 2008), as shown in Fig. 3.3 (Bodelot *et al.*, 2009).

The dichroic mirror, thanks to its filtering properties, transmits the IR radiations towards the IR camera placed in the front of the specimen, and reflects the rest of the radiations towards the visible camera located on the other side. It is a development that ensures a coupled measurement on the same face of specimen, but without suffering a tiled angle of camera(s) with respect to the normal of the specimen surface (for example, in the above solution). Nevertheless, the dichroic mirror may also produce some measurement errors due to its transmission and reflection effects.

A common problem for the single-face measurement is the coating for the specimen surface, which is desired to be non-uniform in the visible vision and be uniform in the IR vision. A special coating developed in the work (Bodelot, 2008) meets such a demand.

3) One-shot measurement

A single IR camera is used to measure both kinematic and thermal fields on the same face of the specimen. In other words, the IR images will be not only used for QIRT but also for DIC. This technique, so-called "one-shot measurement", was recently developed in (Maynadier *et al.*, 2012; Silva & Ravichandran, 2011).

The main advantage of this technique is that it needs neither synchronization nor spatial matching, thus any temporal/spatial bias between the kinematic and thermal fields can be avoided. However, a noticeable problem with this method is that the strain measurement precision should be inevitably lowered as the IR camera generally cannot provide a compa-

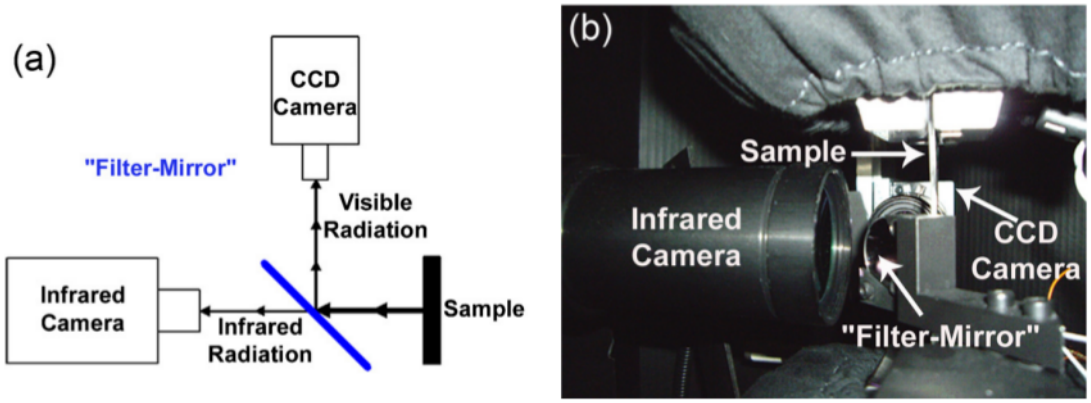

Figure 3.3: The experimental set-up of the filter-mirror solution (Bodelot *et al.,* 2009)

rable high-resolution image as the visible camera. A decrease in performance may also be found on the side of the temperature measurement because of a wide variation in emissivity on the surface coating, which serves for the point tracking in DIC.

After an overview on the available techniques, the two-face measurement technique was chosen in this study. There are two principal reasons:

1) A high demand on the measurement precision from the point of view of the metrology. Except the two-face experimental set-up, in other solutions the coating issues often make troubles for achieving a desirable quantitative measurement.

2) The studied materials in our investigations are oligocrystal and single crystal which exhibit a quasi-identical microstructure on the two faces of the specimen. Thus the ideal condition of a same thermomechanical behaviour on the two faces of the specimen can be approached as far as possible.

In order to apply the two-face measurement technique, several technical difficulties should still be overcome, such as the spatial/temporal matching. The following section will concern about how to apply a precious coupled kinematic-thermal measurement through the two-face experimental set-up.

3.2 Coupled measurement

Two basic problems involve in the two-face coupled measurement: spatial matching and temporal matching.

For solving the problem of the spatial matching, a special reference target was originally developed in this study that enabled to match the two kinds of images captured on the two faces of the specimen. Concerning the temporal matching, a micro-controller was

employed in order to synchronize the two cameras, thus simultaneous measurements can be realized. Finally, in most of the cases, the images provided by the IR and visible cameras have different spatial resolutions, and their respective sampling frequencies are also often different. In this case, interpolation (or data fitting) is a necessary step to be applied on the measurement data for achieving final fully-coupled results.

Hence, this section will be unfolded into three parts: spatial matching, synchronization and data fitting.

3.2.1 Spatial matching

The proposed solution for the spatial matching in this study is to use the reference target. To this end, two reference targets were designed and fabricated, which were of different sizes and patterns in order to fit the experimental studies at different physical scales (macroscale and microscale). The validation test on each target was performed in order to verify its performance on the spatial matching.

3.2.1.1 Reference target

For the purpose of achieving a spatial matching on the images acquired by two different cameras, the conventional method is to make some physical marks on the object surface. Through this method, the marks can be easily recognized in the acquired images, based which the spatial correlation can be actualized, thus the same zone of the specimen can be refound in the two different images. However, one inconvenience for its application in our case is that the marks need to be through the thickness of the specimen, so as to be seen by the two cameras. This treatment may however risk damaging the specimen. Besides, this method has its own deficiency. As the image correlation is fully based on the marks, some very local zones, so the spatial matching accuracy on the whole ZOI (Zone Of Interest) is not guaranteed.

As known that generally the sensor plane of camera is not aligned perfectly parallel to the specimen, thus the captured images are often projective imageries of the specimen surface. Except this projection effect, the optical images may suffer the geometrical distortions owing to the defects of the optical system. All these possible sources of errors are expected to be taken into account in the spatial matching. Thus, a full-field pixel-to-pixel correlation strategy is desired for solving the spatial alignment problem.

Here a schematic example of the non-matched effect is illustrated in Fig. 3.4. In this figure, the red grid and blue grid represent two different images that need to be matched. In order to consider all the unintended non-matched effects (rigid motion, projection and distortion) and to correct them all-in-one, the using of a reference target was proposed.

Firstly, a macro-target was designed, as shown in Fig. 3.5(a), its analytical model. The material object was realized by a perforated metal plate, as Fig. 3.5(b) shows. The target has 18 holes of the same size, which are through the thickness and randomly distributed,

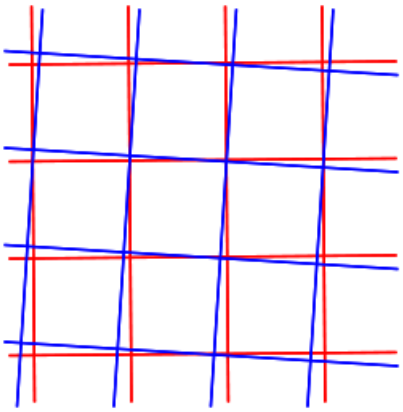

Figure 3.4: A schematic illustration of the non-matched effect

forming a special pattern that appears identical on the two faces of the target. The diameter of the hole is 4 mm, and the ZOI of the target (including only the holes) is about 40 mm $\times$30 mm. This target was expected to be used in the studies at the macroscale for the material aluminum oligocrystal.

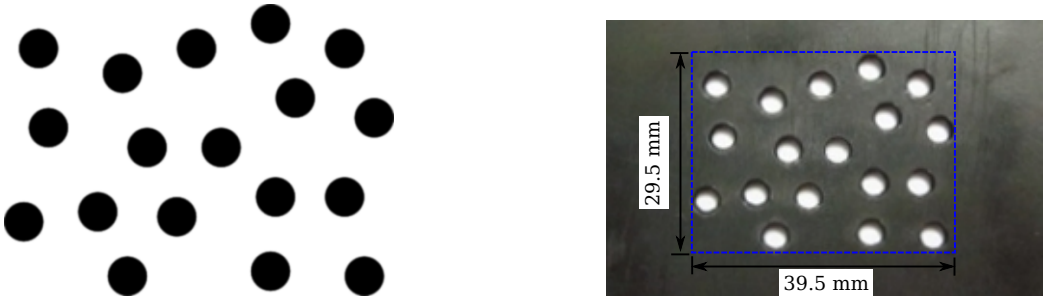

(a) (b)

Figure 3.5: (a) Analytical model of the macro-target; (b) macro-target

The other target, the micro-target, was also developed. Its analytical model is shown in Fig. 3.6(a) and the physical object in Fig. 3.6(b). The micro-target was made of silicon, and was machined through a process of etching and lithography in IEMN (Institut d'Electronique de Microelectronique et de Nanotechnologie - UMR CNRS). It was anticipated to be applied to the microscale investigation on nickel single crystals.

The micro-target is made of 64 holes in total. There are four kinds of holes of different sizes, with the diameters varying from the minimal 0.3 mm to the maximum 0.6 mm. The size of the ZOI is about 9.5 mm $\times$ 7.5 mm. It is important to note here that for the studies on the microscale, the G1 lens was used for the IR camera, accompanied by the use of the micro-target. The G1 means 1 times magnification. In other words, the physical resolution

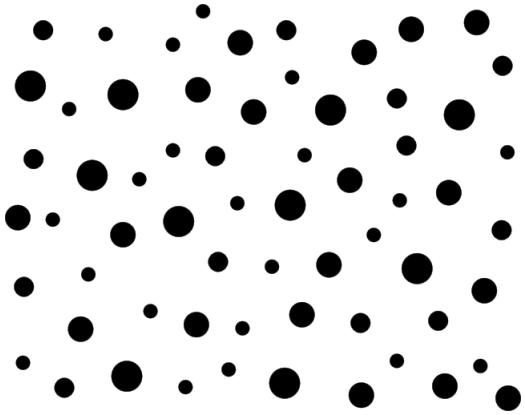

(a)

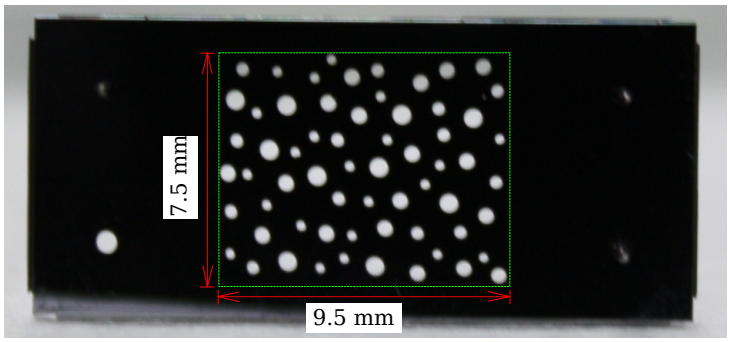

(b)

Figure 3.6: (a) Analytical model of the micro-target; (b) micro-target

of the thermographic image is equal to the size of the pitch detector. It is thus 30 μm × 30 μm for the camera Jade and 15 μm × 15 μm for the Titanium camera, two FLIR cameras employed in our investigations. The field of view of the G1 lens is 9.6 mm × 7.68 mm, compatible with the size of the micro-target. Its field depth is 0.3 mm, with a standard lens-object distance 300 mm.

The working principle of the reference target is explained as following.

In the mechanical test, before testing the specimen the reference target should be placed at exactly the same position where the specimen should be. In that way the target is possessed of the position information of the specimen, since the cameras are always fixed during the test. The images of the target are captured by IR and visible cameras, respectively, and are ready for the image correlation with the analytical model, which here serves as the reference image. The corrected IR and visible images, after the transformations to the reference configuration, can achieve a spatial matching. The assumption made here is that the image with the same pattern should be observed by the IR and visible cameras in the ideal conditions (without any effect of rigid motion, projection and distortion).

The transformation form defines what kind of the non-matching effects expected to be corrected. The choices include rigid transform, similarity transform, affine transform and B-spline transform. Generally an affine transform suffices to correct the most common non-matching effects: rigid motion and projection. If the image suffers a considerable optical distortion effect, then the B-spline transform is recommended. The operation of the image correlation can be implemented by elastix.

The validation tests on the spatial matching effect were performed both on the macro-target and micro-target. Their respective results will be presented in the following parts.

3.2.1.2 Validation on the macro-target

In the test of the two-face measurement, the target is observed by IR and visible two cameras, front and rear. An IR image for one face and another visible image for the other face can therefore be obtained. The validation test is actually to check the spatial matching effect (or overlapping effect) of the two images after being processed by the image correlation based on the analytical model.

It is worth noting that there is a general requirement on the acquired images of the target: the contrast between the hole zone (or the holes) and the out-of-hole zone should be strong as possible. It is a preferential condition for promoting a satisfactory image correlation effect. To this end, some special operations in the image acquisition were managed. On the IR side, the extended BB was placed behind the target with a high temperature (e.g., 60 °C), thus the holes showed much higher temperature than the out-of-hole zone (room temperature, e.g., 20 °C). It can therefore produce a high-contrast thermographic image. On the visible side, a black object with high emissivity can be placed behind the target, so that a white-black contrast image can usually be obtained.

The initial IR and visible images before the image correlation are shown in Fig. 3.7, together with the common analytical model.

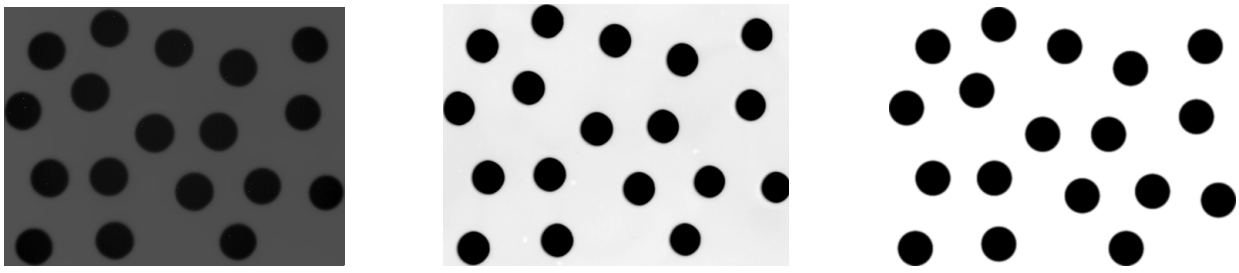

Initial IR image | Initial visible image | Analytical model

Figure 3.7: Relative images before the image correlation

The “rigid motion” and “projection” were considered as the main reasons for the non-matching effect. So the affine transform was applied between the initial images (IR and

visible) and the analytical model, respectively. Their corrected images after the transformation are shown in Fig. 3.8.

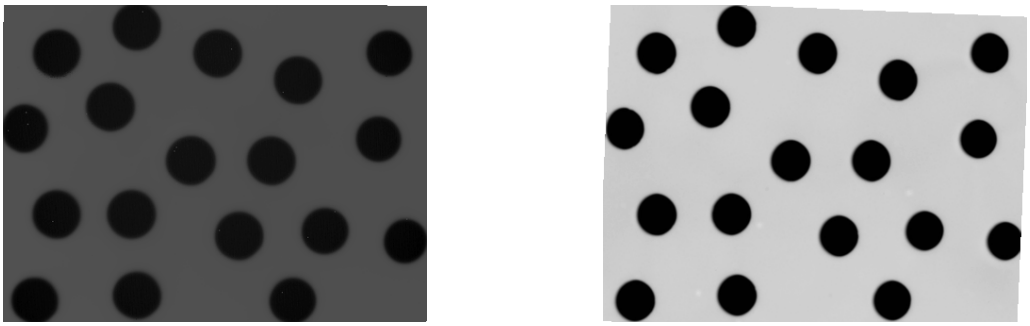

Corrected IR image Corrected visible image

Figure 3.8: Relative images after the image correlation

One can observe the corrected images in Fig. 3.8, where the IR image does not show any apparent transform, while the visible image shows a relatively important rotation comparing to the original image. These effects are related to the initial positions of the cameras placed with respect to the reference target, and are taken into account by the proposed method.

The spatial matching effect can be checked by overlapping one image on the other image, or by making the difference between the two images. The difference images (or residual images) of the IR and visible images, before correction and after correction, are shown in Fig. 3.9(a) and (b), respectively.

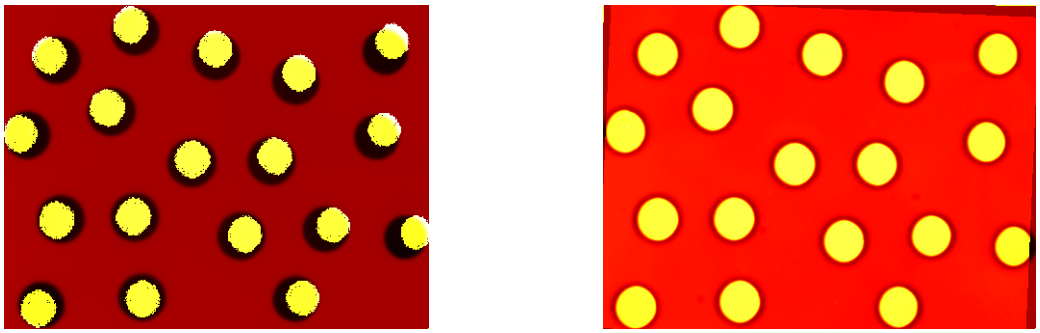

(a) (b)

Figure 3.9: Residual images: (a) before correction; (b) after correction

The residual image before the correction Fig. 3.9(a) shows that the initial IR and visible images can not reach a spatial matching, where the holes from the two images are not well superposed. In particular, some important shifts can be found in the right half image. On the contrary, the residual image after the correction Fig. 3.9(b) exhibits a well-matched

effect, where all the holes are superposed, much better than Fig. 3.9(a). Thus, it means that the spatial matching problem is solved by the proposed solution. And it is validated on the developed macro-target.

3.2.1.3 Validation on the micro-target

The same validation procedure was conducted on the micro-target. So here only the most important results will be presented.

Relative images of the micro-target before image correlation are shown in Fig. 3.10.

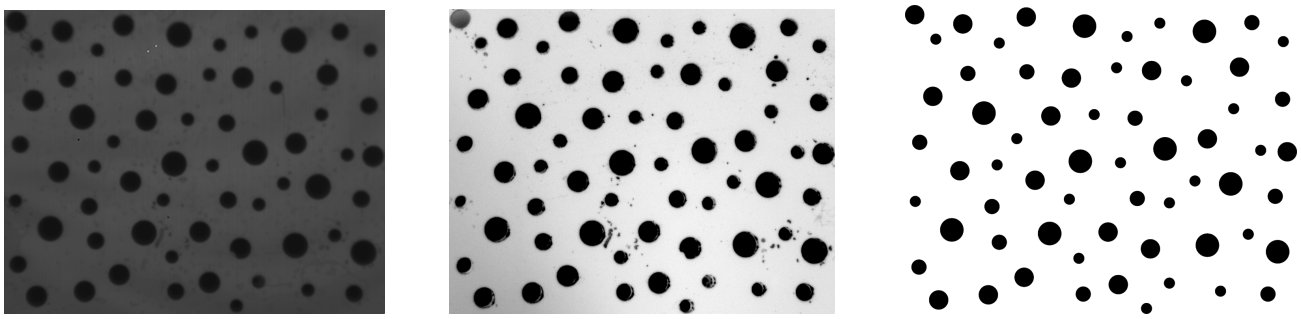

Initial IR image | Initial visible image | Analytical model

Figure 3.10: Relative images before the image correlation

The affine transforms were performed on the initial IR and visible images based on the common analytical model, their respective corrected images are illustrated in Fig. 3.11.

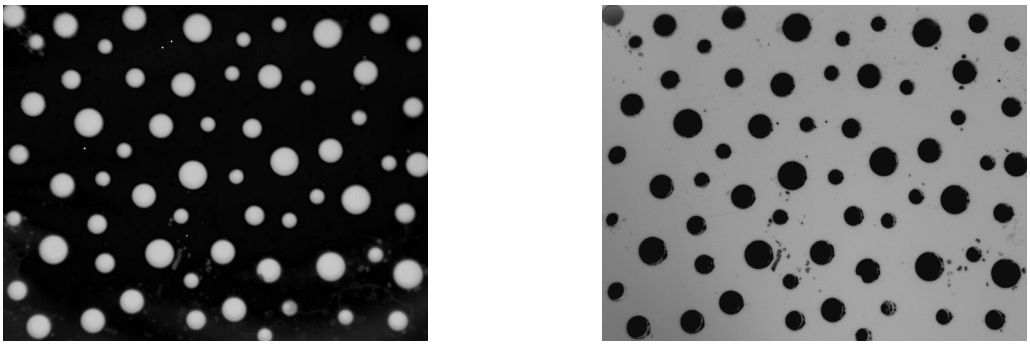

Corrected IR image | Corrected visible image

Figure 3.11: Relative images after the image correlation

From two corrected images no obvious transforms can be observed in a global view. Thus it is essential to check on the residual images. The two residual images, before and after correction, are shown in Fig. 3.12(a) and (b), respectively.

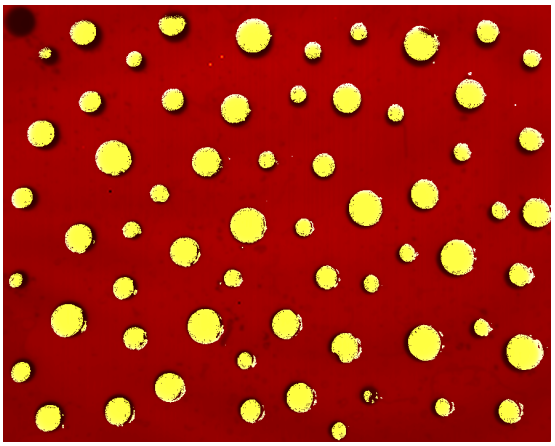

(a)

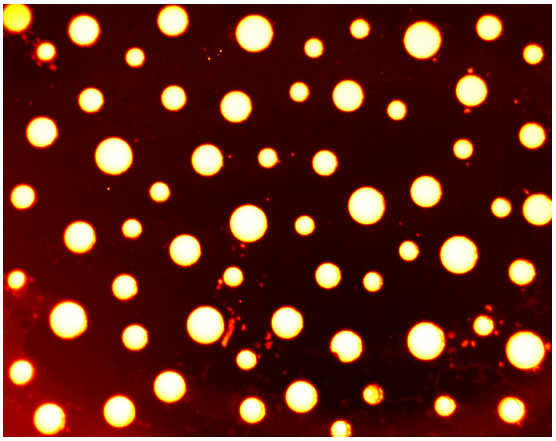

(b)

Figure 3.12: Residual images: (a) before correction; (b) after correction

In the initial residual image Fig. 3.12(a), for most of the holes the hole shapes are kind of distorted, and the hole boundaries are blurred. It is simply because that the holes from the two initial images are not superposed exactly. In contrast, the corrected residual image Fig. 3.12(b) displays a well-matched effect, where the holes are perfectly superposed. Hence, the proposed method is also valid on the micro-target.

The above works show that the spatial matching problem can be tackled by using a reference target. In the following, another concerned issue, the temporal matching, will be studied.

3.2.2 Synchronization

In order to perform the simultaneous measurement, the two cameras (IR and visible) need to be synchronized. A micro-controller was employed in this study for realizing the synchronization.

3.2.2.1 Measurement of time delay

A micro-controller, Arduino Mega 2560, was adopted in this study, as shown in Fig. 3.13.

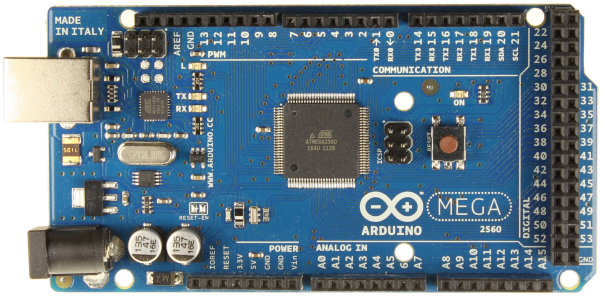

Figure 3.13: Arduino micro-controller

The Arduino micro-controller enables to trigger the two cameras so as to actualize the synchronization of image acquisitions. Nevertheless, it is important to understand that for each camera it generally has a physical time delay (the interval from receiving the signal to taking the image). The accuracy of the synchronization can not be guaranteed unless this time delay is known and taken into account in the controlling program.

For the IR cameras involved in our studies, their time delays are indicated by the manufacturer. It is 2.8 μs for the Titanium camera and 0 μs for the camera Jade. For the visible camera adopted in this study, the Elphel 353 network camera, this time delay is unknown and thus needs to be tested. To this end, a free-fall experiment was designed in order to measure the time delay of the visible camera. The idea about the free-fall experiment is to drop a small object that will pass a reference target, being observed by both of the two cameras (IR and visible). Normally the object will be refound in the recorded videos, then its relative positions in IR and visible images can be used to estimate the time delay of the visible camera.

The employed IR camera in this test was the Titanium camera with a time delay 2.8 μs. We did not find any indications about the time delay of Elphel camera, so it was initially set as 0 μs, i.e., without time delay. These two time delays were considered in the controlling program, and the two cameras were trigged by the micro-controller in the external trigger mode.

A free-fall test was implemented, and after the test the object (a small bolt) was refound in an IR image and in a visible image, respectively, as shown in Fig. 3.14 (a) and (b).

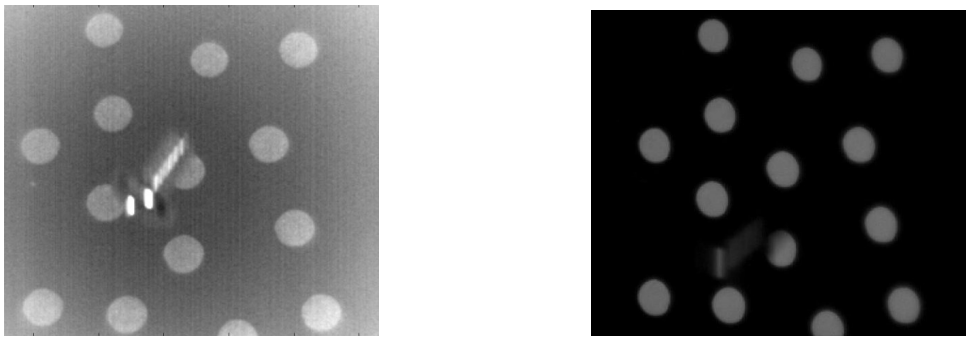

(a) (b)

Figure 3.14: The object in (a) IR image and (b) visible image

A blurred vision of the object is presented in the visible image, which is due to the high speed of the object and a relatively high exposure time set for the visible camera. On the contrary, the object embodies clearly in the IR image as a very low integration time was chosen for the IR camera.

With the knowledges of the flight distance and velocity of the object, and by calculating its position differences in the two above images, the real time delay of the visible camera can be estimated. It was 2.68 ms for an initial test, and 2.57 ms in a repeated test. It is worth noting that the velocity of the object is sensitive to its flight distance, the latter is however not easily to be measured accurately in our tests. It can be the main source of the uncertainties of the estimated results. Anyway, a magnitude of 0.1 ms of error is considered acceptable in this study. Hence, the time delay for the visible camera can be estimated as 2.6 ms for the moment. And it needs to be validated in a verification test by the updated controlling program for achieving a real synchronization.

3.2.2.2 Verification test

The controlling program was updated by adopting the estimated time delay of the visible camera. The controlling flow is shown by Fig. 3.15.

In the controlling flow chart, the time delay of Elphel camera was set as 2.6 ms. It was actually only one of the tested values, other values like 2.65 ms and 2.7 ms were also tried in the verification tests. The idea was to find the most accurate estimated value so as to achieve a perfect synchronization effect. If it is the case, in the free-fall test the object should be found in exactly the same position in the recorded IR and visible images .

The free-fall test was repeated several times with different predicted time delay values. And the best superposition effect was found when the time delay was set as 2.65 ms. The relative captured images are shown in Fig. 3.16.

The object can be found basically in the same vertical position in the two illustrated

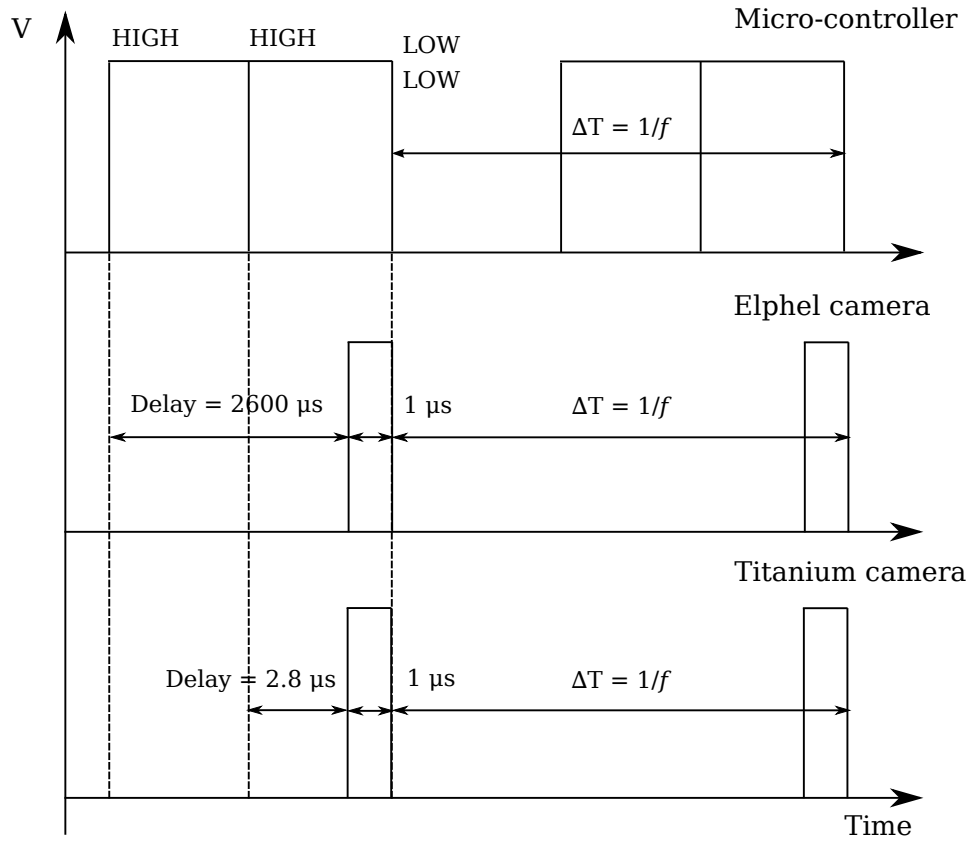

Figure 3.15: Controlling flow

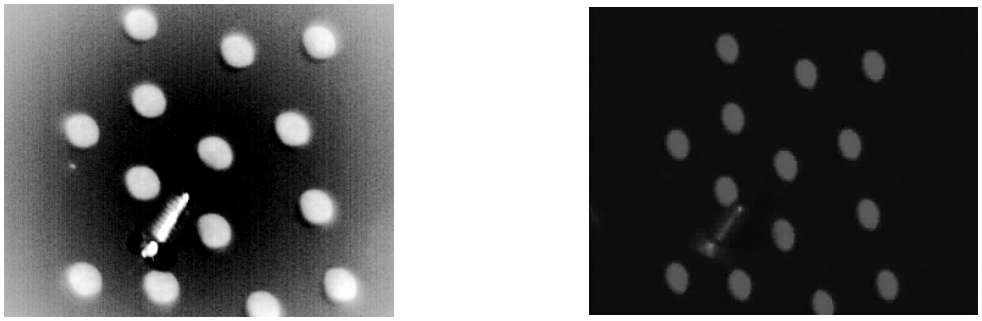

Figure 3.16: The object in (a) IR image and (b) visible image

images, Fig. 3.16(a) and (b). For a difference in the horizontal direction, it is due to the difference in observing angles from the cameras to the reference target. So here only the vertical direction is concerned. This superposition effect is considered rather satisfactory, which has been much improved comparing to the initial result in the preliminary test.

Hence, the synchronization problem was solved thanks to a micro-controller. The performance of the proposed synchronization technique was demonstrated.

3.2.3 Data fitting

In above studies, the spatial and temporal coupling problems in the two-face measurement were basically solved thanks to the reference targets and micro-controller. Nevertheless, please note that for the two involved cameras applied to a specific experiment, generally they are not the same either in spatial resolution or in sampling frequency. In such cases, an interpolation approach is necessary, both spatially and temporally, in order to accomplish final fully-coupled data.

3.2.3.1 Spatial interpolation

The spatial interpolation is done before applying the reference target. In this case the IR and visible images can achieve the same spatial resolution in advance, and then the analytical model of the target can be remade based on this resolution. This operation will facilitate the image correlations with the target.

Generally the visible camera can offer higher spatial resolutions than the IR camera. There are therefore two interpolation strategies. The first is to perform a downsampling on the visible images to achieve the same resolution with the IR images. And the other is to improve the spatial resolution of the IR images by interpolation so as to reach the same resolution with the visible images. The latter solution was adopted in this work as a downsampling strategy on the visible images may filter out some important information on the kinematic fields.

3.2.3.2 Temporal interpolation

The sampling frequencies for the high-end FLIR IR cameras employed in this work can generally reach more than 120 HZ. The adopted visible camera Elphel is, however, not the high-speed type, which can only provide a maximum sampling frequency around 20 HZ. In this case, the temporal interpolations on the kinematic fields are necessary, so as to be fully matched with the thermal fields.

It is worth noting that the temporal interpolation is not performed directly on the visible images but on the calculated displacement fields. The principle is to implement linear interpolations between each two adjacent displacement fields, in order to generate a number of new displacement fields that correspond temporally with the thermal fields. In the end, for each thermal field it should have a corresponding displacement field. In this case, the IR and visible cameras are actually not truly synchronized in the test. As the visible camera has a poorer sampling frequency, the micro-controller ensures only that for each visible image there will be a temporally corresponding IR image.

To explain the interpolation strategy more intuitively, a schematic chart is illustrated in Fig. 3.17. In this example, the sampling frequency for the IR camera is 5 times higher than that of the visible camera. The linear interpolations are implemented between the image (or matrix) pairs I_j and I_{j+1} in the initial kinematic fields, where for each pair 4 new images are generated. Finally the kinematic fields after interpolation can reach the same

temporal resolution with that of the thermal fields. The choosing of the linear interpolation is based on the hypothesis that the displacement field varies linearly in a relatively short time period. It is thus preferable to be applied for the low-speed mechanical test or in the case when a high-speed camera is adopted.

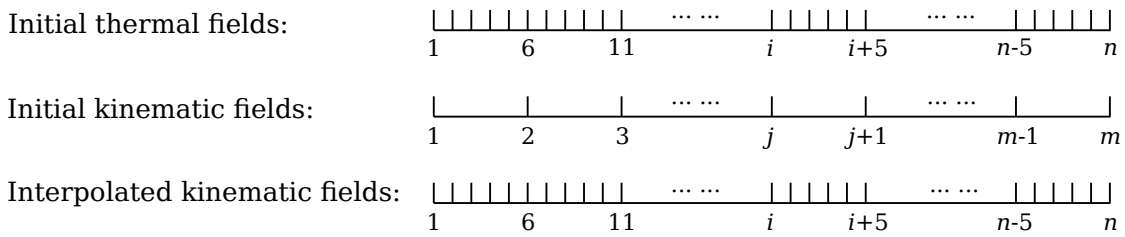

Figure 3.17: Temporal interpolation strategy

3.3 Conclusion

A thorough investigation on the coupled kinematic-thermal measurement has been carried out in this chapter.

First of all, an overview on the technical possibilities for realizing the coupled kinematic-thermal measurement was presented. Currently there are four available techniques in all. And each technique has its advantages and disadvantages. According to our specific research interest, the two-face measurement technique was found the most appropriate.

To implement the two-face measurement, two main technical problems should be solved beforehand. The first problem is the spatial matching of the images obtained from the two different faces of the specimen. Thanks to a developed reference target, this problem was tackled successfully. The second problem is the synchronization of the two different cameras (IR and visible). And it was solved through the multi-trigger controlling by using a micro-controller. Besides, the general problems of the data fitting were also studied, and the spatial/temporal interpolation strategies were applied in order to achieve the final fully-coupled results.

In short, a kinematic-thermal fully-coupled measurement system has been developed in this study. It will be employed in the following experimental investigations on aluminum oligocrystals and nickel single crystals.

Chapter 4

Tests and macroscopic analyses of nickel single crystals

Two kinds of materials are involved in this thesis study: pure aluminum oligocrystal and pure nickel single crystal. The thermomechanical behaviours of them were investigated respectively in the tensile tests, thanks to the developed kinematic-thermal coupled measurements at different scales. The emphasis of our study was placed on the material nickel single crystal, which will be thoroughly studied both in this chapter and the following. For readers interested in the full-field measurements on aluminum oligocrystal deformation, please refer to appendix A.

In this chapter, the studied material nickel single crystal and its specific crystallographic structure are first introduced. Then the experimental protocol for realizing the kinematic-thermal fully-coupled measurements in the tensile tests of nickel single crystals is detailed. Before processing a thorough treatment on the full-field measurement data, some surface observations and measurements on the deformed specimens are carried out in this work. And the out-of-plane deformation due to slip markings emerging on the material surface and its influence on thermographic measurement are particularly investigated.

4.1 Nickel single crystal

The motivation to study the material nickel single crystal is for several considerations. First, the available macroscopic single crystals nowadays are still limited on some particular materials and nickel is one of them. Second, nickel has a relatively low thermal diffusivity, about 4 times lower than aluminum, which provides a favorable condition for the thermal measurement. Moreover, regarding the crystallographic structure single crystals have a simpler structure than oligocrystals, which exclude the influences of grain boundaries (Zhao *et al.*, 2008). Nevertheless, to date still very rare studies of full-field measurements were applied to single crystals (Florando *et al.*, 2007; Efstathiou & Sehitoglu, 2010), and not found for pure nickel single crystal in the public literatures. It is thus of great interest to launch on an investigation on nickel single crystals through the kinematic and thermal full-field measurements.

The studied material is pure nickel single crystal (purity 99.999%) with a dislocation density lower than 10^{12} m^{-2}. The minor chemical compositions of the pure nickel single

crystal are shown in Tab. 4.1 by weight (Lekbir, 2012).

Element	Co	Cr	Cu	Fe	Mg	Mn	Si	Ti	C	S
p.p.m (wt)	8	8	10	10	10	10	8	10	10	10

Table 4.1: Chemical compositions of pure nickel single crystal (Lekbir, 2012)

The nickel single crystal was obtained by the Bridgman-Stockbarger technique (Furukawa & Nakajima, 2001) along the crystal growth direction [100], and was supplied in the initial form of cylindrical rod of diameter 16 mm. Then it was further machined into dogbone specimens via electrical discharge machining. The geometric dimensions of the final obtained specimens are illustrated in Fig. 4.1.

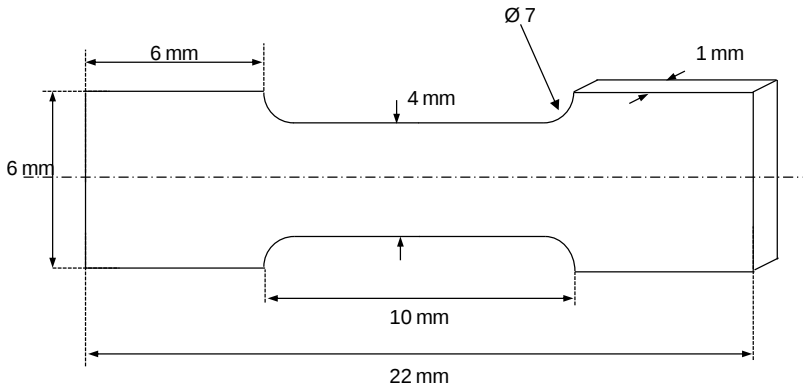

Figure 4.1: The geometry of the nickel single crystal specimen

The specimens were processed by mechanical and electrochemical polishing in order to obtain smooth and flat surfaces. For the detailed experimental protocol, please refer to (Lekbir, 2012).

The crystal structure of nickel is FCC, as shown in Fig. 4.2. Slip in FCC crystals occurs along the close packed plane of type $\{111\}$, and the slip direction is of type $\langle 110 \rangle$. It has therefore 12 possible slip systems of type $\{111\}\langle 110 \rangle$, as detailed in Tab. 4.2.

The specimen surface is in the crystallographic plane (100), and the axial direction is along [001], so is the loading direction, as indicated in Fig. 4.3. Based on these information, the two angles ϕ and λ concerning the Schmid factor (as illustrated in Fig. 4.4) can be obtained. The angle ϕ is given a result of 45° for all the 12 possible slip systems, and for angle λ the result is 54.7° for 8 slip systems and 90° for the other 4 slip systems. The Schmid factor, equal to $cos\phi cos\lambda$, can therefore be calculated for each possible slip system illustrated in Tab. 4.2. The obtained Schmid factor is 0.4 for 8 slip systems (A2, A3, B2, B4, C1, C3, D1, D4) and 0 for the other 4 slip systems (A6, B5, C5, D6).

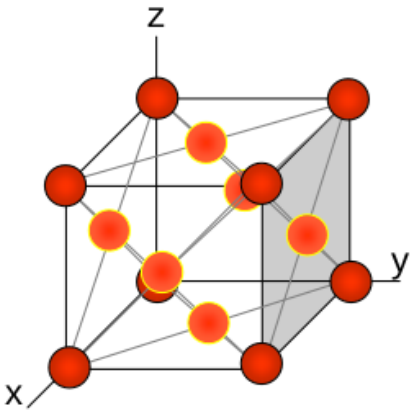

Figure 4.2: The FCC structure

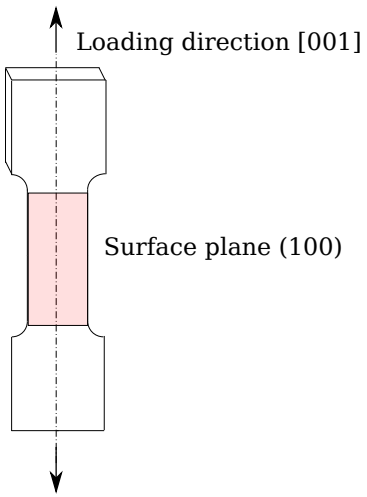

Figure 4.3: Orientation of the specimen

Slip planes	Slip directions	Possible slip systems
A ($\bar{1}11$)	1 2 3 4 5 6	A2 A3 A6
B (111)		B2 B4 B5
C ($\bar{1}\bar{1}1$)	[011] [0$\bar{1}$1] [101] [$\bar{1}$01] [$\bar{1}$10] [110]	C1 C3 C5
D (1$\bar{1}$1)		D1 D4 D6

Table 4.2: The 12 possible slip systems of FCC

From a geometrical point of view, the 8 slip systems with a positive Schmid factor are potential to be activated (and equally stressed) in the tensile test. Among them 4 active slip systems (A3, B4, C3, D4) will intersect with the specimen surface plane (100), resulting in thus two kinds of traces (slip markings) on the specimen surface. They are actually the intersections of the slip planes from two pairs of slip systems: A3-B4 and C3-D4, as the schematic diagram shown in Fig. 4.5. The other 4 active slip systems (A2, B2, C1, D1) all slip in the directions parallel to the specimen surface plane (100), resulting no intersections with the specimen surface. This prediction is in agreement with former experimental observations on the same material (Lekbir, 2012; Oudriss, 2012)

In the former work of Lekbir (Lekbir, 2012) the EBSD measurements have been performed on the same kind of nickel single crystal specimens and their crystallographic orientations were well verified as [100].

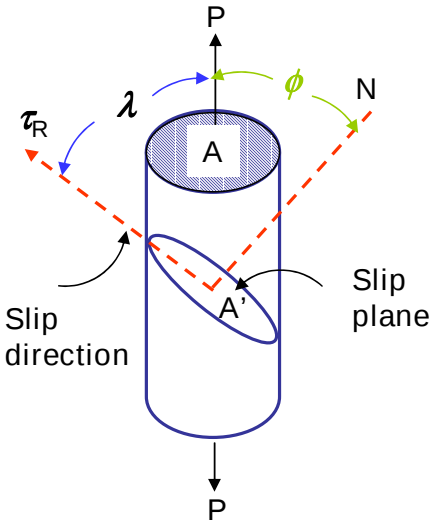

Figure 4.4: Slip plane and slip direction

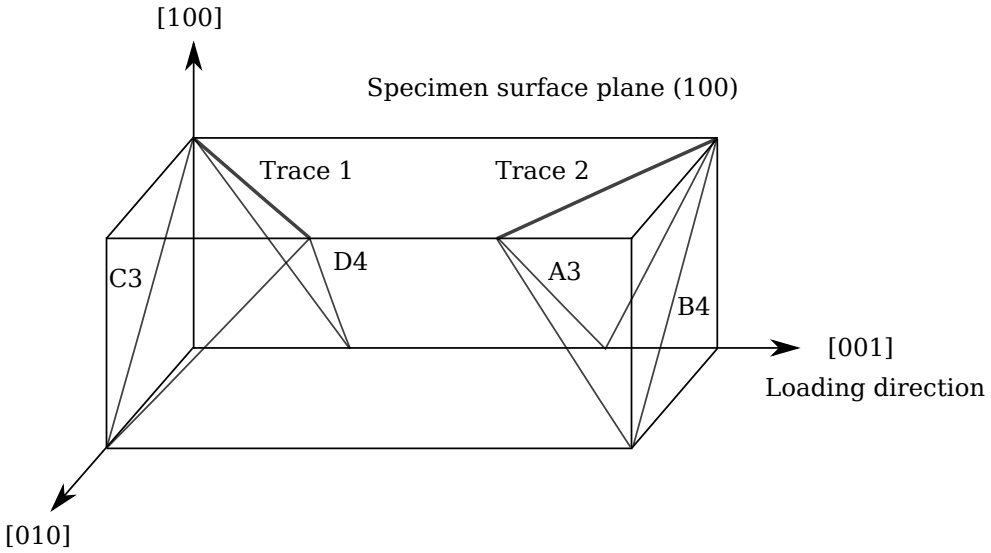

Figure 4.5: Potential slip systems with intersections on the specimen surface

4.2 Experimental protocol

4.2.1 Surface coatings

First of all, some special coatings should be applied to specimen surfaces. The specimen face for kinematic measurement was sprayed by speckled paint using airbrush, as a typical image of the obtained speckled paint illustrated in Fig. 4.6. And the other face for thermal measurement was deposited by a layer of carbon black, in order to obtain a high surface emissivity. Besides, several physical marks were made on the specimen surface, away from the ZOI, serving as location references.

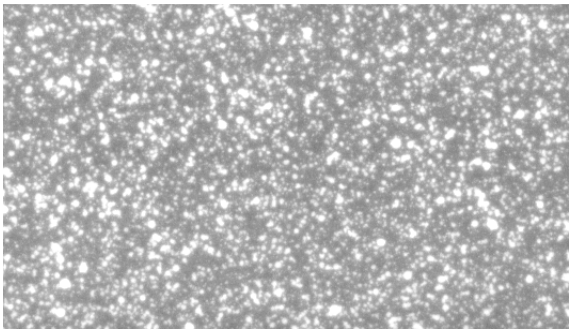

Figure 4.6: A typical image of the obtained speckled paint

4.2.2 Experimental set-up

The kinematic-thermal two-face measurement technique was adopted in this investigation, as the experimental set-up shown in Fig. 4.7. The experimental set-up was basically made by three parts: IR camera, visible camera, and the micro tensile machine placed between them. Besides, a fiber optic was equipped as the light for the kinematic measurement, and a thermocouple was employed in order to monitor the ambient temperature.

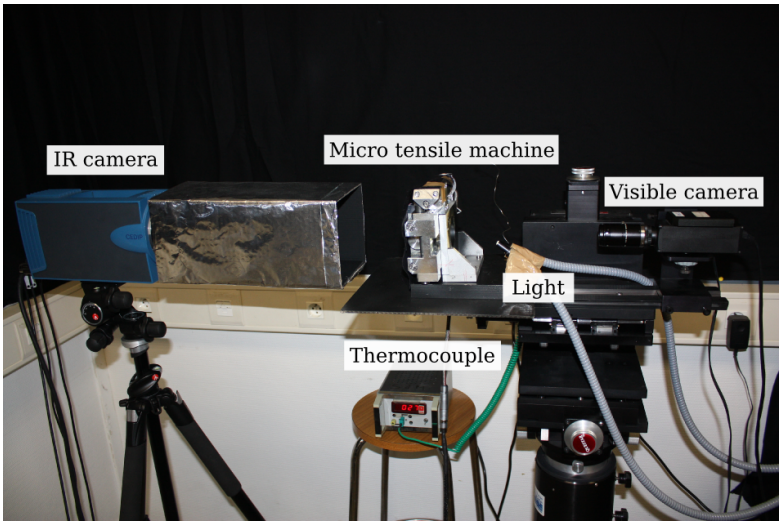

Figure 4.7: The experimental set-up of the two-face measurement

The micro tensile machine is of Kammrath & Weiss GmbH with a maximum force up to 5 KN. Some details of the micro tensile machine with the gripped nickel single crystal specimen can be seen in Fig. 4.8.

Each camera was fixed on a tripod that allowed a macroscale position adjustment. And the developed micro-target in this study enabled a precise spatial matching between the acquired visible and IR images. Fig. 4.9 shows the micro-target gripped in the micro tensile machine.

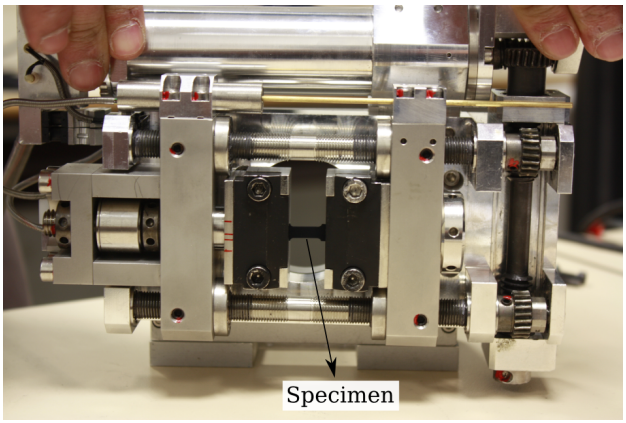

Figure 4.8: The specimen gripped in the micro tensile machine

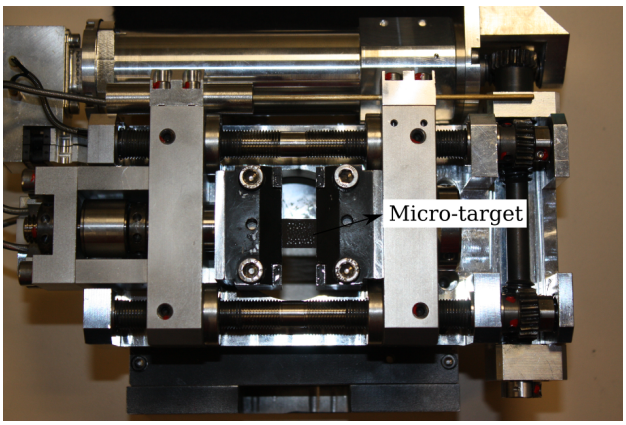

Figure 4.9: The micro-target gripped in the micro tensile machine

For the purpose of minimizing the possible environment interferences on the thermal measurement (e.g., reflection effects, ambient temperature variations), the micro tensile machine was covered by an isolation box during the tensile test, as shown in Fig. 4.10. This special box was painted inside by black paint of high emissivity in order to avoid the reflections on the specimen. And outside it was covered by aluminum foil of very low emissivity, so as to avoid the radiation absorptions from the environment. The experiments were carried out at room temperature, and the isolation solutions ensured a quasi constant ambient temperature surrounding the specimen in the micro tensile machine.

4.2.3 Tests and measurements

Before performing the tensile test, an in-situ temperature calibration was carried out in order to calibrate the IR camera. And the micro-target had been also measured in the same experimental configuration that served for the final spatial alignment of the coupled data.

A series of tensile and cyclic tests were carried out, and two tensile tests were chosen to be investigated particularly in this study. These two tensile tests were conducted in

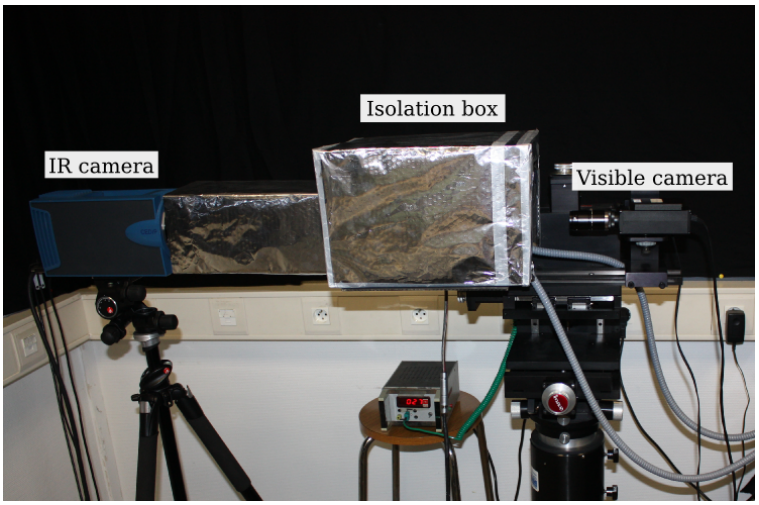

Figure 4.10: The isolation solutions during the tensile test

displacement control mode with different speeds: 19 $\mu m/s$ and 8 $\mu m/s$, equivalent to the strain rates $2 \times 10^{-3}\ s^{-1}$ and $0.9 \times 10^{-3}\ s^{-1}$, respectively. The imposed total strain for the first test was 0.217 and the second 0.236. During the tensile tests, visible and IR images were acquired simultaneously thanks to the micro-controller.

The adopted IR camera was the Jade III MW equipped with the micro-lens G1. It provided an image resolution 320 × 240 pixels and a field of view $9.6 \times 7.2\ mm^2$ with the physical resolution $30 \times 30\ \mu m^2$. The Elphel camera was employed for the kinematic measurement, equipped with a Tamron 50 mm lens. It provided an image resolution 960 × 736 pixels and a field of view $10.4 \times 7.9\ mm^2$ with the physical resolution $11 \times 11\ \mu m^2$. The sampling frequency was 120 HZ for the IR camera and 15 HZ for the visible camera. Their differences both in the spatial and temporal resolutions were solved by the interpolation approaches as presented in chapter 3.

4.3 Surface observation and measurement

The investigations on the specimen surface, both by direct optical observation and profile measurement, were conducted in this study. The surface features of the deformed specimen are essential for providing a basic understanding of the deformation characteristics of nickel single crystals, and are indispensable when to interpret the full-field measurement results.

4.3.1 Optical observation

Removing the coatings on the specimen surfaces after the tensile tests, the true face of the deformed specimens can be revealed. Fig. 4.11(a) and (b) shows the two faces of the deformed specimen in Test 1, respectively.

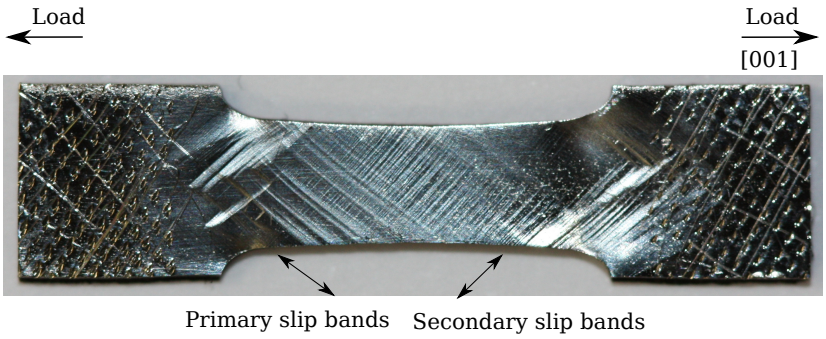

(a)

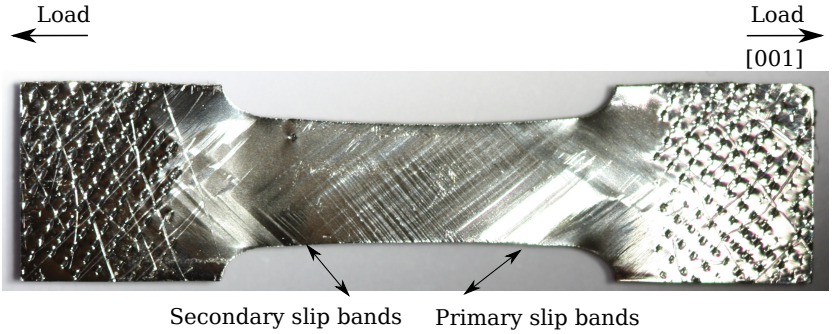

(b)

Figure 4.11: The deformed specimen in Test 1 (a) the face for thermal measurement and (b) the face for kinematic measurement

Fig. 4.11 shows that two groups of slip markings appearing on the specimen surface, as predicted by the crystallographic structure analysis. It can be also observed that one group of slip markings is more pronounced than the other. It is because that an ideal "equally stressed" condition does not actually exist in a real crystal deformation, so the activations of the 8 slip systems with an equal Schmid factor can not be simultaneously occurred in a tensile test. Thus, some slip systems tend to be activated earlier and be deformed more than the others. For the sake of convenience, the more pronounced slip band is called as the primary slip band and the other the secondary slip band.

Some more detailed information about Fig. 4.11(a) can be found in Fig. 4.12. In this close-up observation, the distinction of primary slip bands from secondary slip bands is shown with their respective slip directions. And the slip bands and interslip zones for the primary slip systems can also be distinguished in this photograph thanks to the light reflection. Thus the more regular ones in light color correspond to the slip bands, and the dark zones with varying widths correspond to the interslip zones, which locate right between the slip bands.

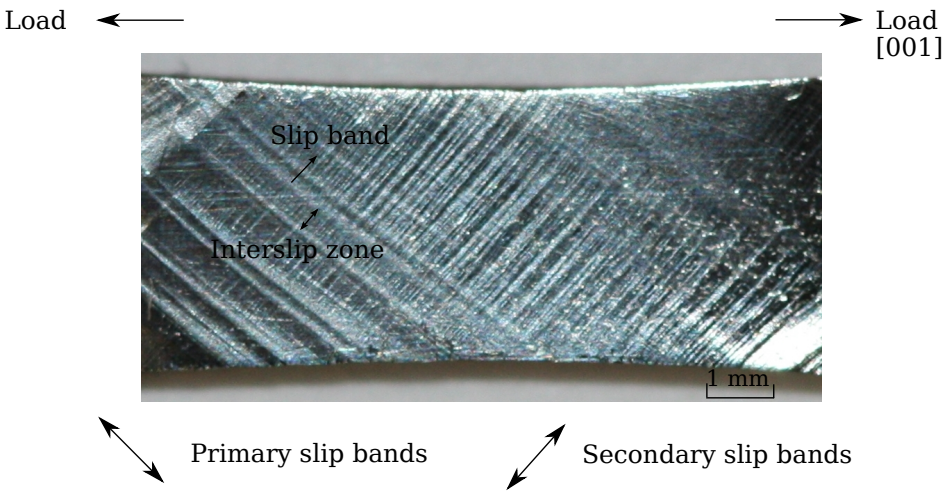

Figure 4.12: A close-up observation on the specimen surface in Test 1

The same observation can be found in Test 2, as the two faces of the deformed specimen shown in Fig. 4.13(a) and (b), respectively.

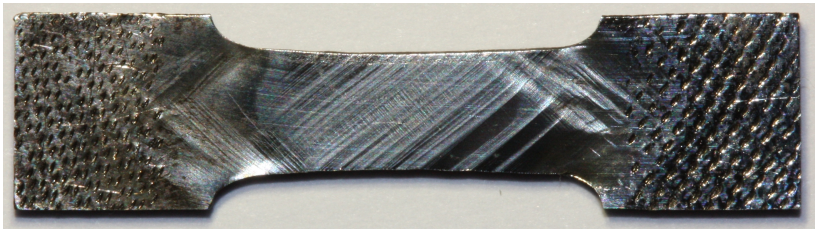

(a)

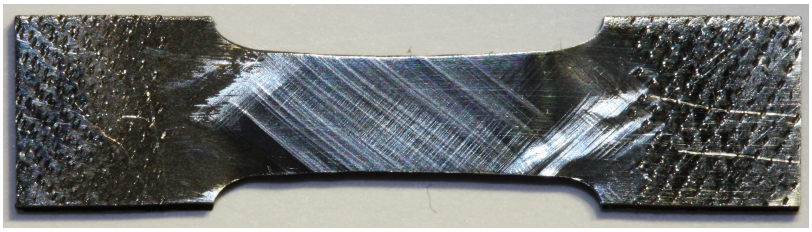

(b)

Figure 4.13: The deformed specimen in Test 2 (a) the face for thermal measurement and (b) the face for kinematic measurement

The surfaces of the deformed specimens were also observed by the microscope under different magnifications. A representative microscopic image is illustrated in Fig. 4.14. The image shows also that the two groups of slip bands can be clearly distinguished, and interestingly the angles between them and the loading direction, i.e., the angle ϕ, can be

determined graphically. The results are indicated on the right of the microscopic image in Fig. 4.14: $\phi_1 = 37°$ for one group of slip bands and $\phi_2 = 53°$ for the other group, and the angle between them is around 90°. Similar results are also verified from other microscopic images and in both of the two tensile tests.

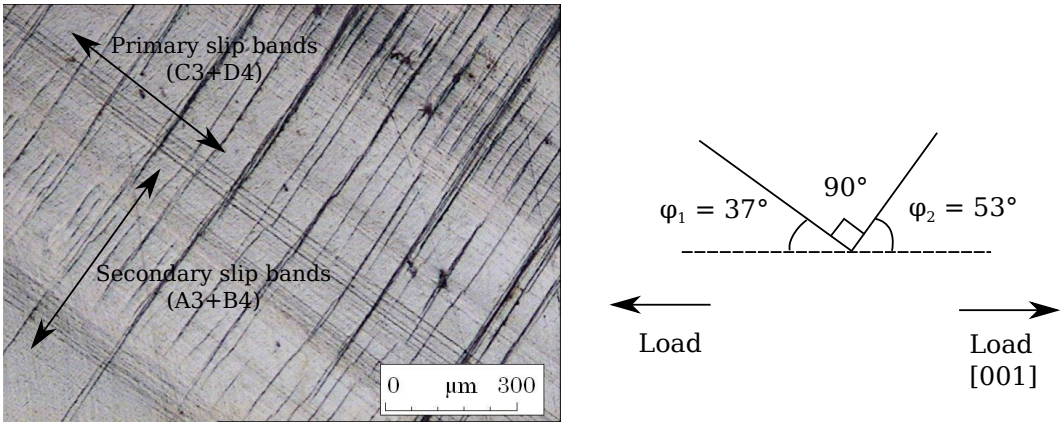

Figure 4.14: A representative microscopic image of the deformed specimen surface and the angle ϕ determined after the deformation

As introduced in the crystallographic structure analysis, the angle ϕ for each potential slip system is 45°, then the question arises: how can the angle ϕ change so greatly after the plastic deformation? This phenomenon is mainly owning to the fact that the non-gimbaled grips in the tensile machine can restrict the freedom of motion of the specimen in the plastic deformation, leading to therefore lattice rotations, so-called the grip effect (Hauser & Jackson, 1961; Jaoul, 1965). This point will be further discussed in chapter 5 integrated with the kinematic field measurements.

4.3.2 Profile measurement

The profile measurements were carried out by an interferometric profilometer (Wyko NT1100) after the tensile tests. Fig. 4.15 shows the profile maps for the deformed specimen in Test 1: (a) the face for thermal measurement and (b) the face for kinematic measurement. The physical resolution of the profile map is 3.2 × 3.2 μm^2 per pixel and the field of view is about 10.8 × 4.4 mm^2. It is worthy to note that the peripheries of the images in saturated white color are the zones outside of the specimen.

The profile maps confirm that the main surface relieves of the deformed specimen are the slip markings, as observed with the naked eyes. The slip markings represent a considerable surface roughening effect: the surface roughness average is 34 ∼ 54 μm, with a maximum height greater than 160 μm. More important, this kind of out-of-plane deformation risks inducing an optical reflection effect, thus interfering the optical full-field measurements. The same problem was also found in the investigation of aluminum oligocrystals, for the relevant analysis please refer to appendix A. Here concerning nickel single crystals, a study on the

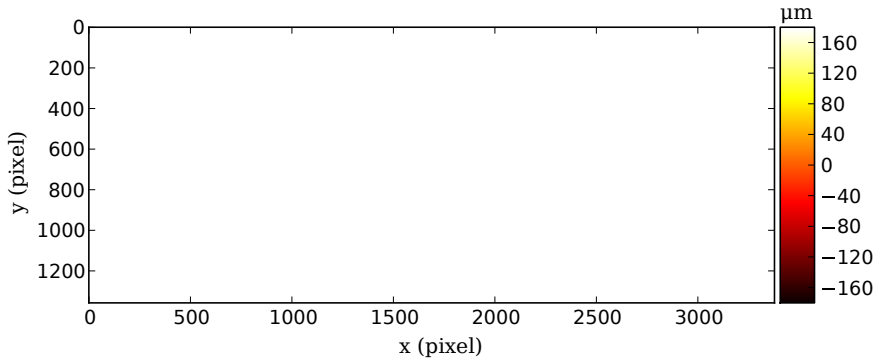

(a)

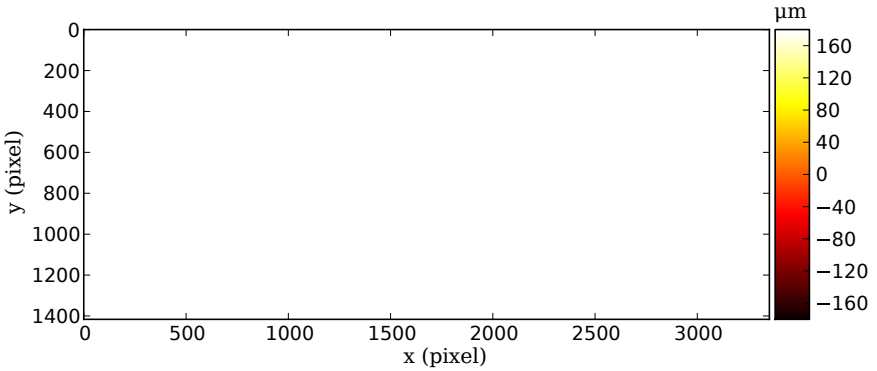

(b)

Figure 4.15: The profile maps of the deformed specimen in Test 1 (a) the face for thermal measurement and (b) the face for kinematic measurement

effect of out-of-plane deformation is presented in the following section.

4.4 Effect of out-of-plane deformation

This section is concerned with only thermographic measurements. All the analyses on the kinematic measurements will be detailed in the next chapter. And as a matter of fact, in our experiments no particular errors associated with out-of-plane deformation were found in the kinematic measurements of nickel single crystals.

Concerning the effect of out-of-plane deformation on thermographic measurement, a general introduction will be first presented. It includes two parts: 1) bibliographic study and 2) theoretical analysis. Then the study will focus on a specific analysis of the out-of-plane effect in the deformation of nickel single crystals.

4.4.1 Bibliographic study

It is well known (Gaussorgues, 1994) that in thermographic measurement a change of angle in the observation of an emitting object can alter the incident radiation, thus leading to a different measurement result. This phenomenon is more popularly read as a variation of apparent emissivity of the material surface. It is actually the same effect when the measuring object suffers an out-of-plane surface deformation, since the lens-object relative position relationship has been changed though in a different way (the IR camera is fixed). Both of the two ways resulting in an alteration of the incident radiation are illustrated by a schematic diagram in Fig. 4.16, where Φ and Φ' represent the incident radiation before and after such a relative position change, respectively.

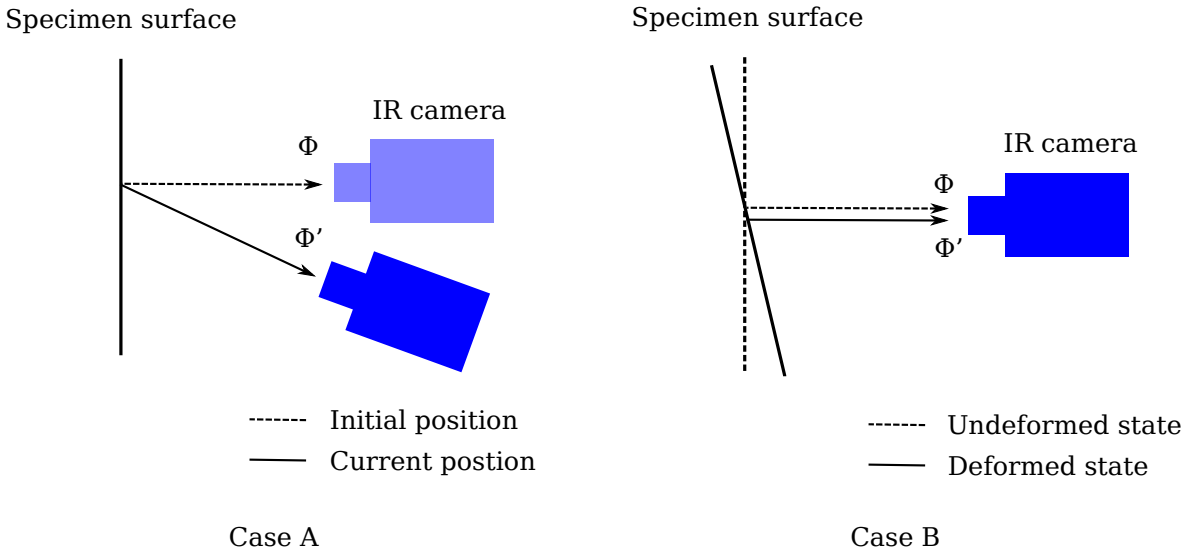

Figure 4.16: The alteration of incident radiation in two different cases: case A - without out-of-plane deformation and IR camera movable; case B - with out-of-plane deformation and IR camera fixed.

Though the effect of out-of-plane deformation on thermographic measurement, or briefly the out-of-plane effect, has long been recognized, to the best of our knowledge it did not draw enough attentions by the researchers in the field of Experimental Solid Mechanics . A main reason should be attributed to the fact that most of such investigations were conducted at a macroscopic scale, where the deformation type was quasi in-plane. Nevertheless, with recent progresses of thermography in being applied to a microstructure scale measurement, the effect of out-of-plane deformation was revealed nonnegligible and in many cases even predominant.

In the study of an aluminum bi-crystal specimen (Saai *et al.*, 2010), the authors observed an apparent out-of-plane deformation occurring on the grain boundary after a tensile test. The surface of one grain shifted around 150 μm with respect to the surface of the other grain, which led to an abrupt geometrical variation at the grain boundary. It was, however, disregarded in the thermographic measurement where the apparent emissivity of material was considered unchanged. In another recent study on monocrystalline shape memory al-

loy (Delpueyo *et al.*, 2012), a visible out-of-plane deformation accompanied with relevant microstructure evolution can also be noticed on the deformed specimen surface. The possible out-of-plane effect was also not approached by the authors. Similar examples can also be found in (Badulescu *et al.*, 2011; Delpueyo *et al.*, 2011). Nevertheless, the negligence of the out-of-plane effect may cause a misinterpretation on the thermal measurements, and even some serious errors in some cases.

The technical challenge for quantifying the out-of-plane effect lies that the real-time varying apparent emissivity accompanied with the out-of-plane deformation is generally not accessible. In our studies, the analysis will focus on only the final deformation state of specimens, by relating the apparent emissivity field with its corresponding specimen surface profile. The first interest is to confirm the geometrical dependence of the thermographic measurements with the advent of out-of-plane deformation. To this end, a theoretical analysis on the out-of-plane effect was conducted in this work, which is presented in the below.

4.4.2 Theoretical analysis

The out-of-plane effect on thermographic measurement is an assembly of several phenomena, e.g., variation of apparent emissivity of specimen surface, change of environment reflection. In order to separate the different active factors, here it is necessary to recall the formulation of energy balance of radiative flux in the thermography imaging, as analyzed in chapter 2.

The received radiative flux by the IR camera Φ_{cam} (or incident flux) for a given pixel $P(x, y)$ can be expressed in the form

$$\Phi_{cam}(x, y) = \varepsilon_{obj}\Phi_{obj}(x, y) + (1 - \varepsilon_{obj})\varepsilon_{amb}\Phi_{amb}(x, y) \tag{4.1}$$

where ε_{obj} and ε_{amb} represent the emissivity of the object and that of the ambiance (or environment), respectively. Φ_{amb} stands for the radiative flux emitted by the ambiance.

It is worth noting that in the above energy balance formulation, the Narcissus effect of IR camera is not taken into account because it is expected to be eliminated in the calibration. Thus, two radiation parts are involved in the incident flux, which are the first term on the right of the equation representing the radiation emitted from the object itself and the second term that from the environment. Now considering a specimen subjected to an out-of-plane deformation during the thermographic measurement, the variation solely due to a geometrical change of the specimen surface is the object emissivity ε_{obj}. This variation will however change both of the two radiation parts from the object and the environment. And in the condition that the ambiance is not perfectly uniform, i.e., ε_{amb} and Φ_{amb} are position dependent, the out-of-plane deformation may also bring an additional variation on the radiation from the environment.

In summary, the first active factor is the emissivity variation due to the out-of-plane deformation, i.e., the effect of the angle of incidence on emissivity. It is associated with the great portion of the total incident radiation. And the second active factor is the influence of the environment reflection, representing as a parasitic effect of the out-of-plane deformation.

Both of the two factors are analyzed in the following.

1) The effect of the angle of incidence on emissivity

The emissivity of a material depends on the angle of observation. The variation of the emissivity of a surface with the angle of incidence means that surfaces that are not flat have a locally varying apparent emissivity, even in the case of a given material (constant emissivity). The geometry of the radiating surface is characterized by its angular emissivity, i.e., the emissivity within a solid angle. A distinction must therefore be made between the directional emissivity ε_h and the angular emissivity ε_Ω (Gaussorgues, 1994). For objects that follow Lambert's law (Pedrotti & Pedrotti, 1993; Warren, 2007), i.e., the emissivity is independent of the angle of observation, it yields

$$\varepsilon_\Omega = \varepsilon_h = \varepsilon_{obj} \tag{4.2}$$

where Ω is the angle between the direction of observation and the normal of the material surface.

Most objects (black and grey bodies) are practically Lambertian for angles not exceeding 55°. At greater angles, the emissivity of the surfaces falls quickly (Gaussorgues, 1994). The problem of the angular emissivity of carbon black was studied in (Poncelet, 2007). The author performed the measurements of emissivity under different angles of observation for two cylindrical specimens deposited by a layer of carbon black. The results are shown in Fig. 4.17, by relating the ratio $\varepsilon_\Omega/\varepsilon_h$ with the $cos\Omega$.

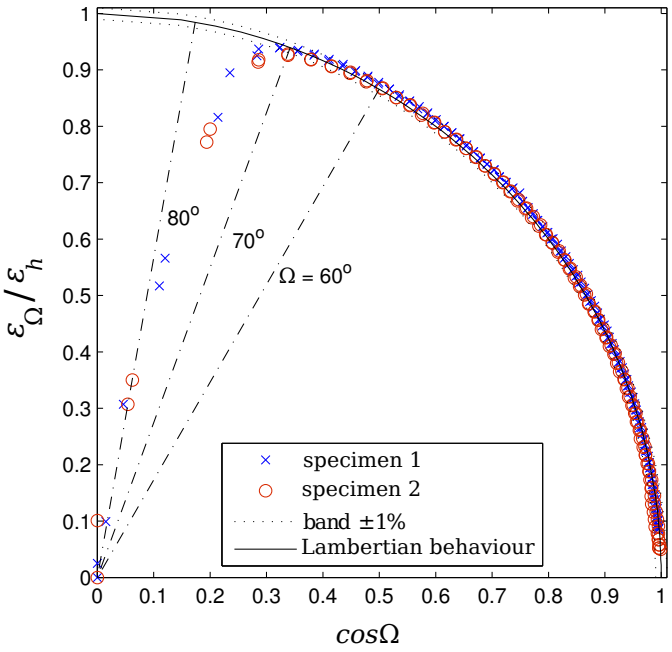

Figure 4.17: Emissivity depending on the angle of observation, reproduced from (Poncelet, 2007)

Fig. 4.17 shows that angular emissivity ε_Ω is nearly constant and equal to the directional

emissivity ε_h for angles below 60°. In this range the decrease of the ratio $\varepsilon_\Omega/\varepsilon_h$ is lower than 1%. So the carbon black was considered as a quasi Lambertian and the effect of the angle of incidence on emissivity was neglected in the study of Poncelet (Poncelet, 2007).

Nevertheless, a loss of emissivity of 1% may be negligible for the studies performed at a macroscopic scale but could be nonnegligible for the investigations at a microstructure scale, in particular considering a context of low energy generation, high thermal diffusion and localized out-of-plane deformation.

2) The influence of the environment reflection

According to the radiative energy balance of Eq. 4.1, a variation of the object emissivity will lead to a inversely proportional variation of the reflected radiation from the environment, provided that the ambient temperature is constant and the ambient emissivity is perfectly uniform. In the reality, this effect is generally more complicated as the last assumption is very difficult to be met. A relative position change between the lens and object means also a corresponding alteration of the environment background, in other words, a change of the environment reflection conditions. The resulting influence on thermographic measurement can be schematically illustrated in Fig. 4.18.

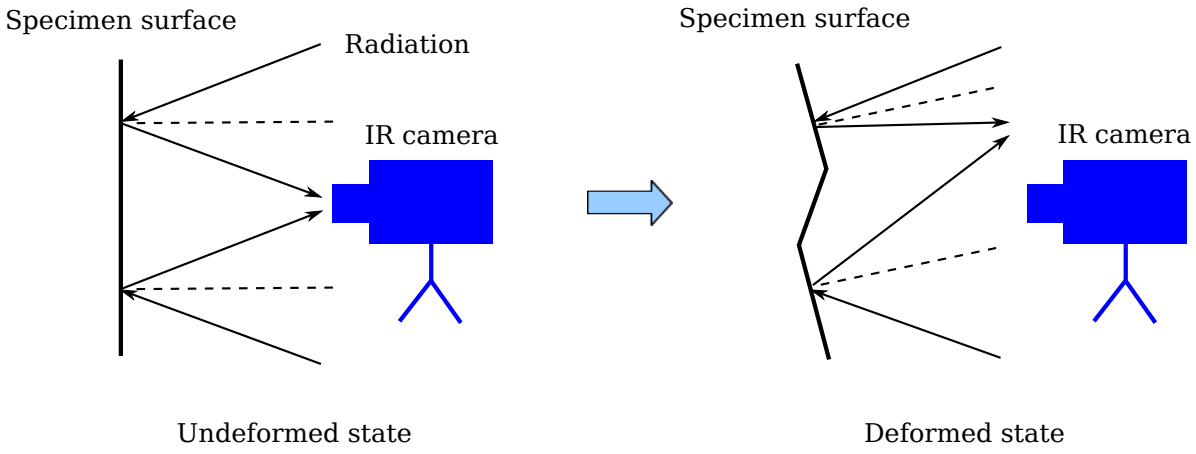

Figure 4.18: A schematic diagram presenting the variation of the reflection effect due to the out-of-plane deformation

In order to minimize this reflection effect due to out-of-plane deformation, the “isolation box” was adopted in the thermographic measurements. The inner surface of the box was sprayed by black paint of high emissivity so as to best provide a uniform radiation source. And the outer surface was covered by aluminum foil of very low emissivity for reducing the radiation absorptions from the environment. In spite of these efforts, the reflection effect is complex by the nature and difficult to be completely eliminated. Nevertheless, the contribution of the environment reflection on the total incident radiation is much less important than the emissivity variation, especially in the case that the coating applied on the object surface is carbon black with a very high emissivity.

Except the two active factors discussed above, there is another perturbation on the thermographic measurement that is owing to the limitation of the 2D imaging. As in our experimental studies, the single-camera set-up was chosen dedicated to a 2D imaging of the planar surface of specimen. The imaging of 3D non-planar surface in 2D vision is problematic in itself. The first involved problem is a loss of information for the measuring non-planar surface. Moreover, the effect of the 2D imaging can be also strongly dependent on the angle of observation. Thus this effect is even more difficult to be quantified. Nevertheless, it is not considered playing an important role in our experiments on oligo- and single crystals, as their deformed specimen surfaces keep yet more or less "in-plane" at a macroscopic scale, where the out-of-plane deformation is generally very local.

The above analysis shows the complexity of the out-of-plane effect. It reveals also that the emissivity variation plays a major role in the alteration of the incident radiation due to the out-of-plane deformation. Hence, a preferential analysis approach is to relate the emissivity map with the profile map of the same deformed specimen surface. This analysis was carried out on nickel single crystals which will be presented in the following section. And in the case that the emissivity map is not available, the thermographic measurement results (without considering the variation of apparent emissivity due to out-of-plane effect) at the final deformation state of specimen is expected to be related to the profile map at the same deformation state. This philosophy was embodied in the analysis of aluminum oligocrystals, please refer to appendix A.

4.4.3 Analysis of out-of-plane effect

The former analyses have revealed the slip bands emerging on the deformed material surface, which are considered as the main out-of-plane deformation. The out-of-plane effect on thermographic measurement is expected to be characterized through the emissivity map. Hence, a correlation analysis between the emissivity map and profile map was carried out.

Firstly, the emissivity field of the deformed specimen was measured. And then the data in both emissivity and profile maps were treated by following several steps of a dedicated analysis approach. Finally, the emissivity-profile variation was compared and discussed. In this work only Test 1 is involved as a case study.

4.4.3.1 Measurement of emissivity field

The surface coating of the deformed specimen was not removed immediately after the tensile test for the purpose of an emissivity measurement. So the indirect measurement method (as detailed in chapter 2) was adopted, in which the two chosen temperatures for the BB were $T_1 = 28°$ and $T_2 = 30°$. The measured emissivity field is shown in Fig. 4.19. The spatial resolution in the image is $30 \times 30\ \mu m^2$.

As tested in the metrology study in chapter 2 that the material emissivity of the surface coating carbon black is 0.97 with a possible minor deviation up to 0.003 in our experiments. The measured emissivity shown in Fig. 4.19 is actually not the material emissivity but

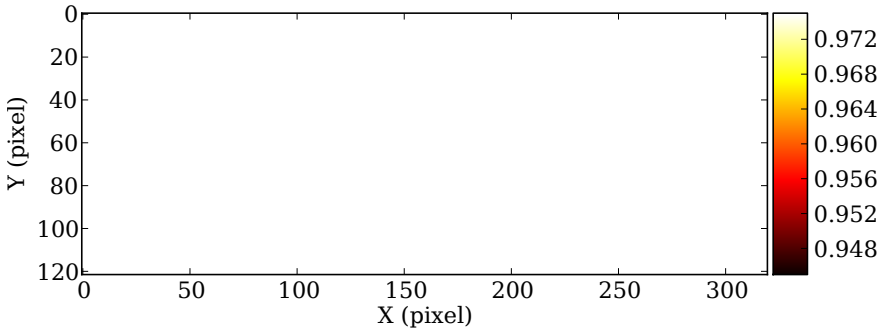

Figure 4.19: Emissivity field of the specimen surface after the tensile test

the angular emissivity (or apparent emissivity) owing to the out-of-plane effect. It shows the angular emissivity on the deformed surface is in the range [0.95, 0.97], with a mean value about 0.962. It means a decrease of emissivity 0.008 in average, or nearly 8.2 ‰, comparing to the directional emissivity 0.97. More important, the emissivity map displays a rather heterogeneous pattern, where the presence of the two groups of slip bands is distinct.

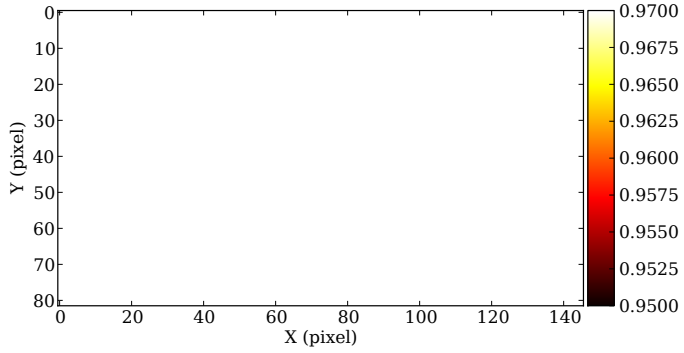

(a)

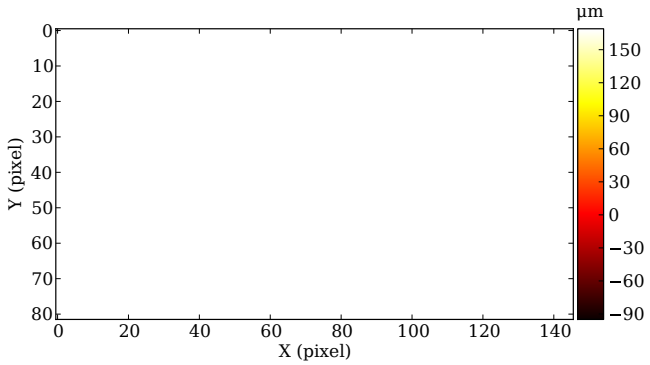

(b)

Figure 4.20: (a) The ZOI of the emissivity map, (b) the ZOI of the profile map

For the ease of comparison, the same ZOI was chosen for the emissivity map and its corresponding profile map after having been spatially matched, as illustrated in Fig. 4.20(a) and (b), respectively. The figure shows that a global correction can be found between the emissivity map and profile map. The data in both maps show however complex features. Thus, a dedicated data treatment procedure was applied in order to promote a further quantitative analysis of the emissivity-profile relationship.

4.4.3.2 Data treatment process

The first difficulty in the data analysis is the mixture of the two families of slip bands appearing on both emissivity and profile maps. Since the separation of the two slip systems is difficult, a sub-zone is thus preferred to be chosen where one slip system is dominant. To this end, the emissivity/profile map was rotated by 45° clockwise in order to make one group of slip bands along right the vertical direction. Then a sub-zone was selected where the concerned slip system was dominant. Here the analysis will be first focused on the emissivity map and then the profile map. The rotated emissivity map with the selected sub-zone is shown in Fig. 4.21.

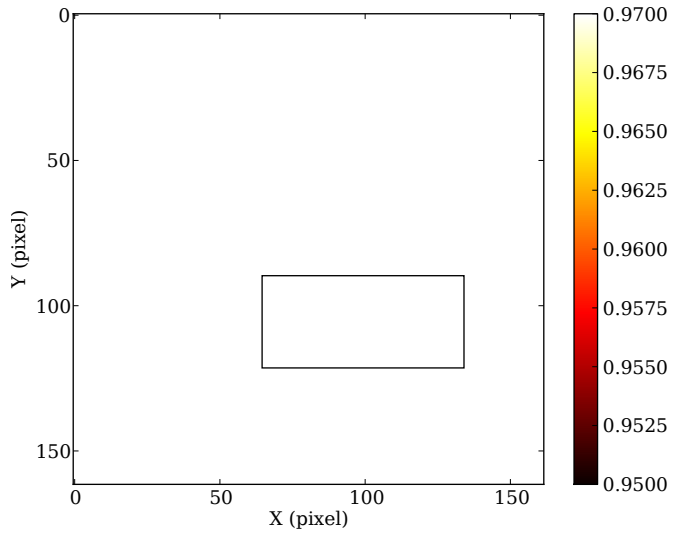

Figure 4.21: The image rotation and selection of the sub-zone in the emissivity map

The selected sub-zone is of a size 30 × 60 pixels. As an individual image, it is illustrated in Fig. 4.22(a). The emissivity distribution shows clearly that the principal heterogeneity is associated with the slip bands along a well-defined slip direction (vertical direction). However, some dispersed "spots" are also present in the emissivity field, which are mainly due to the initial heterogeneity of the surface coating. Since they were observed in the initial thermal field before load in the tensile test, as shown in Fig. 4.23 in which the thermal field is expressed in radiative flux. The initial thermal field shows a number of small black spots that are similar to the ones appearing in the emissivity map. Here it is important to note that these left spots on the emissivity map in the deformed state are not geometrically dependent, so in this analysis they are considered as unexpected noises

and need to be removed from the emissivity field. To this end, a image blurring (or image smoothing) method was applied through a 1D Gaussian filter in Python. The filtering was performed in the vertical direction with a defined standard deviation $\sigma = 2$. The emissivity map after filtering is shown in Fig. 4.22(b).

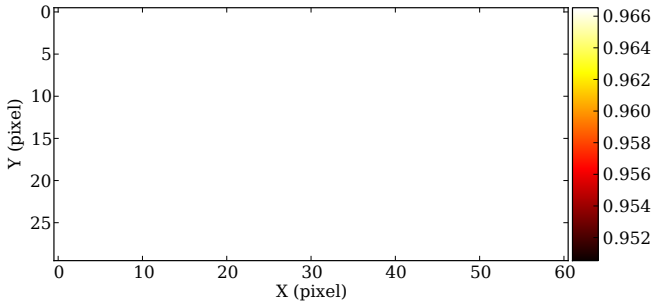

(a)

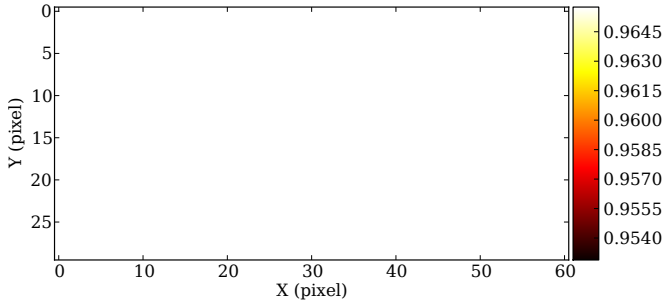

(b)

Figure 4.22: (a) The initial emissivity map (b) the emissivity map after Gaussain filtering

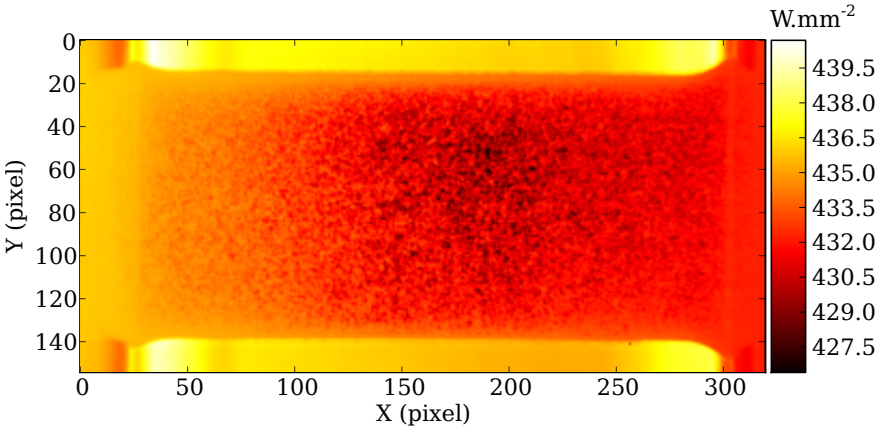

Figure 4.23: The initial thermal field before load in the tensile test

An improved emissivity distribution is displayed in the emissivity map after Gaussain filtering. Nevertheless, it is still not good enough to favor a 2D full-field correlation analysis

with the profile map (the same situation occurred also on the profile map which will be shown later). On the current situation, a 1D analysis was proposed by averaging the data in the vertical slip direction. Fig. 4.24 shows the distribution of the averaged emissivity. It is expected to be compared with the distribution of a pertinent indicator of profile variation on the specimen surface.

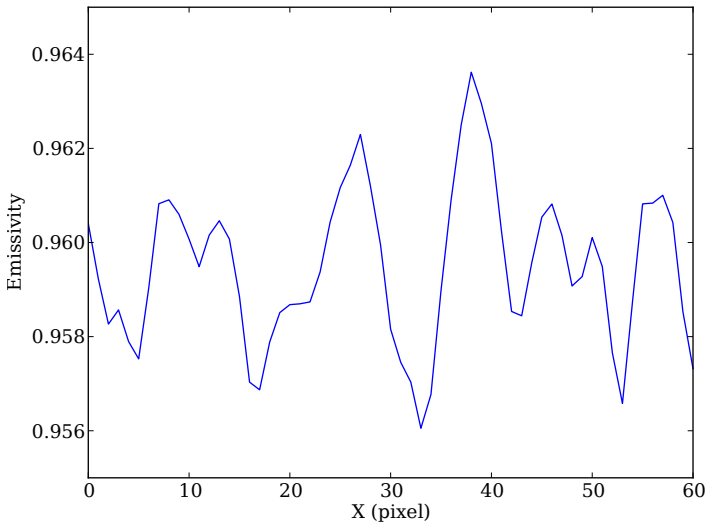

Figure 4.24: The distribution of the averaged emissivity

Concerning the profile map, first of all the same sub-zone was selected as that in the emissivity map, as shown in Fig. 4.25(a). Thus the profile map in Fig. 4.25(a) is spatially matched with the emissivity map in Fig. 4.22(a). As only the profile variation in the slip direction is concerned in this analysis, then the initial profile map was first smoothed by a 1D Gaussain filtering along the vertical direction, with a standard deviation σ=1. The profile map after filtering is illustrated in Fig. 4.25(b). Comparing to the initial profile map, Fig. 4.25(b) shows that the unexpected interferences in the horizontal direction are mostly smoothed out after the filtering.

The same with the analysis of emissivity, a 1D analysis was applied for the profile. Thus the profile data is averaged in the vertical slip direction, resulting a 1D profile distribution as shown in Fig. 4.26.

A key issue in the profile data treatment is to find an indicator that allows to correlate directly with the variation of apparent emissivity. As introduced in theoretical analysis on the out-of-plane effect, $cos\Omega$ can be considered as a parameter pertinent to the angular emissivity according to Lambert's law. In this case, the discrete profile data are preferably to be fitted into analytical functions. To this end, a method so-called "moving parabola fitting" was applied in this work.

The moving parabola fitting is similar to the most common smoothing algorithm "moving average". The difference is that this method replaces each point in the signal not by the average of "m" adjacent points but by their fitting result through a parabolic polynomial.

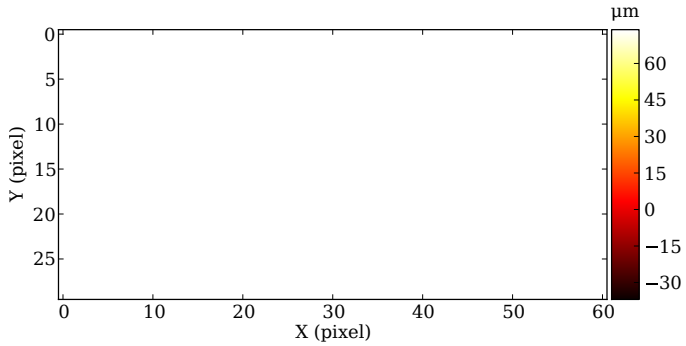

(a)

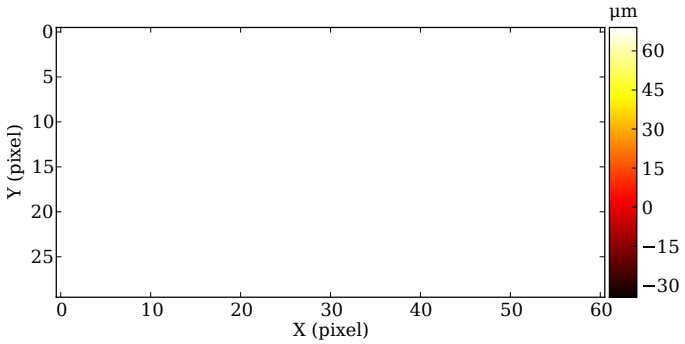

(b)

Figure 4.25: (a) The initial profile map (b) the profile map after Gaussain filtering

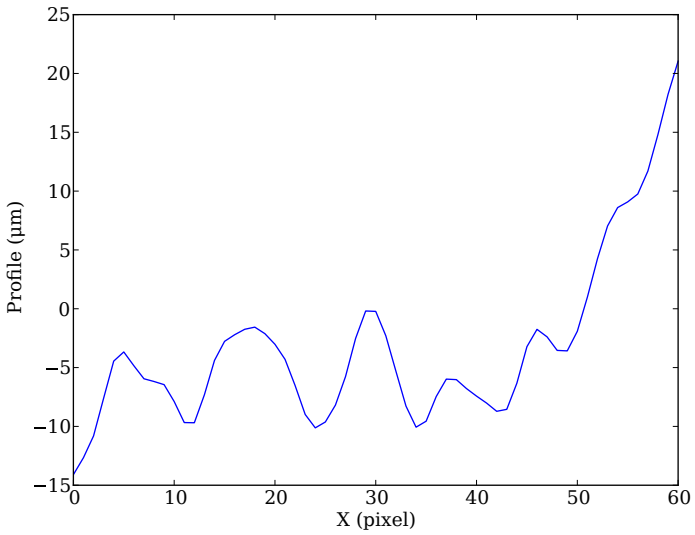

Figure 4.26: The distribution of the averaged profile

The key parameter in this method is the smooth width m, which was defined as $m = 25$ in this study in order to achieve an effect of global trend approximation. The profile distribution after processing this method is shown in Fig. 4.27.

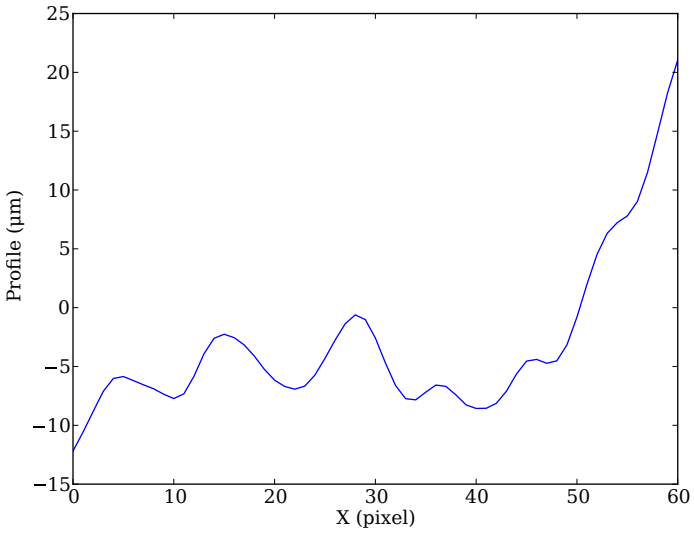

Figure 4.27: The distribution of profile after the moving parabola fitting

From the analytical function for parabolic polynomial fitting, the variation of angle Ω can be calculated. The applied polynomial function is of second-degree that takes the form

$$f = a + bx + cx^2 \tag{4.3}$$

where a, b and c are the constants associated with the profile data, and x represents the axis position.

The angle Ω can be obtained form the first derivative of the above equation which represents the slope of the profile curve:

$$\Omega = tan^{-1}(\left|\frac{\mathrm{d}f}{\mathrm{d}x}\right|) = tan^{-1}(|b + 2c|) \tag{4.4}$$

The Ω defined in the analysis of out-of-plane effect varies from 0° to 90°, thus the derivative is taken by its absolute value. Now with the knowledge of Ω, the indicator $cos\Omega$ for each point can be calculated. Fig. 4.28 illustrates the distribution of $cos\Omega$.

Until now all data treatments are accomplished, and the resulting emissivity-profile relationship is discussed in the follows.

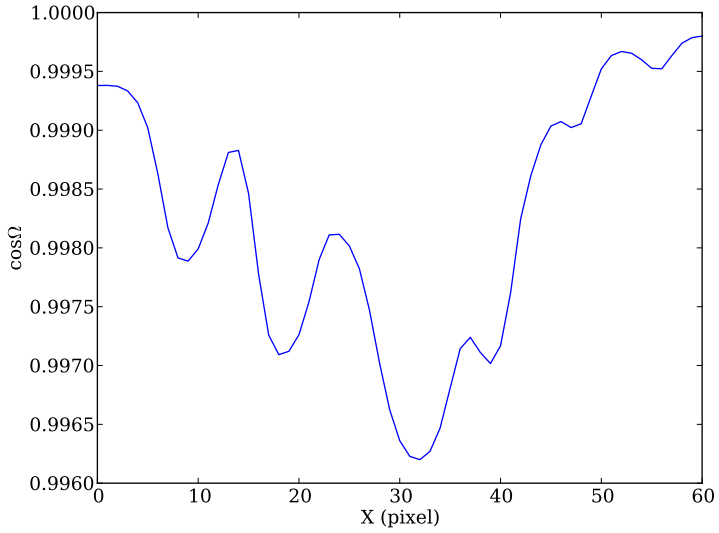

Figure 4.28: The distribution of $cos\Omega$

4.4.3.3 Results and discussion

Fig. 4.28 shows that the values of $cos\Omega$ are very close to 1 ([0.9962, 0.9998]). In other words, the variation of angle Ω is relatively small in absolute values, from near 0° to a maximum around 5°. Nevertheless, as explained before a variation of angle of several degrees may induce an important influence on the apparent emissivity.

Now the important issue is to check the comparison of emissivity versus $cos\Omega$, as shown in the below image by integrating Fig. 4.24 and Fig. 4.28.

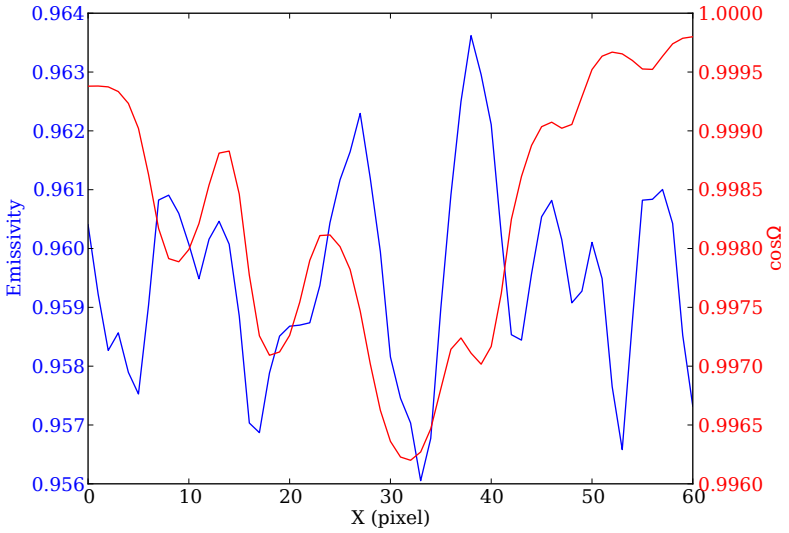

Figure 4.29: Emissivity versus $cos\Omega$

Some correlation on the variation trend of emissivity and $cos\Omega$ can be found in Fig. 4.29. It shows more distinct in the left and central part of image (from about 10 pixel to 40 pixel in the x axis), in which the emissivity generally increases (or decreases) with the increase (or decrease) of $cos\Omega$. It is in good agreement with the former theoretical analysis: the apparent emissivity decreases with the increment of Ω. Nevertheless, in the right part of image (from 40 pixel to 60 pixel) no visible correlation can be confirmed between the two elements. This result is possibly related to the data processing when the profile map was averaged in one dimension. The profile map in Fig. 4.25(b) is reproduced below, in which an irregular profile distribution of elevated values can be noticed in the upper right corner of image, as shown by the zone marked. This local profile variation may change the averaged profile variation in the x direction, thus resulting an apparent non-matching effect between the emissivity and $cos\Omega$ in the concerned zone.

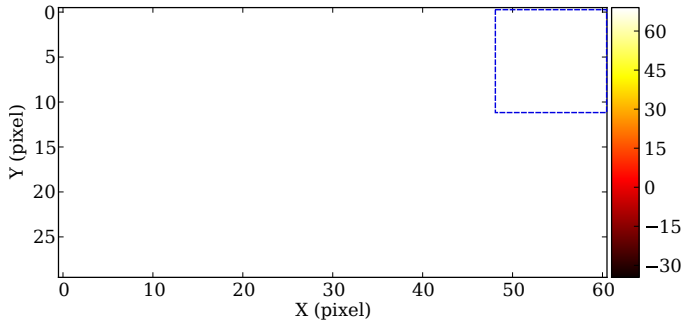

Figure 4.30: An heterogeneity in the profile map

The above analysis shows also that the variation of apparent emissivity due to the out-of-plane deformation is not very important in absolute values, less than 0.01 in the analyzed zone. But in the current context of low strain rate, high thermal diffusion and plus a localized deformation process in the tests of nickel single crystals, the resulting thermal artifacts due to out-of-plane effect can be present even dominant in the measured thermal fields. A typical thermal field (in radiative flux) during Test 1 after the slip band formation is shown in Fig. 4.31, where the emerging "thermal bands" are obvious which correspond to the slip band markings on the material surface.

On the current situation, one has to abandon the expectation for a quantitative temperature measurement, because the thermography does require a precise knowledge of emissivity. Since a direct measurement of emissivity is very difficult during a mechanical test, but if a real-time measurement of surface profile is feasible, the emissivity variation is possible to be estimated from its correlation with the profile variation, for instance, the $cos\Omega$.

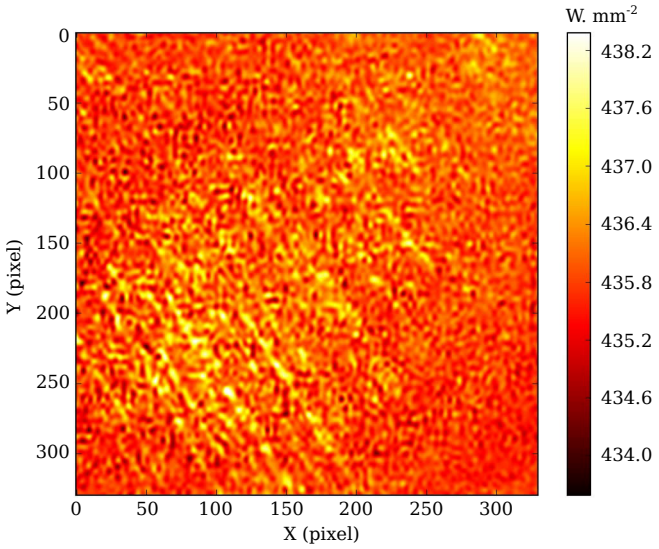

Figure 4.31: The "thermal bands" appearing after the slip band formation in Test 1

4.5 Conclusion

Tests, measurements and macroscopic analyses were carried out for nickel single crystals in this study.

Firstly, the studied material pure nickel single crystal was prepared, and its crystallographic structure was specified. Then the experimental protocol for the kinematic-thermal fully-coupled measurements was detailed, and a series of tensile tests were conducted. A prior step for the full-field analysis was the macroscopic analysis on the deformed specimen surfaces. Thus the optical observation and profile measurement were carried out, in which the presence of an important out-of-plane deformation was remarked.

The out-of-plane effect on thermographic measurement was particularly investigated in this work. Firstly, a theoretical analysis was carried out that summarized the active factors in the out-of-plane effect. Among these factors, the emissivity variation due to the alteration of angle of incidence was considered as the dominant element. And relevant analyses were conducted to relate the emissivity map to its corresponding surface profile, in order to confirm its geometrical dependence. After a set of data treatment steps, a refined ε_Ω-$cos\Omega$ relationship was established. The results demonstrated that the apparent emissivity decreases with the increase of the variation of angle, which is in agreement with the theoretical analysis. Nevertheless, subjected to the out-of-plane effect, the attempt for a quantitative temperature measurement had to be abandoned in this work.

Chapter 5

Full-field analysis of nickel single crystals

Full-field analysis of kinematic-thermal measurements on nickel single crystal deformation is carried out in this study, and most of the works are focused on the kinematic field analysis.

Firstly, a dedicated data treatment strategy is necessary to be developed in order to access the strain fields properly from a crystallographic basis. Then the obtained strain fields are expected to be fully exploited, and a particular interest in this study is focused on the strain heterogeneity phenomenon and its correlation with the work hardening stages of single crystals. For a better understanding of their intrinsic link through dislocation theory, an analysis of microstructure evolution is involved. Moreover, the grip effect and its resulting crystal lattice rotation is also discussed in this work. Finally, an analysis on the thermal evolution during the single crystal deformation is provided as a complementary for the kinematic field analysis.

This study is therefore unfolded into five parts: 1) data treatment strategy, 2) macroscopic analysis, 3) strain heterogeneity and work hardening, 4) grip effect and crystal lattice rotation and 5) thermal field analysis.

5.1 Data treatment strategy

The analyses in the last chapter have demonstrated that a heterogeneous deformation process took place in the plastic deformation of nickel single crystals. The slip markings left on the material surface are the evidence of the localized deformation, which is expected to be characterized quantitatively in the strain fields obtained from the kinematic measurements. Former studies on polycrystals (Seghir *et al.*, 2012) show however that the general data treatment methods of DIC are not perfectly adapted for describing a localized deformation process at the microstructure scale. Hence, a special data treatment strategy of DIC (or image registration) was developed in this study dedicated to characterize the plastic deformation of single crystals in a full-field point of view.

The developed methodology can be broken down into four parts: 1) transformation model, 2) projection basis, 3) approximation approach and 4) validation and error analysis.

They will be introduced successively in this section, and the data analyses will be focused on Test 1 as an example.

5.1.1 Transformation model

As presented in the metrology study in chapter 2, the B-spline is the most suitable transformation model in order to describe a heterogeneous deformation process. A key parameter involved in the B-spline transformation is the choice of the final grid size, which defines how fine the structure is expected to be modeled. In general, with a smaller grid size, the smaller and more local deformation can be described.

The B-spline transformations with several different grid sizes were tested in this study, and the selected ones included 64 × 64 pixels, 16 × 16 pixels and 4 × 4 pixels. An analysis by comparing their resulting displacement fields, especially the first two, was carried out. Fig. 5.1(a) and (b) show the axial displacement fields for the final deformation state obtained by choosing the grid size 64 × 64 pixels and 16 × 16 pixels, respectively.

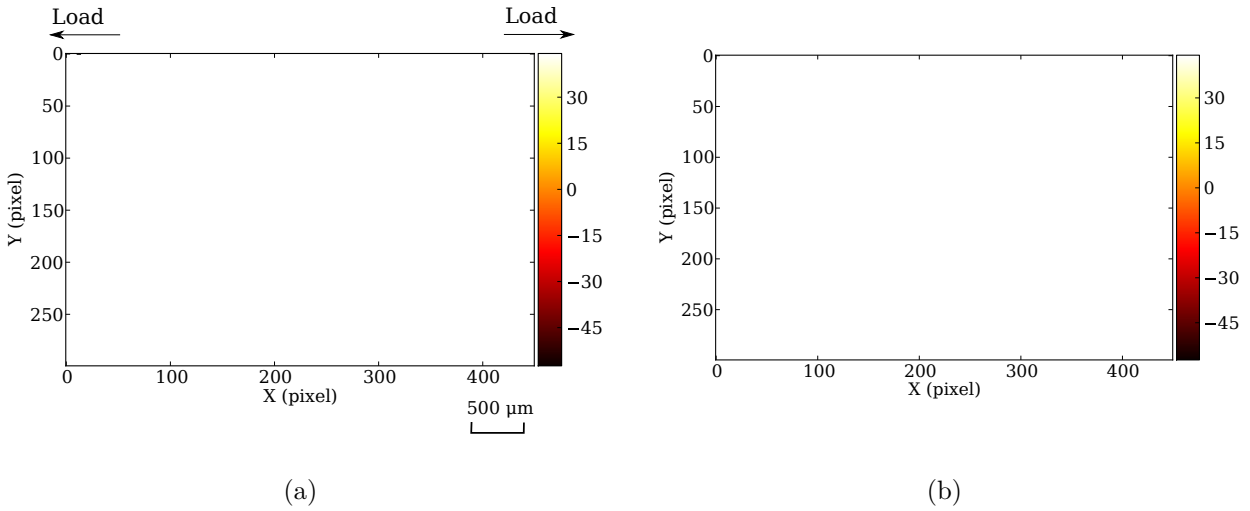

Figure 5.1: The axial displacement fields (in pixel) for the final deformation state obtained by choosing the final grid size (a) 64 × 64 pixels and (b) 16 × 16 pixels

The axial displacement field in Fig. 5.1(a) manifests a rather global and smoothed spatial feature, where no local discontinuity associated with slip activations is noticeable. This result should be attributed to the oversized grids (64 × 64 pixels), thus a "too" global scheme. On the contrary, the axial displacement field shown in Fig. 5.1(b) allows capturing the band-shaped heterogeneities due to the slip manifestations on the material surface. This is the outcome of a smaller grid size adopted (16 × 16 pixels).

Very similar results with the same grid size selections can be found in the transverse displacement fields, as shown in Fig. 5.2 for the final deformation state that corresponds to Fig. 5.1. It can be noticed that the appearing bands in Fig. 5.2(b) are even more distinctive

than those in Fig. 5.1(b). Here it is worthy to note that only one group of slip bands is noticeable in the displacement fields, but not two groups as observed on the specimen surface (as detailed in chapter 4). It is because one group of slip bands (primary slip bands) on the specimen surface is much more pronounced than the other one (secondary slip bands), thus dominating in the measured kinematic fields. In this case, only the manifesting primary slip bands were taken into account in the modeling of the projection basis.

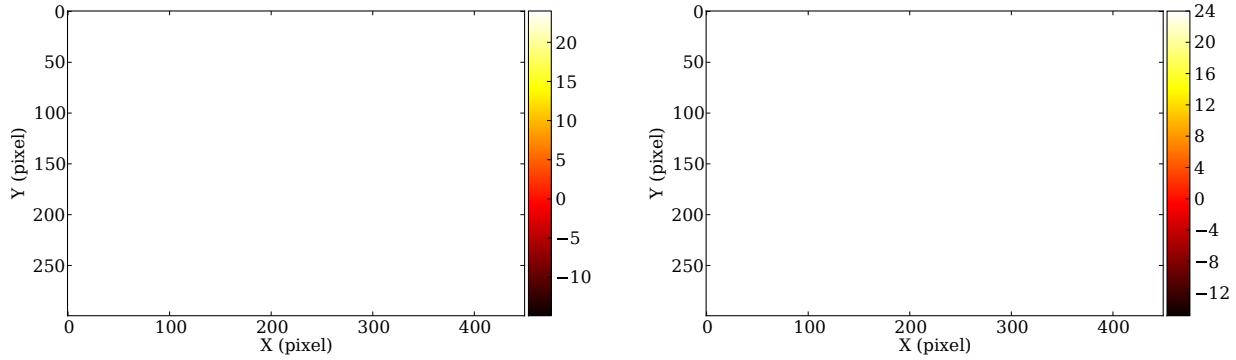

(a) (b)

Figure 5.2: The transverse displacement fields for the final deformation state obtained by choosing the final grid size (a) 64 × 64 pixels and (b) 16 × 16 pixels

A finer final grid 4 × 4 pixels was also attempted in this work. The resulting displacement fields were however found very noisy, in particular for the transverse displacement component, as shown in Fig. 5.3 both the axial and transverse displacement fields. Fig. 5.3 exhibits that the displacements along the slip direction are less well shaped with the interference of noises, from which the concerning slip behaviours of crystal were difficult to be resolved precisely. In this case, the grid size has to be increased so as to capture sufficient kinematic signals and to better distinguish the slip bands.

It is important to emphasize that our strategy for image registration is to choose the parameters that allow to characterize the local kinematic behaviours of slip bands during deformation, and the evaluation is based on the obtained displacement fields. The final grid size is the most important parameter in this strategy, which has shown the resulting displacement fields can be substantially different with altered choices: a oversized grid (64 × 64 pixels) will smooth out the essential local displacements, and a too small grid (4 × 4 pixels) may introduce unnecessary noises in the calculation. The selection of grid size 16 × 16 pixels avoids the two unfavorable situations, thus more approaching to an optimal choice. This point of view can be further verified by the quantification of the obtained displacements with the three different choices.

Concerning both the axial and transverse displacement fields obtained using the three different grid size selections, their respective mean values ($\bar{u}$, $\bar{v}$) and standard deviations ($\sigma(u)$, $\sigma(v)$) are calculated and summarized in Tab. 5.1.

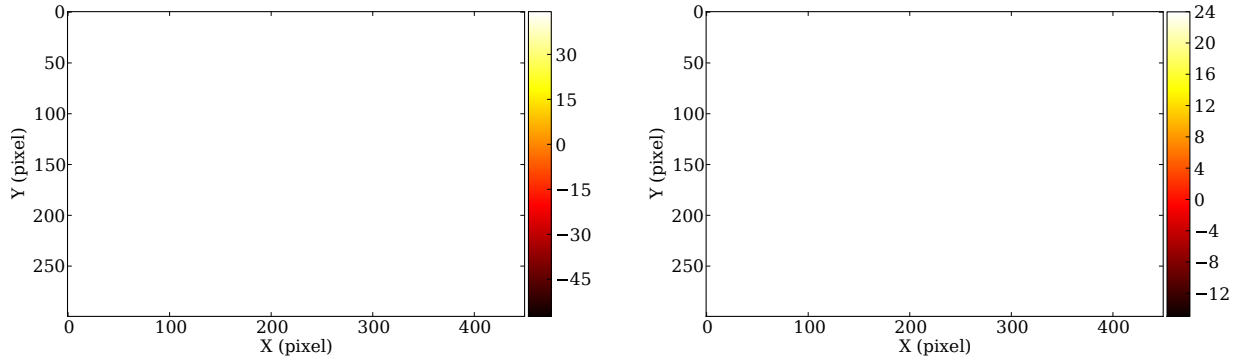

(a) (b)

Figure 5.3: The displacement fields obtained by choosing the final grid size 4 × 4 pixels: (a) axial displacement and (b) transverse displacement

Final grid size	$\bar{u}$ (pixel)	$\bar{v}$ (pixel)	$\sigma(u)$ (pixel)	$\sigma(v)$ (pixel)
64 × 64 pixels	-6.603	4.535	25.414	9.735
16 × 16 pixels	-6.576	4.517	25.413	9.734
4 × 4 pixels	-6.567	4.518	25.405	9.728

Table 5.1: The averages and standard deviations of the displacement fields obtained using B-spline transformations with different final grid size selections

Tab. 5.1 shows that the average displacements given by the three different B-spline transformations demonstrate minor differences, from 0.001 pixel to a maximum 0.036 pixel or about 5‰. Their standard deviations show even smaller gaps, for a maximum 0.009 pixel or about 0.7‰. This result indicates that on the one hand, the above statistics are too global to describe the local displacement variations, and on the other hand, the essential difference between these displacement fields lies on the details of their spatial distribution, as that can be observed in Fig. 5.1-3. The well-shaped bands in the displacement fields shown in Fig. 5.1(b) and 5.2(b) demonstrate that a grid size 16 × 16 pixels allows to preserve the essential mechanical signals related with the slip band activation, and meanwhile avoids the inference of the unexpected noises for the slip band detection. It is thus considered as the most suitable choice in the B-spline transformation in this analysis.

Except the choice on the final grid size (16 × 16 pixels) in the B-spline transformation, other parameters in the image registration algorithm were also determined. It mainly includes: the selection of NCC as the metric, the application of a 3rd order B-spline for the interpolation, and the use of a multi-resolution approach with four decreasing resolutions (8 × 8 pixels, 4 × 4 pixels, 2 × 2 pixels and 1 × 1 pixel). Besides, an initial image registration was also performed through affine transformation before applying the B-spline transformation, which can significantly reduce the difficulty for the image registration.

An indispensable step in the image registration is the error analysis. The residual image provides an appropriate way for the error evaluation, in particular for the local errors, which are the very concerns in this analysis. Because the slip band markings on the specimen surface, with a strong localized characteristic, may lead to a similar out-of-plane effect in the kinematic measurement as that observed in the thermographic measurement. Thus, an error analysis based on the residual image was carried out using the determined image registration algorithm. The residual image for the final deformation state is shown in Fig. 5.4, which represents the maximum possible errors during the whole tensile test.

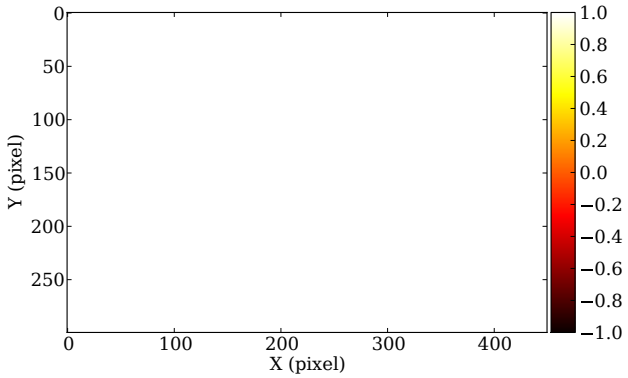

Figure 5.4: The residual image for the final deformation state

The residual image in Fig. 5.4 shows that there are no particular local errors found related with slip bands. It assures that the possible out-of-plane deformation due to slip markings on the specimen surface does not influence the kinematic measurement. It is in contrast with the kinematic measurement in aluminum oligocrystals, where a special pattern associated with the out-of-plane deformation can be clearly observed in the residual image (see appendix A). Nevertheless, an evaluation on the absolute errors produced in the image registration is still a challenging issue, as in most cases an absolutely accurate reference is absent. An experimental error analysis of the adopted DIC system has been presented in chapter 2 that may provide some references for the readers.

All the acquired images during the tensile test were processed by the determined image registration algorithm. It allowed the assessment of the displacement fields (axial and transverse) by the finite difference method. These displacement fields are considered as the initial displacement fields, as they will be further treated through a "projection" technique in the following sections.

In summary, an image registration method with appropriate parameter selections has been achieved in this section, which enabled to provide displacement fields adapted to the observed microstructure. Further data treatment via projection will be followed for a proper characterization of the discontinuities appearing in the initial displacement fields.

5.1.2 Projection basis

The measured displacement field shows the existence of the band-shaped heterogeneities associated with slip activity which needs to be quantified. These bands are actually the kinematic manifestations of the slip bands or interslip bands upon the material surface during the plastic deformation. The interface between a slip band and an interslip band is considered as a "displacement discontinuity", which corresponds to a displacement jump when a local slip activation takes place. The idea of "projection" is to take into account of this displacement discontinuity and to treat the data within a band where the displacement is considered continuous under the current measurement scale, and then band by band for the whole displacement field.

The first step for realizing such a projection scheme is to locate the slip interfaces (or discontinuities) precisely in the displacement fields, thus determining a projection basis. In general, the slip band development during the plastic deformation is accompanied with an increment of slip bands, and in this study more than one system are activated. Here it has to be noted that the projection basis is concerned only with the final deformation state, i.e., the ultimate form of slip bands. And as explained in the last section, only the primary slip bands are taken into account in the kinematic field analysis. Thus the displacement fields involved in this section are the ones corresponding to the final state of deformation. It is also worthy to note that the slip bands and interslip bands are not evident to be differentiated directly from the displacement fields, the concerns of the projection approach is more placed on their interfaces.

In order to better capture the local glide behaviours of slip bands in the displacement fields, the "homogeneous" component of displacement due to the global elongation of specimen are preferred to be removed. As having been presented in the last section, the displacement fields obtained with a grid size 64×64 pixels represent a rather global distribution of displacement without the presence of local glide movements, as shown in Fig. 5.1(a) and 5.2(a). Its average displacements are actually very close to the one obtained with a grid size 16×16 pixels, as shown in Tab. 5.1. Thus, to remove this global component from the displacement fields obtained with a grid size 16×16 pixels provides a possibility to access the displacement components representing the pure local slip behaviours. In practice, a difference can be made between Fig. 5.1(a) and (b) for the axial displacement field and the other between Fig. 5.2(a) and (b) for the transverse displacement field. Their corresponding results are shown in Fig. 5.5(a) and (b), respectively.

Fig. 5.5 shows that a very similar pattern can be found in the resolved axial and transverse displacement fields (but in opposite colors), where the appearing bands are in the same positions. Two kinds of bands can be noticed: the ones with positive values in light color and the others with negative values in dark color. They appear in an alternate mode, which represents exactly the slip behaviours of the adjacent bands that move in the opposite directions. Hence, the sought "interfaces" can be defined as the boundaries between the "light" bands and the "dark" bands.

For a precise location of the slip interfaces, an average displacement was calculated along the slip direction, 45° with respect to the axial direction, as marked in Fig. 5.5(b). The

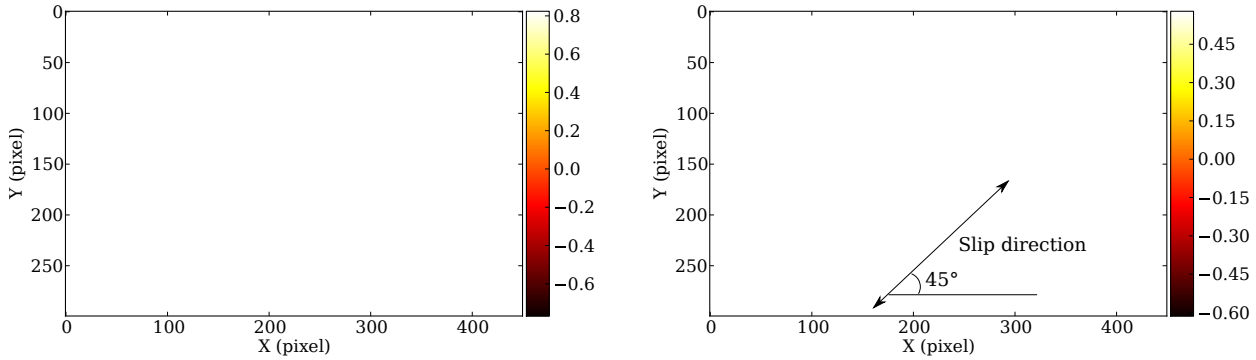

(a) (b)

Figure 5.5: After removing the low frequency (a) axial displacement field and (b) transverse displacement field

resulting average displacement for both axial and transverse displacement fields are illustrated in Fig. 5.6.

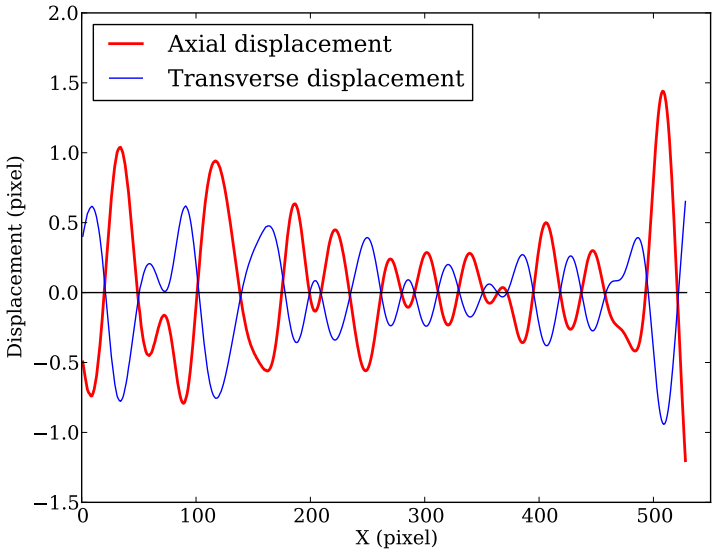

Figure 5.6: Axial and transverse displacements averaged along the slip direction

Fig. 5.6 shows that the averaging axial and transverse displacements along the slip direction are almost symmetric to the axis of zero displacement. In this analysis, an assumption for the interface detection is made: the middle point between the "peak" and "valley" of a wave shown in Fig. 5.6 is considered as an interface point. This method was applied respectively to the axial and transverse displacements, which led to quasi the same results. The detected interface points for the axial displacement are illustrated in Fig. 5.7. It can

be found that for most of the interface points (except two points), they are located right on or very close to the zero displacement axis. It is a logical result as the displacement of an interface between two bands with opposite signs (in displacement) is reasonably approaching to zero.

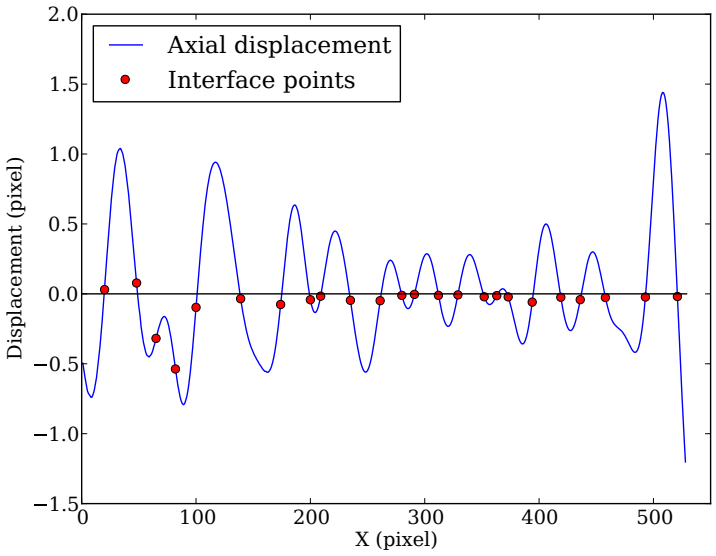

Figure 5.7: The detected interface points

The interfaces determined in Fig. 5.7 can be projected to a 2D field by assuming that the slip bands are straight and along exactly the 45° slip direction. Under this hypothesis, the projection basis can be built up through image segmentation according to the detected slip bands or interslip bands, and the result is shown in Fig. 5.8. There are 24 interfaces in total, thus 25 segmentation zones (or bands) constituted as the projection basis.

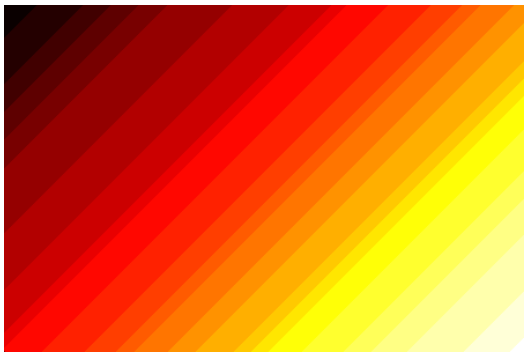

Figure 5.8: The projection basis

The detected interface location can be further verified by overlapping the projection basis (in semitransparent) on the resolved displacement fields in Fig. 5.7. The superposition

images for the axial and transverse displacement fields are illustrated in Fig. 5.9(a) and (b), respectively. The spatial matching effect is considered acceptable for the two superposition images below, where no visible mismatch is noticed in the boundaries of the bands.

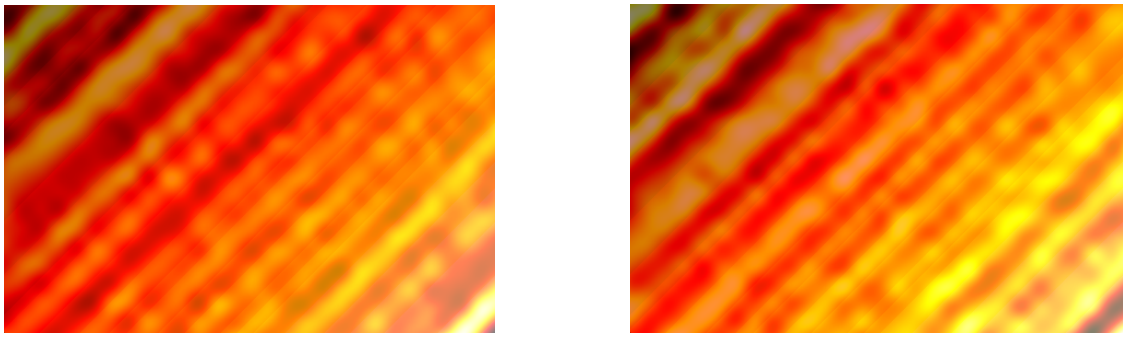

(a) (b)

Figure 5.9: The projection basis overlapped on (a) the resolved axial displacement field and (b) the resolved transverse displacement field

5.1.3 Approximation approach

The projection basis represents the heterogeneous deformation pattern of single crystals: the active slip bands demonstrate a different deformation mechanism than the interslip bands, and the interface between each pair of them acts actually as kinematic discontinuity. If this discontinuity is not taken into account in the strain calculation from displacement fields, a general differential approach, e.g., finite difference method, may produce enormous errors due to the displacement jumps at the slip interfaces. It is the basic motive for applying the projection approach.

Concerning the projection approach, the displacement data in each band of projection basis are expected to be fitted into an analytical function, then the strain in each band can be differentiated directly from the relevant analytical function. In this way, the strain fields can be estimated properly by taking into consideration of the essential heterogeneous deformation pattern of single crystals.

According to (Seghir, 2012), the polynomial can be a suitable choice as the analytical function for the projection. In this work, both the first-degree polynomial interpolation and second-degree polynomial interpolation were tested.

Firstly, concerning the first-degree polynomial interpolation, the axial and transverse displacement fields (u, v) can be fitted respectively into two first-degree polynomial functions g_u and g_v according to

$$g_u = a_0 + a_1 x + a_2 y \tag{5.1}$$

$$g_v = b_0 + b_1 x + b_2 y \tag{5.2}$$

where a_k $(k = 0, 1, 2)$ is a set of constants associated with the axial displacement u and b_k $(k = 0, 1, 2)$ that with the transverse displacement v, and x and y are the two variables in the Cartesian coordinate system.

Here it is important to note that the interpolation was applied within each band, so the fitted functions g_u and g_v are different band by band. The above equations show that the displacements after the first-degree polynomial interpolation are bilinear within each band, thus the solved strain components are constants for each band. It is a relatively simplified approximation approach, which can be easily extended to other analytical solutions if it is necessary.

For the second-degree polynomial interpolation, the displacement fields can be fitted into two second-degree polynomial functions f_u and f_v, as shown in the following

$$f_u = a_0 + a_1 x + a_2 y + a_3 x^2 + a_4 y^2 + a_5 xy \tag{5.3}$$

$$f_v = b_0 + b_1 x + b_2 y + b_3 x^2 + b_4 y^2 + b_5 xy \tag{5.4}$$

where a_k $(k = 0, 1, ...5)$ is a set of constants associated with the axial displacement u and b_k $(k = 0, 1, ...5)$ that with the transverse displacement v, and x and y are the two variables in the Cartesian coordinate system.

The above equations show that the displacements after the second-degree polynomial interpolation are parabolic within each band, thus the solved strain components are bilinear within each band.

Our criterion to determine the interpolation method is to choose the one that can provide a better approximation effect. And the verification is based on the residual images obtained from the displacements after the projection. The initial residual image provided by B-spline transformation without projection is shown in Fig. 5.10(a). And the residual image obtained using the first-degree polynomial interpolation is shown in Fig. 5.10(b) and that using second-degree polynomial interpolation in Fig. 5.10(c).

Firstly, the residual images after projection, both Fig. 5.10(b) and (c), do not show apparent local errors related to the slip bands. But a visible modification of the spatial distribution (of gray levels) can still be noticed in Fig. 5.10(b), comparing to Fig. 5.10(a) and (c). The latter two demonstrate a more similar pattern. Here the mean values and standard deviations for all the three involved residual images are illustrated in Tab. 2.

Tab. 5.2 shows that the mean values of the two residual images after projection are very close to the reference given by B-spline transformation. But the standard deviation of the residual image obtained using the first-degree polynomial interpolation shows an important deviation to the reference one, 0.1123 to 0.0871, about 29.0% higher. While the standard deviation provided by the second-degree polynomial interpolation is 0.0918, only about 5.4%

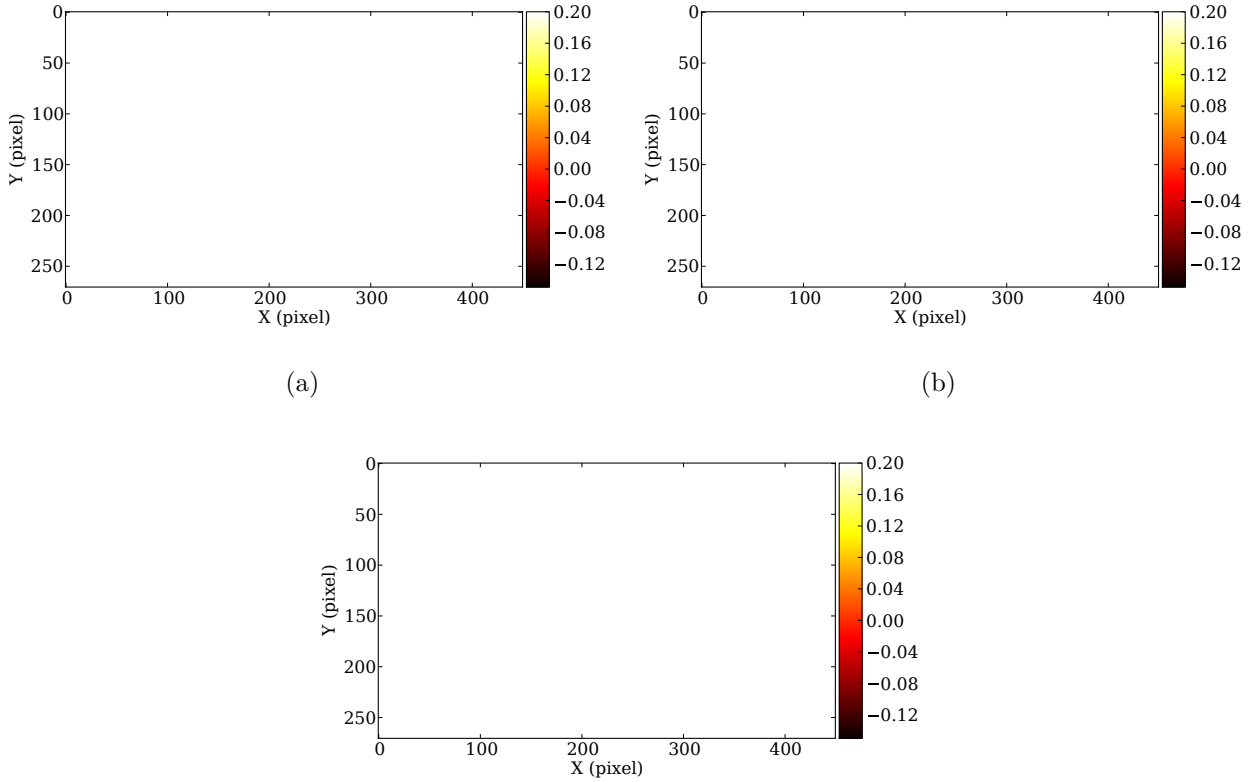

(a) (b)

(c)

Figure 5.10: The residual images obtained (a) without projection, (b) after the projection using the first-degree polynomial interpolation and (c) after the projection using the second-degree polynomial interpolation

Method	Mean value	Standard deviation
B-spline transformation	0.0175	0.0871
First-degree polynomial	0.0182 (+3.7%)	0.1123 (+29.0%)
Second-degree polynomial	0.0180 (+2.9%)	0.0918 (+5.4%)

Table 5.2: The averages and standard deviations of the three residual images in Fig. 5.10

higher than the reference.

The above analysis shows that the second-degree polynomial interpolation demonstrates a better approximation effect than using the first-degree polynomial interpolation, and thus is adopted as the projection approach. Concerning the final deformation state, the axial and transverse displacement fields after processing the projection are shown in Fig. 5.11(a) and (b), respectively. Fig. 5.11 shows that some slip interfaces can be distinguished in the displacement fields after projection. The possible errors in displacement produced in the

projection process will be analyzed in the next section.

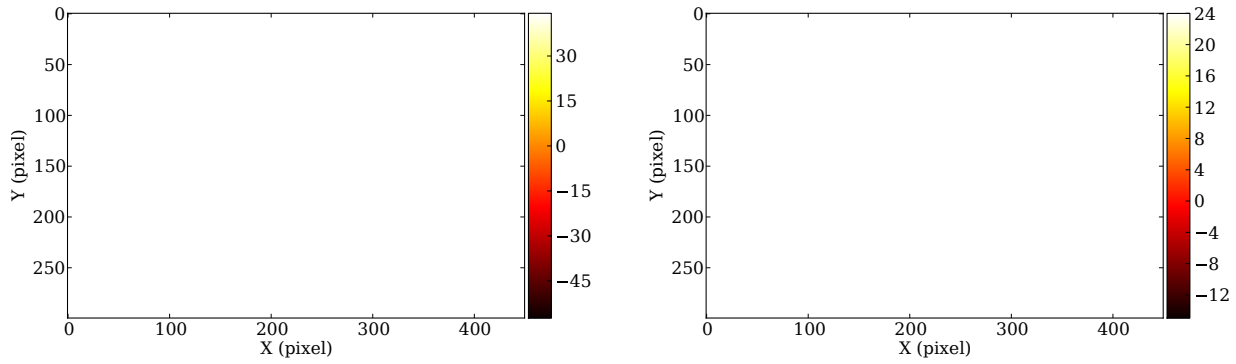

(a) (b)

Figure 5.11: The displacement fields after the projection: (a) axial displacement field and (b) transverse displacement field

Based on the second-degree polynomial functions in Eqs. 5.3 and 5.4, the three in-plane strain components, axial strain (ε_{xx}), transverse strain (ε_{yy}) and shear strain (ε_{xy}), can be obtained through

$$\varepsilon_{xx} = \frac{\partial F_u}{\partial x} = a_1 + a_5 y + 2a_3 x \tag{5.5}$$

$$\varepsilon_{yy} = \frac{\partial F_v}{\partial y} = b_2 + b_5 x + 2b_4 y \tag{5.6}$$

$$\varepsilon_{xy} = \frac{1}{2}(\frac{\partial F_u}{\partial y} + \frac{\partial F_v}{\partial x}) = \frac{1}{2}\left[a_2 + b_1 + (a_5 + 2b_3)x + (b_5 + 2a_4)y\right] \tag{5.7}$$

where be aware that the axial loading direction is along the x direction.

Since the parabolic interpolation is adopted, it leads to a bilinear distribution of strain in each band, as shown by the above equations. Focusing on the final deformation state, Fig. 5.12(a), (b) and (c) show the calculated strain components ε_{xx}, ε_{yy} and ε_{xy}, respectively. The strain fields show that in the final stage of plastic region the axial strain is about 1.7 times higher than the transverse strain in average, and the shear strain exhibits a very low level. This result is reasonable for a slip-dominated deformation of single crystals (Norris, 2006). A complete analysis on the strain fields and its evolution associated with slip systems activating will be presented later after the validation and error analysis in the following section.

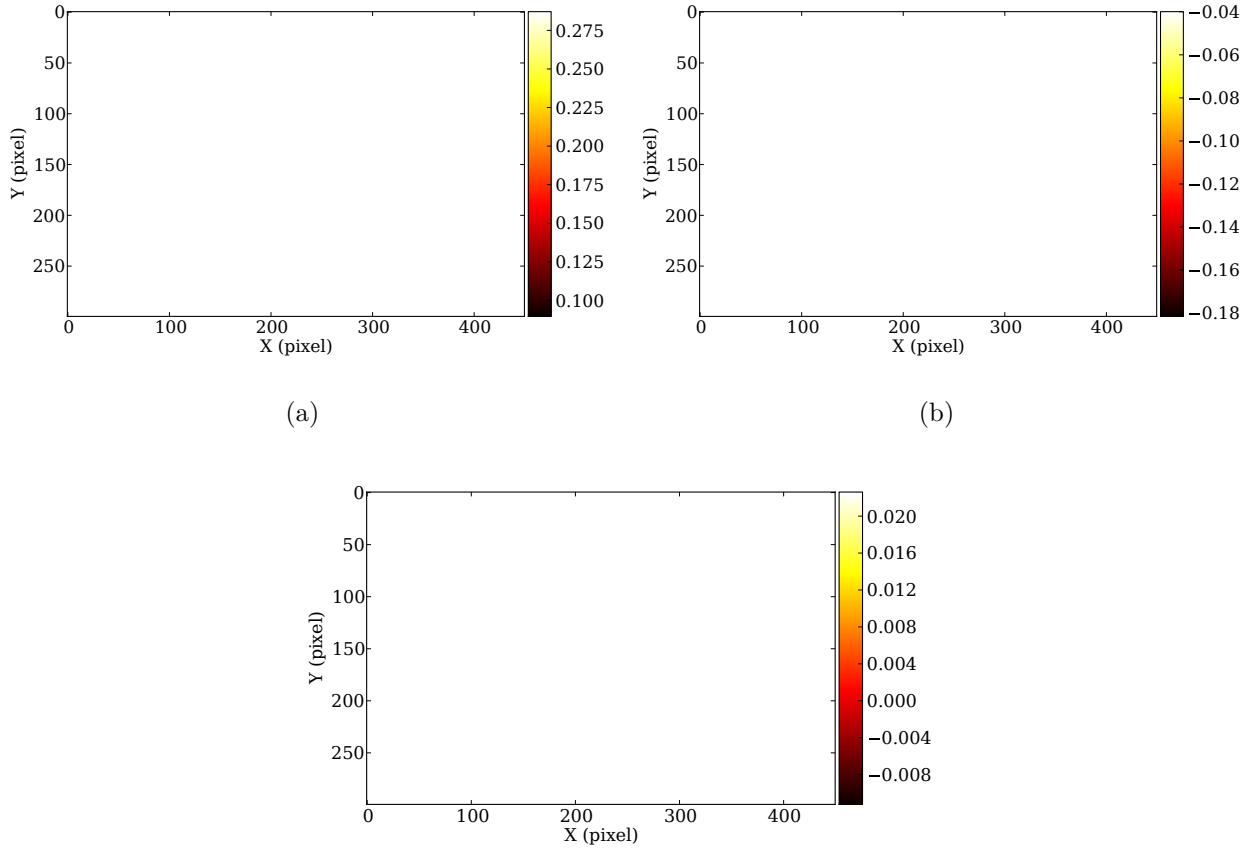

(a) (b)

(c)

Figure 5.12: The strain fields after the projection: (a) axial strain field and (b) transverse strain field, (c) shear strain field

5.1.4 Validation and error analysis

In the last section, an error analysis based on the residual image has been carried out for the projection approach through a second-degree polynomial interpolation. The results showed that the adopted projection approach produced a relatively small deviation in the residual image. Here it is also important to evaluate the possible errors produced in the displacement owning to the projection, which may have a direct influence on the strain calculation.

The displacements provided by the B-spline transformation without projection will still be used as the reference. Now concerning the final deformation state, Fig. 5.13(a) shows the comparison of the axial displacements before and after projection for a line in the horizontal direction. Similarly, Fig. 5.13(b) shows the comparison of the transverse displacements before and after projection for a line in the vertical direction. Both of the two selected lines are in the middle of the displacement field: the one for axial displacement is along the x direction (450 pixels in length) and the other for transverse displacement is along the y direction (300 pixel in length).

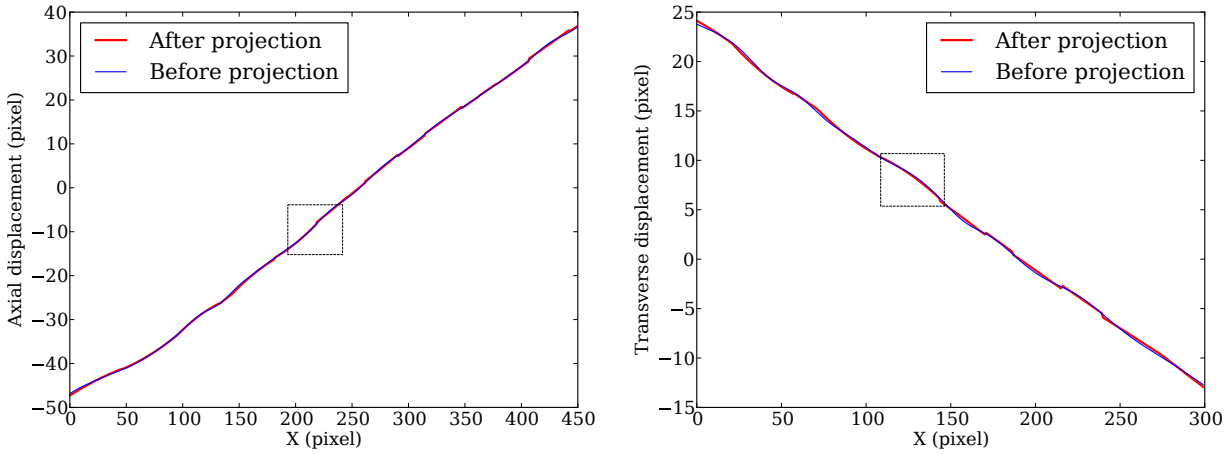

(a) (b)

Figure 5.13: The comparisons of the displacements before and after projection in (a) axial displacement and in (b) transverse displacement

Fig. 5.13 shows that the displacement curves before and after projection are basically overlapped, in which it is difficult to distinguish one from the other. In this case, a local zoom on the illustrated curves was applied. The selected zones for zooming are marked in both Fig. 5.13(a) and (b). And their respective displacement curves after zooming are shown in Fig. 5.14(a) and (b), respectively.

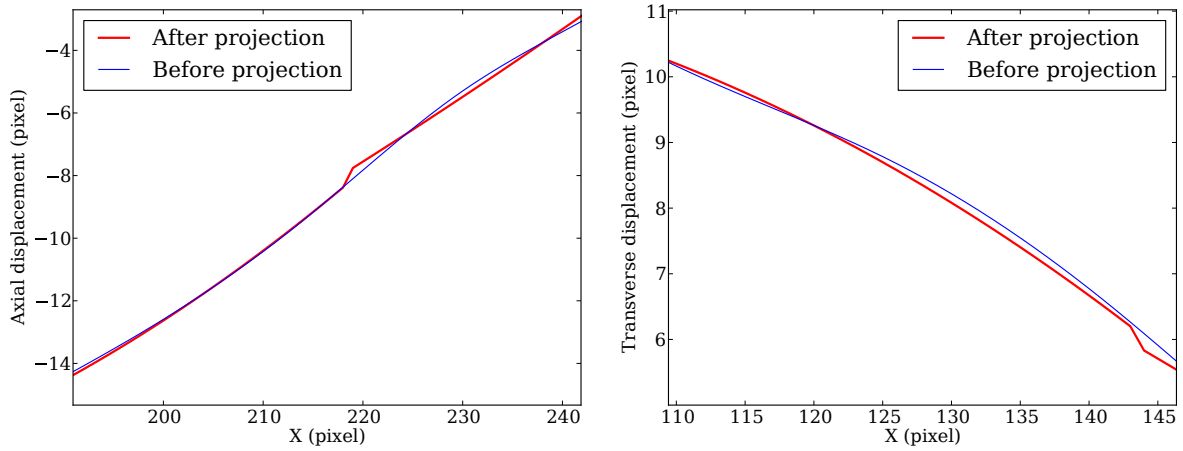

(a) (b)

Figure 5.14: (a) A zoom on the zone marked in Fig. 5.13(a) and (b) a zoom on the zone marked in Fig. 5.13(b)

Fig. 5.14 shows that the displacement variations after projection demonstrates very slight difference to the ones without projection. Nevertheless, some relatively important local variations can still be noticed in the projected displacement curves, which show a local

shift to the initial displacement curve. These local shifts (or discontinuities) are generally corresponding to the location of the slip interfaces, which are a reasonable result by applying the band-based projection approach.

After the analysis dedicated to the final deformation state, a complete verification for the whole deformation history in the tensile test was performed. Each residual image resulted before and after the projection was analyzed, where the average error and standard deviation of errors for each image were calculated. The comparisons of the temporal evolution of the average error and standard deviation of errors before and after projection are illustrated in Fig. 5.15(a) and (b), respectively.

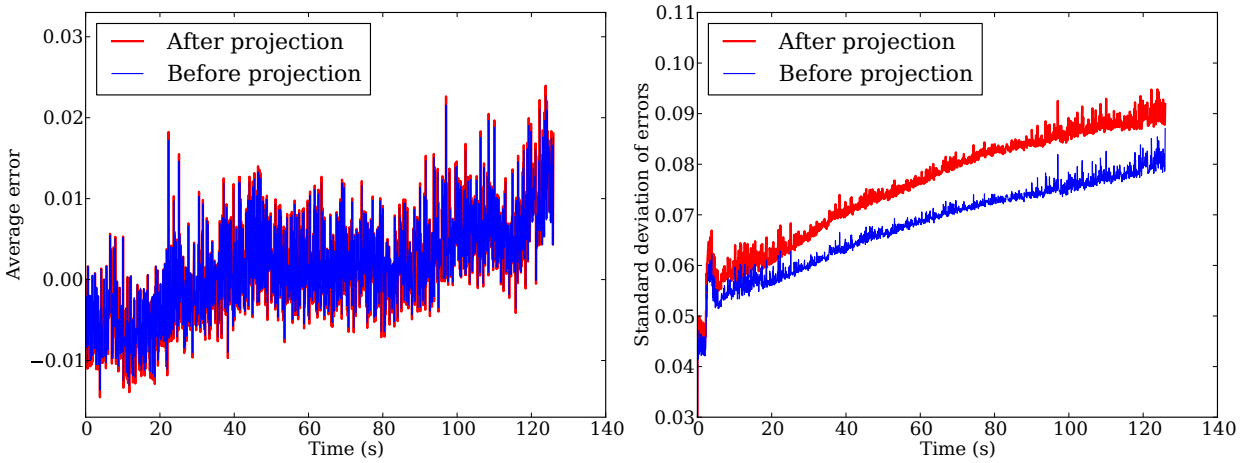

(a) (b)

Figure 5.15: The comparison of the temporal evolution before and after projection in (a) average error and (b) standard deviation of errors

Fig. 5.15(a) shows that the curve of the average error evolution obtained after the projection is quasi fully overlapped with the curve before the projection. For the evolution of the standard deviation of errors before and after projection shown in Fig. 5.15(b), the two curves are really comparable, where the values after the projection show only a little higher in the second half of the curves. Such a raise in spatial dispersion could be due to a more complicated deformation behaviour of crystals at greater deformation levels, such as the activity of the secondary slip bands that are not taken into account in the projection basis. As illustrated in Tab.2, the ultimate error in standard deviation after the projection is about 5.4% higher than the one before projection, which is considered relatively small for the data having processed by an approximation approach.

In conclusion, the approximation approach via projection was validated through the above error analyses. To the present, a complete data treatment strategy on the kinematic measurements has been established. It is a microstructure-based DIC method dedicated to the plastic deformation of single crystals. The obtained strain fields are the central concerns in this work that will be studied in the following sections.

5.2 Macroscopic analysis

Firstly, the main mechanical properties of pure nickel are listed in Tab. 5.3. Some of these parameters are potentially to be used in the relevant analyses in this chapter.

Properties	Parameters
Density ρ	8.908 $g \cdot cm^{-3}$
Thermal conductivity K	90.9 $W \cdot m^{-1} \cdot K^{-1}$
Thermal expansion α	13.4 $\mu m \cdot m^{-1} \cdot K^{-1}$ (25 $^{\circ}C$)
Specific heat C_v	440 $W \cdot m^{-1} \cdot K^{-1}$
Young's modulus E	200 GPa
Shear modulus G	80 GPa
Poisson ratio ν	0.31

Table 5.3: The mechanical properties of the material pure nickel (Oudriss, 2012; Seghir, 2012)

In this section, a macroscopic analysis was conducted for the two concerning tensile tests. Firstly, the shear stress-shear strain curves were derived from the macroscopic stress-strain curves provided by the micro-machine. And then a macroscopic comparison was carried out between the imposed macroscopic strain and the average strain obtained from the kinematic field measurements.

As indicated in the crystallographic analysis of nickel single crystals in chapter 4, the Schmid factor for the 8 equally-stressed slip systems is 0.4. Thus the macroscopic stress-strain (σ-ε) curve given by the micro-machine can be converted to the shear stress-shear strain (τ-γ) curve through

$$\tau = m\sigma,\ \gamma = \frac{1}{m}\varepsilon \tag{5.8}$$

where the Schmid factor $m = 0.4$ and ε represents the longitudinal strain in a conventional engineering definition ($\varepsilon = \triangle L/L_0$).

The obtained τ-γ curves for both Test 1 and Test 2 are illustrated in Fig. 5.16.

Fig. 5.16 shows that the total shear strain imposed on the specimen is 0.54 for Test 1 and 0.59 for Test 2. According to (Oudriss, 2012), at a such shear strain level (higher than 0.3) the specimen would have been experienced all the three work hardening stages with distinctive dislocation structures. This point will be further discussed when combined with

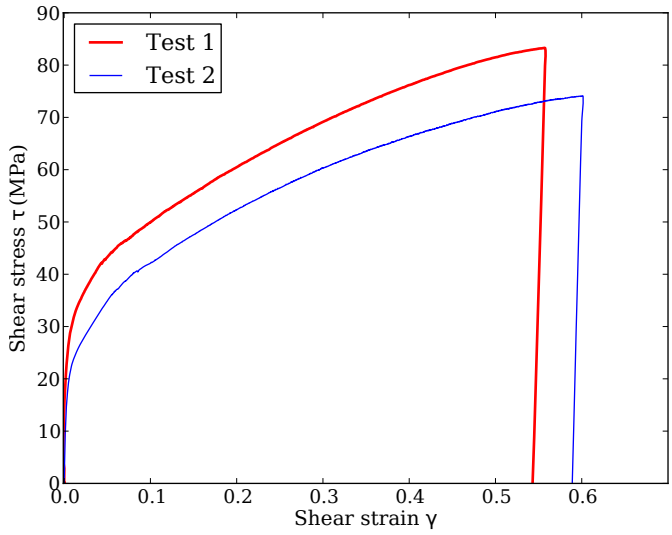

Figure 5.16: The shear stress-shear strain curves for the two tensile tests

the strain field analyses.

A comparison of the two τ-γ curves shows also that the specimen was subjected to higher stresses at a higher strain rate in Test 1 ($2 \times 10^{-3}\ s^{-1}$) than in Test 2 ($0.9 \times 10^{-3}\ s^{-1}$). It demonstrates that the strain rate has an important influence on the mechanical behaviour of nickel single crystals, and consequently on the microstructure evolution.

For an initial macroscopic check on the correctness of the full-field strain measurements, the average strain was calculated for each strain field, and was compared with its temporally corresponding macroscopic strain imposed by the micro-machine. This comparison is illustrated in Fig. 5.17(a) for Test 1 and in Fig. 5.17(b) for Test 2.

Both Fig. 5.17(a) and (b) show that during the tensile test the macroscopic strain given by the machine is always a little higher than the measured value from DIC. This is a reasonable result as the so-called macroscopic strain in this work is evaluated according to the displacement input by the tensile machine but not through a direct measurement, for instance, by strain gauge. In principle, there are mainly two sources of errors. The first error source is that the employed micro tensile machine is not equipped with a servo system, thus the displacement control itself is not of high accuracy. The second error source is related to a general problem of the tensile testing system, as it exists always a small portion of the commanded displacement eventually ascribed to the machine parts apart from the loading specimen. As a consequence, the macroscopic strain given by the tensile machine is generally a little overestimated.

In spite of this reasonable deviation of the macroscopic strain, its evolution is still very comparable to that of the measured average strain by DIC, especially in the first half part of the tensile test. It is also interesting to notice that, the average strain does not show a constant strain rate but is with some important variations at certain points, e.g., around 10 s and 50 s for Test 1, and around 30 s and 120 s for Test 2, as marked in Fig. 5.17. This

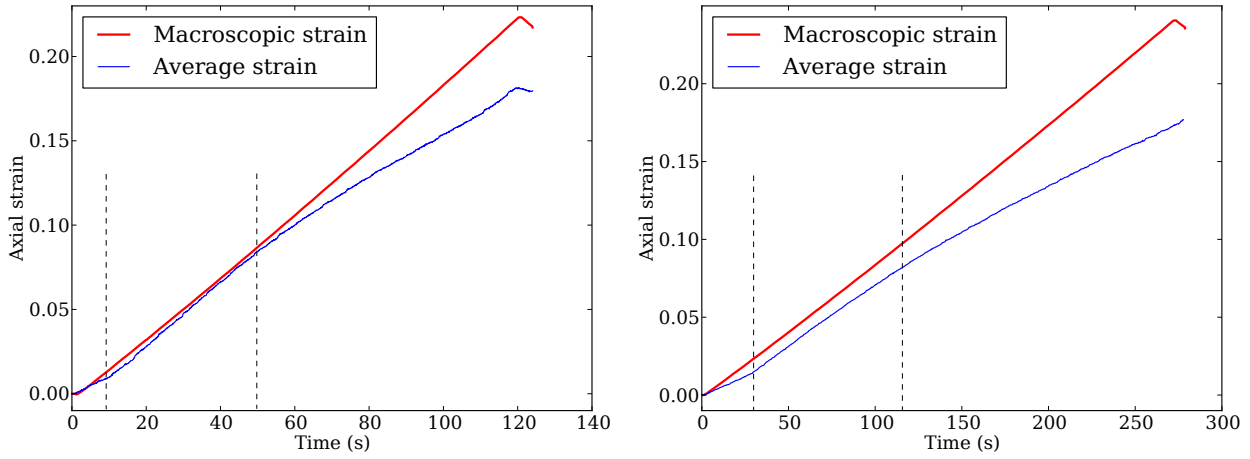

(a) (b)

Figure 5.17: The comparison of the temporal evolution of average strain and macroscopic strain for (a) Test 1 and (b) Test 2

phenomenon is closely linked to the temporal and spatial features of the strain fields, which will be discussed in detail in the next section.

5.3 Strain heterogeneity and work hardening

In this section the strain heterogeneity and its correlation with the work hardening stages in nickel single crystals is studied. As the measured strain fields revealed the strain localizations due to slip activations, in which three distinguishing regimes of deformation evolution can be determined. These three regimes were found closely correlated to the three conventional work hardening stages, and their relationship was attempted to be explained in the framework of the dislocation theory.

This section is unfolded into five parts: 1) introduction, 2) evolution of strain heterogeneity, 3) determination of deformation regimes, 4) microstructure evolution and 5) mechanical interpretation.

5.3.1 Introduction

The deformation behavior of single crystals is comprehensively characterized by the stress-strain curve with three distinguishing stages. Denoted by stage I, II and III, they represent respectively the phases of “easy glide”, “linear hardening” and “parabolic hardening’ (Jaoul, 1965). Since the success of the dislocation theory in explaining the work hardening during plastic deformation, the dislocation structure and its evolutions in different stages have been extensively studied in the past decades (Basinski & Basinski, 1979; Mughrabi, 1983; Kocks & Mecking, 2003; Feaugas & Haddou, 2003). The most common means are through exper-

imental observation of the bulk microstructures thanks to the TEM (Basinski & Basinski, 1979; Feaugas, 1999b), the slip line on the surface observed by optical or SEM (Scanning Electron Microscopy) (Neuhäuser, 1983) and more recently AFM (Atomic Force Microscope) or interferometry (Risbet *et al.*, 2003; Kramer *et al.*, 2005; Zaiser, 2006). They provide the possibilities to observe and characterize the effects of the mobile and stored dislocations on the microstructure evolutions at different scales.

In spite of the significant advances at the microscale and some advanced statistical theories (Zaiser, 2006), the current theories for the quantification of work hardening are still relatively simplified and the predicted results are often found with significant gaps to the reality: the scales transition is often omitted or simplified. As early as in the 1970s Takamura had pointed out that, preoccupied with the dislocation structures, researchers ignored the inhomogeneous nature of deformation and in particular the role of the deformation bands. After a long-term study of his research group (Higashida *et al.*, 1986; Takamura, 1987), they finally confirmed the possibility of explaining in a unified manner the mechanism of work hardening within the framework of the deformation band formation. Indeed their theoretical analysis explains clearly the reason for work hardening from the heterogeneous deformation process, but the only drawback is that their experimental proofs are simply based on surface observations without showing the real-time strain field evolution. This should be attributed to the absence of such a measurement technique at that time. Nowadays the emerging DIC technique provides a powerful tool for full-field strain measurements, with successful applications in polycrystalline deformation (Zhang & Tong, 2004; Seghir *et al.*, 2012) and more recently in single crystal deformation (Florando *et al.*, 2007; Efstathiou & Sehitoglu, 2010). It provides therefore a new occasion to revisit the work hardening problem from the point of view of deformation heterogeneity.

For a better and more straightforward understanding on the strain localization process, a general slip band development history is necessarily to be clarified. The study (Kramer *et al.*, 2005) provides valuable information concerning the multiple slip development in FCC single crystals observed using an in-situ AFM. It proved that three slip development steps were generally experienced: 1) emergence of slip lines, 2) increment of slip density and 3) saturation of slip density and widening of slip bands. This observation is very useful and instructive for the strain field analysis in this study.

5.3.2 Evolution of strain heterogeneity

In this study, an equivalent von Mises strain ε_{eq} was adopted in order to characterize the deformation in each slip plane. Here, the ε_{eq} is defined from the three obtained in-plane strain components (ε_{xx}, ε_{yy}, ε_{xy}) through

$$\varepsilon_{eq} = \sqrt{\frac{2(\varepsilon_{xx}^2 + \varepsilon_{yy}^2)}{3} + \frac{4\varepsilon_{xy}^2}{3}} \tag{5.9}$$

The three in-plane strain components for each acquired image were calculated by the proposed projection method, resulting therefore for each moment a corresponding equivalent von Mises strain ε_{eq}. In this way the evolution of the equivalent von Mises strain during the

tensile test was estimated. Now let us first investigate on Test 1.

Test 1 exhibits three phases with distinctive spatial features in the evolution of the equivalent von Mises strain field. Here the term "regime" is used to represent these strain evolution phases, thus regime I, II and III. The main spatial characteristics for the three regimes are summarized in the following. And for each regime a representative equivalent von Mises strain field is illustrated, in Fig. 5.18(a), (b) and (c), respectively.

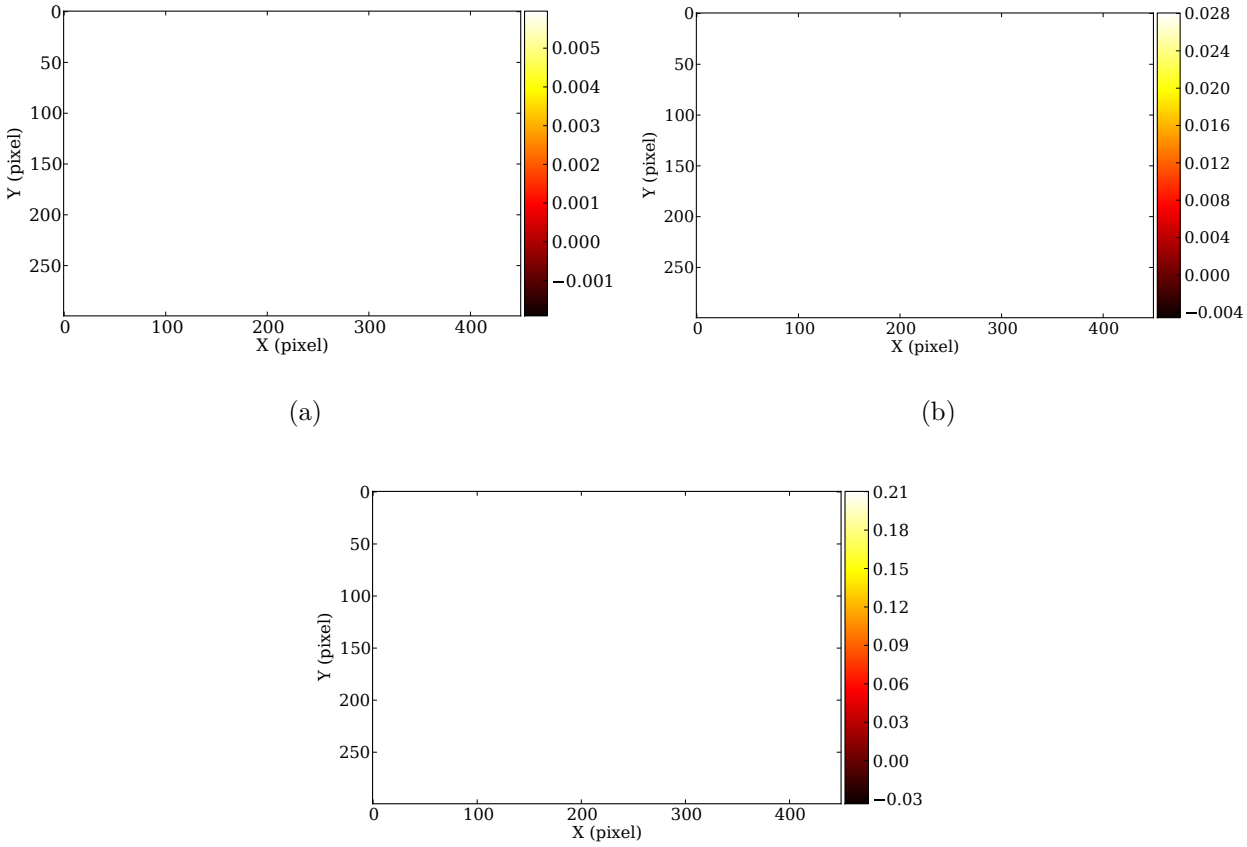

Figure 5.18: The representative equivalent von Mises strain ε_{eq} fields in Test 1 for (a) regime I, (b) regime II, (c) regime III

1) Regime I - Homogeneous deformation regime

The strain field is made of low strain values, in which no special heterogeneities are found associated with slip band activations, as shown in Fig. 5.18(a). Nevertheless, it does not mean that the slip systems are always unactivated, as it is also a problem of measurement resolution. At the current observation scale, the possible influences of the microscopic slip lines on the kinematic fields may not be captured.

2) Regime II - Localized deformation regime

The transition from regime I into II is rather sudden by the emergence of the first strain localization band, while on the same moment the rest of the area keeps still homogeneous, as shown in Fig. 5.18(b). This first emerging slip band shows an equivalent von Mises strain equal to 2.9%, whereas the average ε_{eq} of all the rest 24 bands is only 1.1%, about 38% of the former. From the moment of the first slip band activated, the new bands with elevated strain values emerge in succession until this band formation process terminates.

3) Regime III - Stabilized deformation regime

The spatial pattern of strain fields becomes stabilized in this regime. As shown by Fig. 5.18(c), for the most of the domains the slip bands and interslip zones can be well distinguished as the former exhibits strain values much greater than the latter. It is clear that in this representative strain field the slip bands are generally in yellow color with a strain level from 10% to 21%, while the interslip bands are mostly in red color displaying a strain level lower than 10%. It is also worthy to note that at the end of the tensile test a gradual change can be observed on the stabilized stain pattern. The strain localization bands in certain zones become less organized. This effect is supposed to be related to the activity of secondary slip bands, which become more active and influential to the kinematic field at larger deformations.

The three deformation regimes are, by nature, closely associated with the slip band activations. It is in accordance with the three slip band development steps observed from the exposed material surface in the study (Kramer *et al.*, 2005) for the multiple slip in FCC single crystals. Very similar observations on the three deformation regimes can be found in Test 2. Here for each regime a representative equivalent von Mises strain field is also illustrated, in Fig. 5.19(a), (b) and (c), respectively.

5.3.3 Determination of deformation regimes

A further quantitative analysis was carried out in order to promote a better understanding of the three deformation regimes.

A first concerning is the strain evolution during the slip-dominated plastic deformation, both the strain evolution of slip bands and that of interslip bands. As explained in above description on the deformation regimes, the distinction of slip band from interslip band can be deduced from the strain field by their gaps in strain values as well as their alternate appearing pattern. It is thus interesting to examine their difference in the terms of strain evolution.

For the sake of simplicity, the average strain in each band was used to represent the deformation level of the band. By this means the strain evolution was analyzed band by band, so-called band-based analysis. Concerning first on Test 1, Fig. 5.20 shows the evolution of the equivalent von Mises strain ε_{eq} (in Eq. 5.9) for all the bands involved in the projection basis.

There are 25 bands in total shown in Fig. 5.20. These bands can be classified into two

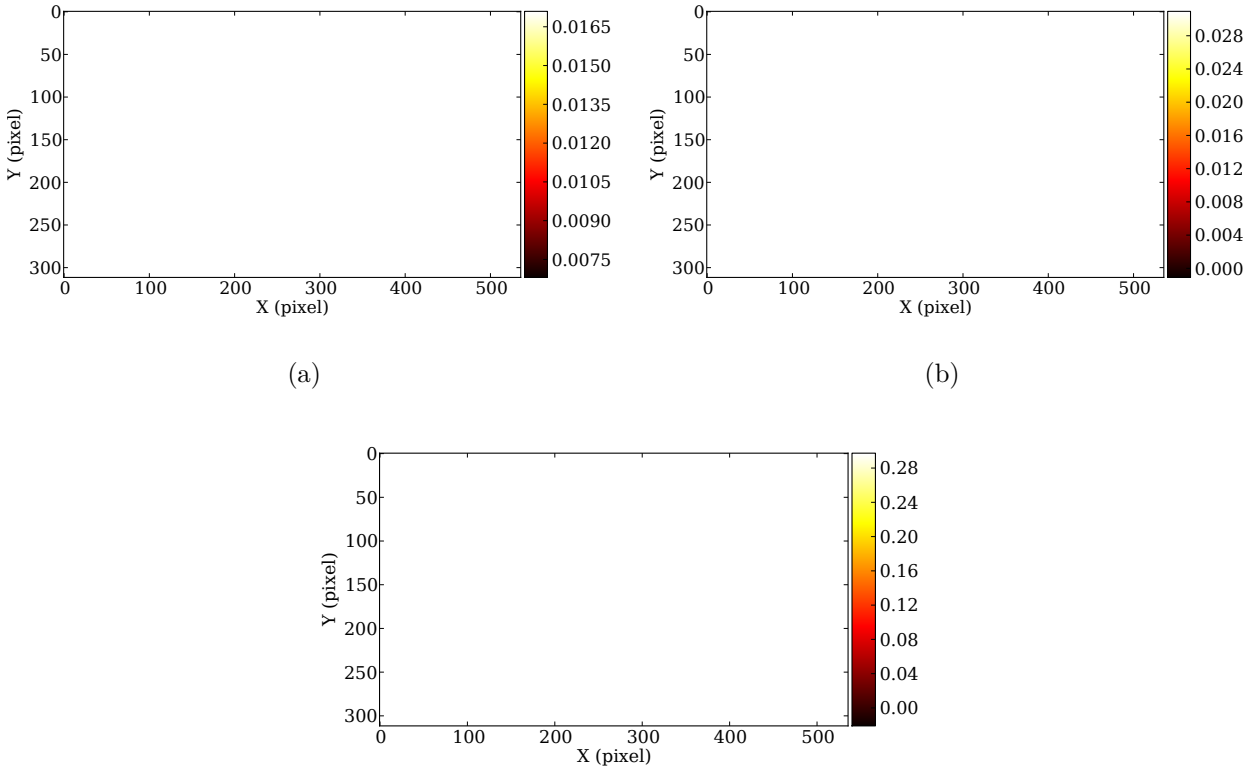

Figure 5.19: The representative equivalent von Mises strain ε_{eq} fields in Test 2 for (a) regime I, (b) regime II, (c) regime III

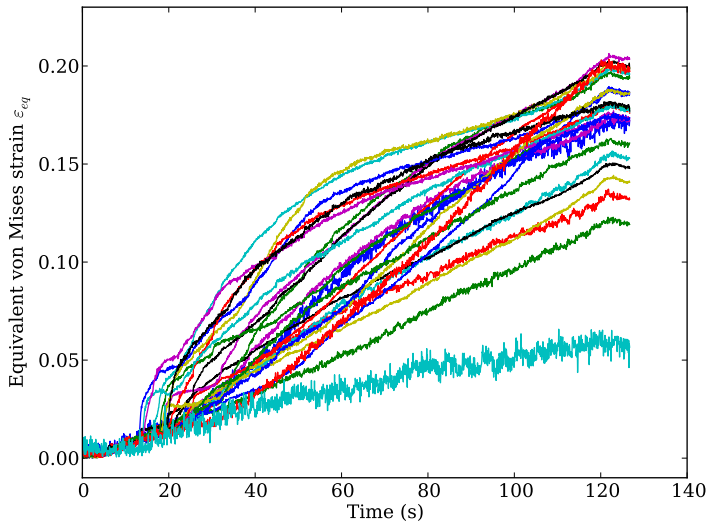

Figure 5.20: The equivalent von Mises strain evolution ε_{eq} for all the 25 bands in Test 1

families according to the existence of a "jump" in the strain evolution. A band in the first family corresponds actually to a slip band on the material surface, which manifests a strain jump once the slip band is activated. Accordingly, a band in the other family corresponds to an interslip band on the material surface that exhibits a monotonous strain evolution without jumps throughout the tensile test. The equivalent von Mises strain evolution of a typical slip band and interslip band is shown in Fig. 5.21.

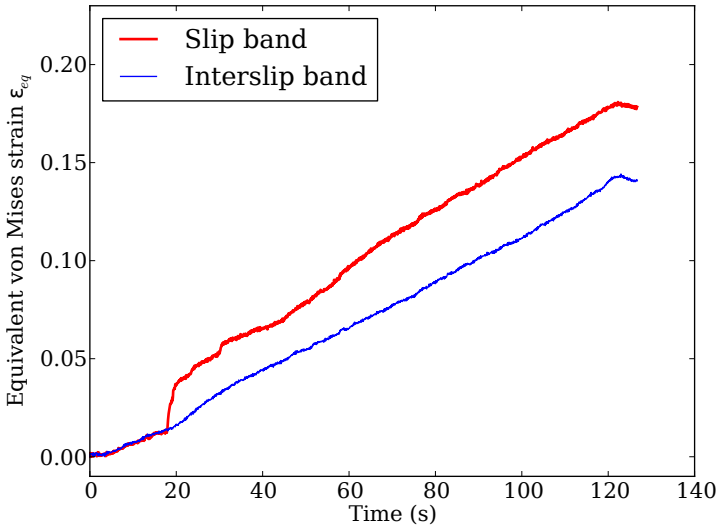

Figure 5.21: The equivalent von Mises strain ε_{eq} evolution for a typical slip band and interslip band in Test 1

Following this temporal analysis, a spatial analysis was also performed by comparing the deformation levels of the bands at the same moment. Here concerning the representative strain fields of the three regimes in Fig. 5.18, their corresponding strain distributions by bands are illustrated in Fig. 5.22, where the x axis i represents a reference number of the band.

Fig. 5.22 shows that a very low and almost equal strain level between different bands characterizes regime I, and then strain tends to be localized in one or certain bands in regime II until a final heterogeneous strain pattern stabilized in regime III. The distinction of the three regimes can be clearly seen in Fig. 5.22. Here more details on the strain evolution trend for each regime are illustrated below.

Fig. 5.23 exhibits the strain evolution trend in regime I, in which three strain curves at different moments (3 s, 6 s , 9 s) are illustrated. It demonstrates that a general low strain level is found in regime I, and the strain in one band does not exhibit a significant difference from that of others. With the time of tensile test, the average strain level increases but the strain distribution pattern remains relatively stable.

The strain evolution trend in regime II can be illustrated in Fig. 5.24, where three strain curves at different moments (11 s, 15 s , 30 s) are displayed. At the moment 11 s, one strain localization emerges in the band 15, which shows much higher strain values than

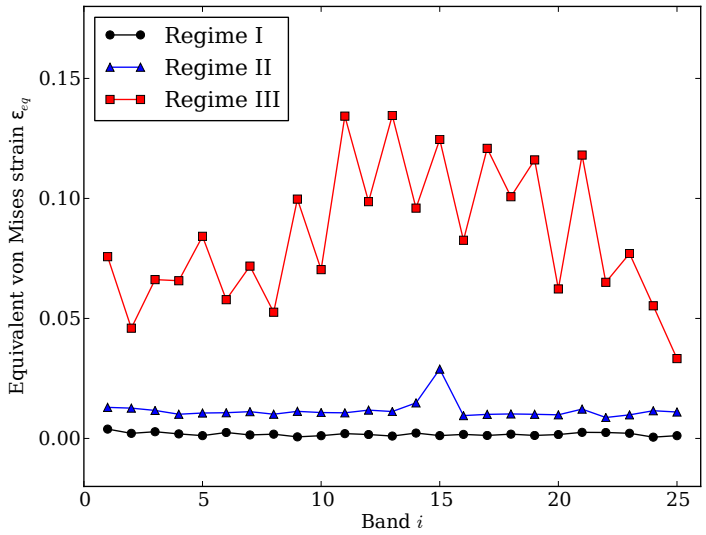

Figure 5.22: The representative curves of strain distributions of bands for the three regimes in Test 1

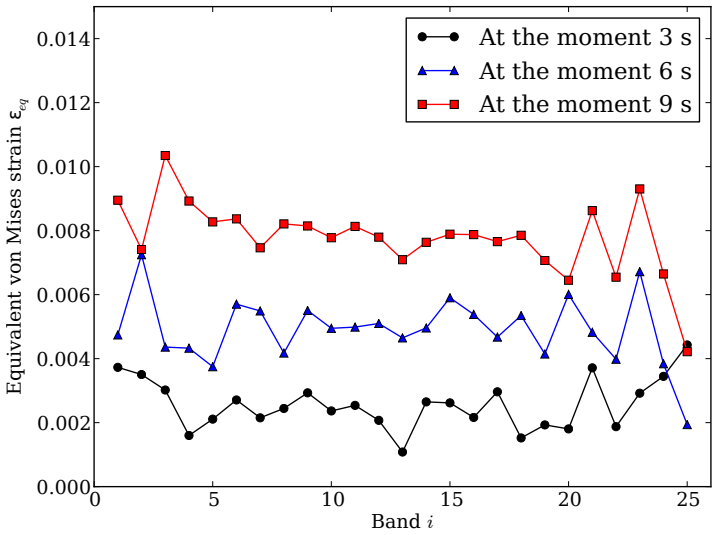

Figure 5.23: The strain evolution trend in regime I

other bands. With the time of tensile test, more bands with strain localization present, as shown by the other two strain curves at the moments 15 s and 30 s. Thus, the regime II can be characterized as a dynamic process with the strain localization phenomenon.

Fig. 5.25 exhibits the strain evolution trend in regime III, in which three strain curves at different moments (60 s, 70 s , 80 s) are illustrated. Apart from their difference in absolute strain levles, the three illustrated strain curves demonstrate a very similar pattern. This indicates that the strain pattern with respect to the band tends to be stabilized in regime III.

The above analysis reveals that the main feature of the three regimes can be characterized in such a simple and straightforward manner. Hence, based on this analysis approach, a

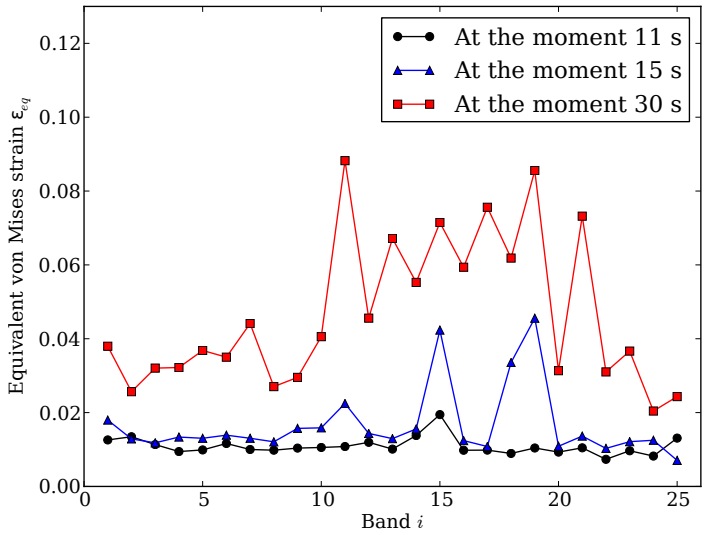

Figure 5.24: The strain evolution trend in regime II

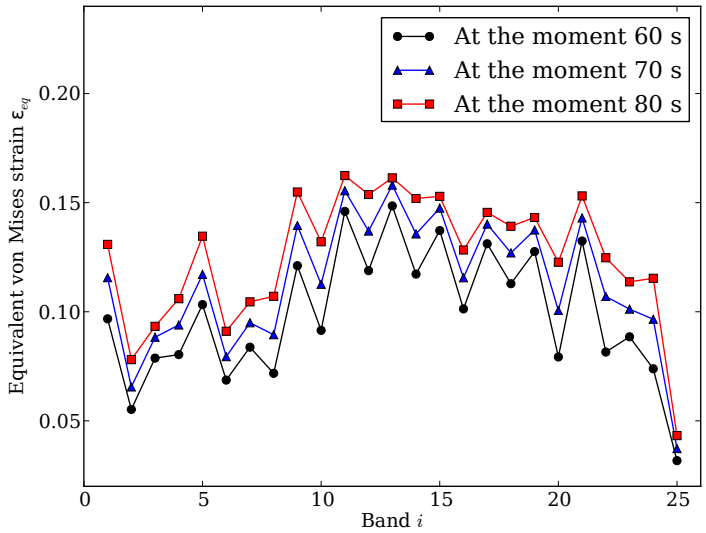

Figure 5.25: The strain evolution trend in regime III

sensitive indicator σ_B was proposed in order to differentiate and determine the three regimes quantitatively. The indicator σ_B represents the standard deviation of strain levels of the N bands, defined for each time t by

$$\sigma_B(t) = \sqrt{\frac{1}{N}\sum_{i=1}^{N}(\varepsilon_{eq}(i,t) - \mu(t))^2} \tag{5.10}$$

and

$$\mu(t) = \frac{1}{N}\sum_{i=1}^{N}(\varepsilon_{eq}(i,t)) \tag{5.11}$$

where i represents the number of the band.

Fig. 5.26 shows the evolution of $\sigma_B(t)$ during the tensile test and a determination of the three regimes which can be characterized by: a quasi-constant in regime I, an important evolution in regime II and a stabilized variation in regime III. It is in accordance to the former descriptions on the three regimes: homogeneous deformation - a low and stable σ_B, localized deformation - a rapidly growing σ_B and stabilized deformation - a high and stable σ_B. Then the boundaries of the three regimes are marked in Fig. 5.26 by the points R_1 and R_2, and with their corresponding macroscopic shear strains γ=5.0% and γ=23.4%, respectively.

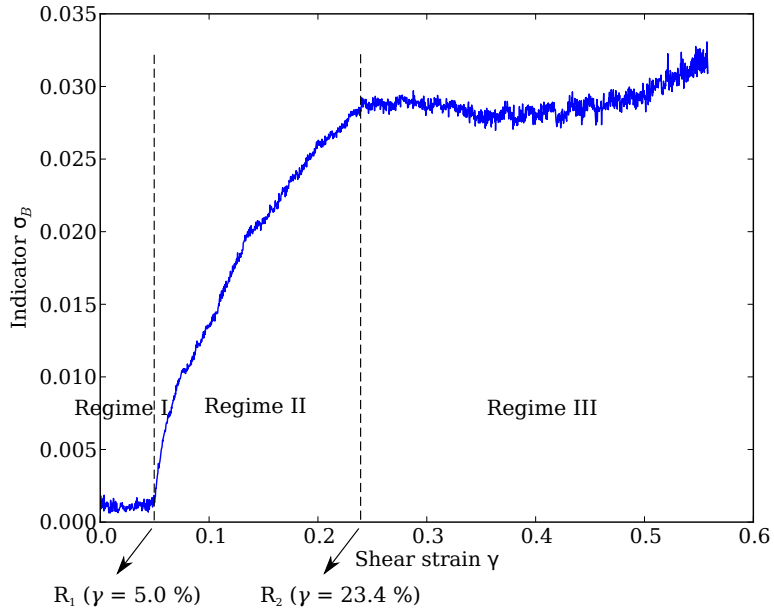

Figure 5.26: The temporal evolution of the indicator σ_B during the tensile test and determination of the three regimes in Test 1

Fig. 5.27 shows the τ-γ curve of Test 1 and the conventional determination on the work hardening stages through τ-θ ($\theta = d\tau/d\gamma$) variations. The boundary between stage I and stage II can be determined without ambiguity, as denoted by S_1 corresponding to a shear strain γ=6.7%. However, the determination of the boundary between stage II and stage III is not that evident, as the θ shows a gradual decrease in the transition from stage II to III. In this case, a reference shear strain range for their delimitation point S_2 is given: S_2=[21%, 27%], as marked in Fig. 5.27.

Fig. 5.26 and 5.27 exhibit that the shear strain range for the three deformation regimes I, II and III are very comparable to that of their corresponding work hardening stages I, II, and III. The difference between R_1 and S_1 is only 1.6%, and the R_2 is within the reference range for S_2. Here it is worthy to note that the accuracy of the traditional method for a quantitative determination of the work hardening stages is limited, especially considering the current noise level of the τ-θ curve. So the genuine gaps between regimes and stages could be even smaller.

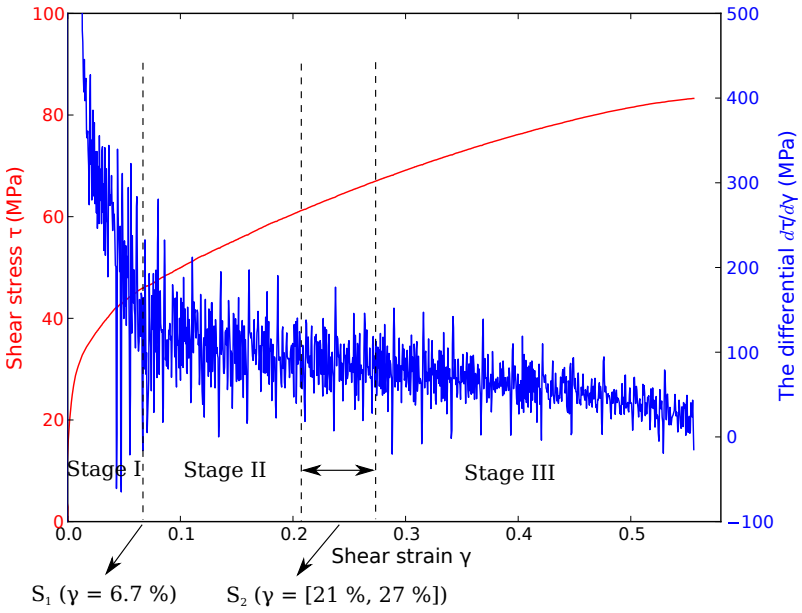

Figure 5.27: The τ-θ curve and determination of the three work hardening stages in Test 1

The same analysis was carried out on Test 2. Fig. 5.28 shows the evolution of the indicator σ_B and the determination on the three regimes. The delimitation point R_1 between regime I and regime II can be determined without any ambiguity, which is given a shear strain value γ=6.5%. However, the delimitation point R_2 between regime II and regime III is not easily determined, as the indicator σ_B demonstrates a gradual evolution in the transition from regime II to III. In this case, a reference range γ=[25%, 35%] is provided for seperating the regimes II and III, as shown in Fig. 5.28.

The τ-γ curve of Test 2 and the determination of the three work hardening stages are shown in Fig. 5.29. The first delimitation point S_1 is determined corresponding to a shear strain γ=8.0%, and the second point S_2 is given by a reference shear strain range S_2=[23%, 30%]. Comparing to the three corresponding deformation regimes, S_1 shows a gap of 1.5% in shear strain to R_1, and the two reference shear strain ranges [23%, 30%] for S_2 and [25%, 35%] for R_2 share a common region [25%, 30%]. It has to be noted that the displayed τ-θ curve has already been smoothed slightly in order to remove the unexpected noises. Even so, under the current noise level the τ-θ curve can not provide an exact determination on the three stages. Nevertheless, on the whole, the division on the three deformation regimes is comparable to that on the three work hardening stages, as presented in both of the two tensile tests.

In view of the high similarity between the three deformation regimes and the three work hardening stages, a relevant mechanical interpretation is necessarily to be given. According to the dislocation theory, the dislocation structure is a key to understand the work hardenging problem. Thus the evolution of dislocation structures in nickel single crystals during the plastic deformation will be introduced before interpreting the intrinsic link between the regimes and the stages.

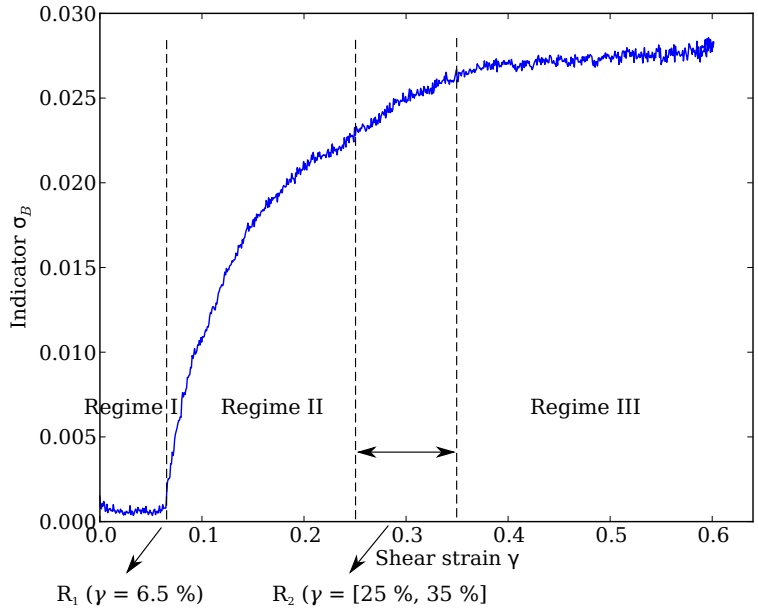

Figure 5.28: The temporal evolution of the indicator σ_B during the tensile test and determination of the three regimes in Test 2

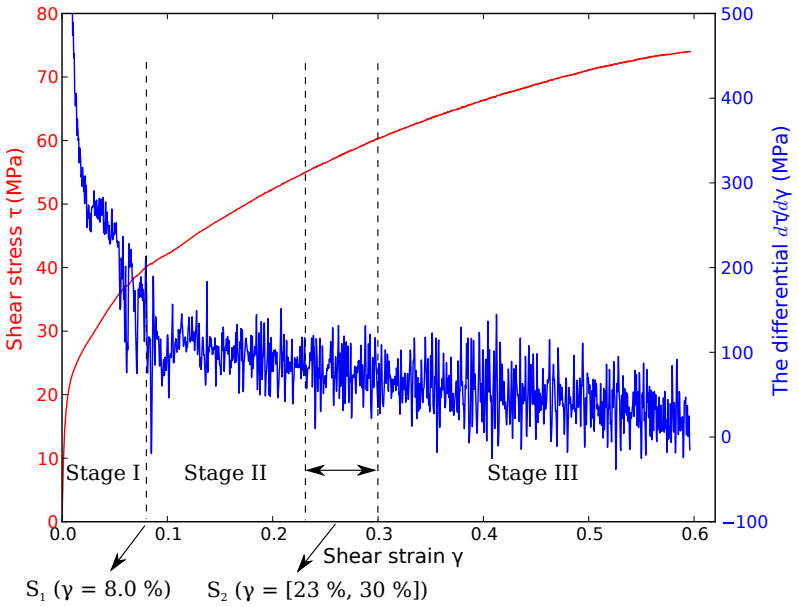

Figure 5.29: The τ-θ curve and determination of the three work hardening stages in Test 2

5.3.4 Microstructure evolution

An introduction has been presented in the bibliographic study concerning the microstructure evolution of nickel single crystals in monotonic tests. Different dislocation structures were observed in stage I (dipoles, multipoles, dislocation pile-ups), stage II (dipole clusters,

Lomer-Cottrell locks, grids) and stage III (disoriented cells) in the works (Oudriss, 2012; Lekbir, 2012). The studied material was the same and under almost the same testing conditions as in this work, except that a lower strain rate was applied in their tensile tests. As known that the work hardening stages of single crystals are generally not dependent on the strain rate (Sevillano, 1993), thus the relevant microstructure observation results in the mentioned works have certain referential values for this investigation.

For a quantitative characterization of work hardening stages, the dislocation density was used as an indicator. As known that the heterogeneous distribution of dislocations can be described as a combination of the "hard" zones of high dislocation density (ρ_w) contained in the cell walls and "soft" zones of low dislocation density (ρ_c) lied in the inter-wall areas (within the cells). It can be schematically illustrated by Fig. 5.30, where λ represents the diameter of the cells and e the thickness of the walls.

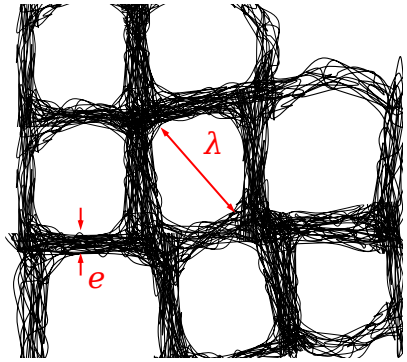

Figure 5.30: A schematic diagram of the hard wall zones and the soft inter-wall zones

A total dislocation density ρ_t can be expressed as

$$\rho_t = f_w \cdot \rho_w + (1 - f_w) \cdot \rho_c \tag{5.12}$$

where f_w represents the fraction of the hard zones, which is given by

$$f_w = \frac{< e >}{< e > + < \lambda >} \tag{5.13}$$

where $<e>$ and $<\lambda>$ represent the average size of the hard zones and of the soft zones, respectively.

Tab. 5.4 summarizes the main characterization parameters of dislocation structures measured at different shear strain levels in the works (Oudriss, 2012; Lekbir, 2012). The dislocation structures were observed using TEM and the determination of the dislocation densities was realized by a statistical method initially proposed by Smith and Gurthman (Hirsch, 1965).

With the data in Tab. 5.4 the dislocation density as a function of shear strain can be illustrated by Fig. 5.31, in which the three different dislocation density terms ρ_w, ρ_c and ρ_t are all involved. The work hardening stage II and III are also marked in the figure, which

γ	$<\lambda>$ (nm)	$<e>$ (nm)	f_w (%)	ρ_w $(10^{12}m^{-2})$	ρ_c $(10^{12}m^{-2})$	ρ_t $(10^{12}m^{-2})$
0%	-	-	-	-	-	1.0
4%	12000	700	6	60	4.0	6.2
11%	2807	401	12	260	15	45
30%	1207	234	18	520	48	120
50%	1000	210	25	950	44	270
70%	980	227	24	900	53	250
83%	770	159	21	850	57	220

Table 5.4: The parameters to characterize the dislocation structure evolution in plastic deformation of nickel single crystals, reproduced from the work (Oudriss, 2012)

shows that the boundary between stage I and II is around 4% and that between stage II and III around 30%. The division on the three stages is close to our results with a reasonable deviation. This verifies the strain rate independence of the work hardening stages in nickel single crystals. More important, Fig. 5.31 reveals that dislocation density experienced an important increment in stage II and then stabilized in stage III during the plastic deformation. It provides a crucial clue for the mechanical interpretation on the deformation regimes and its intrinsic correlation with the work hardening stages.

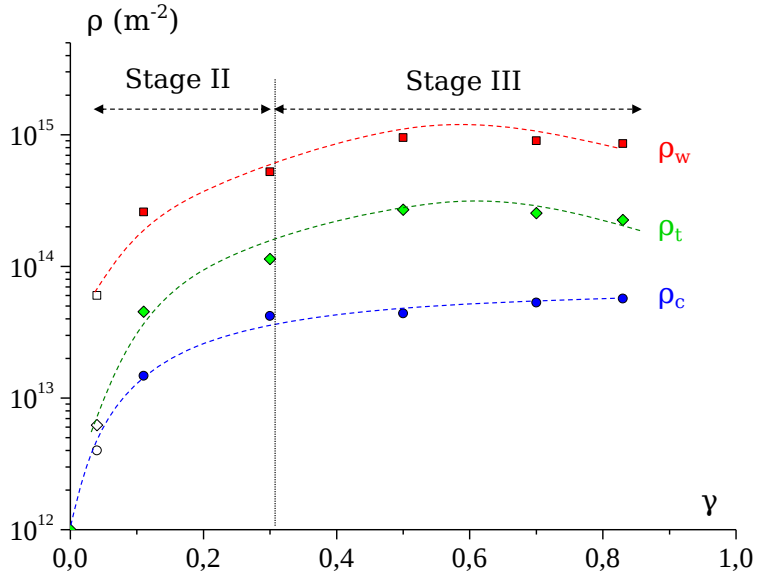

Figure 5.31: The dislocation density as a function of shear strain, reproduced from the work (Oudriss, 2012)

5.3.5 Mechanical interpretation

The proposal of the deformation regimes is expectantly to be exploited in the understanding of work hardening problem of single crystals. Some primary mechanical interpretations have been achieved in this study.

Firstly, the classical defined stage I, the "easy glide" stage, was actually absent for the current case of multiple slip, though the term is still used in this study to refer the initial stage before "linear hardening". Its corresponding regime I can be interpreted as a phase without slip manifestations at a macroscopic scale. Thus it can be understood that in stage I the impact of the slip activations on the macroscopic stress-strain curve has not yet been effectuated, leading therefore to no apparent plastic strain hardening. It is in accordance with the microscopic observations at this stage that few new dislocation sources were generated and the dislocation density did not show an important increment.

In stage II, the linear work hardening is generally understood as an effect of the massive dislocation movements that interact with each other and with barriers on the intersecting slip planes. It was verified in the microscopic observations by the formations of dipole clusters and Lomer-Cottrell locks, and also by the evolution of dislocation density that showed a rapid increment in this stage. Thus, it is reasonable to conclude that the macroscale strain localizations within slip bands emerging in regime II are the kinematic manifestations of the massive dislocations on the material surface. And it is remarked that the continuous strain jump mode band by band and a resulting quasi linear evolution of the strain heterogeneity indicator σ_B coincide exactly with the "linear" hardening characteristic. The indicator σ_B derived from strain fields can be regarded as an "equivalent" to the dislocation density as a sensitive parameter of work hardening.

The final stage III "parabolic hardening" is classically interpreted by the cross-slip effect of dislocations. The relevant mechanical response is a decrement of strain hardening rate due to the stabilized dislocation density, both of which were verified in this study by the macroscopic stress-strain curve and the observation of dislocation structures, respectively. The stabilization of dislocation density in stage III is consistent with the stabilized indicator σ_B in regime III. At this final stage, no more strain jump appeared indicates that no new dislocation source activated.

In the end, a close correlation between the regimes of strain heterogeneity and work hardening stages has been demonstrated. And their intrinsic links were initially established through dislocation theories and were verified by the dislocation density evolution. This study can be considered as a first step to study the work hardening problem of single crystals from the point of view of strain heterogeneity. A further in-depth research is necessary to be carried out in order to clarify the interactions between the dislocation movement and strain localization, and their specific effects on the work hardening process.

The work of Takamura (Takamura, 1987) provides a good example on the perspective study. In his work, the generation and development of "deformation bands" were associated with the dislocation movements, and were considered as the main cause of work hardening. It is important to note that the deformation band is a different concept than the strain localization band in the full-field measurement. The deformation bands are generated in a tensile test due to the lateral constraints of non-gimbaled grips, i.e., the grip effect. And this concept is normally only for the case of simple slip. Thus the theory of Takamura can not applied directly to our work. Nevertheless, the grip effect exists in our tests, and it leads to certain crystal lattice rotations in the plastic deformation. This effect will be studied in the following section.

5.4 Grip effect and crystal lattice rotation

The theme of this section is the grip effect and its resulting crystal lattice rotation in nickel single crystals. Firstly, a general theoretical analysis on the grip effect will be given, and the resulting crystal lattice rotation in nickel single crystals after the tensile tests will be initially verified through the surface observation. Then the problem will be further studied based on the results of full-field measurements.

This section will be therefore unfolded into two parts: 1) theoretical analysis and verification and 2) results of full-field measurement.

5.4.1 Theoretical analysis and verification

As known that single crystals can deform in two different ways. The first is slip on one slip system only at the beginning of deformation, followed by slip on many slip systems. And the second way is that the deformation occurs on many slip systems from the start of deformation. In the first case one slip system has a higher resolved shear stress than any other; in the latter case, two or more slip systems are stressed equally. When deformation on one slip system only occurs, the deformation is known as "easy glide". This portion of the stress-strain curve is characterized by a low and fairly uniform slope. It has been found experimentally that the slope and the length of easy glide of a single crystal are orientation dependent. And this dependence was explained by the grip effect in the work (Hauser & Jackson, 1961) from a purely geometrical point of view. This interpretation can be summarized as follows.

When a single crystal shears on a slip plane, this shear has in general a component on a plane perpendicular to the tensile axis, and the shear component will tend to displace one grip laterally relative to the other. As lateral displacement of one grip relative to another is impossible during a tensile test (for non-gimbaled grips), this shear tendency interacts with the grips to produce a shear stress assumed to be proportional to the shear strain tendency. This shear stress, referred to as total grip effect, can be resolved on all the slip systems. The total grip effect resolved onto the active slip plane, always opposes the applied shear stress and therefore gives rise to a slope of the easy glide. When the total grip effect adds to the applied shear stress on a latent slip system, it will force this system to be activated. When the secondary system activated by the total grip effect forms Lomer-Cottrell locks with the primary slip system, it will terminate easy glide. The total grip effect being orientation dependent, the same is true for the slope and the length of easy glide (Hauser & Jackson, 1961).

The above analysis is consistent with the interpretation of work hardening by Takamura (Takamura, 1987). In his theory, the formation of deformation bands due to grip effect is considered as the termination of easy glide and the onset of the work hardening (stage II). The formed deformation bands can lead to the activation of the secondary slip system and related dislocation structures evolution, resulting in therefore a work hardening effect. To illustrate better the formation of deformation bands and its comparison with the

case of non grip effect, Fig. 5.32 shows the different deformation heterogeneities developed in a single crystal specimen subjected to a simple slip.

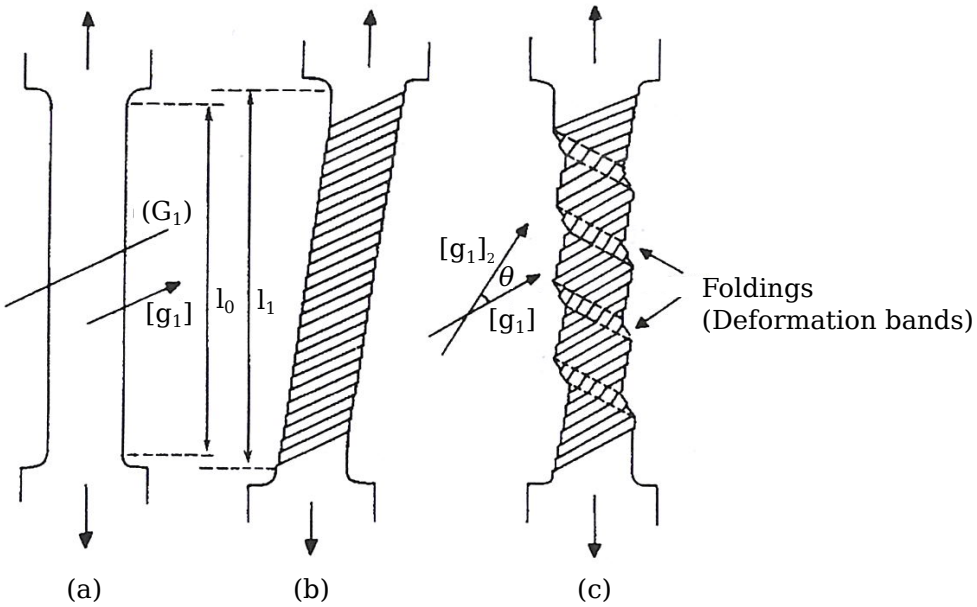

Figure 5.32: The development of deformation heterogeneities of single crystals, reproduced from the work (Jaoul, 1965)

In Fig. 5.32, (a) represents the undeformed state of the single crystal specimen, and (b) and (c) correspond to its deformed states stretched by gimbaled grips and non-gimbaled grips, respectively. In the first case, the formation of deformation bands can be avoided thanks to the special gimbaled grips with a "6 degrees of freedom", which were used in the works (Florando *et al.*, 2006; Lassila *et al.*, 2007). The latter case is the most usual case, where the deformation bands (or kink bands), appearing as the "foldings" on the specimen surface, are developed owing to the lateral constraints of the non-gimbaled grips. The grip effect must lead to a crystal lattice rotation, as the angle θ marked in Fig. 5.32 (c), It is the angle between the slip direction $[g_1]$ (of the primary slip system) in a unrestricted deformation state and the slip direction $[g_1]_2$ occured in a restricted deformation state.

From a purely geometrical consideration, a formula was given in the work (Jaoul, 1965) on calculating the rotation angle θ:

$$\theta = \frac{1}{2} Arctan(sin^2\phi sin\lambda cos\lambda) \tag{5.14}$$

The angle θ can be obtained through the angles ϕ and λ known from the crystallographic structure of single crystals. In this study, ϕ equals to 45° and λ 54.7° as detailed in chapter 4. If it was the simple slip, the angle θ can be obtained as a value of 6.6°.

However, the problem is more complicated in the case of multiple slips than in a simple slip. Concerning our study, 8 potential slip systems in the nickel single crystal have the same Schmid factor and fully symmetric structures with respect to the loading direction.

From a purely geometrical point of view, the 8 slip systems will be equally stressed in the tensile test, and the grip-induced constrains for each slip system will be canceled each other out. As a result, no grip effect will be produced (and so does the crystal lattice rotation). However, it is not what occurred in the present case. The analysis in chapter 4 has already shown that the potential slip systems were not likely stressed equally in the tensile tests and one slip system always tended to be dominated in the plastic deformation. As a consequence, one group of slip markings shows much more pronounced than the other group on the deformed specimen surface. And a visible bending can be found in the deformed specimens, as shown by Fig. 4.11 and Fig. 4.13 for both of the two tensile tests.

Fig. 4.14 shows the angle ϕ (of the primary slip system) in the deformed state is 37° but not the expected 45° for Test 2. It indicates that a crystal lattice rotation took place and the rotation angle θ equals to 8°. It is very close to the predictive value of 6.6° for the case of simple slip. The angle θ was determined from the surface observations based on different image sources and at different length scales (visible camera, microscope, profile map) for both Test 1 and Test 2. The measured θ converges to a small range [5°, 9°], and the average is about 7°. The measurement zones were basically in the center of the specimen surface. Hence, it can be concluded that the global lattice rotation in multiple slips is rather comparable to the predicted one in simple slip. It is therefore interesting to examine the lattice rotation effect via the full-field measurements.

5.4.2 Results of full-field measurements

The rotation ω can be generally obtained through

$$\omega = \frac{1}{2}(\frac{\partial u_x}{\partial y} - \frac{\partial u_y}{\partial x}) \tag{5.15}$$

where u_x and u_y are the two components of the in-plane displacement in x and y directions.

In the present case, as the initial displacement measurements have been treated by the projection method, the above equation has therefore a specific expression:

$$\omega = \frac{1}{2}(\frac{\partial F_u}{\partial y} - \frac{\partial F_v}{\partial x}) = \frac{1}{2}\left[a_2 - b_1 + (a_5 - 2b_3)x + (2a_4 - b_5)y\right] \tag{5.16}$$

The rotation ω was calculated for the two concerned tensile tests, and both its spatial and temporal features were investigated. Firstly, the spatial distribution of ω in the final deformation state of Test 1 is shown in Fig. 5.33.

Fig. 5.33 shows that the field of rotation demonstrates a very similar pattern to other strain components (axial, transverse and shear strains) at the same deformation state (refer to Fig. 5.12). It is thus interesting to examine the temporal evolution of the rotation, especially checking on the existence of the "jump phenomenon" associated with the slip band activation. To do so, the band-based analysis was performed. Fig. 5.34 shows the evolution of ω for all the bands during Test 1.

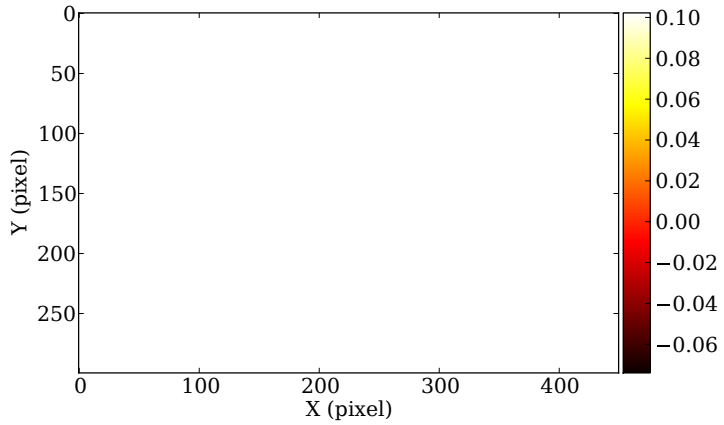

Figure 5.33: The field of rotation ω for the final deformation state in Test 1

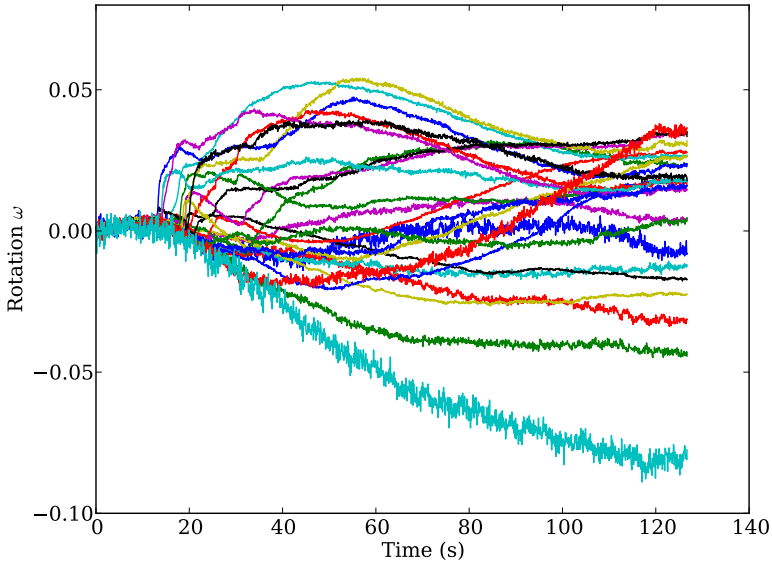

Figure 5.34: The evolution of ω for all the bands during Test 1

About half of the bands in Fig. 5.34 exhibit a jump in rotation at a certain moment during the tensile test. The rest of the bands generally show a monotonic evolution and for some bands with negative values. Here the evolution of the rotation ω is expected to be compared with the evolution of the equivalent von Mises strain ε_{eq}. A specific band was firstly selected for this comparison, and the selected one is a slip band with the first strain jump appearance. The comparison is illustrated in Fig. 5.35.

Fig. 5.35 demonstrates that a jump occurs on exactly the same moment for the rotation and for the equivalent von Mises strain. The same observations were found in other slip bands, and was also confirmed by Test 2. This indicates that the rotation evolves synchronously with the equivalent von Mises strain ε_{eq}. Hence, the proposal and classification of the three deformation regimes are also valid in the evolution of rotation during the plastic

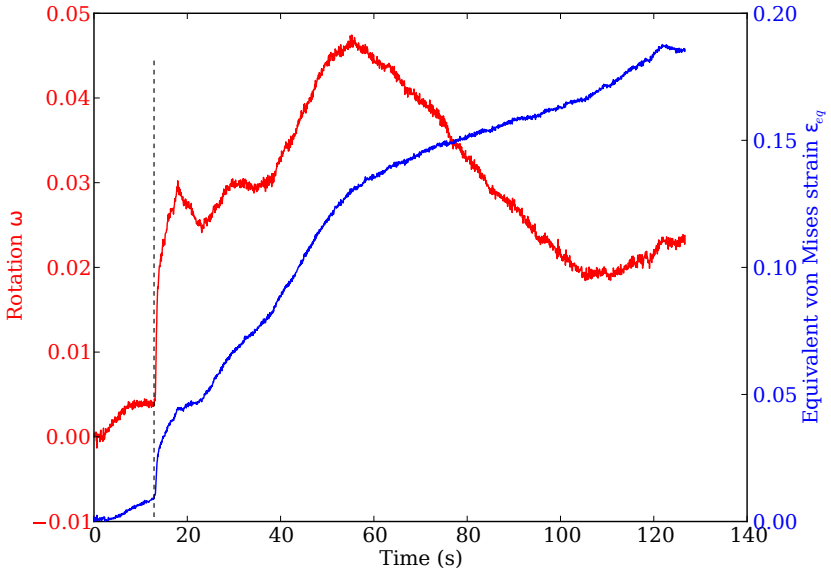

Figure 5.35: The comparison of the evolution of rotation ω and that of equivalent von Mises strain ε_{eq} for a selected slip band in Test 1

deformation of nickel single crystals.

The analyzed strain fields in this study did not demonstrate the existence of deformation band for the case of multiple slips, which is a key concept in the work hardening theory of Takamura. Nevertheless, similar to the deformation band, the crystal lattice rotation is another reflection of the grip effect. The evolution of rotation confirms again that the strain localization (or strain jump) indicates the onset of the work hardening. And the same as Takamura who considers the development of deformation bands is responsible for the hardening stage II (Takamura, 1987), it is characterized in this study by regime II with a deformation localization characteristic.

5.5 Thermal field analysis

As having been studied particularly in chapter 4, the out-of-plane effect influences severely on the thermographic measurement, and thus hinders a quantitative temperature evaluation. Nevertheless, the measured temperature before the emergence of the first slip band, i.e., the out-of-plane deformation, is still valid for conducting a macroscopic thermal analysis in elasto-plastic transition. With the activation of slip bands, the varying emissivity becomes unaccessible, and so the true contribution on the measured "thermal heterogeneities" from temperature is unknown. In such a situation, a flux analysis, replacing the temperature analysis, is expected to be carried out. Hence, two analysis works are involved in this section: 1) macroscopic elasto-plastic transition and 2) flux evolution and slip activation.

Except the out-of-plane effect, another unfavorable situation encountered in this work

is the low level of temperature increment in the tensile tests. For instance, the total temperature increment in Test 1 is lower than 150 mK, the same for Test 2. This result should be first of all ascribed to the very low strain rates applied, which are $2 \times 10^{-3}\ s^{-1}$ in Test 1 and $0.9 \times 10^{-3}\ s^{-1}$ in Test 2. The strain rate in Test 1 was, however, the upper limit of the employed micro tensile machine. It took about 2 minutes for the specimen being deformed 22% longitudinally in Test 1 and near 5 minutes in Test 2 to attain the same level of deformation. So there is no doubt that a great part of the heat generation was lost during the tensile test. And a variation of ambient temperature was even accountable on the temperature evolution of specimen, which was actually the case found in Test 2. Thus, the analysis of this part will be focused only on Test 1, the one with the highest strain rate.

5.5.1 Macroscopic elasto-plastic transition

The macroscopic temperature evolution was obtained by averaging the measured temperature in the ZOI on the specimen surface, and was compared with the shear stress-shear strain evolution. Fig. 5.36 displays the macroscopic shear stress-shear strain curve combined with the temperature evolution with shear strain during the tensile test. Three points A, B and C are labeled on the τ-γ curve which are pertinent to the yield strength of material. A detailed figure focusing on the elastic domain and elasto-plastic transition is illustrated in Fig. 5.37.

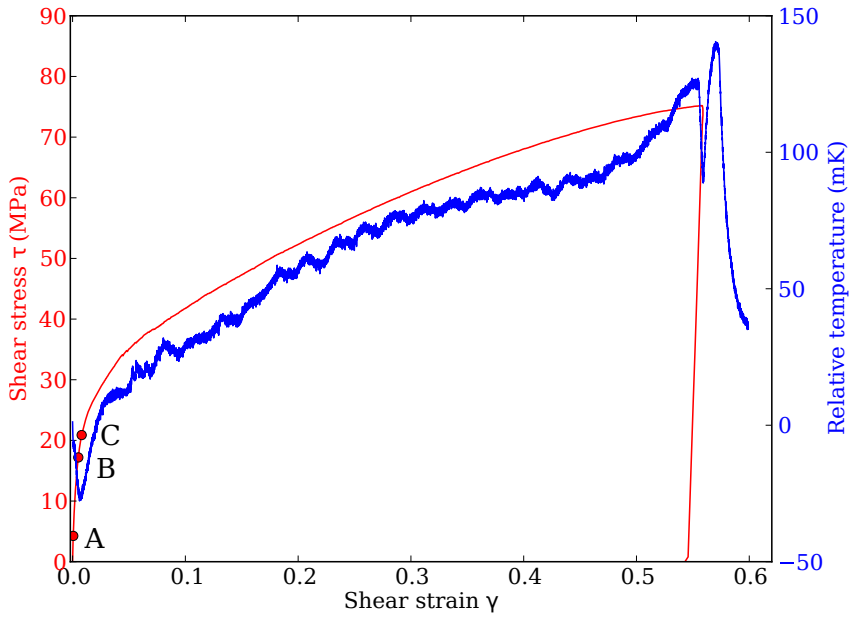

Figure 5.36: Macroscopic shear stress-shear strain and temperature-shear strain evolution during Test 1

In Fig. 5.37, the data points A, B and C are defined and obtained by:

1) Point A - it corresponds to the proportional limit of material. Up to this amount of stress, stress is proportional to strain (Hooke's law), so the stress-strain graph before point

A is a straight line. It was obtained from the experimental stress-strain data by a linear regression through the method of least squares.

2) Point B - it corresponds to the elastic limit of material based on the thermoelasticity. Up to this amount of stress, temperature is supposed to be proportional both to strain and to stress (Eq. 1.20 and Eq. 1.21). In this analysis, it was obtained by applying a linear regression on the temperature-strain data.

3) Point C - it corresponds to the offset yield point $R_{p0.2}$, a term commonly used in the engineering. It was obtained by shifting the determined linear part of stress-strain curve by 0.5% in shear strain, or 0.2% in longitudinal strain according to Eq. 5.8.

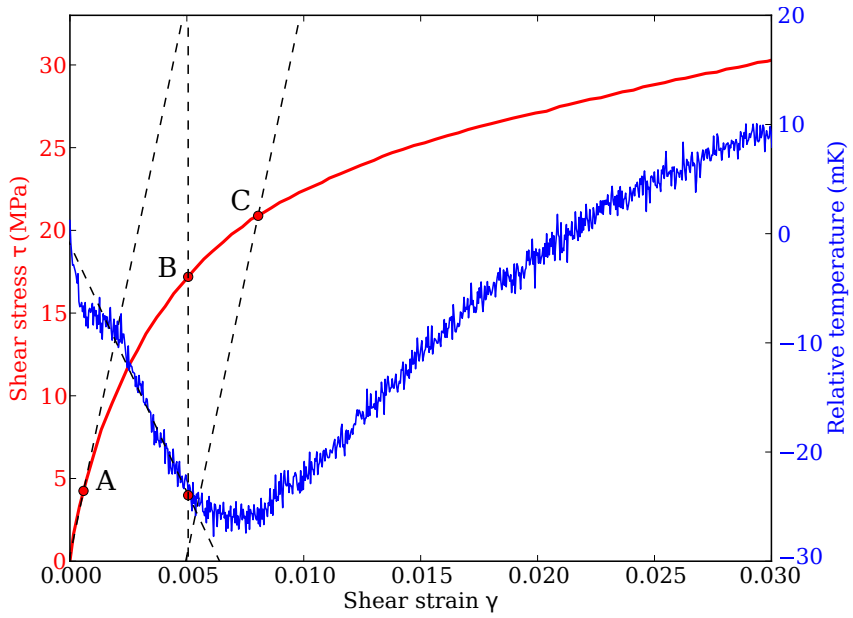

Figure 5.37: Macroscopic shear stress-shear strain and temperature-shear strain evolution focusing on the elastic domain and elasto-plastic transition in Test 1

The values of shear stress, shear strain and relative temperature for the points A, B and C are listed in Tab. 5.5.

Point	Shear stress τ (MPa)	Shear strain γ	Relative temperature ΔT (mK)
A	4.25	0.058%	-7.14
B	17.19	0.506%	-23.96
C	20.88	0.805%	1.65

Table 5.5: The shear stress, shear strain and relative temperature for the three points

Thus, a relationship on the shear stresses of the three points can be obtained:

$$\tau_A < \tau_B < \tau_C \tag{5.17}$$

The results show that the elastic limit τ_B determined from the temperature evolution via thermoelasticity is much higher than the proportional limit τ_A but a little lower than the offset yield strength τ_C. Here it is important to note that the experimental determined elastic limit τ_B in this analysis is only valid for a strain-temperature linearity, which should be reasonably lower than the ideal one that supports a linear relationship between stress, strain and temperature.

Tab. 5.5 shows the temperature variation (or relative temperature) for the elastic limit point B is -23.96 mK, which is considered as the experimental value of ΔT_{lim}, the maximum elastic variation of temperature. ΔT_{lim} can also be evaluated through shear stress τ_B (or its corresponding axial stress σ_B) based on the thermoelasticity:

$$\Delta T_{lim} = -T_0 \frac{\alpha}{\rho C_v} \sigma_B = -T_0 \frac{\alpha}{\rho C_v} m \tau_B \tag{5.18}$$

where the parameters α, ρ and C_v of pure nickel are listed in Tab. 5.3, the initial temperature T_0=24.57 K and Schmid factor m=0.4.

The evaluated ΔT_{lim} is -197 mK, much greater than the measured -23.96 mK in absolute values. This important deviation is probably due to the very low strain rate applied in the tensile test and the possible heat exchanges with the environment. As the basic assumption for the above thermoelasticity equation is to satisfy an adiabatic condition and having a strain rate high enough to neglect the heat conduction effects. Hence, Eq. 5.18 is actually not applicable to the real case of our test.

Another concern in this work is to compare the elastic limit determined by thermoelasticity (τ_B) with the CRSS (Critical Resolved Shear Stress) of single crystals. The CRSS is the value of resolved shear stress at which yielding begins. In a microscopic point of view, the CRSS or "microscopic flow stress", τ_c, is the resolved shear stress to be applied in order to sustain the long-range propagation of dislocations under the superposed effects of all coexisting structural features, which represent obstacles of differing strengths resisting dislocation glide (Sevillano, 1993).

A precise estimation of CRSS for a given crystal is still a challenge issue. Firstly, it is orientation dependent, e.g., the τ_c needed for activating a simply slip is considerably lower than that for activating a multiple slip under the same other conditions (Hauser & Jackson, 1961). Secondly, it strongly depends on the microstructure details within the crystal, such as point defects, extraneous atoms in solution, dislocation density and second phases. For instance, the CRSS of pure nickel is reasonably lower than that of nickel alloys. Actual values of the CRSS of real materials range between two absolute bounds. The upper bound is represented by the "ideal strength" for a shear collapse of the perfect lattice, τ_i. The lower bound, by the Peierls-Nabarro stress, τ_p, the stress for dislocation glide in the absence of any other lattice imperfection. Any kind of obstacle to dislocation movement raises the flow stress above the unavoidable Peierls-Nabarro stress (Sevillano, 1993).

According to the theoretical estimations in (Macmillan, 1983; Kelly & Macmillan, 1986), the resolved shear stress τ_i for homogeneous crystallographic slip, i.e., elastic collapse of the lattice, is a high fraction of the elastic shear modulus:

$$G/30 \leq \tau_i \leq G/10 \tag{5.19}$$

The shear modulus of the studied nickel is 80 GPa (Oudriss, 2012), so τ_i has a value

$$\tau_i = 2.7 \sim 8.0 \text{ GPa} \tag{5.20}$$

Thus, the ideal critical flow stress τ_i is two orders higher than the predicted CRSS τ_c ($=\tau_B$=17.19 MPa) based on thermoelasticity. Regarding the classical Peierls-Nabarro stress τ_p, it can be estimated according to (Nabarro, 1967; Hirth & Lothe, 1968) via

$$\tau_p/G = [2/(1-\nu)] \exp(-2\pi w/b) \tag{5.21}$$

with w the dislocation width, $w = h/(1-\nu)$, h being the lattice spacing of the glide plane and ν the Poisson's ratio.

The parameter h/b for FCC metals measured in the experiments is about 1.4 (Takeuchi & Suzuki, 1989), and the Poisson's ratio for nickel is 0.31, so the Peierls-Nabarro stress τ_p can be evaluated:

$$\tau_p = 8.4 \times 10^{-6} G = 0.67 \text{ MPa} \tag{5.22}$$

The estimated lower bound of the critical flow stress τ_p is about two orders lower than the predicted CRSS τ_c based on the thermoelasticity of material, thus the relationship

$$\tau_p < \tau_c (= \tau_B) < \tau_i \tag{5.23}$$

is valid for the nickel single crystal deformation in this study.

This result shows the CRSS of a given crystal may vary exceedingly great depending on the substructure and microstructure within the material, and the thermographic measurement can provide a relatively simple way to evaluate the CRSS.

5.5.2 Flux evolution and slip activation

With the transition into plastic domain and especially after the macroscopic slip bands emergence, the temperature measurement is no longer dependable. Thus, an analysis based on radiative flux was adopted in this work.

From the thermographic measurement, the evolution of the average radiative flux in the ZOI was calculated and used to compare with the macroscopic shear stress-shear strain curve, as shown in Fig. 5.38. The three deformation regimes, obtained through the kinematic field analysis, are also labeled in this figure.

In the strain field analysis, the starting point of regime I was generally considered as the onset of plastic deformation but was not determined with a specific value in macroscopic

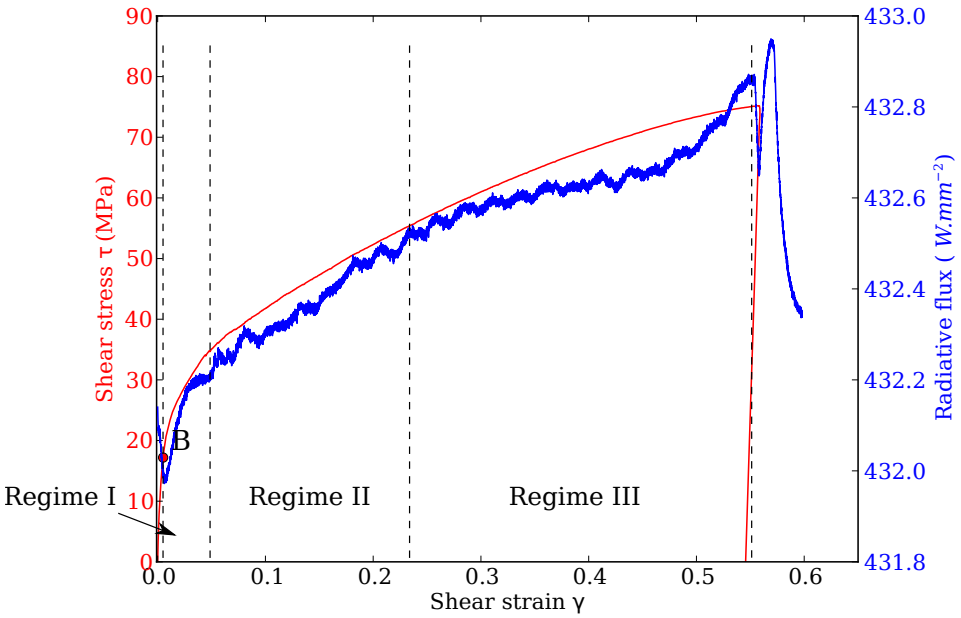

Figure 5.38: Macroscopic shear stress-shear strain and average radiative flux-shear strain evolution during Test 1

shear strain. Here the point B, the elastic limit determined from thermoelasticity, can be considered as a reference for the starting point of regime I. Besides, it can be also noted in Fig. 5.38 that in the unloading process, the thermoelasticity embodies by a rapid increment in radiative flux. It is however also noticeable that a fall in flux exists before its rising, which is owning to the fact that there was a short pause of the tensile machine (about 0.5 s) before the unloading.

Here a main concerning on the flux evolution is its connection with slip band activations. For a close observation, a local zoom of Fig. 5.38 focusing on the regime I and II is illustrated in Fig. 5.39. The circles labeled on the τ-γ curve correspond to the moments with the strain jump phenomenon (or strain localization within a certain band), which is considered as a signal of the slip band activation. In Fig. 5.39, it can be also observed from the flux evolution that certain flux "jumps" (important local increments) are present. It is thus interesting to compare the strain jumps with the flux jumps.

Fig. 5.39 shows that for the first four slip band activations, there is a sudden increment (or jump) in flux after each slip band activation, with a very short delay or without delay. These flux jumps are suspicious due to an increment of plastic deformation energy by the slip band activation. However, for the last four slip band activations shown in the above figure, they are not accompanied with flux jump phenomenon, and on the contrary their fluxes are in a decrease evolution trend. Actually, such flux jumps can be also observed in regime III, the stabilized deformation regime without new slip band activations, as shown in Fig. 5.38. So for the flux jumps not accompanied with slip band activations, these wave-like heat evolution are probably due to the heat exchange with the ambiance during deformation, since a very low strain rate was applied in the tensile test (adiabatic condition unsatisfied).

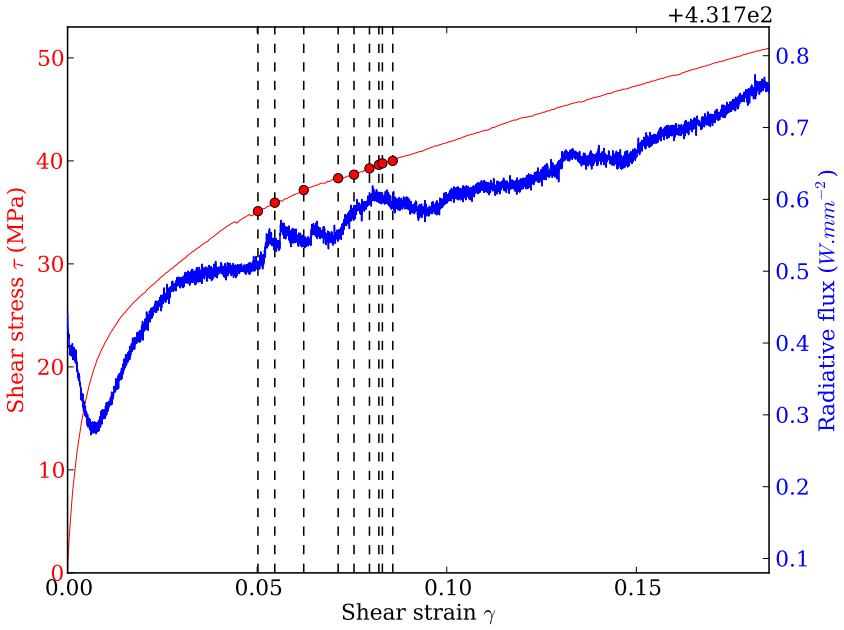

Figure 5.39: Macroscopic shear stress-shear strain and average radiative flux-shear strain evolution focusing on the regime I and II in Test 1

5.6 Conclusion

A thorough kinematic field analysis of nickel single crystals has been carried out in this chapter, complemented with a thermal field analysis at the end of this work.

Firstly, a crystallographic-based data treatment strategy on the kinematic field measurement had been developed dedicating to the plastic deformation of single crystals. The developed methodology enabled to identify the displacement discontinuities associated with slip systems activation and a proper access to the strain fields through a projection approach. Before going into the strain fields, the macroscopic mechanical behaviour of nickel single crystals was demonstrated, and the kinematic measurement results were initially verified by comparing the axial strain evolution at a global level.

The emphasis of this work was placed on section “strain heterogeneity and work hardening”. The study showed that three deformation regimes can be determined from the strain field evolution, namely the homogeneous deformation regime, the localized deformation regime and the stabilized deformation regime. And they were assumed to be corresponding to the three conventional work hardening stages, i.e., “easy glide”, “linear hardening” and “parabolic hardening”. Indeed, a temporal correspondence was validated for each regime-stage pair even with a slight deviation. The intrinsic link between the deformation regimes and hardening working stages was interpreted through the dislocation theory, and the interpretation was supported by the dislocation density evolution from the microstructure

observations. This study revealed that the mechanism of work hardening is hopefully to be investigated from the point of view of strain heterogeneity.

A following section was concerned with the grip effect and the consequent crystal lattice rotation. A general introduction on the grip effect was first given. And concerning the specific crystallographic structure of the studied nickel single crystal specimen, the possible lattice rotation in the tensile test was evaluated and was verified via the surface observations. An analysis of full-field measurements was also conducted. It showed that the evolution of lattice rotation, as an indicator of the grip effect, was synchronous with the evolution of plastic strain. This result supports the proposal of the three deformation regimes, and is therefore helpful for a further understanding on the work hardening mechanism of nickel single crystals.

A thermal field analysis was carried out in the last section. Firstly, the elastic limit was determined through the temperature evolution of material based on the thermoelasticity. The results show that it is higher than the proportional limit but lower than the offset yield point obtained from the macroscopic stress-strain curve. When comparing to the CRSS estimated from the dislocation theory, the measured elastic limit is found within the scope of prediction. Then in the plastic region, the flux evolution of material was examined by being related to the slip system activation. It shows that for certain slip bands when they are activated with strain jumps, their fluxes demonstrate corresponding jumps. While for other slip band activations, they are not necessarily accompanied with flux jump phenomenon. An explanation for the latter is that as an adiabatic condition is not satisfied in our tests, these flux jumps are possible due to the heat exchange with the ambiance during deformation. Nevertheless, a definite conclusion can not be easily drawn from the available experimental data in this work.

A common problem in the thermal analyses is that an expected adiabatic experimental condition is not satisfied subjected to a low strain rate applied in the tensile tests. This unfavorable factor greatly discouraged our initiatives for a quantitative temperature measurement and then for a further study on building an experimental energy balance on the microstructure scale. In a perspective work, an adiabatic experimental condition is expected to be better satisfied. This is possible to be achieved by two ways. First, the test is preferred to be carried out in a vacuum environment. Second, a higher strain rate is anticipated to be applied in the tensile test. These solutions enable approaching to an adiabatic experimental condition, assuring therefore a more reliable temperature measurement.

Conclusion and perspectives

This thesis work was proposed for a better understanding of plastic deformation in oligo- and single crystals through kinematic-thermal full-filed measurements. There are mainly two interests involved in this research proposal. The first interest is the experimental energy balance that is anticipated to be built at the microstructure scale based on kinematic-thermal fully-coupled measurements. And the second interest is the strain/energy evolution during plastic deformation of oligo- and single crystals, which is expected to be characterized and exploited in understanding better the micromechanism of crystal deformation, such as the work hardening phenomenon.

In order to fulfill the above research objectives, an adaptable measurement system was necessarily to be built first of all. It was basically made of two parts: IRT for thermal measurement and DIC for kinematic measurement. A metrological study was carried out for both of the two techniques, in which the main achievements involved are:

1) A complete calibration procedure for realizing QIRT had been established, which took into account of the most important factors in a thermographic measurement, including non-uniformity correction, integration time selection, emissivity measurement, etc.

2) An in-plane DIC measurement system had been built up. Relevant algorithms for executing DIC computation were developed in elastix, and its performance for displacement measurement and strain assessment was tested through an experimental error analysis.

A subsequent step was the coupling of the two measurements, both spatially and temporally. To do so, the two-face measurement technique was first chosen as the solution for realizing such a kinematic-thermal fully-coupled measurement. Then the reference targets were developed in order to solve the spatial matching problem of IR/visible images, and a multi-trigger was adopted for actualizing simultaneous measurements.

Tensile tests for aluminum oligocrystal and nickel single crystal were conducted respectively, being combined with the kinematic-thermal fully-coupled measurements. One of the most remarkable phenomena for the plastic deformation at such grain and subgrain scales was the out-of-plane deformation, such as the intrusions/extrusions at grain boundaries in oligocrystals and slip band markings in single crystals. Our study showed that the out-of-plane deformation could induce a particular influence on the thermographic measurement, affecting therefore its measurement accuracy severely, so-called the out-of-plane effect. This problem was studied in this work for both of the two materials concerned, and the emphasis was placed on the nickel single crystal.

The out-of-plane effect is an assembly of several phenomena, among them the apparent emissivity variation due to the alteration of angle of incidence (by the out-of-plane deformation) was considered as the dominant factor. Then the emissivity map was managed to be related to its corresponding surface profile of deformed specimen, in order to confirm its geometrical dependence. Such a comparison analysis was carried out for nickel single crystals, which showed that a general correlation can be found between the emissivity distribution and profile variation: the apparent emissivity decreases with the increment of profile variation. Though the out-of-plane effect has been verified and clarified, its resulting errors in thermographic measurement is still difficult to be eliminated, as the variation of apparent emissivity (or profile) was not accessible in our tests. Similar results were found in the analysis of aluminum oligocrystal deformation. The obtained thermal fields were strongly affected by the effect of out-of-plane deformation.

In spite of the out-of-plane effect, a thermal field analysis for nickel single crystals was carried out. In the unaffected elastic region, the temperature evolution was used for the determination of elastic limit. It was verified within the reasonable range of CRSS predicted via dislocation theory and higher than the macroscopic proportional limit. In the following plastic region with the presence of out-of-plane effect, an analysis on the radiative flux evolution was conducted. It showed that some slip band activations were companied with flux jumps but others were not. Then another explanation for the appearing flux jumps was due to the heat exchange with the ambiance during deformation which led to the wave-like heat evolution. Nevertheless, no definite conclusion was drawn on this issue in this work.

A major problem encountered in the thermal analysis is that an expected adiabatic experimental condition was not satisfied in our tests, mostly owing to a very low strain rate applied. Plus the out-of-plane effect, they greatly discouraged our initiative for a quantitative temperature measurement and to take the thermal evolution as an indicator of microstructural change. Hence, the initial objective for building an experimental energy balance has to be abandoned. Then our research attentions turned to focusing on the kinematic field analysis in nickel single crystal deformation.

The first contribution on the kinematic field analysis dedicated to single crystal deformation is the proposal of a crystallographic-based data treatment strategy. The developed methodology enabled to characterize the displacement discontinuities associated with slip band activations, and provided a proper access to the strain fields through a projection approach. Thanks to this technical development, the strain field evolution can be characterized in connection with the slip activation and development during deformation.

A major contribution of this study is the proposal of the three deformation regimes and its correlation with the three conventional work hardening stages. The kinematic field analysis showed that three deformation regimes can be determined from strain field evolution during deformation, namely regime I - homogeneous deformation regime, regime II - localized deformation regime and regime III - stabilized deformation regime. Their one-to-one correspondence to the three macroscopic work hardening stages I, II, and III was verified in both of the two tensile tests analyzed. The intrinsic link between regimes and stages was interpreted based on dislocation theory, and this interpretation was supported by the relevant microstructure observations, such as the evolution of dislocation density. For a further

understanding, the experimental boundary condition, i.e., the grip effect, was also investigated. The kinematic field measurements demonstrated clearly the heterogeneous lattice rotation of crystal during deformation, which was coherent with the plastic strain evolution pattern. In brief, this work shows that the mechanism of work hardening is hopefully to be better understood from the point of view of strain heterogeneity.

This thesis study revealed some basic features of plastic deformation at the microstructure scale, and demonstrated the unique advantages of applying kinematic-thermal full-field measurements to the relevant experimental studies. Some perspectives are proposed here for more further works to follow this very promising research line:

1) Towards an accurate temperature measurement by IRT in case of nonnegligible out-of-plane deformation, an appropriate technique for in-situ profile measurement during tensile test is desired. It is possible to be realized by incorporating the tensile machine with the interferometric profilometer testing stage. Besides, a more quantitative emissivity-profile relationship is necessarily to be established, which enables emissivity evaluation from the profile measurement during the test. This necessitates to join the emissivity measurement in the above testing system, so as to determine the emissivity-profile relationship from the emissivity-profile coupled measurement data in a tensile test.

2) As the origin of the unexpected out-of-plane effect in optical measurements, the out-of-plane deformation is hoped to be obviated or at least limited. A practical solution for oligocrystal is to enhance the thickness of specimen. And for single crystals, the slip planes of potential slip systems are expected being parallel to the specimen surface, so as to avoid their intersections on the specimen surface (slip band markings). For FCC single crystals, it is possible only for the case of simple slip, e.g., for $[\bar{1}49]$ oriented single crystal with specimen surface in the (111) slip plane (Mecke *et al.*, 1982).

3) An adiabatic experimental condition is expected to be better satisfied in a perspective test. It can be achieved by two ways. First, the test is preferred to be carried out in a vacuum environment. Thus, a vacuum equipment should be developed and incorporated with the kinematic-thermal measurement system. Second, a higher strain rate is anticipated to be applied in the tensile test. It is hopefully to be achieved by employing more capable tensile machines equipped with adapted grips for the single crystal specimen. These solutions enable approaching to an adiabatic experimental condition, assuring therefore a more reliable temperature measurement.

4) The study of the work hardening problem from the point of view of strain heterogeneity is expected to be carried forward. For instance, a multi-scale experimental measurement is strongly encouraged, and other microstructure observation techniques, such as TEM, SEM and AFM, are also favorable to be integrated. Besides, the full-field kinematic/thermal measurements are desired to be well utilized for the validation and refinement of crystal plasticity finite element modeling and simulation.

5) For a comprehensive understanding of the work hardening mechanism of crystal deformation, the lattice rotation due to grip effect constitutes an important element. The single crystal specimen oriented preferable for simple slip will facilitate the characterization

of lattice rotation and allow a direct connection with work hardening theory proposed by Takamura (Takamura, 1987). Besides, it is interesting to develop a loading device equipped with gimbaled grips that allows a "6 degrees of freedom" (Florando *et al.*, 2006) for the tested single crystal. In this case, the single crystal deformation with and without grip effect can be compared, and the influence of the grip effect on the work hardening can be better evaluated.

References

Amiri, M., & Khonsari, M.M. 2010. Rapid determination of fatigue failure based on temperature evolution: Fully reversed bending load. *International Journal of Fatigue*, **32**(2), 382–389.

Aravas, N., Kim, K.S., & Leckie, F.A. 1990. On the calculations of the stored energy of cold work. *Journal of Engineering Materials and Technology*, **112**, 465–470.

Audenino, A.L., Crupi, V., & Zanetti, E.M. 2003. Correlation between thermography and internal damping in metals. *International Journal of Fatigue*, **25**(4), 343–351.

Badulescu, C., Grédiac, M., Haddadi, H., Mathias, J.D., Balandraud, X., & Tran, H.S. 2011. Applying the grid method and infrared thermography to investigate plastic deformation in aluminium multicrystal. *Mechanics of Materials*, **43**(1), 36–53.

Bailey, J.E., & Hirsch, P.B. 1960. The dislocation distribution, flow stress, and stored energy in cold-worked polycrystalline silver. *Philosophical Magazine*, **5**(53), 485–497.

Baker, I., Liu, L., & Mandal, D. 1995. The effect of grain size on the stored energy of cold work as a function of strain for polycrystalline nickel. *Scripta Metallurgica et Materialia*, **32**(2), 167–171.

Basinski, S.J., & Basinski, Z.S. 1979. Plastic deformation and work hardening. *In:* Nabarro, F.R.N. (ed), *Dislocations in Solids*. Amsterdam: North-Holland.

Belgen, M.H. 1967. Structural stress measurements with an infrared radiometer (Structural stress measurements in terms of induced temperature increments, using IR radiometer). *Isa Transactions*, **6**, 49–53.

Berthel, B. 2007. *Multiaxialité, hétérogénéités intrinsèques et structurales des essais d'auto-échauffement et de fatigue à grand nombre de cycles*. Ph.D. thesis, Université Montpellier II.

Berthel, B., Wattrisse, B., Chrysochoos, A., & Galtier, A. 2007. Thermographic analysis of fatigue dissipation properties of steel sheets. *Strain*, **43**(3), 273–279.

Berthel, B., Chrysochoos, A., Wattrisse, B., & Galtier, A. 2008. Infrared image processing for the calorimetric analysis of fatigue phenomena. *Experimental Mechanics*, **48**(1), 79–90.

Besnard, G., Hild, F., & Roux, S. 2006. "Finite-element" displacement fields analysis from digital images: application to Portevin-Le Châtelier bands. *Experimental Mechanics*, **46**(6), 789–803.

Bever, M.B., Holt, D.L., & Titchener, A.L. 1973. *The stored energy of cold work*. Oxford: Pergamon Press.

Blochwitz, C., & Veit, U. 1982. Plateau behaviour of fatigued FCC single crystals. *Crystal Research and Technology*, **17**(5), 529–551.

Bodelot, L. 2008. *Étude couplée des champs cinématiques et thermiques à l'échelle de la microstructure des matériaux métalliques*. Ph.D. thesis, Université des Sciences et Technologies de Lille I.

Bodelot, L., Sabatier, L., Charkaluk, E., & Dufrénoy, P. 2009. Experimental setup for fully coupled kinematic and thermal measurements at the microstructure scale of an AISI 316L steel. *Materials Science and Engineering: A*, **501**(1–2), 52–60.

Boulanger, T., Chrysochoos, A., Mabru, C., & Galtier, A. 2004. Calorimetric analysis of dissipative and thermoelastic effects associated with the fatigue behavior of steels. *International Journal of Fatigue*, **26**(3), 221–229.

Buque, C. 2001. Dislocation structures and cyclic behaviour of [011] and [-111]-oriented nickel single crystals. *International Journal of Fatigue*, **23**(8), 671–678.

Caillard, D., & Martin, J. 2003. *Thermally activated mechanisms in crystal plasticity, Pergamon Materials Series, vol. 8.* Amsterdam: Elsevier.

Carpenter, H.C.C., & Elma., C. 1921. The production of single crystals of aluminium and their tensile properties. *Proceedings of the Royal Society A*, **100**, 329–353.

Castelein, P. 2003. Vision IR: du composant à l'image, Caractérisation et modélisation de composants matriciels infrarouge. *C. R. Physique*, **4**, 1167–1174.

Chang, J.Y., Hu, W.F, Cheng, M.H., & Chang, B.S. 2002. Digital image translational and rotational motion stabilization using optical flow technique. *IEEE Transactions on Consumer Electronics*, **48**(1), 108–115.

Chrysochoos, A. 1987. *Dissipation et blocage d'energie lors d'un écrouissage en traction simple*. Ph.D. thesis, Université des Sciences et Techniques du Languedoc.

Chrysochoos, A., & Louche, H. 2000. An infrared image processing to analyse the calorific effects accompanying strain localisation. *International Journal of Engineering Science*, **38**(16), 1759–1788.

Chrysochoos, A., Maisonneuve, O., Martin, G., Caumon, H., & Chezeaux, J.C. 1989. Plastic and dissipated work and stored energy. *Nuclear Engineering and Design*, **114**(3), 323–333.

Chrysochoos, A, Berthel, B, Latourte, F, Galtier, A, Pagano, S, & Wattrisse, B. 2008a. Local energy analysis of high-cycle fatigue using digital image correlation and infrared thermography. *The Journal of Strain Analysis for Engineering Design*, **43**(6), 411–422.

Chrysochoos, A., Berthel, B., Latourte, F., Pagano, S., Wattrisse, B., & Weber, B. 2008b. Local energy approach to steel fatigue. *Strain*, **44**(4), 327–334.

Chrysochoos, A., Huon, V., Jourdan, F., Muracciole, J.M., Peyroux, R., & Wattrisse, B. 2010. Use of full-field digital image correlation and infrared thermography measurements for the thermomechanical analysis of material behaviour. *Strain*, **46**(1), 117–130.

Chu, T.C., Ranson, W.F., & Sutton, M.A. 1985. Applications of digital-image-correlation techniques to experimental mechanics. *Experimental Mechanics*, **25**(3), 232–244.

Clarebrough, L.M., Hargreaves, M.E., & Loretto, M.H. 1958. The influence of grain size on the stored energy and mechanical properties of copper. *Acta Metallurgica*, **6**(12), 725–735.

Clarebrough, L.M., Hargreaves, M.E., & Loretto, M.H. 1961. Stored energy and electrical resistivity in deformed metals. *Philosophical Magazine*, **6**(66), 807–810.

Connesson, N., Maquin, F., & Pierron, F. 2011. Experimental energy balance during the first cycles of cyclically loaded specimens under the conventional yield stress. *Experimental Mechanics*, **51**(1), 23–44.

Crupi, V. 2008. An Unifying Approach to assess the structural strength. *International Journal of Fatigue*, **30**(7), 1150–1159.

Cuitiño, A.M., & Ortiz, M. 1993. Computational modelling of single crystals. *Modeling and Simulation in Material Sciences and Engineering*, **1**(3), 225–263.

Delpueyo, D., Balandraud, X., & Grédiac, M. 2011. Applying infrared thermography to analyse martensitic microstructures in a Cu-Al-Be shape-memory alloy subjected to a cyclic loading. *Materials Science and Engineering: A*, **528**(28), 8249–8258.

Delpueyo, D., Grédiac, M., Balandraud, X., & Badulescu, C. 2012. Investigation of martensitic microstructures in a monocrystalline Cu-Al-Be shape memory alloy with the grid method and infrared thermography. *Mechanics of Materials*, **45**, 34–51.

Diehl, J. 1956. Zugverformung von Kupfer-Einkristallen (Tensile tests on copper single crystals). *Zugverformung von Kupfer-Einkristallen*, **47**, 331–341.

Diligent, S., Gautier, E., Lemoine, X., & Berveiller, M. 2001. Lattice orientation dependence of the stored energy during cold-rolling of polycrystalline steels. *Acta Materialia*, **49**(19), 4079–4088.

Doudard, C., Poncelet, M., Calloch, S., Boue, C., Hild, F., & Galtier, A. 2007. Determination of an HCF criterion by thermal measurements under biaxial cyclic loading. *International Journal of Fatigue*, **29**(4), 748–757.

Dudderar, T.D., & Simpkins, P.G. 1977. Laser speckle photography in a fluid medium. *Nature*, **270**, 45–47.

Dumoulin, S., Louche, H., Hopperstad, O.S., & Borvik, T. 2010. Heat sources, energy storage and dissipation in high-strength steels: Experiments and modelling. *European Journal of Mechanics-A/Solids*, **29**(3), 461–474.

Efstathiou, C., & Sehitoglu, H. 2010. Strain hardening and heterogeneous deformation during twinning in Hadfield steel. *Acta Materialia*, **58**(5), 1479–488.

El Bartali, A., Aubin, V., & Degallaix, S. 2008. Fatigue damage analysis in a duplex stainless steel by digital image correlation technique. *Fatigue and Fracture of Engineering Materials and Structures*, **31**(2), 137–151.

Ezanno, A., Doudard, C., Calloch, S., & Heuzé, J.L. 2013. A new approach to characterizing and modeling the high cycle fatigue properties of cast materials based on self-heating measurements under cyclic loadings. *International Journal of Fatigue*, **47**, 232–243.

Fargione, G., Geraci, A., Rosa, G. La, & Risitano, A. 2002. Rapid determination of the fatigue curve by the thermographic method. *International Journal of Fatigue*, **24**(1), 11–19.

Farren, W.S., & Taylor, G.I. 1925. The heat developed during plastic extension of metals. *Proceedings of The Royal Society of London*, **107**, 422–451.

Favier, D., Louche, H., Schlosser, P., Orgéas, L., Vacher, P., & Debove, L. 2007. Homogeneous and heterogeneous deformation mechanisms in an austenitic polycrystalline Ti-50.8 at.% Ni thin tube under tension. Investigation via temperature and strain fields measurements. *Acta Materialia*, **55**(16), 5310–5322.

Feaugas, X. 1999a. *Contribution à la compréhension des mécanismes de déformation plastique et d'endommagement des matériaux : un point de vue expérimental*. Mémoire d'HDR: Université de Technologie de Compiègne.

Feaugas, X. 1999b. On the origin of the tensile flow stress in the stainless steel AISI 316L at 300 K: back stress and effective stress. *Acta Materialia*, **47**(13), 3617–3632.

Feaugas, X., & Gaudin, C. 2001. Different levels of plastic strain incompatibility during cyclic loading: in terms of dislocation density and distribution. *Materials Science and Engineering: A*, **309-310**, 382–385.

Feaugas, X., & Haddou, H. 2003. Grain-size effects on tensile behavior of nickel and AISI 316L stainless steel. *Metallurgical and Materials Transactions A*, **34**(10), 2329–2340.

Feaugas, X., & Haddou, H. 2007. Effects of grain size on dislocation organization and internal stresses developed under tensile loading in fcc metals. *Philosophical Magazine*, **87**(7), 989–1018.

Feaugas, X., & Pilvin, P. 2009. A polycrystalline approach to the cyclic behaviour of f.c.c. alloys - intra-granular heterogeneity. *Advanced Engineering Materials*, **11**(9), 703–709.

Florando, J.N., Rhee, M., Arsenlis, A., LeBlanc, M.M., & Lassila, D.H. 2006. Calculation of the slip system activity in deformed zinc single crystals using digital 3-D image correlation data. *Philosophical Magazine Letters*, **86**(12), 795–805.

Florando, J.N., LeBlanc, M.M., & Lassila, D.H. 2007. Multiple slip in copper single crystals deformed in compression under uniaxial stress. *Scripta Materialia*, **57**(6), 537–540.

Francois, D, Pineau, A, & Zaoui, A. 1992. *Comportement mécanique des matériaux: Élasticité et plasticité*. Paris: Hermès.

Furukawa, Y., & Nakajima, K. 2001. *Advances in Crystal Growth Research.* Amsterdam: Elsevier.

Gaussorgues, G. 1994. *Infrared Thermography.* London: Chapman & Hall.

Genov, R., & Cauwenberghs, G. 2004. Dynamic MOS sigmoid array folding analog-to-digital conversion. *IEEE Transactions on Circuits and Systems I: Regular Papers*, **51**(1), 182–186.

Giancane, S., Chrysochoos, A., Dattoma, V., & Wattrisse, B. 2009. Deformation and dissipated energies for high cycle fatigue of 2024-T3 aluminium alloy. *Theoretical and Applied Fracture Mechanics*, **52**(2), 117–121.

Gibbs, J.W. 1902. *Elementary principles in statistical mechanics.* New York: Charles Scribner's Sons.

Godfrey, A., Cao, W.Q., Liu, Q., & Hansen, N. 2005. Stored energy, microstructure, and flow stress of deformed metals. *Metallurgical and Materials Transactions A*, **36**, 2371–2378.

Grédiac, M., & Hild, F. 2011. *Mesures de champs et identification en mécanique des solides.* Paris: Lavoisier.

Greene, R.J., Patterson, E.A., & Rowlands, R.E. 2008. *Thermoelastic Stress Analysis, Springer Handbook of Experimental Solid Mechanics.* New York: Springer.

Haddou, H. 2003. *Influence de la taille de grain et de l'énergie de défaut d'empilement sur l'état de contraintes internes développé au cours de la déformation plastique en traction simple et en fatigue oligocyclique(alliages c.f.c).* Ph.D. thesis, Université de Technologie de Compiègne.

Hauser, J.J., & Jackson, K.A. 1961. Effect of grip constraints on the tensile deformation of f.c.c. single crystals. *Acta Metallurgica*, **9**(1), 1–13.

Herve, P., Cedelle, J., & Negreanu, I. 2012. Infrared technique for simultaneous determination of temperature and emissivity. *Infrared Physics and Technology*, **55**(1), 1–10.

Higashida, K., Takamura, J., & Narita, N. 1986. The formation of deformation bands in f.c.c. crystals. *Materials Science and Engineering*, **81**, 239–258.

Hill, D.L.G., Batchelor, P.G., Holden, M., & Hawkes, D.J. 2001. Medical image registration. *Physics in Medicine and Biology*, **46**(3), R1–R45.

Hirsch, P. B. 1965. *Electron microscopy of thin crystals.* London: Butterworths.

Hirth, J.P., & Lothe, J. 1968. *Theory of dislocations.* New York: MacGraw-Hill.

Jaoul, B. 1965. *Étude de la plasticité et application aux métaux.* Paris: Dunod.

Jiang, L., Wang, H., Liaw, P.K., Brooks, C.R., Chen, L., & Klarstrom, D.L. 2004. Temperature evolution and life prediction in fatigue of superalloys. *Metallurgical and Materials Transactions A*, **35**, 839–848.

Kahn-Jetter, Z.L., & Chu, T.C. 1990. Three-dimensional displacement measurements using digital image correlation and photogrammic analysis. *Experimental Mechanics*, **30**(1), 10–16.

Kasem, H., Thevenet, J., Boidin, X., Siroux, M., Dufrénoy, P., Desmet, B., & Desplanques, Y. 2010. An emissivity-corrected method for the accurate radiometric measurement of transient surface temperatures during braking. *Tribology International*, **43**(10), 1823–1830.

Kelly, A., & Macmillan, N.H. 1986. *Strong solids*. Oxford: Clarendon Press.

Klein, S., & Staring, M. 2011 (Sept.). *Elastix: the manual*.

Klein, S., Staring, M., & Pluim, J.P.W. 2007. Evaluation of optimization methods for nonrigid medical image registration using mutual information and B-splines. *IEEE Transactions on Image Processing*, **16**(12), 2879–2890.

Kocks, U.F., & Mecking, H. 2003. Physics and phenomenology of strain hardening: the FCC case. *Progress in Materials Science*, **48**, 171–273.

Kocks, U.F., & Scattergood, R.O. 1969. Elastic interactions between dislocations in a finite body. *Acta Metallurgica*, **17**(9), 1161–1168.

Koehler, J.S. 1941. On the Dislocation Theory of Plastic Deformation. *Physical Review*, **60**, 397–410.

Kramer, D.E., Savage, M.F., & Levine, L.E. 2005. AFM observations of slip band development in Al single crystals. *Acta Materialia*, **53**(17), 4655–4664.

Krapez, J.C., & Pacou, D. 2002 (April 01-04). Thermography detection of damage initiation during fatigue tests. *Pages 435–449 of: Proceedings of the 24th International Conference on Thermal Sensing and Imaging Diagnostic Applications*.

Krapez, J.C., Pacou, D., & Bertin, C. 1999 (Sept 29-30). Application of lock-in thermography to a rapid evaluation of fatigue limit in metals. *Pages 379–385 of: Proceedings of the 5th International Workshop on Advanced Infrared Technology and Applications*.

Kuchnicki, S.N., Cuitiño, A.M., & Radovitzky, R.A. 2006. Efficient and robust constitutive integrators for single-crystal plasticity modeling. *International Journal of Plasticity*, **22**(10), 1988–2011.

Kumar, A., Sarkar, S., & Agarwal, R.P. 2007. A novel algorithm and hardware implementation for correcting sensor non-uniformities in infrared focal plane array based staring system. *Infrared Physics and Technology*, **50**(1), 9–13.

Langford, C., & Cohen, M. 1969. Strain hardening of iron by severe plastic deformation. *Transactions of the ASM*, **62**, 623–638.

Lassila, D.H., LeBlanc, M.M., & Florando, J.N. 2007. Zinc Single-Crystal Deformation Experiments Using a "6 Degrees of Freedom" Apparatus. *Metallurgical and Materials Transactions A*, **38**(9), 2024–2032.

Lau, A.S. 1977 (April 18-21). The Narcissus effect in infrared optical scanning systems. *Pages 57–62 of: Stray-light problems in optical systems, Proceedings of the Seminar, Reston, Va., Society of Photo-Optical Instrumentation Engineers.*

Lee, M.G., Lim, H., Adams, B.L., Hirth, J.P., & Wagoner, R.H. 2010. A dislocation density-based single crystal constitutive equation. *International Journal of Plasticity*, **26**(7), 925–938.

Lekbir, C. 2012. *Effet de la déformation plastique du nickel monocristallin sur l'état d'équilibre de l'hydrogène en surface et subsurface.* Ph.D. thesis, Université de La Rochelle.

Lemaitre, J., & Chaboche, J.L. 1994. *Mechanics of Solid Materials.* Cambridge: Cambridge University Press.

Lester, H., & Arridge, S.R. 1999. A survey of hierarchical non-linear medical image registration. *Pattern Recognition*, **32**(1), 129–149.

Liew, S.C. 2006. Electromagnetic Waves. *Centre for Remote Imaging, Sensing and Processing*, Retrieved 2006–10–27.

Louche, H., & Chrysochoos, A. 2001. Thermal and dissipative effects accompanying Lüders band propagation. *Materials Science and Engineering: A*, **307**(1-2), 15–22.

Luong, M.P. 1995. Infrared thermographic scanning of fatigue in metals. *Nuclear Engineering and Design*, **158**(2-3), 363–376.

Luong, M.P. 1998. Fatigue limit evaluation of metals using an infrared thermographic technique. *Mechanics of Materials*, **28**(1-4), 155–163.

Macmillan, N.H. 1983. The Ideal Strength of Solids. *Pages 95–165 of:* Latanision, R.M., & Pickens, J.R. (eds), *Atomistics of Fracture.* Springer US.

Magid, K.R., Florando, J.N., Lassila, D.H., LeBlanc, M.M., Tamura, N., & Morris, J.W. 2009. Mapping mesoscale heterogeneity in the plastic deformation of a copper single crystal. *Philosophical Magazine*, **89**(1), 77–107.

Maintz, J.B.A., & Viergever, M.A. 1998. A survey of medical image registration. *Medical Image Analysis*, **2**, 1–36.

Man, J., Obrtilík, K., & Polák, J. 2009a. Extrusions and intrusions in fatigued metals. Part 1. State of the art and history. *Philosophical Magazine*, **89**(16), 1295–1336.

Man, J., Klapetek, P., Man, O., Weidner, A., Obrtilík, K., & Polák, J. 2009b. Extrusions and intrusions in fatigued metals. Part 2. AFM and EBSD study of the early growth of extrusions and intrusions in 316L steel fatigued at room temperature. *Philosophical Magazine*, **89**(16), 1337–1372.

Maquin, F. 2006. *Méthodologie expérimentale d'étude du comportement thermo-mécanique des matériaux sous sollicitations cycliques.* Ph.D. thesis, Ecole Nationale Supérieure d'Arts et Métiers (ENSAM).

Maquin, F., & Pierron, F. 2009. Heat dissipation measurements in low stress cyclic loading of metallic materials: From internal friction to micro-plasticity. *Mechanics of Materials*, **41**(8), 928–942.

Maynadier, A., Poncelet, M., Lavernhe-Taillard, K., & Roux, S. 2012. One-shot measurement of thermal and kinematic fields: InfraRed Image Correlation (IRIC). *Experimental Mechanics*, **52**(3), 241–255.

Mecke, K., & Blochwitz, C. 1982. Saturation dislocation structures in cyclically deformed nickel single crystals of different orientations. *Crystal Research and Technology*, **17**(6), 743–758.

Mecke, K., Blochwitz, C., & Kremling, V. 1982. The development of the dislocation structures during the fatigue process of F.C.C. single crystals. *Crystal Research and Technology*, **17**(12), 1557–1570.

Meyendorf, N.G.H., Rosner, H., Kramb, V., & Sathish, S. 2002. Thermo-acoustic fatigue characterization. *Ultrasonics*, **40**(1-8), 427–434.

Morabito, A.E., Chrysochoos, A., Dattoma, V., & Galietti, U. 2007. Analysis of heat sources accompanying the fatigue of 2024 T3 aluminium alloys. *International Journal of Fatigue*, **29**(5), 977–984.

Mountain, D.S., & Webber, J.M.B. 1978 (October 10-13). Stress pattern analysis by thermal emission (SPATE). *Pages 189–196 of: Proc. SPIE 0164, 4th European Electro-Optics Conference*.

Mudau, A.E., Willers, C.J., Griffith, D., & le Roux, F.P.J. 2011 (April 24-26). Non-uniformity correction and bad pixel replacement on LWIR and MWIR images. *Pages 1–5 of: Electronics, Communications and Photonics Conference (SIECPC), 2011 Saudi International*.

Mughrabi, H. 1968. Electron microscope observations on the dislocation arrangement in deformed copper single crystals in the stress-applied state. *Philosophical Magazine*, **18**(156), 1211–1217.

Mughrabi, H. 1978. The cyclic hardening and saturation behaviour of copper single crystals. *Materials Science and Engineering*, **33**(2), 207–223.

Mughrabi, H. 1983. Dislocation wall and cell structures and long-range internal stresses in deformed metal crystals. *Acta Metallurgica*, **31**(9), 1367–1379.

Mughrabi, H. 1993. Microstructure and mechanical properties. *In:* Mughrabi, H (ed), *Plastic deformation and fracture of materials*. Weinheim: VCH.

Nabarro, F.R.N. 1967. *Theory of crystal dislocations*. Oxford: Oxford University Press.

Nabarro, F.R.N., Basinski, Z.S., & Holt, D.B. 1964. The plasticity of pure single crystals. *Advances in Physics*, **13**(50), 391–400.

Naderi, M., & Khonsari, M.M. 2010. An experimental approach to low-cycle fatigue damage based on thermodynamic entropy. *International Journal of Solids and Structures*, **47**(6), 875–880.

Nakada, Y. 1965. Orientation dependence of energy dissipation during plastic deformation of f.c.c. crystals. *Philosophical Magazine*, **11**, 251–261.

Negreanu, I. 2009. *Détermination de la température à partir de la radiation infrarouge au cours des essais dynamiques*. Ph.D. thesis, Ecole Polytechnique.

Neuhäuser, H. 1983. Slip line formation and collective dislocation motion. *In:* Nabarro, F.R.N. (ed), *Dislocations in Solids*. Amsterdam: North-Holland.

Nocedal, J., & Wright, S.J. 1999. *Numerical optimization*. New York: Springer-Verlag.

Norris, A.N. 2006. Poisson's ratio in cubic materials. *Proceedings of the Royal Society A*, **462**, 3385–3405.

Offermann, S., Bissieux, C., & Beaudoin, J.L. 1996. Thermoelastic stress analysis with standard thermographic equipment by means of statistical noise rejection. *Research in Nondestructive Evaluation*, **7**(4), 239–251.

Offermann, S., Beaudoin, J.L., Bissieux, C., & Frick, H. 1997. Thermoelastic stress analysis under nonadiabatic conditions. *Experimental Mechanics*, **37**(4), 409–413.

Offermann, Stephan, Bissieux, Christian, & Beaudoin, Jean Louis. 1998. Statistical treatment applied to infrared thermoelastic analysis of applied and residual mechanical stresses. *Revue Générale de Thermique*, **37**(8), 718–724.

Oliferuk, W., & Maj, M. 2009. Stress-strain curve and stored energy during uniaxial deformation of polycrystals. *European Journal of Mechanics-A/Solids*, **28**(2), 266–272.

Orteu, J.J. 2009. 3-D computer vision in experimental mechanics. *Optics and Lasers in Engineering*, **47**(3-4), 282–291.

Oudriss, A. 2012. *Influence des hétérogénéités métallurgiques sur les processus de diffusion et de piégeage de l'hydrogène dans le nickel*. Ph.D. thesis, Université de La Rochelle.

Pan, B., Qian, K.M., Xie, H.M., & Asundi, A. 2009. Two-dimensional digital image correlation for in-plane displacement and strain measurement: a review. *Measurement Science and Technology*, **20**(4), 062001.

Pastor, M.L., Balandraud, X., Grédiac, M., & Robert, J.L. 2008. Applying infrared thermography to study the heating of 2024-T3 aluminium specimens under fatigue loading. *Infrared Physics and Technology*, **51**(6), 505–515.

Pedersen, O.B. 1990. Overview no. 89 Mechanism maps for cyclic plasticity and fatigue of single phase materials. *Acta Metallurgica et Materialia*, **38**(7), 1221–1239.

Pedrotti, F.L., & Pedrotti, L.S. 1993. *Introduction to Optics*. New Jersey: Prentice-Hall International.

Philibert, J., Vignes, A., Bréchet, Y., & Combrade, P. 1998. *Métallurgie: du minerai au matériau*. Paris: Edition Masson.

Pluim, J.P.W., Maintz, J.B.A., & Viergever, M.A. 2003. Mutual-information-based registration of medical images: a survey. *IEEE Transactions on Medical Imaging*, **22**(8), 986–1004.

Poncelet, M. 2007. *Mesures thermographiques de champs de dissipation accompagnant la fatigue à grand nombre de cycles des aciers*. Ph.D. thesis, Ecole Normale Supérieure de Cachan.

Poncelet, M., Doudard, C., Calloch, S., Hild, F., Weber, B., & Galtier, A. 2007. Prediction of self-heating measurements under proportional and non-proportional multiaxial cyclic loadings. *Comptes Rendus Mécanique*, **335**(2), 81–86.

Poncelet, M., Doudard, C., Calloch, S., Weber, B., & Hild, F. 2010. Probabilistic multiscale models and measurements of self-heating under multiaxial high cycle fatigue. *Journal of the Mechanics and Physics of Solids*, **58**(4), 578–593.

Poncelet, M., Witz, J.F., Pron, H., & Wattrisse, B. 2011. A study of IRFPA camera measurement errors: radiometric artefacts. *Quantitative InfraRed Thermography Journal*, **8**(1), 3–20.

Ratliff, B.M., Hayat, M.M., & Tyo, J.S. 2005. Generalized algebraic scene-based nonuniformity correction algorithm. *Journal of the Optical Society of America A*, **22**(2), 239–249.

Risbet, M., Feaugas, X., Guillemer-Neel, C., & Clavel, M. 2003. Use of atomic force microscopy to quantify slip irreversibility in a nickel-base superalloy. *Scripta Materialia*, **49**(6), 533–538.

Rittel, D., Bhattacharyya, A., Poon, B., Zhao, J., & Ravichandran, G. 2007. Thermomechanical characterization of pure polycrystalline tantalum. *Materials Science and Engineering: A*, **447**(1-2), 65–70.

Rosa, G. La, & Risitano, A. 2000. Thermographic methodology for rapid determination of the fatigue limit of materials and mechanical components. *International Journal of Fatigue*, **22**(1), 65–73.

Rueckert, D., & Schnabel, J.A. 2011. Medical Image Registration. *Pages 131–154 of:* Deserno, Thomas Martin (ed), *Biomedical Image Processing*. Biological and Medical Physics, Biomedical Engineering. Springer Berlin Heidelberg.

Rueckert, D., Sonoda, L.I., Hayes, C., Hill, D.L.G., Leach, M.O., & Hawkes, D.J. 1999. Nonrigid registration using free-form deformations: Application to breast MR images. *IEEE Transactions on Medical Imaging*, **18**, 712–721.

Saai, A., Louche, H., Tabourot, L., & Chang, H.J. 2010. Experimental and numerical study of the thermo-mechanical behavior of Al bi-crystal in tension using full field measurements and micromechanical modeling. *Mechanics of Materials*, **42**(3), 275–292.

Sangid, M.D., Maier, H.J., & Sehitoglu, H. 2011a. An energy-based microstructure model to account for fatigue scatter in polycrystals. *Journal of the Mechanics and Physics of Solids*, **59**(3), 595–609.

Sangid, M.D., Maier, H.J., & Sehitoglu, H. 2011b. A physically based fatigue model for prediction of crack initiation from persistent slip bands in polycrystals. *Acta Materialia*, **59**(1), 328–341.

Schlosser, P., Louche, H., Favier, D., & Orgéas, L. 2007. Image processing to estimate the heat sources related to phase transformations during tensile tests of NiTi tubes. *Strain*, **43**(3), 260–271.

Schulz, M., & Caldwell, L. 1995. Nonuniformity correction and correctability of infrared focal plane arrays. *Infrared Physics and Technology*, **36**(4), 763–777.

Seeger, A., & Kronmüller, H. 1962. Stored energy and recovery of deformed F.C.C. metals. *Philosophical Magazine*, **7**(78), 897–913.

Seghir, R. 2012. *Experimental and numerical investigation of thermomechanical couplings and energy balance in metallic polycrystals*. Ph.D. thesis, Ecole Centrale de Lille.

Seghir, R., Witz, J.F., Charkaluk, E., & Dufrénoy, P. 2012. Improvement of thermomechanical full-field analysis of metallic polycrystals using crystallographic data. *Mechanics and Industry*, **13**(6), 395–403.

Seghir, R., Witz, J.F., Bodelot, L., Charkaluk, E., & Dufrénoy, P. 2013. Improvement of thermomechanical full-field analysis of metallic polycrystals using crystallographic data. *Quantitative InfraRed Thermography Journal*, **10**(1), 74–95.

Seitz, F., & Read, T.A. 1941. Theory of the Plastic Properties of Solids. I. *Journal of Applied Physics*, **12**, 100–118.

Sevillano, G. 1993. Flow stress and work hardening. *In:* Mughrabi, H (ed), *Plastic deformation and fracture of materials*. Weinheim: VCH.

Shi, Y., Zhang, T.X., Cao, Z.G., & Hui, L. 2005. A feasible approach for nonuniformity correction in IRFPA with nonlinear response. *Infrared Physics and Technology*, **46**(4), 329–337.

Silva, M.L., & Ravichandran, G. 2011. Combined thermoelastic stress analysis and digital image correlation with a single infrared camera. *Journal of Strain Analysis for Engineering Design*, **46**, 783–793.

Stanley, P. 2008. Beginnings and Early Development of Thermoelastic Stress Analysis. *Strain*, **44**(4), 285–297.

Stroh, A.N. 1953. A theoretical calculation of the stored energy in a work-hardened material. *Proceedings of the Royal Society of London A*, **218**, 391–400.

Sutton, M.A., Wolters, W.J., Peters, W.H., Ranson, W.F., & McNeill, S.R. 1983. Determination of displacements using an improved digital correlation method. *Image and Vision Computing*, **1**(3), 133–139.

Sutton, M.A., Yan, J.H., Tiwari, V., Schreier, H.W., & Orteu, J.J. 2008. The effect of out-of-plane motion on 2D and 3D digital image correlation measurements. *Optics and Lasers in Engineering*, **46**(10), 746–757.

Sutton, M.A., Orteu, J.J., & Schreier, H. 2009. *Image correlation for shape, motion and deformation measurements: Basic Concepts, Theory and Applications.* New York: Springer.

Tabourot, L., Fivel, M., & Rauch, E. 1997. Generalised constitutive laws for f.c.c. single crystals. *Materials Science and Engineering: A*, **234-236**, 639–642.

Takamura, J. 1987. Formation of deformation bands and work hardening of FCC crystals. *Transactions of the Japan Institute of Metals*, **28**(3), 165–181.

Takeuchi, S., & Suzuki, T. 1989. Lattice defects in ceramics. *In:* Kettunen, P. O., Lepistö, T. K., & Lehtonen, M. E. (eds), *Strength of metals and alloys.* Oxford: Pergamon.

Taylor, G.I. 1934. The mechanism of plastic deformation of crystals. Part I. Theoretical. *Proceedings of The Royal Society of London A*, **145**, 362–387.

Taylor, G.I., & Quinney, H. 1934. The latent energy remaining in a metal after cold working. *Proceedings of The Royal Society of London*, **143**, 307–326.

Thévenaz, P., & Unser, M. 2000. Optimization of mutual information for multiresolution image registration. *IEEE Transactions on Image Processing*, **9**, 2083–2099.

Tylecote, R.F. 1976. *A history of metallurgy.* London: The Metals Society.

Unser, M. 1999. Splines: A perfect fit for signal and image processing. *IEEE Signal Processing Magazine*, **16**(6), 22–38.

Wang, X.G., Crupi, V., Guo, X.L., & Zhao, Y.G. 2010. Quantitative Thermographic Methodology for fatigue assessment and stress measurement. *International Journal of Fatigue*, **32**(12), 1970–1976.

Warren, J.S. 2007. *Modern Optical Engineering, 4th Ed.* New York: McGraw-Hill Professional.

Westerweel, J. 1997. Fundamentals of digital particle image velocimetry. *Measurement Science and Technology*, **8**(12), 1379.

Williams, R.O. 1961. The stored energy in deformed copper: The effect of grain size and silver content. *Acta Metallurgica*, **9**(10), 949–957.

Williams, R.O. 1965. The stored energy of copper deformed at 24 K. *Acta Metallurgica*, **13**(3), 163–168.

Wolfenden, A. 1967. The energy stored in copper single crystals. *Acta Metallurgica*, **15**(6), 971–978.

Wolfenden, A. 1968. The ratio of stored to expended energy during the deformation of copper and aluminum single crystals at 78 K. *Acta Metallurgica*, **16**(8), 975–980.

Wolfenden, A. 1971. The energy stored in polycrystalline copper deformed at room temperature. *Acta Metallurgica*, **19**(12), 1373–1377.

Yang, B., Liaw, P.K., Wang, H., Jiang, L., Huang, J.Y., Kuo, R.C., & Huang, J.G. 2001. Thermographic investigation of the fatigue behavior of reactor pressure vessel steels. *Materials Science and Engineering: A*, **314**(1-2), 131–139.

Zaiser, M. 2006. Scale invariance in plastic flow of crystalline solids. *Advances in Physics*, **55**(1-2), 185–245.

Zhang, N., & Tong, W. 2004. An experimental study on grain deformation and interactions in an Al-0.5%Mg multicrystal. *International Journal of Plasticity*, **20**(3), 523–542.

Zhao, Z., Ramesh, M., Raabe, D., Cuitiño, A.M., & Radovitzky, R. 2008. Investigation of three-dimensional aspects of grain-scale plastic surface deformation of an aluminum oligocrystal. *International Journal of Plasticity*, **24**(12), 2278–2297.

Appendix A

Investigations on aluminum oligocrystals

Investigations on aluminum oligocrystals are presented in this chapter.

First of all, the studied material pure aluminum oligocrystal and its specific crystallographic structure are introduced. Then the experimental protocol for realizing the kinematic-thermal fully-coupled measurements is detailed, and the profile measurement is performed on the deformed specimen after the tensile test. Finally, the effects of out-of-plane deformation on both thermographic and kinematic measurements are studied in this appendix.

A.1 Aluminum oligocrystal

The primary motivation to study aluminum is its facility to obtain the desired microstructure: oligocrystal specimen. An oligocrystal specimen with very limited number of grains can simplify the mechanical behaviours of material and facilitates a microstructure-based analysis (Zhao *et al.*, 2008). The disadvantage, however, is also visible by choosing pure aluminum as it has a very high thermal diffusivity. It is about 7 times higher than the low carbon steel and up to 22 times higher than 316L steel. This may bring some difficulties for the thermographic measurement and demand a high sampling frequency in the image acquisition. Nevertheless, aluminum alloys is yet one of the most studied metallic materials in thermographic measurements in recent years (Morabito *et al.*, 2007; Pastor *et al.*, 2008; Maquin & Pierron, 2009).

A.1.1 Specimen preparation

The oligocrystal specimen can be prepared by the strain-annealing method (Carpenter & Elma., 1921; Philibert *et al.*, 1998), from a very pure aluminum (purity 99.99%) plate. The strain-annealing method is summarized in Fig. A.1 (Saai *et al.*, 2010).

The preparation of the oligocrystal specimens, following the strain-annealing method, required three steps.

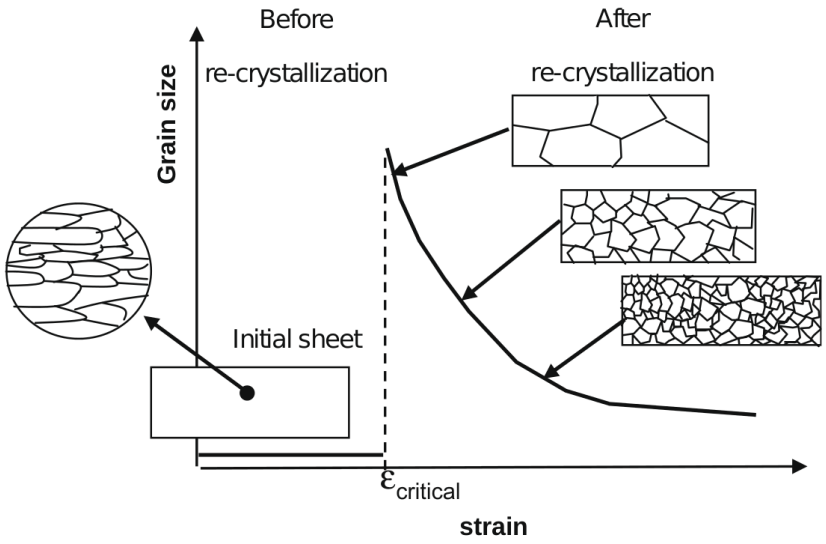

Figure A.1: The schematic map of the strain-annealing method: variation in grain size obtained after recrystallization as a function of applied tensile strain

1. The specimens cut from the original metal sheet were firstly annealed at 545 °C for 1 h. This first annealing allows removing of the residual stresses resulting from the manufacturing process.

2. Annealed specimens were then stretched by around 3.5% longitudinal strain which corresponds to the "critical strain" value necessary to obtain, after a second annealing of recrystallization, maximum grain size.

3. Stretched specimens were finally annealed at 545 °C for 1 h.

It is worthy to note that the purity of aluminum is essentially important for obtaining the well-grown coarse grains. To our practical experiences, a less pure aluminum (like purity 99.5%) is often found difficult to be well recrystallized, and as a result there will be always small non-recrystallized small grains mixed in the coarse grains throughout the specimen.

The final obtained oligocrystal specimen contained about 10 grains in a single layer. The average diameter of the grains can attain 15 mm, and the thickness of the specimen was 1.5 mm. In order to observe the grain texture of the oligocrystal specimen, a chemical etching was necessary. The chemical etching can form an oxide layer with variable thickness on the specimen surface that allowed distinguishing the grains with the naked eyes. Fig. A.2 shows the surface of an oligocrystal specimen after the chemical etching.

A.1.2 Crystallographic structure

In order to promote a crystallographic-based analysis, the grain texture of the oligocrystal specimen is expected to be extracted. In particular, concerning the anticipated two-face measurement, one important issue is the identity of the grain textures appearing on the two

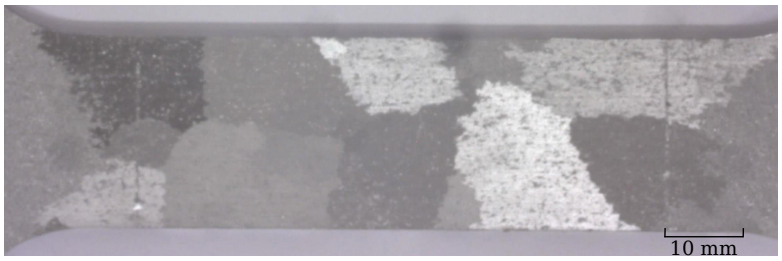

Figure A.2: The surface of an oligocrystal specimen after recrystallization and chemical etching

faces of the specimen. In other words, the grain boundaries are expected be perpendicular to the specimen surface. This can best ensure a quasi identical mechanical behaviour manifesting on the two faces of the specimen at a grain scale.

A dedicated test was carried out so as to verify the identity (or spatial matching effect) of the grain textures on the two faces of the specimen. This was a so-called controlled image registration test, with a schematic diagram shown in Fig. A.3.

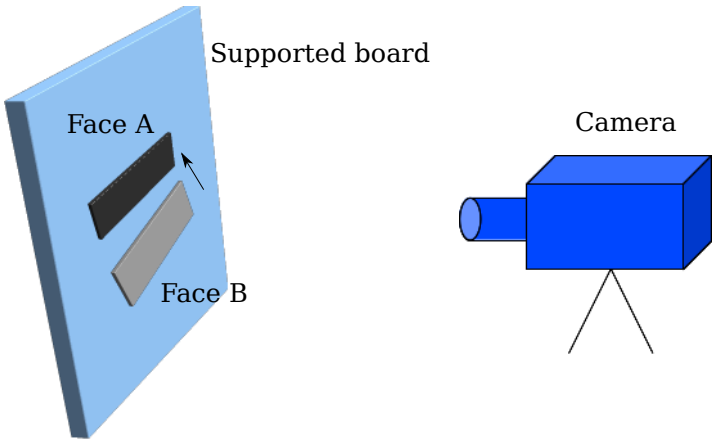

Figure A.3: The schematic diagram of the controlled image registration test

An image was firstly taken on one face of the specimen, namely the face A. Then the specimen was turned over so that the other face, the face B, can be observed, and the other image was taken. Be aware that the specimen was always restrained upon the support board, so the transformation model between the two images should be the type of rigid body. And because the grain textures of the two faces showed a very similar pattern, so the two images were possible to be correlated through the image registration process using affine transformation. While the two faces of specimen existed still a "considerable" difference for a general image registration, so the more versatile correlation criterion MI was utilized. And finally the two images were successfully correlated.

The oligocrystal specimen anticipated for the following mechanical test was examined by the proposed method. Fig. A.4 shows the grain textures of the two faces of the specimen

(face A for kinematic measurement and face B for thermal measurement) and the overlay of the extracted grain boundaries. The figure shows that the overlapping of grain boundaries is satisfactory on a grain scale, in particular for the coarse grains in the center of the specimen. For some small grains, like the ones located in the upper left corner of the specimen, their overlapping effect are less satisfactory. For these particular zones, it should be very attentive when the coupled measurement results are expected to be compared. For most of the grains, we can assure that the grain boundaries are basically perpendicular to the specimen surface.

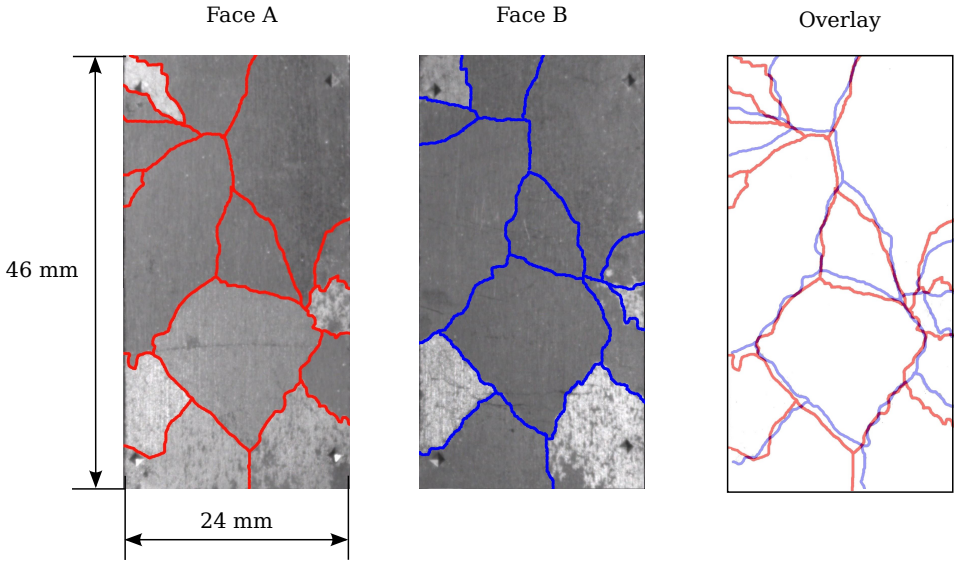

Figure A.4: Grain textures of the specimen surfaces and the overlay of the grain boundaries

A.2 Experimental protocol

First of all, some surface treatments should be applied to the specimen. The surface for kinematic measurement was sprayed by speckled paint, and the other surface for thermal measurement was deposited by a layer of carbon black. In addition, four physical marks were made on each specimen face as the location references.

Before carrying out the tensile test, an in-situ temperature calibration was conducted for the IR camera. And the reference target had also been measured in the same experimental configuration that served for the final spatial alignment of the coupled data.

A tensile test was performed at room temperature and at a constant crosshead velocity of 1 mm/s, equivalent to an axial strain rate $1.25 \times 10^{-2}\ s^{-1}$. The test lasted 3.4 s, thus the total imposed strain on the specimen was 4.25×10^{-2}. Visible and IR images were acquired simultaneously during the test thanks to the two-face measurement system, as shown in Fig. A.5. On the side of the thermographic measurement, there was an isolation box bridging the IR camera and the specimen in order to avoid the possible influences from the environment. And on the other side for the kinematic measurement, LEDs were utilized for

the illumination.

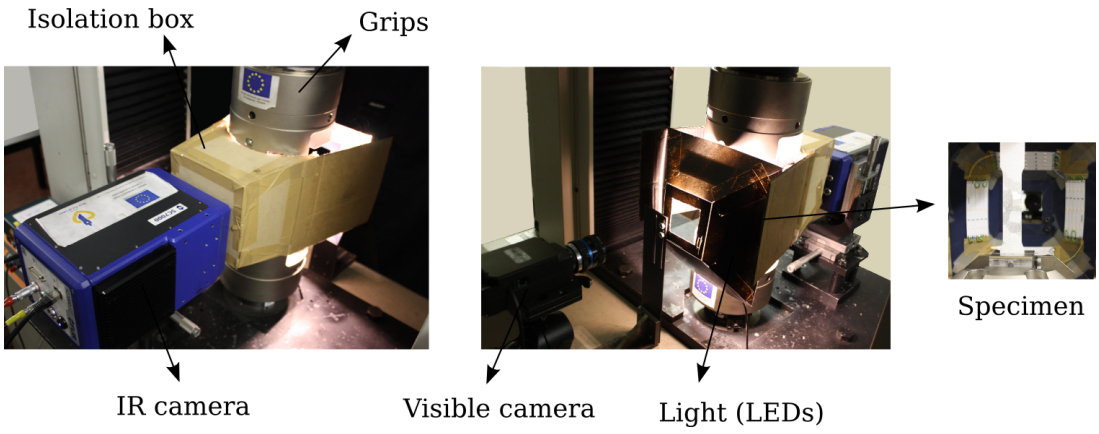

Figure A.5: Experimental set-up of the two-face measurement system

Visible images were recorded by Elphel camera at a frequency of 20 Hz. It provided an image resolution 1712 × 1552 pixels and a field of view 42.8 × 38.8 mm^2 with the physical resolution 25 × 25 μm^2. IR images were acquired by FLIR Titanium camera at 100 Hz. It provided an image resolution 472 × 368 pixels and a field of view 49.6 × 38.6 mm^2 with the physical resolution 105 × 105 μm^2. The IT adopted for IR camera was 3 ms that enabled a dynamic level around 1.0 × 10^4 DL.

After the tensile test, the deformed specimen was measured by an interferometric profilometer (Wyko NT1100) that provided the surface profiles for the two faces of the specimen.

The first noticeable phenomenon found in the results was that the specimen had suffered a strong out-of-plane deformation during the tensile test. The deformed specimen was actually curved with deformed grain shapes in three dimensional, as shown by the photograph in Fig. A.6.

Figure A.6: The deformed specimen after a tensile test

Interestingly, the out-of-plane deformation exhibits a close link with the grain texture. Fig. A.6 shows the most important geometrical changes are basically along the grain boundaries, and the deformation within the grain exhibits a more or less continuous feature. This suggests that the grain interactions were rather strong in the plastic deformation, and the grain boundaries functioned actually as geometric barriers of the in-plane deformation.

The deformation localization brought a surface roughening effect on the specimen. The profilometry measurements show that the surface roughness average of the deformed specimen is about 70 μm, and the maximum height can reach around 700 μm, almost the half of the specimen thickness. Fig. A.7 shows the surface profile maps for both of the two faces of the specimen. The physical resolution of the profile maps is 13 $\times$ 13 μm^2 per pixel with a field of view about 47 $\times$ 22 mm^2. It can be noticed that the two profile maps show a similar pattern and vary comparable in absolute values with the very opposite signs. They also exhibits a great similarity to the initial grain textures as shown in Fig. A.4. The out-of-plane deformation can therefore be understood as a kind of "foldings" based on the grain boundaries.

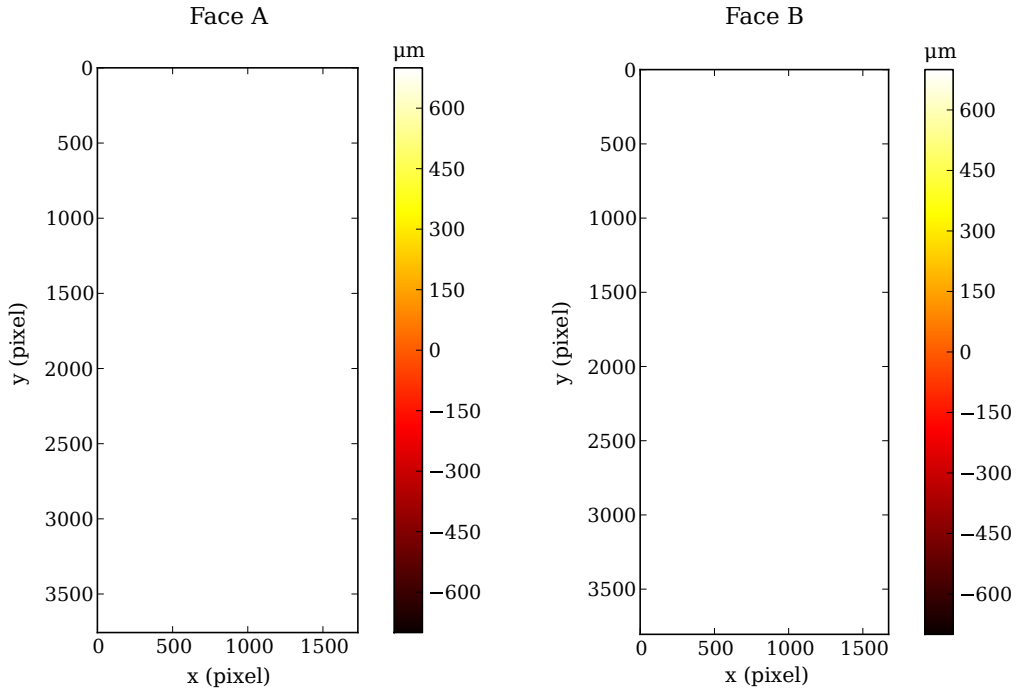

Figure A.7: Surface profiles of the deformed specimen

The out-of-plane deformation can induce a complex optical interference effect on both thermographic and kinematic measurements. The relevant analyses for aluminum oligocrystals are presented in the next sections, and the emphasis is placed on the thermographic measurement. Here we suggest the readers to peruse a theoretical analysis on the out-of-plane effect detailed in chapter 4 before following the analyses below.

A.3 Out-of-plane effect on thermographic measurement

A.3.0.1 Thermographic measurement results

In the thermographic measurement, the emissivity map of specimen surface in the final deformed state is unfortunately not available. Thus, only the emissivity of specimen surface

in the initial undeformed state can be used. It was measured as 0.97 since a layer of carbon black was deposited on the specimen surface. In such situations, a classical QIRT approach for temperature calibration (as detailed in chapter 2) was adopted, in which the emissivity was considered constant (= 0.97). In other words, the out-of-plane effect was not taken into account (or corrected) in the calibration. As a direct result, the calibrated temperature field must be influenced by the out-of-plane effect, which in this analysis is expected to be compared with its corresponding surface profile of specimen.

Concerning the final deformation state of specimen, two relevant temperature fields are interesting to be illustrated. The first one is the temperature field obtained at the end of the tensile test, corresponding to the maximum load (the test was without unloading). It is shown in Fig. A.8(a), where the temperature is expressed in relative temperature (by subtracting the initial temperature before loading). Fig. A.8(a) shows that the total temperature increment of specimen in the test is only about 0.23 °C in average but with a strong heterogeneous distribution. The other interesting temperature field is the one obtained 10 s after the tensile test, as shown in Fig. A.8(b). It corresponds actually to the last thermographic image recorded by the IR camera. The temperature field in Fig. A.8(b) shows an average value around 0.16 °C, having dropped about 0.07 °C from the peak.

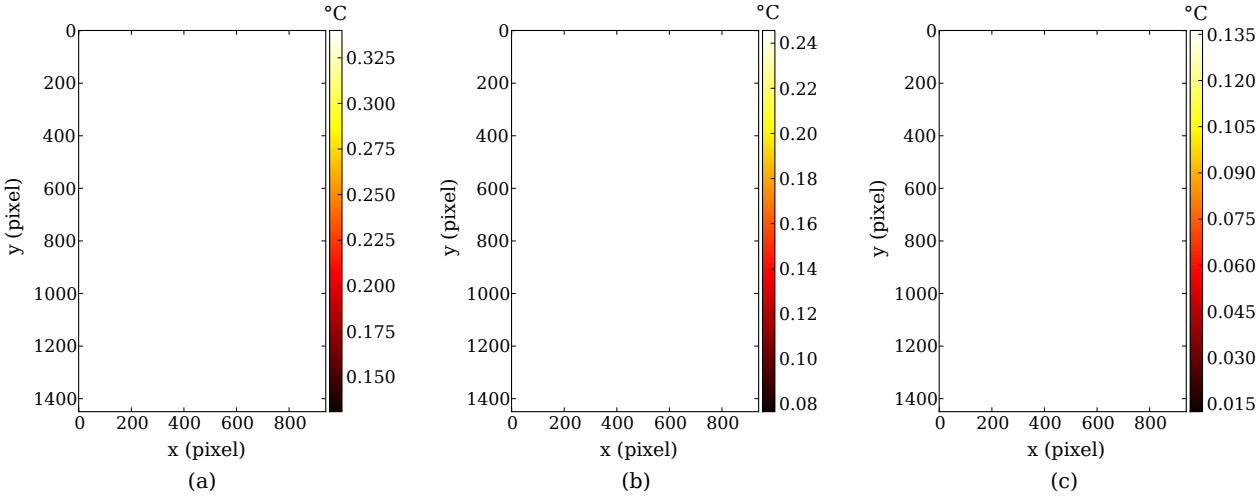

Figure A.8: (a) The temperature field obtained at the end of the test, (b) the temperature field obtained 10 s after the test and (c) the difference between (a) and (b)

It is remarkable that the temperature fields in Fig. A.8(a) and (b) demonstrate a very similar pattern in spite of their difference in absolute values. This point can be seen clearer by making their difference, resulting therefore a residual temperature field shown in Fig. A.8(c). It can be noticed that the pronounced heterogeneities in both Fig. A.8(a) and (b) are disappeared in Fig. A.8(c) which shows only a global and gradual spatial variation. If the temperature heterogeneities appeared in Fig. A.8(a) represent the true temperature variation of specimen surface but not its geometric variation, it is not reasonable that Fig. A.8(b) shows such a similar temperature heterogeneity with Fig. A.8(a) even through 10 s of cooling after the test. It is particularly abnormal when the testing material is aluminum with a very high thermal conductivity. This point can be even better seen from Fig. A.8(c)

that demonstrates the temperature variation between the two states in Fig. A.8(a) and (b) is rather global and gradual. Hence, it suggests that at least a nonnegligible part of the measured temperature is practically the artifact due to the out-of-plane effect, and this part plays a very important role in the heterogeneous distribution of measured temperature.

Since the measured temperature is a mixture of true temperature and temperature artifact due to out-of-plane effect, the artifact temperature T_{art} can be estimated via

$$T_{art} = T_{mea} - T_{tru} \tag{A.1}$$

where T_{mea} and T_{tru} stand for the measured temperature and true temperature, respectively. All the temperature terms involved represent the relative temperatures.

The temperature artifact T_{art} is expected to be resolved from Eq. A.1 for the comparison with the profile map. Since T_{tru} is not experimental accessible, a practical solution is through a complete cooling of the specimen after the tensile test until the temperature being in an equilibrium state. In this case, T_{tru} equals to zero, and T_{art} equals directly to T_{mea}. This step was, however, unfortunately absent in our test. And in all the available data, the one closest to such an ideal condition is the temperature field shown in Fig. A.8(b), obtained 10 s after the test. To take advantage of this thermal data, a hypothesis has to be made by assuming T_{tru} is uniform and equals to the average of T_{mea} in Fig. A.8(b) at this moment, i.e., $T_{tru} = 0.16$ °C. In the light of the very high conductivity of aluminum, this assumption is considered reasonable. Hence, T_{art} can be estimated by subtracting T_{tru} from T_{mea} in Fig. A.8(b), and the result is illustrated in Fig. A.9(a).

Fig. A.9(a) shows that the estimated T_{art} has both negative and positive values varying from -0.08 °C to 0.08 °C. A possible case is that in the initial configuration of lens-object, the angle of incidence was not perfectly 90° but a little lower. So when the out-of-plane deformation is produced, it may induce both decrement and increment of emissivity on the specimen surface. This leads to corresponding underestimated and overestimated temperatures in the calibration, and thus negative and positive values in the artifact temperature field. In the case of a perfect directional emissivity in the initial configuration, the T_{art} should be below zero due to out-of-plane effect. Nevertheless, the T_{tru} is an estimate in this work that has, inevitably, a deviation in absolute terms. But this will not change the spatial distribution of T_{art}, which is the key for its correlation with the profile map.

The profile map and analytical grain texture of specimen surface are shown in Fig. A.9(b) and (c), respectively. A similarity in distribution pattern between the temperature artifact and profile map is remarkable in Fig. A.9. And both of them exhibit a clear dependence on the grain texture (or crystallographic structure). Here it is also interesting to illustrate their corresponding residual image in the kinematic measurement, which represents the errors of image registration, as shown in Fig. A.9(d). The residual image exhibits a similar pattern to the other three images in Fig. A.9, which indicates the present measurement errors (both thermographic and kinematic) are caused by a common optical effect due to the out-of-plane deformation. The next step is to conduct a quantitative correlation between the temperature artifact and surface profile by taking advantage of their common grain texture.

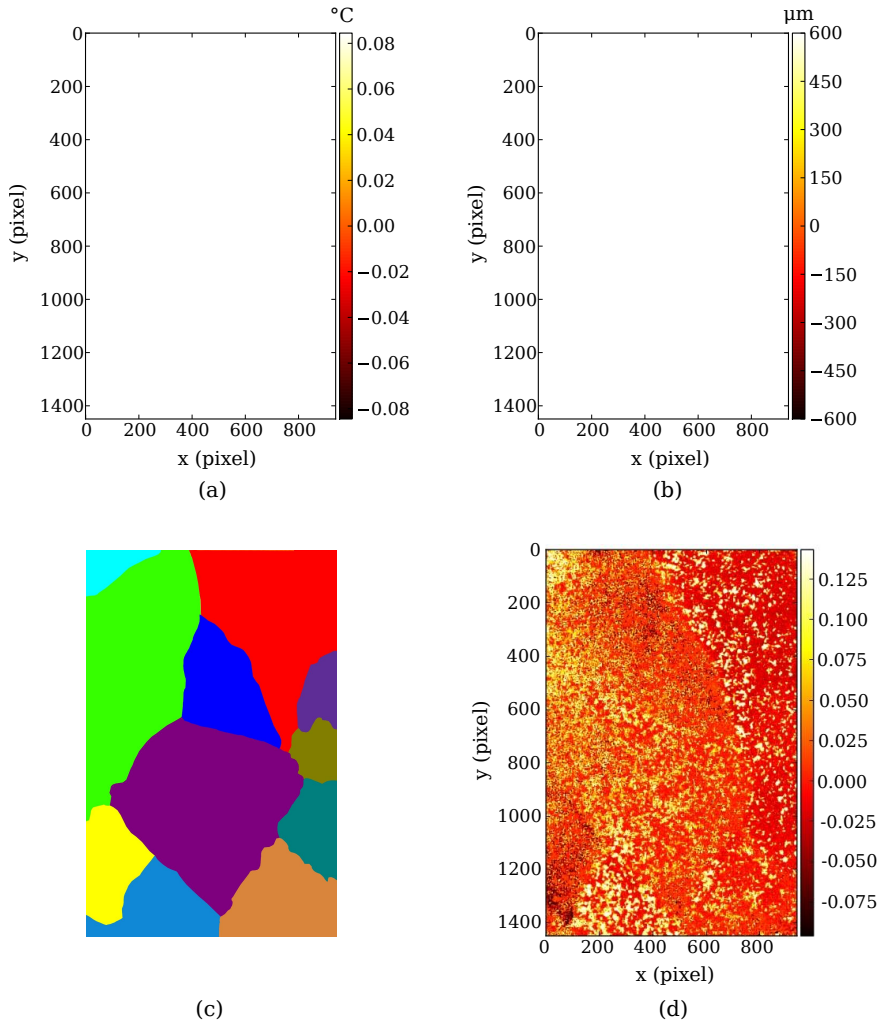

Figure A.9: (a) The estimated artifact temperature field, (b) the profile map, (c) the grain texture and (d) the residual image in the kinematic measurement

A.3.0.2 Grain texture based correlation analysis

In order to establish a quantitative relationship between the temperature artifact and specimen surface profile, some simplifying approach has to be taken. A key point is to capture their main spatial features that are closely associated with the grain texture. To this end, a grain texture based analysis is conducted in which the grains are considered as the basic analysis units.

Firstly, the profile map is expected to be expressed in a quantity that associates more directly with the out-of-plane effect. Then the term "variation of angle" is adopted, which represents the variation in angle of the deformed specimen surface with respect to its undeformed state. It practically equals to the angle of observation Ω. The idea is to calculate an approximate Ω for each grain and then use it to compare with the temperature artifact T_{art} grain by grain. To to do, a projection approach was employed. The profile data $P(x_i)$ in each grain can be fitted in planar surface according to

$$P_c(x_i) = \alpha P(x_i) + \beta \tag{A.2}$$

where $P_c(x_i)$ represents the profile data after the fitting via the first-degree polynomial with coefficients α and β, and x_i stands for the axis position of the point i in each grain.

The profile map after processing the plane fitting is shown in Fig. A.10(a). Then, the Ω for each grain can be calculated from Eq. A.2 through

$$\Omega = tan^{-1}\alpha \tag{A.3}$$

The resulting full-field distribution of Ω is illustrated in Fig. A.10(b). In addition, a grain texture with the reference grain number is also illustrated in order to identify each grain, as shown in Fig. A.10(c).

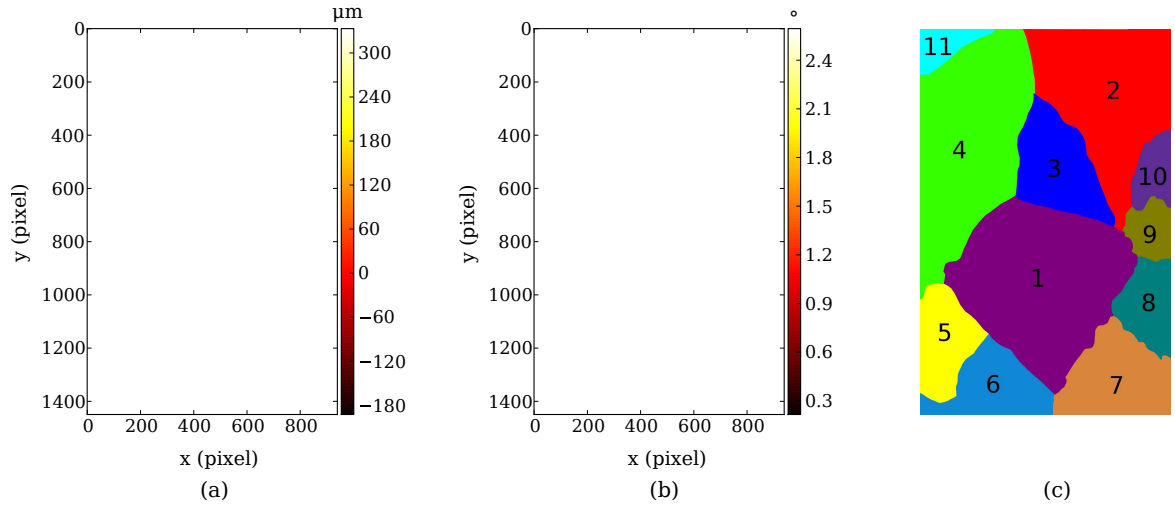

Figure A.10: (a) The profile map after the plane fitting, (b) the distribution of the estimated variation of angle Ω and (c) the grain texture with the grain number

Fig. A.10(b) shows that the angle Ω varies from 0.2° to 2.6° depending on the grain, with an average value around 1.2°. A variation of angle about 1° may bring only a minor variation of the apparent emissivity. However, this variation in apparent emissivity has a strong heterogeneous distribution feature. Thus, it is not surprising that it may play an important role in the measured thermal fields, especially under an experimental condition of very high thermal diffusion of testing material.

Since the variation of angle for each grain is provided, now its corresponding temperature artifact is sought. The most direct way is to calculate the average T_{art} for each grain, as the result shown in Fig. A.11(a). For the ease of comparison, here the map of variation of angle Ω is reproduced in Fig. A.11(b).

The data of Ω-T_{art} pairs for all the 11 involved grains are illustrated in Tab. A.1. Here the reference number for each grain is corresponding to that labeled in Fig. A.10(c).

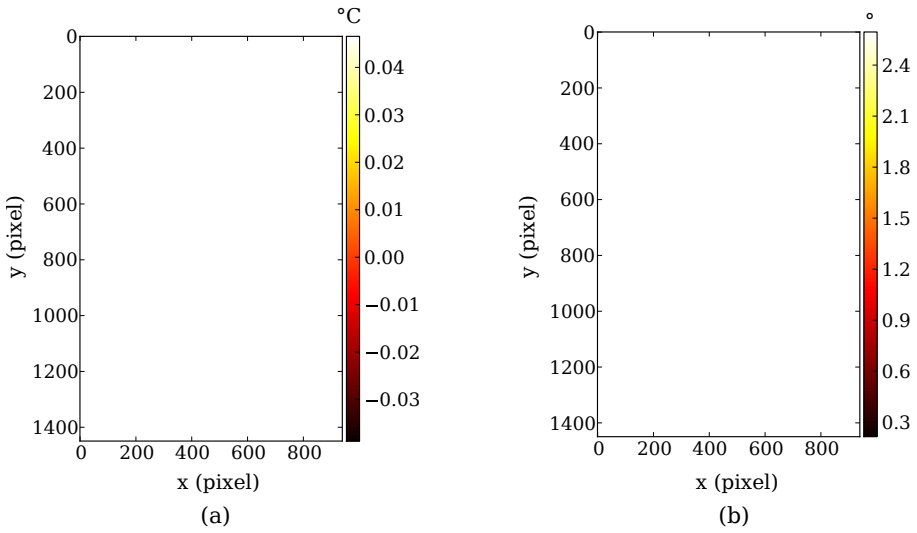

Figure A.11: (a) The simplified distribution of temperature artifact T_{art} by grain, (b) the simplified distribution of variation of angle Ω by grain

Grain number	1	2	3	4	5	6
Ω (°)	0.802	0.215	2.595	0.527	1.141	0.588
T_{art} (°C)	-0.006	-0.001	0.047	0.016	0.004	-0.033
Grain number	7	8	9	10	11	
Ω (°)	1.302	0.721	1.336	1.385	1.249	
T_{art} (°C)	-0.013	-0.028	-0.039	-0.012	0.009	

Table A.1: The data Ω-T_{art} pairs for all the involved grains

The Ω-T_{art} pairs for all grains shown in the above table can be displayed in the same graph, as shown in Fig. A.12. The present results, however, do not demonstrate a distinct correlation between the two parameters T_{art} and Ω. In view of the current level of data scattering, a conclusion can not be easily made in the Ω-T_{art} relationship.

Here it is important to note that there are different sources of errors that can be present in the above analysis. First, the parameter more appropriate to evaluate the out-of-plane effect is the apparent emissivity but not the estimated temperature artifact T_{art}. Moreover, the assessment of T_{art} is limited to the available data in the work and therefore has to be made under certain assumptions. In the estimation of the variations of angle Ω for the grains, the plane fitting is not always suitable. For example, in the grains 2 and 4 their profiles do not exhibit a near planer variation but with a certain degree of local variations within the grain. In this case, applying a plane fitting will greatly modify their initial profiles. Besides, the grain 3 also shows a relatively important deviation to the majority of data, but without a clear explanation. If the grains 2-4 are excluded in this comparison analysis, the Ω-T_{art} can demonstrate a better correlation: a positive correlation is supposed

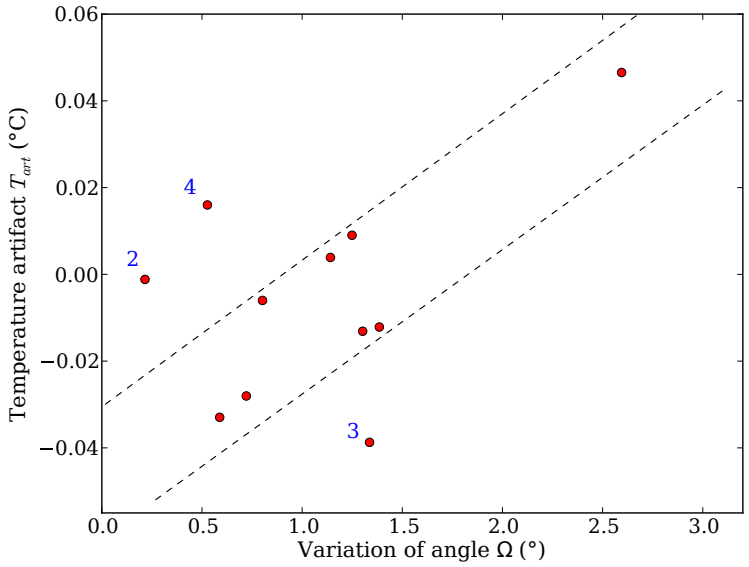

Figure A.12: Variation of angle Ω versus temperature artifact T_{art}

between the two elements, as the dashed lines indicated in Fig. A.12. Nevertheless, this is not the conclusion of this analysis. To confirm this hypothesis, we do need more data (of more grains) in Fig. A.12 which is however restricted to the limited number of grains of oligocrystal specimen.

A.4 Out-of-plane effect on kinematic measurement

The influence of the out-of-plane displacement (or deformation) in the DIC measurement has long been noticed, so the stereo-DIC system was developed for realizing a 3D measurement (Kahn-Jetter & Chu, 1990; Orteu, 2009). Concerning our case of a 2D-DIC measurement system, the out-of-plane effect on kinematic measurement is similar to that occurred in the thermographic measurement. Among the different influential elements, the reflection effect is considered as the dominant factor because of the presence of an illumination. In addition, the out-of-plane motion can change the object-lens distance, leading therefore a variation in physical resolution of the acquired images during the tensile test. This modification of spatial resolution may bring about nonnegligible errors in displacement, which can be much amplified in the strain computation (Sutton *et al.*, 2008).

The evaluation of the errors in the kinematic measurement can be realized through the residual image. In the test of aluminum oligocrystal, the residual images demonstrated that important errors were produced in the image registration since the out-of-plane deformation took place. Fig. A.13(a) shows the residual image for the final deformation state, where a special pattern closely associated with the specimen surface profile is noticeable. Its corresponding axial strain field concerning the final deformation state is shown in Fig. A.13(b), in which the loading direction is along the vertical direction. This computed strain field

displays a very similar pattern to the residual image, which are actually the parasitic errors due to the out-of-plane deformation. Hence, the kinematic measurement in this work for aluminum oligocrystals is not exportable for a precise and quantitative displacement and strain assessment.

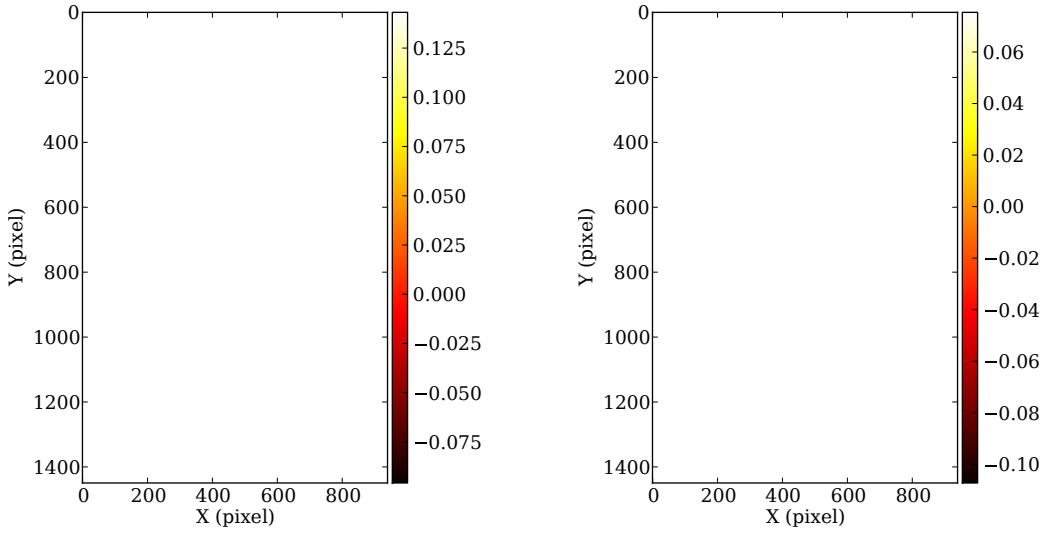

(a) (b)

Figure A.13: Concerning the final deformation state: (a) the residual image and (b) the axial strain field

In general, the out-of-plane effect on kinematic measurement is hopefully to be eliminated or at least greatly reduced by employing a stereo-DIC measurement system. It is interesting to be applied in a perspective study.

A.5 Conclusion

Tests, measurements and macroscopic analyses for aluminum oligocrystals are presented in this appendix.

Firstly, the studied material pure aluminum oligocrystal was prepared, and its crystallographic structure was specified. Then the experimental protocol for the kinematic-thermal fully-coupled measurements was detailed, and a tensile test was carried out. A remarkable phenomenon found in the experimental results was that the oligocrystal specimen had been suffered by a strong out-of-plane deformation in the tensile test, as verified by both optical observation and profile measurement on the deformed specimen.

The out-of-plane effect embodied first on the thermographic measurement, as that found in the measurement on nickel single crystals. In this analysis, subjected to the absence of an emissivity measurement, an artifact temperature field related to the out-of-plane deformation was estimated in order to characterize the out-of-plane effect. And then an analysis

was conducted to relate the temperature artifact with the profile map, and a comparison of Ω-T_{art} was analyzed particularly. The results showed that a positive correlation was possibly existed between the two elements, but a definite conclusion can not be drawn in this work as we did need more data to confirm it.

The out-of-plane effect embodied also on the kinematic measurement for aluminum oligocrystals. This can be verified in a relatively simple way through the residual image in the DIC computation. The analysis showed that the out-of-plane effect was present in the residual image and led to important errors in the computed strain fields. Thus, the kinematic measurement results on aluminum oligocrystal specimen were also not exploitable in this work. But this problem is hopefully to be eliminated or at least to be greatly reduced by employing a stereo-DIC measurement system in a perspective study.

Abstract:
This study investigates the plastic deformation based on kinematic and thermal full-field measurements and using oligo- and single crystal specimens to take advantage of their simple structures. Firstly, a metrology associated with the digital image correlation and infrared thermography is presented. Then the two techniques are coupled both in space and in time in order to follow the strain and temperature evolution of each material point during the deformation of specimen (Lagrangian Thermography). This kinematic-thermal coupled measurement has subsequently been applied to aluminum oligocrystals and nickel single crystals in the tensile tests, and the results are analyzed with respect to their respective crystallographic structures. The first phenomenon observed is the appearance, during the test, of out-of-plane deformation noticeable at the microstructure scale. This effect changes the apparent emissivity of the specimen, which disrupts thermal measurements at the local scale demonstrated by the presence of a correlation between the emissivity and the surface relief. The second phenomenon is the appearance of the bands of deformation during the tests on nickel single crystals. The kinematic measurements have then necessitated the development of a crystallographic-based projection approach which allows a good evaluation of strain field evolution. The strain heterogeneities are closely related to the slip activations according to the three distinctive regimes well determined, corresponding biuniquely to the three conventional work hardening stages.

Keywords: infrared thermography, digital image correlation, out-of-plan deformation, nickel single crystal, deformation regimes.

Titre : Étude de la déformation plastique des oligocristaux et des monocristaux basée sur des mesures de champs cinématiques et thermiques

Résumé :
Cette étude examine la déformation plastique sur la base de mesures de champs cinématiques et thermiques en utilisant des éprouvettes oligo- et monocristallines pour profiter de leurs structures simples. Dans un premier temps, la métrologie associée à la corrélation d'images numériques et la thermographie infrarouge est présentée. Ensuite, les deux techniques sont couplées à la fois dans l'espace et dans le temps en vue de suivre les évolutions de la déformation et de la température de chaque point matériel lors de la déformation de l'éprouvette (Thermographie Lagrangienne). Cette mesure couplée cinématique-thermique a ensuite été mise en oeuvre lors d'essais de traction sur des oligocristaux d'aluminium et sur monocristaux de nickel, et les résultats sont analysés en lien avec leurs structures cristallographiques respectives. Le premier phénomène constaté est l'apparition, durant l'essai, de déformations hors-plan notables à l'échelle de la microstructure. Cette effet modifie l'émissivité apparente de l'éprouvette ce qui perturbe les mesures thermiques à l'échelle locale démontré par la présence d'une corrélation entre l'émissivité et le relief apparu en surface. Le second phénomène est l'apparition de bandes de déformation durant les essais sur les monocristaux de nickel. Les mesures cinématiques ont alors nécessité le développement d'une approche de projection basée sur la cristallographie qui permet une bonne évaluation de l'évolution du champ de déformation. Les hétérogénéités de déformation sont étroitement liées aux activations du glissement selon trois régimes distinctifs bien déterminés correspondant de façon biunivoque aux trois stades classiques d'écrouissage.

Mots-clés : thermographie infrarouge, corrélation d'images numériques, déformation hors-plan, nickel monocristallin, régimes de déformation.